Wind and Boundary Driven Planetary Geostrophic Circulation in a Polar Basin

Estanislao Gavilan Pascual-Ahuir

A thesis submitted for the degree of

Doctor of Philosophy

January, 2019

School of Natural and Environmental Sciences

Faculty of Science, Agriculture and Engineering

Newcastle University

Abstract

The Arctic Ocean circulation is controlled by the interaction of many factors such as bathymetry, wind stress and volume transport across the straits connecting the basin to its marginal seas. In addition, stratification plays an important role in the 3–dimensional circulation, shielding the deep warm, salty water of Atlantic origin from the surface cold, relatively fresh layer. However, it is not clear how these factors interact together and how their relative contribution to the circulation will change as the Arctic warms. This thesis focuses on a subset of the factors determining the circulation of the Arctic. We confine our attention to homogeneous wind and boundary forced flows in a polar basin with a range of idealised topographies. New analytical solutions using a beta–sphere approximation first proposed by Imawaki and Takano (1974) are obtained for boundary and wind forced planetary geostrophic circulation. These solutions are compared with equivalent numerical solutions using the NEMO modelling system to evaluate the fidelity of the beta–sphere approximation. Then, numerical solutions are determined for planetary geostrophic flow in basins more representative of the Arctic, containing a transpolar ridge and variable width continental shelves. We found the role of shelf break currents connecting the straits is ubiquitous. A new dispersion relation for planetary waves is derived on the beta–sphere and compared with the equivalent dispersion relation on the polar plane (LeBlond, 1964). The thesis also examines numerical time dependent solutions of the unsteady circulation driven by harmonically perturbation transport varying in time across one (typically the Bering) of three straits. Vorticity waves then determine the evolution of the resulting sea surface height anomaly field. It is demonstrated that a non–uniform width shelf fundamentally controls the partition of the circulation between the Davis and Nordic Strait when the Bering Strait transport is perturbed. The final chapter of the thesis briefly sums up the most important results obtained in this study.

To Pilar Giner Albalate

Acknowledgements

This thesis is the result of 4 years of research at Newcastle University. During this time I have benefited from the guidance and patience of my supervisors who shared with me invaluable knowledge in numerical modelling and physics. I always will be indebted to Prof. Andrew Willmott and Dr. Maria Luneva who have given me the opportunity to take part in this study and taught me to be inquisitive. A big thank to Dr. Miguel Morales Maqueda who also helped to overcome the different challenges that I encountered in numerical modelling.

I would like to give special thanks to the institutions of Newcastle University and National Oceanographic Centre in Liverpool for their computer installations and resources, without which I would not have been able to complete this investigation.

I would like to thank Dr. Agatha De Boer for letting me participate in an exciting collaboration project with Stockholm University. It was the first time I was able to work in a team with another institution.

I would like to acknowledge the support of my family and friends from both countries (Spain and UK) who were always concerned about my well-being and my project. Specially, Alessandro Carchen, Brian Newman, Theodora Koukaki and Richard Carter who also helped me to correct the grammar of this thesis. Finally, I am deeply indebted to my beloved Li Mengmeng who has been always there to encourage me and making me smile in the most difficult moments.

Contents

List of Figures

List of Tables

Chapter 1

Introduction

A retreat of the summer sea ice extent has been observed in the Arctic Ocean during the 21st century (Wang and Overland, 2009; Stroeve *et al.*, 2012; Walsh *et al.*, 2017). The sea ice extent record showed a recession in every month from 1978 to 2013 (Meier *et al.*, 2014). In particular, the annual average of sea ice extent had a negative trend of -4.5% along the latter record, although during the years $2001-2013$ this slope was even more pronounced (-6%). Comiso (2011) noted a decline of the sea ice area during the period $1978-2010$ observing the perennial and the multi–year winter ice area decreased 12.2% and 13.4% per decade, respectively. The loss of sea ice in the Arctic Ocean has a number of important consequences for the physics and biogeochemistry of the basin and its role in the regional and global climate. For example, the location and rates of deep water formation will change (Rahmstorf *et al.*, 2015), methane hydrates on the shelf might become unstable (Vandenberghe *et al.*, 2012) and primary (e.g. phytoplankton) production might increase (Arrigo and Dijken, 2015). Furthermore, the retreat of the Greenland the ice sheet will contribute to the increase of sea level (Kjeldsen *et al.*, 2015). Therefore, an understanding of Arctic System Science is paramount to unravel the complexity of the processes coupling the biology, geology, biogeochemistry, and physics of the Arctic Ocean and its coupling to the atmosphere. One facet of this interdisciplinary field of study is the change of the circulation of the Arctic Ocean that will occur (perhaps, in a few decades) compared with the present–day where sea ice cover is predominantly seasonal.

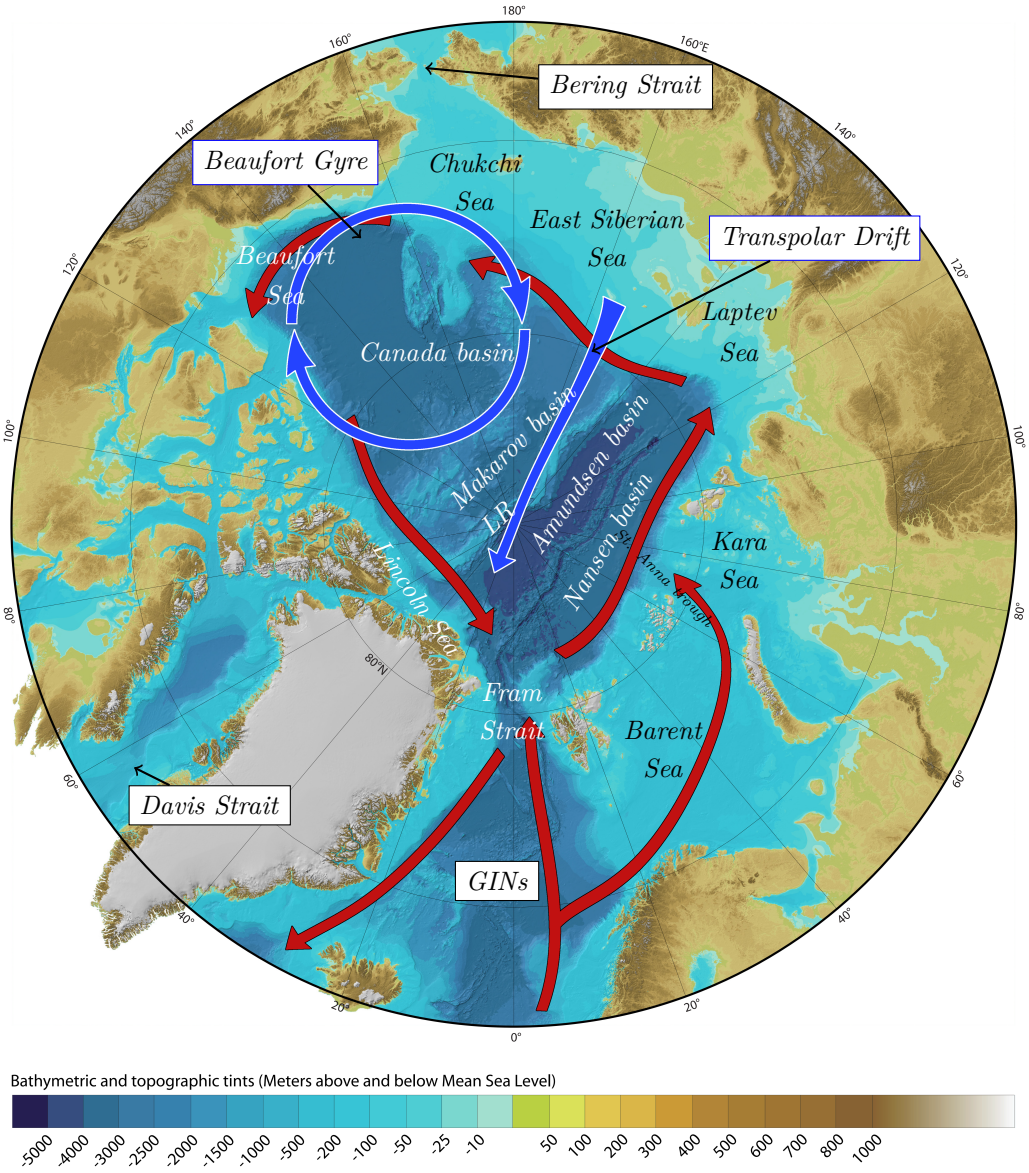

Figure 1.1: Arctic Ocean (after Jakobsson *et al.*, 2012). Red and blue arrows represent the Atlantic and the Arctic water circulation, respectively.

The Arctic Ocean is contained in a polar basin connected to the global ocean via the Greenland–Iceland–Norway Seas (GINs), Bering and Davis Straits (Figure 1.1). The International Hydrographic Organisation (IHO, 2002) defined the Arctic Ocean as the area inside the Bering Strait, Davis Strait and Iceland representing 4.3% (or approximately $15.5 \times 10^6\ km^2$) of the total ocean area. However, Jakobsson (2002) considered the Arctic Ocean as the volume of water limited by the Bering Strait, Canadian shelf, Fram Strait and Barent Sea decreasing its area to $9.5 \times 10^6\ km^2$. The Arctic Ocean is partitioned by the Lomonosov Ridge (LR) into two deep basins; the Amerasian and Eurasian Basin. The Amerasian Basin includes the Canada and Makarov Basin which are bounded by the East Siberian, Chukchi, Beaufort, Canada and Lincoln shelf seas. The Eurasian basin

is formed by the Amundsen and Nansen Basin which are bounded by the Fram Strait, Barent, Kara and Laptev Seas. Another noteworthy statistic is that 53.3% of the Arctic Ocean is covered by shelf seas (Jakobsson *et al.*, 2012).

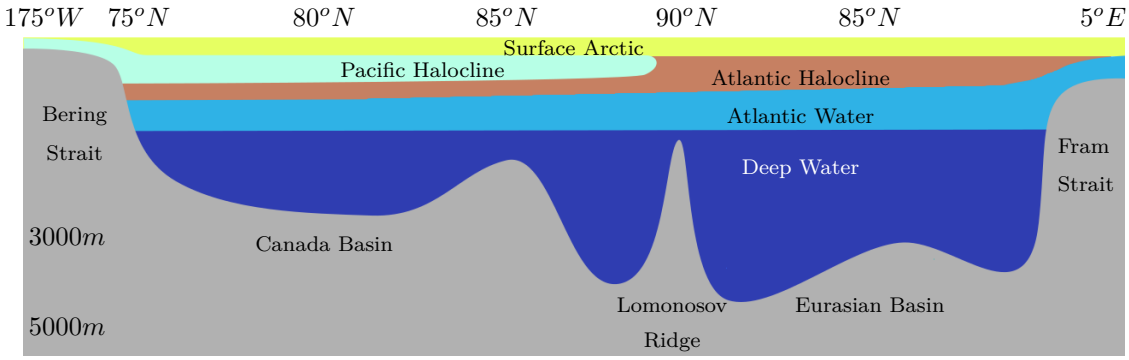

Figure 1.2: Water masses in the Arctic Ocean (*Source: Wikimedia Commons*).

The physical proprieties of the water masses of the Arctic Ocean show three distinct types (see Figure 1.2); Arctic Water, Atlantic Water and Deep Water (Pickard and Emery, 2002; Rudels, 2015). The Arctic Water layer ranges from the sea surface to 200 m (Pickard and Emery, 2002). The circulation in this layer is characterised by two main wind driven surface currents; the Beaufort Gyre and the Transpolar Drift current. The Beaufort Gyre is an anticyclonic wind-driven closed circulation located in the Canadian basin whereas the transpolar drift is a current which crosses the basin, passing through the North Pole towards the Fram Strait (see blue arrows in Figure 1.1). This layer is itself comprised of three sub–layers which vary in salinity and temperature. The surface Arctic (0 to 50 m) has salinity and temperature influenced by the run-off, melting and freezing of sea ice. Second, there is a sub-surface Arctic layer spanning the depth range 50 to 100 m whose hydrographic properties depend on location in the Arctic Ocean. In the Eurasian basin the temperature remains almost constant in the top 100 m below which there is a strong halocline (see Figure 1.2). The Canada basin displays a similar salinity profile but the temperature attains a maximum at 50–100 m and minimum (approximately at 150 m) before increasing again (Steele *et al.*, 2004). This particular peak in the temperature is due to the inflow from the Bering Strait (first maximum) followed by the Atlantic halocline. The lower Arctic is characterised by intermediate waters between fresh and salty from the surface Arctic and Atlantic layers. The Atlantic layer is characterised by a warm and salty layer spanning the depth range 150 to 900 metres at Spitsbergen (Aksenov *et al.*, 2010). However, this layer becomes increasingly deeper due to mixing processes

reaching 500–900 metres in the Canadian basin (Zhong and Zhao, 2014). The Atlantic water enters into the Arctic basin through the Fram Strait and the Barent Seas forming the Arctic Circumpolar Boundary current (Aksenov *et al.*, 2011). Subsequently, it flows cyclonically following the shelf–break of the Siberian shelf and then the Canada shelf exiting through the Fram Strait forming the East Greenland current (see red arrows in Figure 1.1). Lastly, there is a deep cold salty water layer below 900 m that also circulates cyclonically (Rudels, 2015).

Traditionally, the Arctic Ocean has been considered a "Mediterranean sea" of type B due to its limited connection to the rest of the oceans and its positive balance between precipitation minus evaporation. The circulation in these types of marginal seas is controlled by thermohaline forcing which, ultimately, depends on the balance between inflows and outflows present in the basin (Tomczak and Godfrey, 2002). Therefore, it was initially thought that volume transport across the main straits (Davis, Fram and Bering Straits) controlled the Arctic Ocean circulation (Nansen, 1902). Gordienko (1958) suggested that the North Atlantic (NA) current was controlling the Arctic Ocean circulation because it represented the highest volume transport across the straits into the Arctic basin. The NA current inflow has been extensively studied, showing strong seasonal and inter-annual variability with transport ranging $3 - 15$ Sv (Beszczynska-Möller *et al.*, 2012; Aksenov *et al.*, 2011; Rudels, 2015). Furthermore, its variability has a high correlation with the North Atlantic Oscillation (NAO) index (Wanner *et al.*, 2001). There are also a number of studies relating the NAO index to the Arctic Ocean circulation (Dickson *et al.*, 2000; Delworth *et al.*, 2017). The NAO index is an regional atmospheric sea surface pressure pattern, characterised by an anticyclonic and cyclonic cell over the Azores and Iceland, respectively. The positive phase of the NAO index strengthens the NA current transport into the Arctic basin. This warms the surface Arctic layer, thinning the sea ice, which leads to an increased export of sea ice via East Greenland Current (Dickson *et al.*, 2000). During the negative phase of the NAO, the NA current decreases creating colder conditions in the Arctic basin, and increased thermodynamic sea ice formation. This mechanism was able to explain the observed anomalous freshwater exported from the Arctic Ocean (Dickson *et al.*, 2000). However, there was significant export of freshwater into the Atlantic, namely the Great Salinity Anomaly (GSA) event in the late 1960s which could not be explained by the NAO index (Aagaard and Carmack, 1989). Modelling and predicting the phases of the NAO index are still in their infancy (Stephenson *et al.*, 1999; Kim *et al.*, 2012).

Thompson and Wallace (1998) studied another atmospheric climate signature, namely the atmospheric polar vortex in the North Hemisphere which has its centre in the Arctic basin; often referred to as the Arctic Oscillation (AO). In comparison with NAO index, the AO is the North Annular Mode (i.e. hemisphere scale patterns) which can alter the wind stress regime in the Arctic basin depending on the phase. The positive phase of the AO is characterised by the strengthening of the polar vortex (or cyclonic wind stress regime) increasing the intensity of the transpolar current and decreasing the height of the Beaufort Gyre (Rigor *et al.*, 2002; Zhang *et al.*, 2003). This produces an increasing divergence of sea ice, warming the surface Arctic layer and thinning the ice. In addition, there is an increase of freshwater and sea ice export across the Fram Strait. In the negative phase of the AO index (anticyclonic wind stress pattern), the opposite happens; there is a decrease in the strength of the polar vortex, enhancing the formation of a strong anticyclonic wind stress regime in the Beaufort Sea. The change in the wind stress regime enhances the convergence of sea ice and sea ice formation in the Beaufort gyre, by shielding the surface Arctic layer from the solar radiation. This idea was further supported by the numerical study of Proshutinsky and Johnson (1997) and the observations (Zhang *et al.*, 2003; Rabe *et al.*, 2014). However, there are studies that claim the AO is actually a phenomenon produced as a consequence of the Pacific–North American oscillation and NAO (Deser, 2000; Ambaum *et al.*, 2001). Also, the variability of the AO index does not explain the formation of the GSA at the end of 1960s.

Proshutinsky and Johnson (1997) proposed that the barotropic Arctic Ocean circulation is driven by wind stress that exhibits two distinct oscillatory patterns over a quasi–decadal time scale. Their index, namely the AOO (Arctic Ocean Oscillation), is not obtained by analysing the surface pressure anomalies. Instead, they compute the index using the mean annual sea surface height (SSH) field. They calculate the difference between the sea surface elevation peak at the centre and the periphery of the closed circulation in the Arctic basin (i.e. Beaufort Gyre). Subsequently, it is divided by the distance between both points (Proshutinsky *et al.*, 2015). Thus, a positive (negative) index is determined by a positive (negative) horizontal gradient of sea surface elevation. The positive phase of the AOO index (anticyclonic wind regime) is characterised by a strong Beaufort Gyre, cooling the Arctic surface layer, increasing the sea ice formation and decreasing the strength of the inflow and outflow through the Barent Sea and Fram Strait respectively. The negative phase of the AOO index (cyclonic wind regime) is characterised by a decrease in strength of the Beaufort Gyre, increasing the export of sea ice. This phase

enhances the inflow from NA current, warming the Arctic surface layer (Proshutinsky and Johnson, 1997). Dukhovskoy *et al.* (2006) developed a simple box model to explain how the anticyclonic and cyclonic regimes were coupled with the ocean currents. Furthermore, they recognised the importance of the GINs controlling the periodicity of these wind stress regimes. This box model offers an explanation of GSA anomaly and also the anomalous persistent anticyclonic wind stress regime observed since the early 2000s. Dukhovskoy *et al.* (2006) results suggested that the latter event is a consequence of the anomalous freshwater flux into the Arctic basin from the GINs. Also, this index is supported by numerical experiments of Proshutinsky *et al.* (2011) conducted in a closed basin with realistic topography using a coupled atmosphere–ocean–sea ice model. This study showed that the wind–driven circulation could reproduce observed conditions in the Arctic Ocean. However, Proshutinsky *et al.* (2011) could not explain the variability of the NA current though the Fram Strait. Also, other numerical studies assert that similar surface Arctic layer circulation can be generated by buoyancy forcing (Spall, 2013).

The relative importance of the driving mechanisms of the Arctic Ocean circulation remain unclear, particularly as the region experiences rapid warming (Polyakov *et al.*, 2010; Semenov and Latif, 2012). Clearly, the wind stress, the strength of the NA current, and buoyancy forcing all play a role in controlling the circulation. In addition, the topography steers the quasi–geostrophic circulation leading to rim currents (Aksenov *et al.*, 2011) the direction of which appears to be linked to their potential vorticity (Yang, 2005; Karcher *et al.*, 2007). Although these studies investigate the Arctic Ocean circulation using a variety of numerical models (i.e. barotropic, baroclinic, coupled sea ice–ocean models), there is clearly scope to develop "process models" to investigate the particular driving mechanisms that are at play in this basin.

In this thesis we study the impact of topography, wind stress and the forcing associated with barotropic currents through the major Arctic straits on planetary barotropic geostrophic circulations in an idealised polar basin. Chapter 2 develops a new analytic source–sink boundary driven barotropic planetary geostrophic circulation model in a polar basin with simple topography using a "beta–sphere" approximation first proposed by Imawaki and Takano (1974). Although the shelf geometry is highly idealised it indicates the importance of topographic steering on planetary geostrophic circulation, albeit in the absence of wind stress forcing. The results of Chapter 2 also reveal the importance of planetary waves in spinning-up the large scale circulation. These waves are studied in their own right in Chapter 3, in the context of a polar basin. Chapter 3 derives the dis-

persion relation for inertia-gravity waves as well as planetary waves using the "β-sphere approximation". The results of Chapter 2 and 3 are used in understanding the results in Chapter 4 which employs the NEMO (Madec, 2008) numerical community ocean model to study the planetary geostrophic circulation in a polar basin with more realistic representations of the Arctic basin topography such a ridge and a non-uniform width continental shelf. The NEMO model simulations also provide a benchmark to valid the approximate analytical results derived in Chapter 2. Wind-driven circulation in a polar basin is studied in Chapter 5 and 6. Chapter 5 develops an analytical model for an wind–driven planetary geostrophic circulation in a polar basin. Chapter 6 employs NEMO model to study the circulation driven by a more realistic representations of the wind stress as discussed in (Proshutinsky and Johnson, 1997). So far all the previous chapter only study steady source-sink flow. Chapter 7 explores another important aspect of the Arctic Ocean circulation; driving of the Arctic SSH anomaly field by unsteady volume transport through the Arctic straits. Specifically, we study the SSH anomaly field generated by unsteady perturbation volume transport fluxes imposed across one, or more, straits on the boundary of the polar basin. The aim is to study the structure of the SSH anomaly field as a function of the period of the unsteady volume transport across the straits both with, and without, topography. Chapter 8 summarises the most important results in the thesis and proposes the direction of future research aimed at understanding the structure of ice-free circulation in the Arctic.

Chapter 2

Source-sink driven planetary flows in a polar basin; analytical studies

2.1 Introduction

The development of analytical process models describing the barotropic circulation of an ocean in a polar cap - a prototype model for the Arctic Ocean - remain few and far between in the published literature. The reason for this is clear, as noted by LeBlond (1964). LeBlond considers the linearised equations governing unsteady, barotropic circulation on a tangent plane to the spherical Earth at the pole. The paper sets out to develop an approximation equivalent to the well known mid-latitude "β-plane". Let θ be the co-latitude (or the difference between 90^o and the latitude), in which case the Coriolis parameter $f = 2\Omega\cos\theta$ where Ω is the angular frequency of the rotation of the Earth. In terms of plane polar coordinates (r, φ) in the plane of projection LeBlond (1964) notes that

$$\begin{aligned} f &= 2\Omega\left(1 - \frac{\theta^2}{2} + ...\right), \\ &= 2\Omega\left(1 - \frac{1}{2}\left(\frac{r}{R}\right)^2 + ...\right), \end{aligned} \tag{2.1}$$

where R and r are the radius of the Earth and the radial distance from the North pole, respectively. For dynamics on the "polar plane" with the horizontal length scales satisfying the constraint.

$$\left(\frac{r}{R}\right)^2 << 1,$$

LeBlond (1964) introduces the "polar β-plane approximation" in which

$$f \approx 2\Omega, \tag{2.2a}$$

$$\frac{df}{dr} \approx -\frac{2\Omega r}{R^2}, \tag{2.2b}$$

which follows immediately from (2.1).

The analytical treatment of linearised barotropic dynamics on the polar plane is clearly complicated by the non-uniform meridional gradient of the Coriolis parameter, as expressed by (2.2b). Nevertheless, analytical results have been obtained in a polar basin on the polar plane by Luneva *et al.* (2012) a study of geostrophic adjustment and by Willmott and Luneva (2015) for a study of barotropic steady wind and boundary driven circulation. In the latter study it is not surprising to find that exact solutions for the circulation are given in terms of a class of orthogonal polynomials, namely Bessel functions, and this arises from a non-constant coefficient barotropic potential vorticity equation by virtue of (2.2b). Computationally simpler approximate steady-state solutions for such flows are also presented by Willmott and Luneva (2015) using boundary layer methods that exploit a small parameter based on the magnitude of bottom friction.

An alternative, and somewhat overlooked method, for developing analytical solutions for steady, boundary driven flow on a polar cap (with simple topography) is the subject of this study. We utilise an approximation first proposed by Imawaki and Takano (1974) for simplifying the linearised barotropic vorticity equation on a spherical cap in the presence of dissipation. Full spherical geometry is retained in the derivation of this equation and thereafter the co-latitude is fixed in the coefficients of this partial differential equation. Analytical solutions for the resulting constant coefficient second order partial differential equation can then be obtained using classical methods. Indeed, we utilise this approximation in this chapter to develop new analytical solutions for steady barotropic circulation in a polar cap in the presence of simple shelf topographic features which are driven by exchange of fluid through open boundaries.

"The Imawaki and Takano approximation" will hereafter be referred as the "β-sphere" approximation in this thesis. Alternatively the abbreviation "IT approximation" is also a viable candidate, used in Willmott and Gavilan Pascual-Ahuir (2017), was demonstrated to be extremely accurate by Kitauchi and Ikeda, 2009, at least for steady-state planetary circulation. These authors derived the exact analytical solution in terms of Legendre polynomials for steady, source-sink driven flow in a polar cap in the presence of Laplacian friction.

In this Chapter, we present the analytical solution for a barotropic steady planetary source-sink circulation in a circular flat bottom and step-shelf polar basin using the "β-

sphere" approximation. This problem is firstly solved using linear bottom friction as a dissipation term. Secondly, the same problem is solved using the Laplacian eddy diffusivity as a dissipation term. In comparison to Imawaki and Takano (1974), we only consider a simplified lateral friction (i.e. boundary layer approximation). Thirdly, these solutions are extended to a step-shelf basin. Finally, we consider a basin with 3 gaps representing the three main straits in the Arctic basin; Bering, Davis and GINs straits.

2.2 Analytical approach

We consider an ocean of uniform density, ρ, on a polar cap. A spherical polar coordinate system is adopted where θ and φ denote the co-latitude and longitude (i.e azimuthal) angle, respectively, and θ_B is the co-latitude of the boundary of the polar cap. Therefore, $\theta \in [0, \theta_B)$ and $\varphi \in [0, 2\pi)$. The unit vectors $\hat{\boldsymbol{k}}, \hat{\boldsymbol{\theta}}, \hat{\boldsymbol{\varphi}}$ form a right-handed triad where

$$\hat{\boldsymbol{k}} \wedge \hat{\boldsymbol{\theta}} = \hat{\boldsymbol{\varphi}},$$

and $\hat{\boldsymbol{k}}$ is directed in the radial direction (see Figure 2.1) The steady-state linearised shallow water momentum equations take the form

$$f\hat{\boldsymbol{k}} \times \mathbf{u} = -g\nabla\eta + Dissipation + \frac{\boldsymbol{\tau}}{\rho H}, \tag{2.3}$$

where $\boldsymbol{u} = u\hat{\boldsymbol{\varphi}} + v\hat{\boldsymbol{\theta}}$, $f = 2\Omega\cos\theta$, $\boldsymbol{\tau}$ is the wind stress, η is the dynamic free surface elevation and g is the gravitational acceleration. We consider two forms for the dissipation term:

$$-\frac{\mu}{H}\boldsymbol{u}, \tag{2.4a}$$

$$\frac{A_H}{R^2}\boldsymbol{u}_{\theta\theta}, \tag{2.4b}$$

Expression (2.4a) represents linear (Rayleigh) bottom friction where μ is the constant bottom friction parameter and H is the undisturbed ocean depth. Alternatively, we introduce an approximate form for the eddy viscosity in the (2.4b), where A_H is the constant eddy viscosity and R is the radius of the Earth. Imawaki and Takano (1974) adopt the Laplacian eddy viscosity $A_H\nabla_H^2\boldsymbol{u}$ in their study of source-sink driven flow on a flat bottom spherical cap, where ∇_H^2 is the Laplacian operator. We extend the solutions of Imawaki and Takano by introducing a step–shelf, but in doing so, we retain the dominant terms in the Laplacian frictional boundary layers that are present at the uniform width shelf edge, $\theta = \theta_S$, and adjacent to the polar cap boundary $\theta = \theta_B$. Therefore, (2.4b)

retains the term with the highest number of derivatives in the $\hat{\boldsymbol{\theta}}$-direction which is a familiar approach in the analysis of boundary layer dynamics (Pond and Pickard, 1983, Chapter 9). A rigid-lid approximation is adopted allowing the introduction of a transport streamfunction $\psi(\varphi, \theta)$ where

$$Hu = \frac{1}{R}\psi_\theta, \qquad Hv = \frac{-1}{R\sin\theta}\psi_\varphi. \tag{2.5}$$

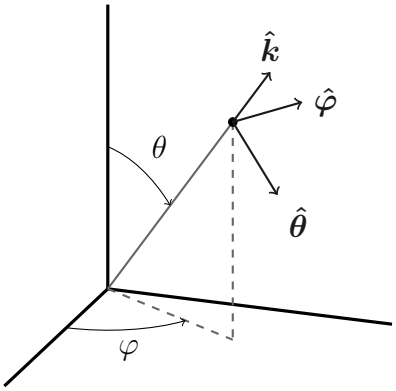

Figure 2.1: Schematic of the spherical polar coordinate system showing the unit vectors $\hat{\boldsymbol{k}}$, $\hat{\boldsymbol{\theta}}$ and $\hat{\boldsymbol{\varphi}}$ that form a right-handed triad

2.2.1 Source-sink driven solutions in the presence of bottom friction

a Flat bottom basin

In this subsection we derive solutions for the steady-state planetary geostrophic circulation in a circular flat bottom basin where the north pole is located at the centre of the domain. The circulation is driven by a prescribed inflow/outflow across two open boundaries. The open boundaries, or gaps, are located at co-latitude θ_B. The mid-point of each gap lies on the diameter of $\varphi = 0$ and $\varphi = \pi$ (see Figure 2.2).

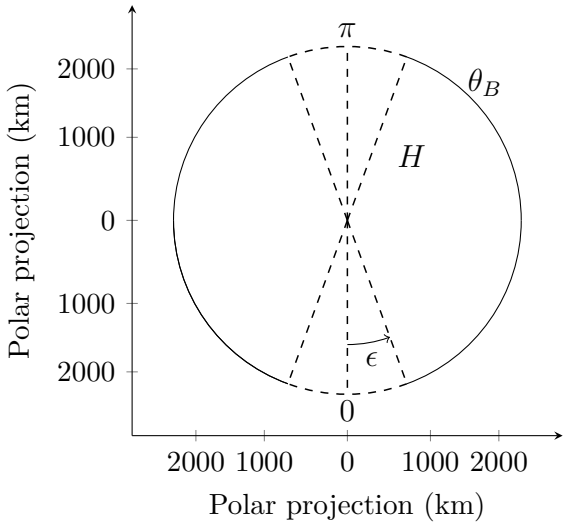

Figure 2.2: Circular polar basin with diametrically opposed gaps on the boundary.

We adopt bottom friction (2.4a) in this subsection and set $\boldsymbol{\tau} = 0$. The vorticity equation is obtained by taking the curl of (2.3).

$$-fu_\varphi - (fv\sin\theta)_\theta = \left(\mu\frac{u\sin\theta}{H}\right)_\theta - \left(\mu\frac{v}{H}\right)_\varphi. \tag{2.6}$$

In terms of ψ, defined by (2.5), the vorticity equation takes the form

$$-f\frac{1}{HR}\psi_{\varphi\theta} - \left(-\frac{f}{HR}\psi_\varphi\right)_\theta = \left(\mu\frac{\sin\theta}{H^2R}\psi_\theta\right)_\theta - \left(\mu\frac{-1}{H^2R\sin\theta}\psi_\varphi\right)_\varphi. \tag{2.7}$$

Expanding the partial derivatives we obtain

$$-\frac{2\Omega\sin\theta}{HR}\psi_\varphi = \frac{\mu}{H^2R}\left(\cos\theta\psi_\theta + \sin\theta\psi_{\theta\theta}\right) + \frac{\mu}{H^2R\sin\theta}\psi_{\varphi\varphi}. \tag{2.8}$$

We multiply equation (2.8) by $\mu^{-1}H^2R\sin\theta$ and rearrange:

$$\psi_{\varphi\varphi} + A\psi_{\theta\theta} + B\psi_\theta + C\psi_\varphi = 0, \tag{2.9}$$

where the coefficients A, B and C in (2.9) are defined as

$$A \equiv \sin^2\theta, \qquad B \equiv \sin\theta\cos\theta, \qquad C \equiv 2\Omega H\mu^{-1}\sin^2\theta. \tag{2.10}$$

Hereafter, we apply the "β-sphere approximation" and fix $\theta = \theta_f$ in (2.10), the typical value being mid-way between the pole and $\theta = \theta_B$ (i.e. $\theta_f = 0.5\theta_B$). The sensitivity of the solutions to θ_f is considered later. Equation (2.9) then becomes a constant coefficient linear 2^{nd} order partial differential equation which can be solved using classical analytical techniques.

We prescribe the streamfunction on the basin boundary:

$$\psi(\varphi,\theta_B) \equiv \psi_B(\varphi) = \psi_0 \begin{cases} \varphi/\epsilon & if \quad 0 \le \varphi \le \epsilon, \\ 1 & if \quad \epsilon \le \varphi \le \pi-\epsilon, \\ 1-[\varphi-(\pi-\epsilon)]/\epsilon & if \quad \pi-\epsilon \le \varphi \le \pi+\epsilon, \\ -1 & if \quad \pi+\epsilon \le \varphi \le 2\pi-\epsilon, \\ -1+[\varphi-(2\pi-\epsilon)]/\epsilon & if \quad 2\pi-\epsilon \le \varphi \le 2\pi. \end{cases} \tag{2.11}$$

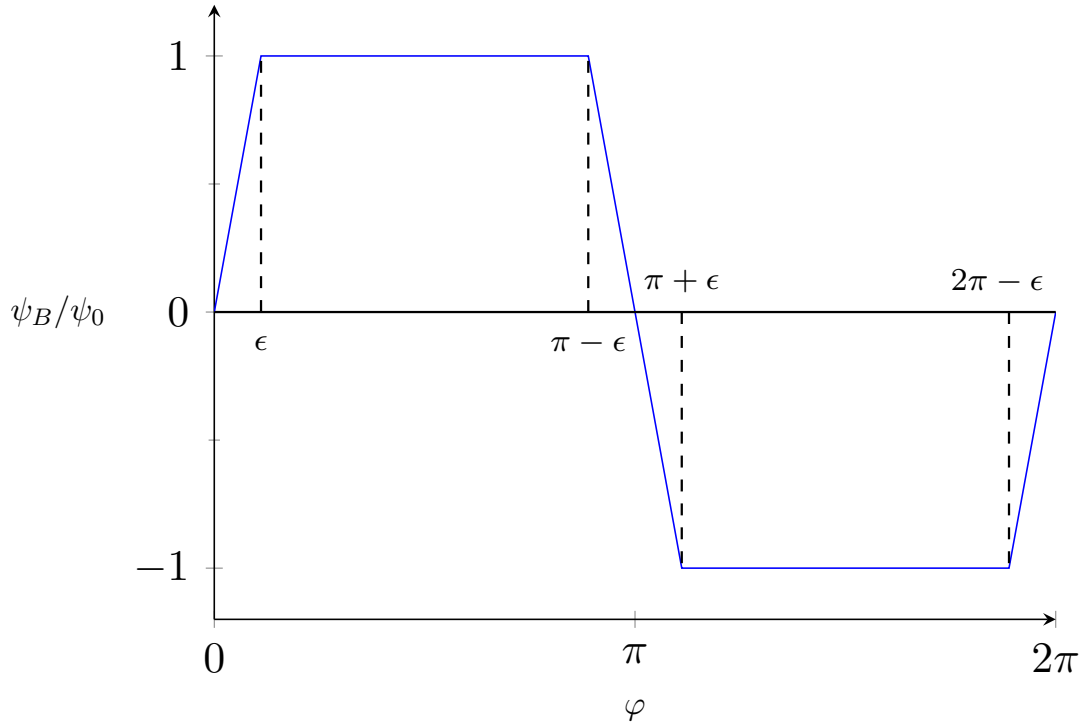

Figure 2.3: Schematic of the scaled streamfunction prescribed on the boundary (2.11). The width of each strait is $2\epsilon R\sin\theta_B$.

The streamfunction (2.11) describes steady boundary flow across the gaps located at $[-\epsilon,\epsilon]$ and $[\pi-\epsilon,\pi+\epsilon]$. The direction and magnitude of the flow can be obtained by the integration of total transport across the straits. Across the strait $[-\epsilon,\epsilon]$, the transport is given by

$$T = R\sin\theta_B \int_{-\epsilon}^{\epsilon} Hv\,\mathrm{d}\varphi, \tag{2.12}$$

where T is the total transport and v is the velocity component in the θ–direction. Substituting (2.5) into (2.12) yields,

$$\begin{aligned} T &= \int_{-\epsilon}^{\epsilon} -\psi_\varphi\,\mathrm{d}\varphi, \\ &= -\psi|_{-\epsilon}^{\epsilon} = -2\psi_0. \end{aligned} \tag{2.13}$$

Therefore, the volume transport (2.13) is directed towards the pole when $\psi_0 > 0$. Across the other strait we find the opposite situation (see slope Figure 2.3) occurs.

At the pole (2.9) requires that

$$\psi_{\varphi\varphi} = 0 \quad \text{at} \quad \theta = 0. \tag{2.14}$$

We seek a solution of (2.9) of the form

$$\psi(\varphi, \theta) = a_0(\theta) + \sum_{n=1}^{N} \left[a_n(\theta) \cos n\varphi + b_n(\theta) \sin n\varphi\right], \tag{2.15}$$

where a_n $(n = 0, 1, .., N)$ and b_n $(n = 1, .., N)$ are functions to be determined. Note (2.15) ensures ψ will be 2π–periodic in φ. Substituting (2.15) into (2.9) and collecting the coefficients of $\cos(n\varphi)$ and $\sin(n\varphi)$ we obtain

$$\left.\begin{aligned} -a_n n^2 + A\ddot{a}_n + B\dot{a}_n + Cb_n n = 0 \\ -b_n n^2 + A\ddot{b}_n + B\dot{b}_n - Ca_n n = 0 \end{aligned}\right\} \quad n \geq 1, \tag{2.16a}$$

and

$$A\ddot{a}_0 + B\dot{a}_0 = 0. \tag{2.16b}$$

Introduce the complex function

$$Z_n = a_n + ib_n \quad n \geq 1, \tag{2.17}$$

in which case (2.16a) can be combined in a single equation for Z_n

$$A\ddot{Z}_n + B\dot{Z}_n - \left(n^2 + inC\right) Z_n = 0 \quad n \geq 1, \tag{2.18}$$

where $\dot{Z}_n \equiv dZ_n/d\theta$. The general solution for (2.18) given by

$$Z_n = R_n e^{\lambda_{1n}\theta} + S_n e^{\lambda_{2n}\theta}, \tag{2.19}$$

where λ_{1n} and λ_{2n} are the roots of the auxiliary equation

$$A\lambda_n^2 + B\lambda_n - \left(n^2 + inC\right) = 0, \tag{2.20}$$

Thus,

$$\left.\begin{matrix} \lambda_{1n} \\ \lambda_{2n} \end{matrix}\right\} = \frac{-B}{2A} \pm \frac{1}{2A}\{B^2 + 4A\left(n^2 + inC\right)\}^{1/2}, \tag{2.21}$$

The arbitrary constant R_n and S_n are be obtained by subjecting (2.19) to

$$Z_n = 0 \qquad \text{at} \qquad \theta = 0, \tag{2.22a}$$

$$Z_n = \hat{Z}_n = \hat{a}_n + i\hat{b}_n \qquad \text{at} \qquad \theta = \theta_B, \tag{2.22b}$$

where

$$\left.\begin{aligned} \hat{a}_n &= \frac{1}{\pi}\int_0^{2\pi} \psi_B \cos(n\varphi)\, \mathrm{d}\varphi \\ &= 0 \\ \hat{b}_n &= \frac{1}{\pi}\int_0^{2\pi} \psi_B \sin(n\varphi)\, \mathrm{d}\varphi \\ &= \frac{2\psi_0}{\pi n^2 \epsilon}\sin(n\epsilon)\,(1-\cos(n\pi)) \end{aligned}\right\} \quad n \geq 1. \tag{2.23}$$

Boundary condition (2.22a) follows immediately from (2.14).

Turning to $a_0(\theta)$ we note that the general solution of (2.16b) is given by

$$a_0 = C_1 - C_2 e^{-B\theta/A}, \tag{2.24}$$

where C_1 and C_2 are arbitrary constants. Applying the boundary condition (2.22a) at the pole we obtain

$$a_0 = C_1\left(1 - e^{-B\theta/A}\right), \tag{2.25}$$

This term in the streamfunction expansion corresponds to a "swirling flow" (i.e. in the $\hat{\boldsymbol{\varphi}}$–direction) independent of longitude. Now across the gaps we are only imposing inflow/outflow in the "$\hat{\boldsymbol{\theta}}$–direction". Therefore, across these gaps there is no circulation component in the "$\hat{\boldsymbol{\varphi}}$–direction" (i.e. $\hat{a}_0 = 0$) yielding $C_1 = 0$ and hence $a_0(\theta) = 0$. The solution (2.19) can be written

$$Z_n = \hat{Z}_n\left(\frac{e^{\lambda_{1n}\theta} - e^{\lambda_{2n}\theta}}{e^{\lambda_{1n}\theta_B} - e^{\lambda_{2n}\theta_B}}\right), \tag{2.26}$$

and $\hat{Z}_n$ is given by (2.22b) and (2.23). Using a MATLAB script (see Appendix A.2.1) it is straightforward to compute (2.26) getting the coefficients a_n and b_n. Then, we obtain $\psi(\varphi, \theta)$ from (2.15). The convergence of the Fourier expansions (2.15) are considered in Figure 2.4. Figure 2.4 (a) shows the relative error between $N = 50$ and $N = 150$ in terms of percentage. We can see that there is not much difference in (2.15) using $N = 50$ or $N = 150$. Tiny differences are obtained close to the boundary but they almost vanish using $N = 100$ (see Figure 2.4 (b)). Here, we use $N = 150$ because it gives a smooth behaviour on the boundary.

The streamfunction (2.15) is contoured in Figure 2.5 (a). The parameters values use to calculate ψ are listed in Table 2.1. The flow enters into the polar basin from the bottom gap and leaves through the top gap. The inlet flow turns westward (eastward) as soon as it is inside the basin in the North (South) Hemisphere. Hereafter, part of the

flow diverges to the right forming two strong boundary currents; one anticyclonic and the other cyclonic.

The equivalent circulation on the "f-sphere" is shown in in Figure 2.5 (b). On the f-sphere the fourth term in (2.9) vanishes (see Appendix A.1) producing a circulation which is symmetric about the diameter defined by $\varphi = 0$ and $\varphi = \pi$.

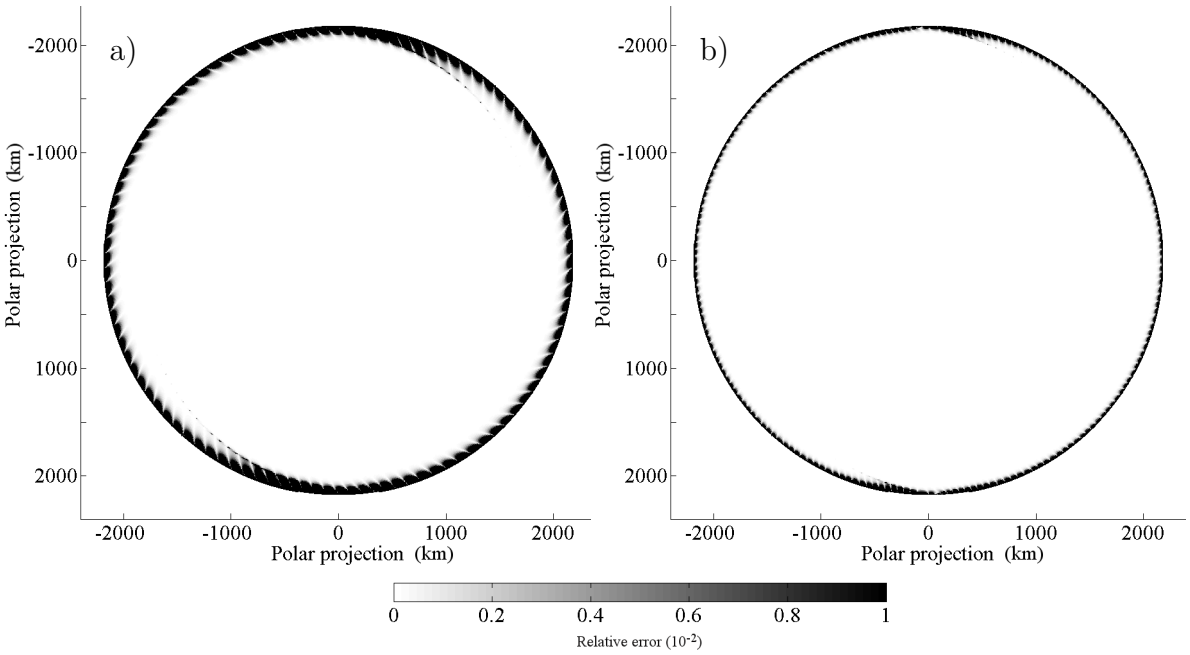

Figure 2.4: Convergence of the Fourier series (2.15) expressed in relative error. a) $|\psi(\varphi,\theta)_{50} - \psi(\varphi,\theta)_{150}|/\psi(\varphi,\theta)_{150}$ expressed in percentage; b) $|\psi(\varphi,\theta)_{100} - \psi(\varphi,\theta)_{150}|/\psi(\varphi,\theta)_{150}$ expressed in percentage.

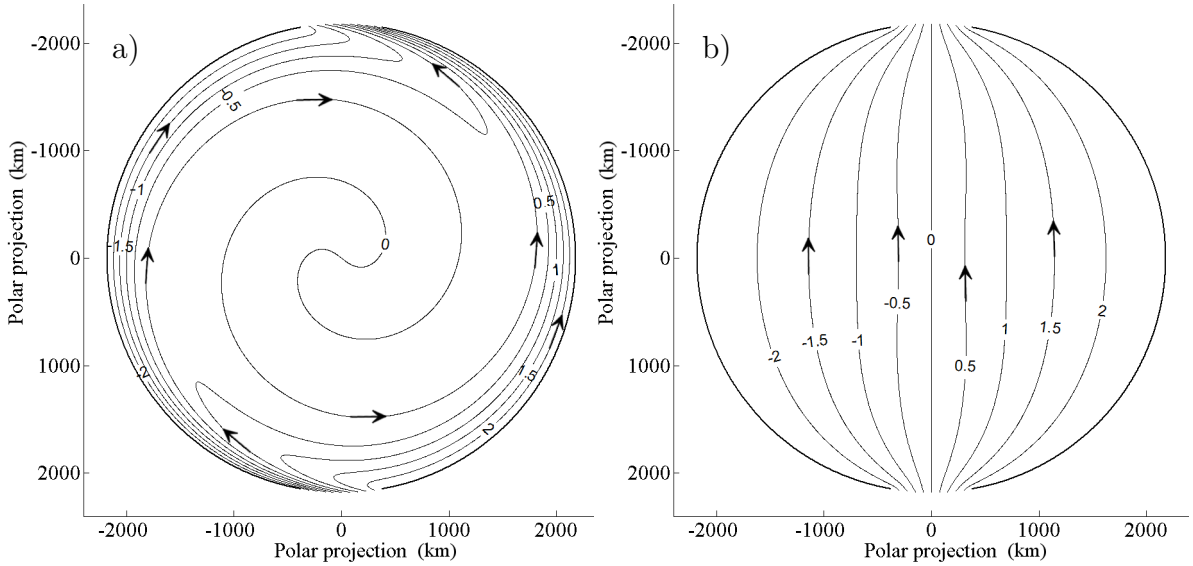

Figure 2.5: Source-sink planetary geostrophic circulation in a flat bottom. a)"β-sphere approximation"; b)"f-sphere approximation". The streamlines denote isolines of flow transport in Sverdrups ($1Sv = 10^6\ m^3 s^{-1}$).

Figure 2.6 (a) and (b) show the circulation when the bottom friction is $10^{-3}\ ms^{-1}$ and $10^{-5}\ ms^{-1}$, respectively. Thus, for fixed μ, increasing H effectually reduces the strength of bottom friction. As bottom friction decreases (i.e. μ decrease or H increases) the circulation is confined to wall boundary layers of width proportional to $\mathrm{O}\left[(\mu/H)^{1/2}\right]$ (Luneva *et al.*, 2012) leaving the interior stagnant. Figure 2.5 (a) clearly shows that fluid entering the basin bifurcates into clockwise and counter-clockwise branches.

We now consider how varying the fixed value of the co–latitude in the coefficients (2.10) impacts on the above solutions. The values $\theta_f = 0.25\theta_B$ and $\theta_f = \theta_B$ are used in Figure 2.6 (c) and (d), respectively. Remarkably, the solutions are insensitive to θ_f in the range $0.25\theta_B \leq \theta \leq \theta_B$. However, closer to the pole we anticipate that the "β-sphere approximation" will become inaccurate because A, B and $C \to 0$ as $\theta \to 0$.

Table 2.1: Parameter values use to calculate source/sink driven flow

Symbol	Variable(Unit)	Value
T	Source-sink strength (Sverdrups)	5
R	Radius of the Earth (m)	6.370×10^6
H	Depth (m)	1000
H_1	Step shelf depth (m)	250
H_2	Deep basin (m)	1000
μ	Control value of bottom friction (ms^{-1})	10^{-4}
A_H	Control value of horizontal Eddy viscosity (m^2/s)	10000
N	Number of summation terms in Fourier expansions $(-)$	150
2ϵ	Source-sink gap size (rad)	$\pi/18$
θ_B	Co-latitude at the boundary (rad)	$\pi/9$
θ_S	Shelf Edge (rad)	$\pi/18$

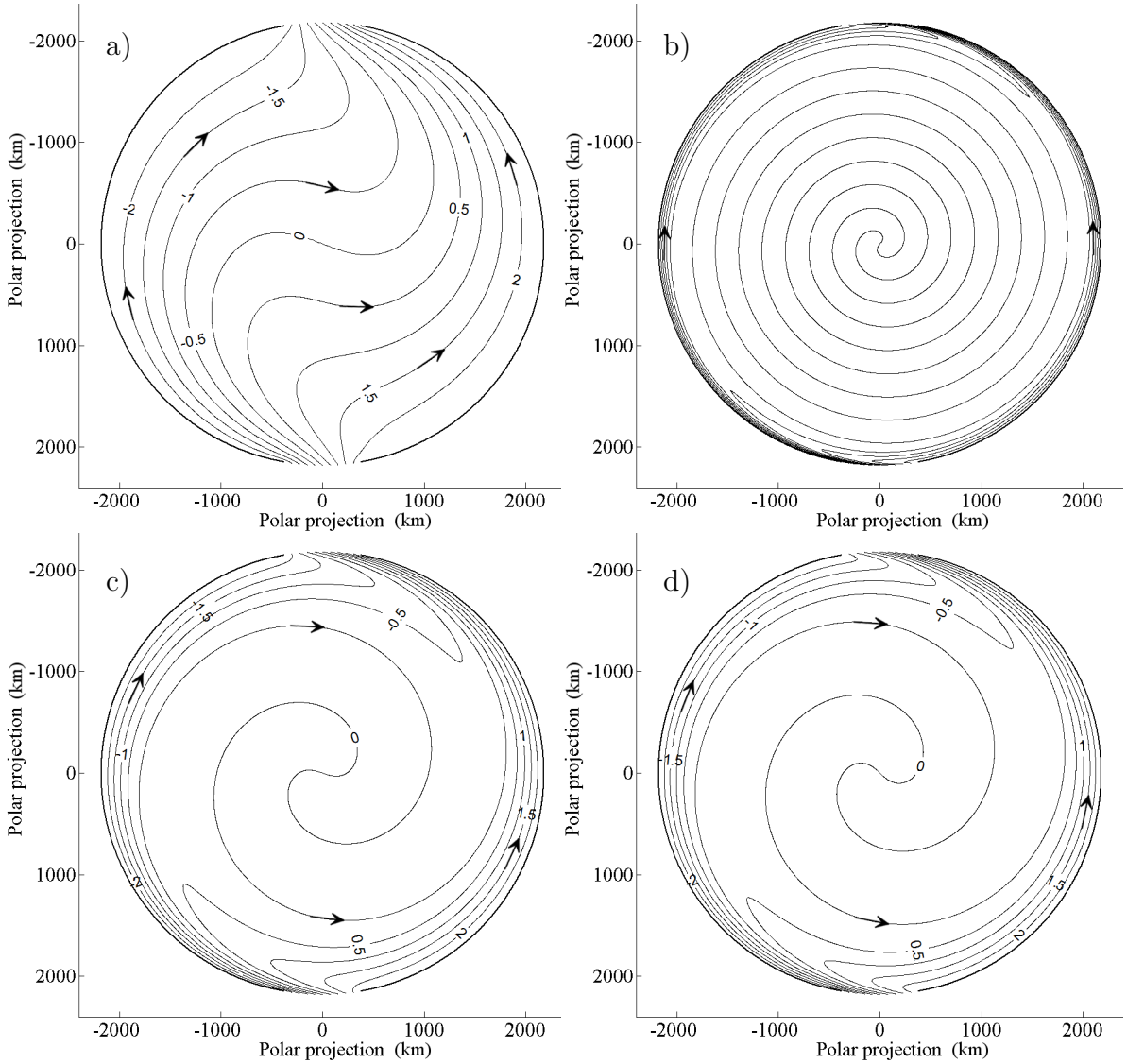

Figure 2.6: Source-sink planetary geostrophic circulation in a flat bottom basin. a) High bottom friction (10^{-3} ms^{-1}); b) Low bottom friction (10^{-5} ms^{-1}); c) As in Figure 2.5 (a) except $\theta_f = 0.25\theta_B$ and $N = 80$; d) as in (c) except $\theta_f = \theta_B$. The streamlines denote isolines of flow transport in Sverdrups ($1Sv = 10^6$ m^3s^{-1}).

b Flat bottom with a shear in the inflow

The previous section investigated the circulation driven by a uniform source–sink boundary velocity profiles across two straits. However, some studies suggest that a change in the potential vorticity (PV) balance can affect the direction of circulation (Yang, 2005; Karcher *et al.*, 2007). One would anticipate that for planetary geostrophic dynamics the relative vorticity at the source/sink straits will not impact on the basin circulation. The PV, or Π, is given by $\Pi = (f + \xi)/H$ where f and ξ are the planetary and relative vorticity, respectively. However, the relative vorticity of these flows is considerably smaller

than f, thus the Π is commonly expressed as f/H. We now consider a concrete example where the relative vorticity across the inflow strait is non–zero. The relative vorticity is the rotation, or curl, of a fluid (i.e. $\boldsymbol{\xi} = \boldsymbol{\nabla} \times \boldsymbol{u}$). For barotropic planetary flows, the relative vorticity is given by the vertical component (i.e. $\xi = \hat{\boldsymbol{k}} \cdot \nabla \times \boldsymbol{u}$). In spherical polar coordinates, the vertical component is

$$\xi = \frac{1}{R \sin\theta} \left[(\sin\theta u)_\theta - v_\varphi \right]. \tag{2.27}$$

Note that we only consider an inflow which is normal to the boundary (i.e $u = 0$), therefore (2.27) at the source $\partial v / \partial \varphi \neq 0$. At the sink the velocity is again assumed to be uniform (see Figure 2.7).

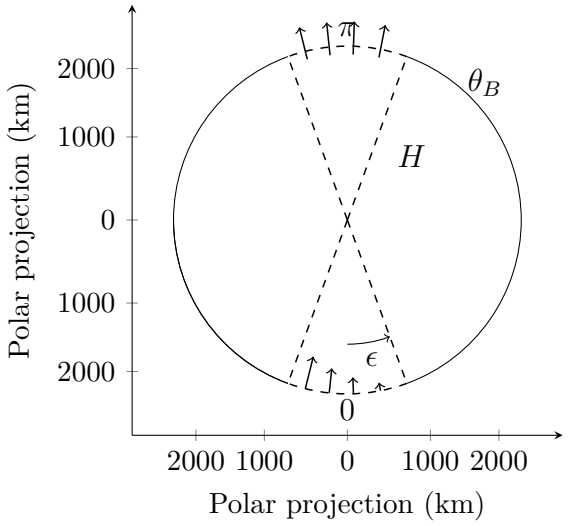

Figure 2.7: Circular polar basin with diametrically opposed gaps on the boundary. A spatially sheared inflow and a spatially uniform outflow are specified.

Consider the inflow strait spanning $-\epsilon \leq \varphi \leq \epsilon$. We specify a uniform sheared meridional velocity field of the form

$$v = \frac{v_0}{2\epsilon} (\epsilon - \varphi), \tag{2.28}$$

where v_0 is the maximum speed across the strait. Using the definition of the transport streamfunction (2.5) and (2.28) we observe that

$$\frac{H v_0}{2\epsilon} (\epsilon - \varphi) = -\frac{1}{R \sin\theta_B} \frac{\partial \psi}{\partial \varphi}, \tag{2.29}$$

where θ_B is the co–latitude of the boundary of the basin. Integrating (2.29) with respect of φ we obtain

$$\psi = -\frac{H v_0 R \sin\theta_B}{2\epsilon} \left(\epsilon\varphi - \frac{\varphi^2}{2} \right) + \hat{\psi}, \tag{2.30}$$

where $\hat{\psi}$ is an arbitrary constant. Applying the boundary conditions $\psi(\epsilon) = \psi_0$ we find that

$$\hat{\psi} = \frac{Hv_0R\epsilon\sin\theta_B}{4} + \psi_0, \tag{2.31}$$

and therefore

$$\psi = \frac{Hv_0Rsin\theta_B}{2\epsilon}\left(\frac{\varphi^2}{2} - \epsilon\varphi + \frac{\epsilon^2}{2}\right) + \psi_0. \tag{2.32}$$

We can determine v_0 by applying the boundary condition $\psi(-\epsilon) = -\psi_0$, whence

$$v_0 = \frac{-2\psi_0}{HR\epsilon\sin\theta_B}. \tag{2.33}$$

At the outflow (sink) strait spanning $[\pi - \epsilon, \pi + \epsilon]$ we specify a uniform meridional velocity as before. Thus, on the basin boundary the streamfunction takes the form

$$\psi_B = \psi_0 \begin{cases} 1 - \epsilon^{-2}\left(\varphi^2/2 - \epsilon\varphi + \epsilon^2/2\right) & \text{if } |\varphi| \le \epsilon, \\ 1 & \text{if } \epsilon \le \varphi \le \pi - \epsilon, \\ 1 - \left[\varphi - (\pi - \epsilon)\right]/\epsilon & \text{if } \pi - \epsilon \le \varphi \le \pi + \epsilon, \\ -1 & \text{if } \pi + \epsilon \le \varphi \le 2\pi - \epsilon, \end{cases} \tag{2.34}$$

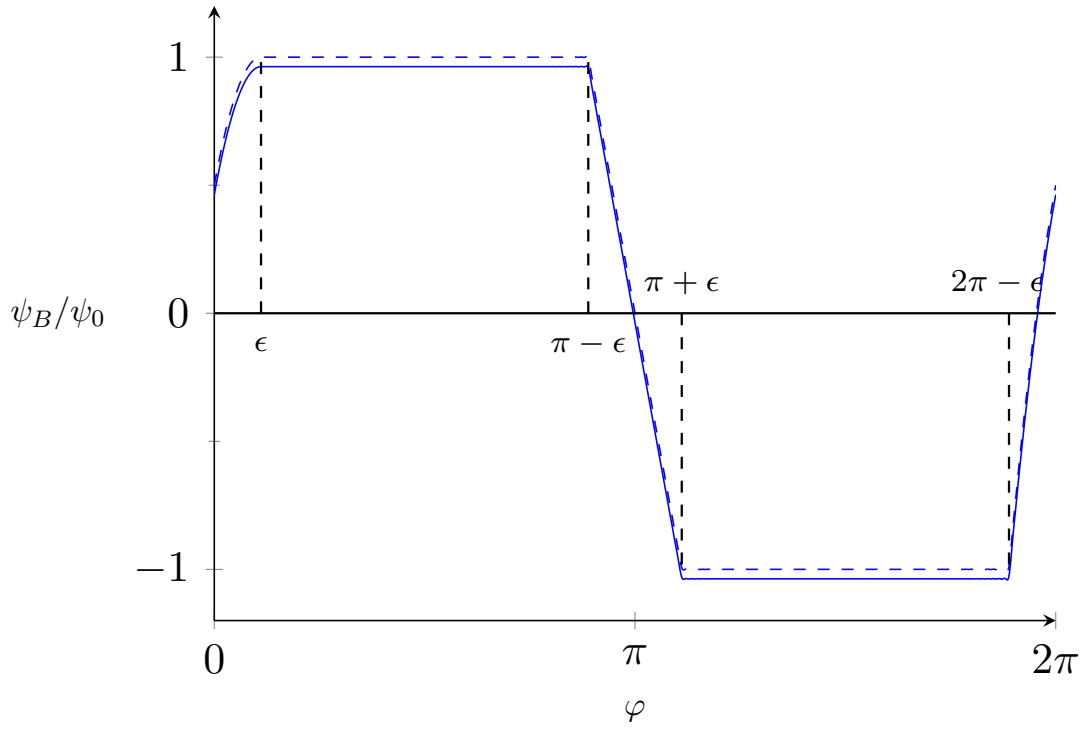

Figure 2.8: Schematic of the scaled streamfunction prescribed on the boundary (2.34). Dashed and continuous line denote the define in (2.34) together with its transpose satisfying $\hat{a}_0 = 0$, respectively. Note that width of each strait is $2\epsilon R\sin\theta_B$.

The boundary streamfunction (2.34) is plotted with dashed line in Figure 2.8. In contrast to boundary streamfunction plotted Figure 2.3, we observe that the first derivative ψ_B is continuous at $\varphi = \epsilon$.

Once more, the solution of (2.9) is given in form of (2.15). The coefficients a_n and b_n are obtained from (2.26) where $\hat{Z}_n$ are Fourier expansions coefficients corresponding to (2.34) which are given below:

$$\left.\begin{aligned} \hat{a}_n &= \frac{2\psi_0}{\pi}\left(\frac{\sin(\epsilon n) - \epsilon n \cos(\epsilon n)}{n^3\epsilon^2}\right) \\ \hat{b}_n &= \frac{2\psi_0}{\pi}\left(\frac{\sin(\epsilon n)\,(1-\cos(\pi n))}{n^2\epsilon}\right) \end{aligned}\right\} \quad n \geq 1, \tag{2.35a}$$

and

$$\hat{a}_0 = \frac{\psi_0}{3\pi\epsilon}. \tag{2.35b}$$

Note that (2.35b) is not zero. Therefore, ψ_B has to be transposed to a level where there is no net swirling flow (i.e. $\hat{a}_0 = 0$, see continuous line in Figure 2.8) ensuring that the source/sink flow were normal to the boundary.

Figure 2.9 shows contours of the streamfunction (2.15) using the ocean basin parameters of Table 2.1 and $N = 150$. The inflow bifurcates forming two counterrotating boundary layer currents exiting through the outflow strait. In comparison with Figure 2.5 (a), we observe that the anticlockwise boundary current has been strengthened, but there is no other major change. Reversing the sign of the velocity shear at the inflow strait produces an identical circulation to that shown in Figure 2.9. This result is expected because the relative vorticity in this domain is really small ($\sim 10^{-7}$) whereas the planetary vorticity is much bigger ($\sim 10^{-4}$). Therefore, there are not significant changes in the polar circulation.

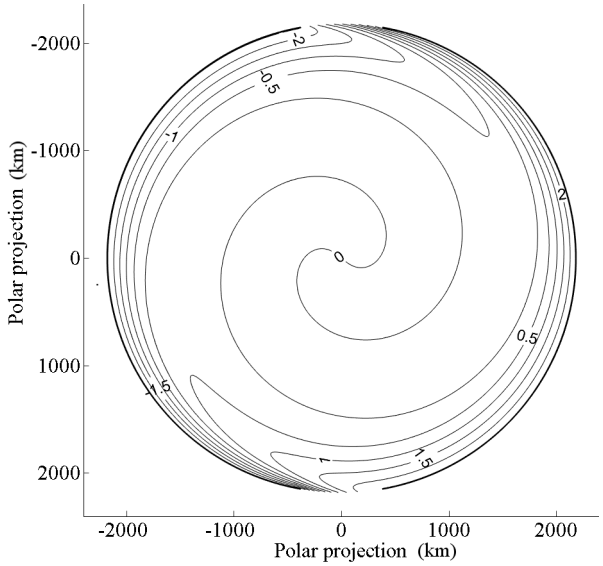

Figure 2.9: Source-sink planetary geostrophic circulation in a flat bottom polar basin with a sheared inflow velocity. The streamlines denote isolines of flow transport in Sverdrups ($1Sv = 10^6\ m^3 s^{-1}$).

c Step-shelf

The method of solution in the previous section can be extended to a polar basin with a uniform width step-shelf (Figure 2.10):

$$H(\theta) = \begin{cases} H_1, & \text{if } \theta_S \leq \theta \leq \theta_B, \\ H_2, & \text{if } 0 \leq \theta \leq \theta_S, \end{cases} \tag{2.36}$$

where $H_1 < H_2$.

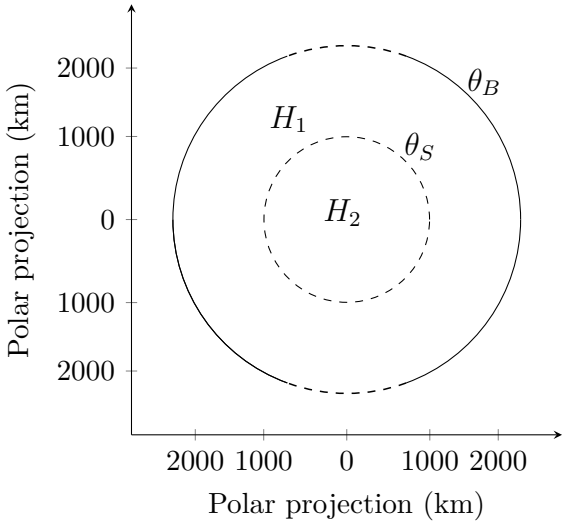

Figure 2.10: Polar basin with a step-shelf.

Let $\psi_1(\varphi,\theta)$ and $\psi_2(\varphi,\theta)$ denote the streamfunction on the shelf $\theta_S \le \theta \le \theta_B$ and in the deep basin $0 \le \theta \le \theta_S$, respectively. On the shelf and in the deep basin the vorticity equation takes the form

$$\psi_{1\varphi\varphi} + A\psi_{1\theta\theta} + B\psi_{1\theta} + C_1\psi_{1\varphi} = 0, \tag{2.37a}$$

$$\psi_{2\varphi\varphi} + A\psi_{2\theta\theta} + B\psi_{2\theta} + C_2\psi_{2\varphi} = 0, \tag{2.37b}$$

where

$$C_j \equiv 2\Omega H_j \mu^{-1} \sin^2\theta \qquad (j = 1, 2)\,.$$

As in the flat bottom solution, ψ_2 must satisfy boundary condition (2.14) and ψ_1 must satisfy boundary condition (2.11). At the shelf edge we demand continuity of the meridional transport and pressure gradient. The former matching condition is satisfied provided

$$\psi_1 = \psi_2 \quad \text{at} \quad \theta = \theta_S. \tag{2.38}$$

Using (2.3) and (2.4a), the latter matching condition requires that

$$\left[fv + \mu \frac{u}{H} \right] = 0 \quad \text{at} \quad \theta = \theta_S, \tag{2.39}$$

where the square brackets in (2.39) denote "jump conditions". In terms of the transport streamfunction (2.39) becomes

$$\left[\frac{-f\psi_\varphi}{HR\sin\theta} + \frac{\mu\psi_\theta}{H^2 R} \right] = 0 \quad \text{at} \quad \theta = \theta_S,$$

Expanding this jumping condition yields

$$\frac{-f\psi_{1\varphi}}{H_1 R\sin\theta} + \frac{\mu\psi_{1\theta}}{H_1^2 R} = \frac{-f\psi_{2\varphi}}{H_2 R\sin\theta} + \frac{\mu\psi_{2\theta}}{H_2^2 R} \quad \text{at} \quad \theta = \theta_S. \tag{2.40}$$

We multiply (2.40) by RH_1^2 to obtain

$$\frac{-fH_1\psi_{1\varphi}}{\sin\theta} + \mu\psi_{1\theta} = \frac{-fH_1^2\psi_{2\varphi}}{H_2\sin\theta} + \frac{\mu H_1^2\psi_{2\theta}}{H_2^2}, \quad \text{at} \quad \theta = \theta_S. \tag{2.41}$$

Once again, we seek solutions of (2.37) of the form

$$\psi_1(\varphi,\theta) = a_0(\theta) + \sum_{n=1}^{N} \left[a_n(\theta)\cos n\varphi + b_n(\theta)\sin n\varphi \right], \tag{2.42a}$$

$$\psi_2(\varphi,\theta) = A_0(\theta) + \sum_{n=1}^{N} \left[A_n(\theta)\cos n\varphi + B_n(\theta)\sin n\varphi \right], \tag{2.42b}$$

where the coefficients a_n, b_n are self-contained within each subsection (i.e. a_n's are distinct from those the previous solution). Let

$$z_n = a_n + ib_n, \quad Z_n = A_n + iB_n \quad n \ge 1.$$

In terms of these complex functions (2.38) and (2.41) take the form

$$z_n = Z_n \qquad \text{at} \qquad \theta = \theta_S, \tag{2.43}$$

and

$$\frac{H_1 f_S}{\sin\theta_S} in z_n + \mu \dot{z}_n = \frac{H_1 \hat{s} f_S}{\sin\theta_S} in Z_n + \hat{s}^2 \mu \dot{Z}_n \qquad \theta = \theta_S. \tag{2.44}$$

where $\hat{s} = (H_1/H_2) < 1$ and $f_S = 2\Omega\cos\theta_S$. Function z_n satisfies the equation (2.18) with C replaced by C_1. Similarly Z_n satisfies (2.18) with C replaced by C_2. Their general solutions are given

$$z_n = f_n e^{\lambda_{1n}\theta} + g_n e^{\lambda_{2n}\theta}, \tag{2.45a}$$

$$Z_n = F_n e^{\omega_{1n}\theta} + G_n e^{\omega_{2n}\theta}, \tag{2.45b}$$

where λ_{1n}, λ_{2n} are given by (2.21) with C replaced by C_1 and ω_{1n}, ω_{2n} are given by the same expressions with C replaced by C_2. Coefficients f_n, F_n, g_n and G_n are constants to be determined by applying the boundary and matching conditions. Application of (2.22) and (2.44) yields:

$$F_n + G_n = 0, \tag{2.46a}$$

$$f_n e^{\lambda_{1n}\theta_B} + g_n e^{\lambda_{2n}\theta_B} = \hat{z}_n, \tag{2.46b}$$

$$f_n e^{\lambda_{1n}\theta_S} + g_n e^{\lambda_{2n}\theta_S} = F_n e^{\omega_{1n}\theta_S} + G_n e^{\omega_{2n}\theta_S}, \tag{2.46c}$$

$$\begin{aligned} f_n e^{\lambda_{1n}\theta_S}\left(\frac{inH_1 f_S}{\sin\theta_S} + \mu\lambda_{1n}\right) + g_n e^{\lambda_{2n}\theta_S}\left(\frac{inH_1 f_S}{\sin\theta_S} + \mu\lambda_{2n}\right) = \\ F_n e^{\omega_{1n}\theta_S}\left(\frac{in\hat{s}H_1 f_S}{\sin\theta_S} + \mu\hat{s}^2\omega_{1n}\right) + G_n e^{\omega_{2n}\theta_S}\left(\frac{in\hat{s}H_1 f_S}{\sin\theta_S} + \mu\hat{s}^2\omega_{2n}\right). \end{aligned} \tag{2.46d}$$

It is straightforward to solve (2.46) for the coefficients f_n, g_n, F_n and G_n and subsequently the coefficients a_n, A_n, b_n and B_n in (2.42) using (2.45). Note that the axi-symmetric swirling flow component associated with the coefficients a_0 and A_0 is again set to zero following the arguments in section 2.2.1a. The Equations (2.46) are a system of linear algebraic equations for the coefficients f_n, g_n, F_n and G_n. Using a MATLAB code it is straightforward to solve (2.46) by writing the equations in matrix form and then using *linsolve* algorithm (source code in see Appendix A.2.2). *Linsolve* solves the linear equations using LU factorization by partial pivoting for square matrix. This method is divided in two main steps forward and backward substitution. The backward substitution is the same as the Gaussian elimination. However, the forward substitution adds the exchange

of rows to the algebra in order get the triangular matrix. If it is not specified, the model parameters used are given in Table 2.1.

Figure 2.11 shows contour of the streamfunction calculated using $N = 150$ in (2.42). The shelf edge is shown by the dashed line. The flow enters into the polar basin from the source point located on lower part of the domain and immediately bifurcates. The clockwise flowing boundary current is stronger than the anticlockwise recirculating current at the entry of the domain. The deep basin is essentially stagnant reflecting the fact that the frictional boundary layer at the shelf edge is not able to support significant cross-shelf edge transport. Indeed, over the majority of the shelf the geostrophic flow is closely aligned with isolines of $f\,(\theta)$, as expected from unforced planetary flow.

The influence of the bottom friction on the circulation is demonstrated in Figures 2.12 (a) and (b). As μ increases (see Figure 2.12 (a)) weak circulation is supported in the deep basin. On the shelf at the inflow gap the counter-clockwise branch of the circulation is larger than the clockwise branch. As μ decrease Figure 2.12 (b) shows that the source and sink are connected by a narrow wall of boundary layers with the circulation in the majority of the domain stagnant. Note the deep basin has one single contour line.

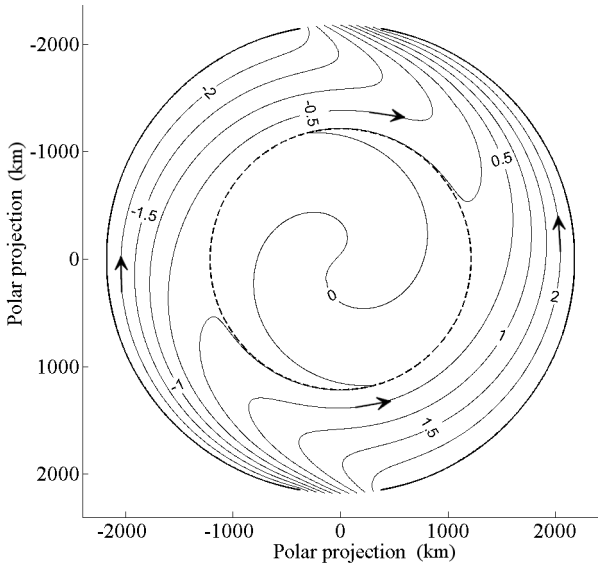

Figure 2.11: Steady source–sink planetary geostrophic circulation in a step-shelf domain. The streamlines denote isolines of flow transport in Sverdrups ($1Sv = 10^6\ m^3 s^{-1}$).

Figures 2.12 (c) and 2.12 (d) investigate varying the width of the shelf (θ_S) on the circulation. In Figure 2.12 (c) the shelf step width is 500 km which is narrower than in Figure 2.11. Although the area of the step–shelf has been decreased, the circulation is qualitatively the same as Figure 2.11. Here the bottom frictional boundary layer is smaller

than the shelf width thus, the flow is still geostrophic (outside the boundary layer). However, if the step–shelf width is smaller than the frictional boundary layer, the geostrophic balance breaks and the flow start crossing the shelf. Willmott and Luneva (2015) demonstrate that the width of the bottom frictional boundary layer, $W \sim (\mu_0/f_0)^{1/2} r_b$, adjacent to the basin boundary, where f_0 is the Coriolis parameter evaluated at the pole, μ_0 is the coefficient of the bottom friction with dimension s^{-1} and r_b is the radius of the polar basin. Using the ocean parameter in Table 2.1, we obtain that $\mu_0 \equiv \mu/H = 2 \times 10^{-6}$ s^{-1} and $W \sim 114$ km. In order to reproduce the observation of this effect, we slightly increase the size of the bottom friction to $5 \times \mu = 10^{-4}$ ms^{-1} giving $W \sim 255$ km. Figure 2.12 (d) shows contours of the streamfunction (2.42) using a shelf width of 200 km and a bottom friction of $\mu = 5 \times 10^{-4}$ ms^{-1}. We observe a deep basin circulation close to the shelf break, although the majority of the deep basin is again stagnant.

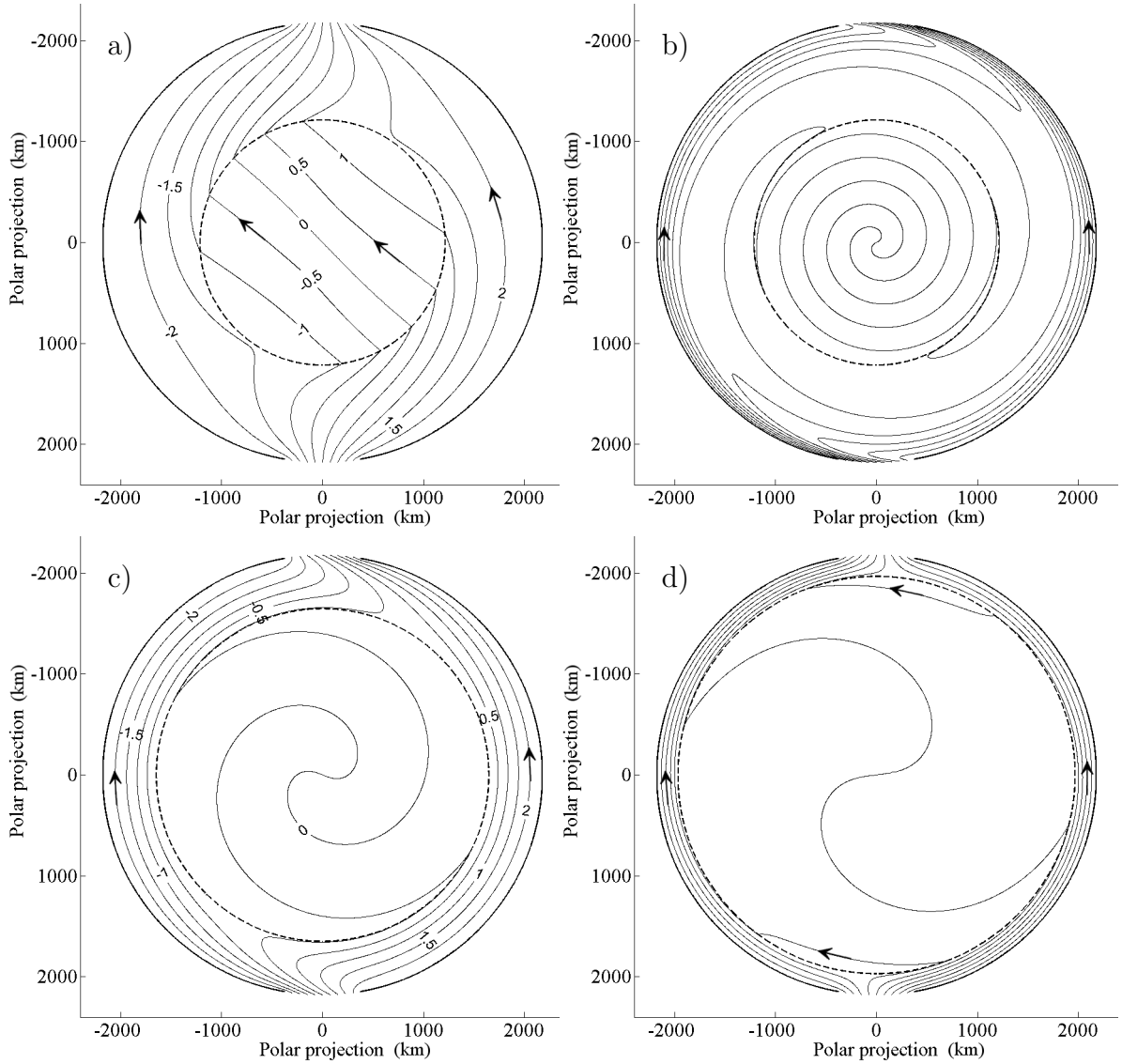

Figure 2.12: As in Figure 2.11 except, a) $\mu = 10^{-2}\ ms^{-1}$; b) $\mu = 10^{-5}\ ms^{-1}$; c) step–shelf width $\sim 500\ km$ (i.e. $\theta_S = 0.75\theta_B$); d) step–shelf width $\sim 200\ km$ (i.e. $\theta_S = 0.9\theta_B$). The streamlines denote isolines of flow transport in Sverdrups ($1Sv = 10^6\ m^3 s^{-1}$).

d Integral constraints on the circulation in a basin with step–shelf

Further insight about the dynamics of the steady–state circulation shown in Figure 2.11 and 2.12 can be obtained by integrating the curl of the momentum equation (2.3) in presence of linear bottom friction and absence of wind (i.e. $\boldsymbol{\tau} = 0$) over the deep basin.

$$\iint_S \nabla \times \left(f\hat{\boldsymbol{k}} \times \mathbf{u} \right) \cdot \mathrm{d}\boldsymbol{S} = -\frac{\mu}{H_2} \iint_S (\nabla \times \boldsymbol{u}) \cdot \mathrm{d}\boldsymbol{S}, \tag{2.47}$$

where H_2 and μ are constants and $\mathrm{d}\boldsymbol{S} = \hat{\boldsymbol{k}}\,\mathrm{d}S$ is the area element (see Figure 2.13).

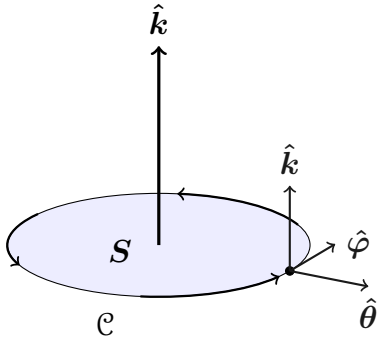

Figure 2.13: Schematic of the surface of the deep basin; $\hat{\boldsymbol{k}}$ is the unit vector perpendicular to the surface; $\mathcal{C}$ is the shelf break (i.e. $\theta = \theta_S$); $\hat{\boldsymbol{k}}$, $\hat{\boldsymbol{\theta}}$ and $\hat{\boldsymbol{\varphi}}$ are the unit vectors at any point of $\mathcal{C}$.

Application of Stokes' theorem to left hand side of (2.47) yields

$$\iint_S \nabla \times \left(f\hat{\boldsymbol{k}} \times \mathbf{u}\right) \cdot \mathrm{d}\boldsymbol{S} = \oint_{\mathcal{C}} \left(f_S\hat{\boldsymbol{k}} \times \mathbf{u}\right) \cdot \mathrm{d}\boldsymbol{l}, \tag{2.48}$$

where $\mathrm{d}\boldsymbol{l} = \hat{\boldsymbol{\varphi}}\,\mathrm{d}l$. Substituting (2.48) in (2.47)

$$\oint_{\mathcal{C}} \left(f_S\hat{\boldsymbol{k}} \times \mathbf{u}\right) \cdot \mathrm{d}\boldsymbol{l} = -\frac{\mu}{H_2} \iint_S \nabla \times \boldsymbol{u} \cdot \mathrm{d}\boldsymbol{S}. \tag{2.49}$$

Upon using commutativity and scalar triple product, (2.49) can be re–arranged as

$$\oint_{\mathcal{C}} \mathbf{u} \cdot \left(\hat{\boldsymbol{\varphi}} \times f_S\hat{\boldsymbol{k}}\right)\,\mathrm{d}l = -\frac{\mu}{H_2} \iint_S (\nabla \times \boldsymbol{u}) \cdot \hat{\boldsymbol{k}}\,\mathrm{d}S. \tag{2.50}$$

Noting that $\left(\hat{\boldsymbol{\varphi}} \times \hat{\boldsymbol{k}}\right) = \hat{\boldsymbol{\theta}}$ and $(\nabla \times \boldsymbol{u}) \cdot \hat{\boldsymbol{k}}$ is the vertical component of the relative vorticity. (2.50) can be re-written

$$\oint_{\mathcal{C}} f_S\mathbf{u} \cdot \hat{\boldsymbol{\theta}}\,\mathrm{d}l = -\frac{\mu}{H_2} \iint_S \xi\,\mathrm{d}S. \tag{2.51}$$

Finally, noting that $\mathbf{u} \cdot \hat{\boldsymbol{\theta}}$ is the velocity component in the meridional direction (i.e. v, normal to the shelf break) (2.51) becomes

$$f_S \oint_{\mathcal{C}} v\,\mathrm{d}l = -\frac{\mu}{H_2} \iint_S \xi\,\mathrm{d}S \tag{2.52}$$

In the steady state $\oint_{\mathcal{C}} v\,\mathrm{d}l = 0$ (otherwise, the deep basin will empty or fill), thus the surface integral of the relative vorticity in the deep basin have to be zero. There are two scenarios for which this can be satisfied. First, the deep basin is stagnant in which case $\xi = 0$, such as Figure 2.11. Second, the circulation is non–zero and irrotational as in the deep basin shown in Figure 2.12 (a).

2.2.2 Source-sink driven solutions in the presence of lateral viscosity

a Flat bottom

In this section, We reconsider the uniform source-sink driven flow but now in the presence of Laplacian friction in a circular polar basin with a flat bottom. Qualitatively, the form of the circulation can be determined using the approximate form (2.4b) of the Laplacian viscosity operator. The viscosity terms retained in (2.4b) reflect the fact that the structure of the diffusive boundary layer adjacent to $\theta = \theta_B$, is controlled by the largest derivatives in the $\hat{\theta}$-direction. Use of (2.4b) greatly simplifies the analysis of the problem, in comparison with retaining all of the viscosity terms which was the approach taken by Imawaki and Takano (1974) for a flat bottom basin. Setting $\boldsymbol{\tau} = 0$ and taking the curl of (2.3) yields,

$$-f\frac{1}{HR}\psi_{\varphi\theta} - \left(-\frac{f}{HR}\psi_{\varphi}\right)_{\theta} = \frac{A_H}{R^2}\left[\left(-\frac{1}{HR\sin\theta}\psi_{\varphi}\right)_{\theta\theta\varphi} - \left(\frac{1}{HR}\psi_{\theta\theta}\sin\theta\right)_{\theta}\right].$$

Expanding the derivatives on both sides of this equation gives

$$-\frac{2\Omega\sin\theta}{HR}\psi_{\varphi} = \frac{A_H}{R^3H}\left(\frac{-\sin^3\theta - 2\sin\theta\cos^2\theta}{\sin^4\theta}\psi_{\varphi\varphi} + \frac{\cos\theta}{\sin^2\theta}\psi_{\varphi\varphi\theta} - \frac{1}{\sin\theta}\psi_{\varphi\varphi\theta\theta} + \frac{\cos\theta}{\sin^2\theta}\psi_{\varphi\varphi\theta} - \cos\theta\psi_{\theta\theta\theta} - \sin\theta\psi_{\theta\theta\theta\theta}\right), \tag{2.53}$$

which can be re-written as

$$-\frac{2\Omega\sin\theta}{HR}\psi_{\varphi} = \frac{A_H}{R^3H}\left(\frac{(\cos^2\theta - 1) - 2\cos^2\theta}{\sin^3}\psi_{\varphi\varphi} + \frac{2\cos\theta}{\sin^2\theta}\psi_{\varphi\varphi\theta} - \frac{1}{\sin\theta}\psi_{\varphi\varphi\theta\theta} - \cos\theta\psi_{\theta\theta\theta} - \sin\theta\psi_{\theta\theta\theta\theta}\right). \tag{2.54}$$

Multiply (2.54) by $HR^3A_H^{-1}\sin^{-1}\theta$ to obtain

$$-\frac{2\Omega R^2}{A_H}\psi_{\varphi} = \frac{-1-\cos^2\theta}{\sin^4\theta}\psi_{\varphi\varphi} + \frac{2\cos\theta}{\sin^3\theta}\psi_{\varphi\varphi\theta} - \frac{1}{\sin^2\theta}\psi_{\varphi\varphi\theta\theta} - \frac{\cos\theta}{\sin\theta}\psi_{\theta\theta\theta} - \psi_{\theta\theta\theta\theta}. \tag{2.55}$$

Finally rearranging the terms we obtain the "boundary layer approximation" for the vorticity equation

$$\psi_{\theta\theta\theta\theta} + P_1\psi_{\theta\theta\theta} + P_2\psi_{\varphi\varphi} - P_3\psi_{\varphi\varphi\theta} + P_4\psi_{\varphi\varphi\theta\theta} - P_5\psi_{\varphi} = 0, \tag{2.56}$$

where

$$P_1 \equiv \cot\theta, \quad P_2 \equiv \frac{1+\cos^2\theta}{\sin^4\theta}, \quad P_3 \equiv \frac{2\cos\theta}{\sin^3\theta}, \quad P_4 \equiv \csc^2\theta, \quad P_5 \equiv 2\Omega R^2A_H^{-1}. \tag{2.57}$$

Once again, we employ the "β-sphere approximation" fixing $\theta = \theta_f$ in the coefficients $P_j\,(j = 1, .., 5)$, as in the previous section we set $\theta_f = 0.5\theta_B$. Then (2.56) becomes a constant coefficient linear 4^{th} order partial differential equation which can be solved using classical methods

The streamfunction at the boundary has been already defined in (2.11). In addition, we impose the "no-slip" boundary condition

$$\psi_\theta = 0 \quad \text{at} \quad \theta = \theta_B. \tag{2.58}$$

At the pole, we impose

$$\left.\begin{aligned} \psi_{\varphi\varphi} &= 0 \\ \psi_\theta &= 0 \end{aligned}\right\} \quad \text{at} \quad \theta = 0. \tag{2.59}$$

The first of (2.59) follows immediately from the evaluation of (2.56) at the pole, while the second of (2.59) ensures the zonal velocity vanishes (see Imawaki and Takano, 1974).

We seek a solution of (2.56) of the form (2.15), and follow the method of solution in section 2.2.1a. When (2.15) is substituted in (2.56) and the coefficients of $\cos(n\varphi)$ and $\sin(n\varphi)$ are collected, we obtain

$$\left.\begin{aligned} a_n^{IV} + P_1 \dddot{a}_n - P_2 a_n n^2 + P_3 \dot{a}_n n^2 - P_4 \ddot{a}_n n^2 - P_5 b_n n = 0 \\ b_n^{IV} + P_1 \dddot{b}_n - P_2 b_n n^2 + P_3 \dot{b}_n n^2 - P_4 \ddot{b}_n n^2 + P_5 a_n n = 0 \end{aligned}\right\} \quad n \geq 1. \tag{2.60a}$$

and

$$a_0^{IV} + P_1 \dddot{a}_0 = 0. \tag{2.60b}$$

where $a_0^{IV} \equiv d^4 a_n / d\theta^4$ and $\dddot{a}_0 \equiv d^3 a_n / d\theta^3$. In terms of $Z_n = a_n + i b_n$ equations (2.60a) can be written as

$$Z_n^{IV} + P_1 \dddot{Z}_n - P_4 \ddot{Z}_n n^2 + P_3 \dot{Z}_n n^2 - (P_2 n - i P_5)\, Z_n n = 0 \quad n \geq 1. \tag{2.61}$$

The general solution of (2.61) is given by

$$Z_n = \sum_{j=1}^{4} k_{jn} e^{\lambda_{jn}\theta}, \tag{2.62}$$

where λ_{jn} are the roots from the auxiliary equation

$$\lambda_n^4 + P_1 \lambda_n^3 - P_4 \lambda_n^2 n^2 + P_3 \lambda_n n^2 - n\,(P_2 n - i P_5) = 0. \tag{2.63}$$

Equation (2.63) is a quartic polynomial with four complex roots. Note that since the coefficients of (2.63) are not real the roots will not be real or complex conjugate pairs.

The arbitrary constants k_{jn} are to be determined using the boundary conditions above. Applying (2.11), (2.58) and (2.59) we obtain

$$\hat{Z}_n = k_{1n}e^{\lambda_{1n}\theta_B} + k_{2n}e^{\lambda_{2n}\theta_B} + k_{3n}e^{\lambda_{3n}\theta_B} + k_{4n}e^{\lambda_{4n}\theta_B}, \tag{2.64a}$$

$$0 = \lambda_{1n}k_{1n}e^{\lambda_{1n}\theta_B} + \lambda_{2n}k_{2n}e^{\lambda_{2n}\theta_B} + \lambda_{3n}k_{3n}e^{\lambda_{3n}\theta_B} + \lambda_{4n}k_{4n}e^{\lambda_{4n}\theta_B}, \tag{2.64b}$$

$$0 = k_{1n} + k_{2n} + k_{3n} + k_{4n}, \tag{2.64c}$$

$$0 = \lambda_{1n}k_{1n} + \lambda_{2n}k_{2n} + \lambda_{3n}k_{3n} + \lambda_{4n}k_{4n}. \tag{2.64d}$$

The treatment of a_0 is identical as in section 2.2.1a. The "the swirling flow component" associated with this term in the streamfunction is set to zero reflecting the fact that across the gaps in the boundary of the basin the prescribed inflow/outflow is in the θ–direction.

The λ_{jn} were numerically calculated from (2.63) using the *root* algorithm from MATLAB. However, this method might not find the exact values due to round-off error. In fact, Figure 2.14 shows the roots λ_{jn} $(j = 1, .., 4)$ for the first twenty values n (i.e. $n = 1, .., 20$). We can see how some of them are badly computed giving the values of others λ_{jn}. This imprecision was corrected using the Newton–Raphson method where the error and the number of repetitions were set to 10^{-6} and 100, respectively (see Appendix A.3.1).

Given the roots λ_{jn}, we solve (2.64) for the coefficients k_{jn} and subsequently the coefficients a_n and b_n in (2.15) using (2.62). Equations (2.64) are a system of linear algebra equations for the coefficients k_{jn}. This system was again solved using the *linsolve* algorithm of MATLAB (Appendix A.3.2). The convergence of (2.15) is assessed in Figure 2.15. Figure 2.15 (a) shows the relative error between $N = 50$ and $N = 350$. It can be noted that the difference between solutions excess 1% in many areas. Even though the solution looks more convergent when $N = 300$ (see Figure 2.15 (b)), there are still areas where the solution does not converge as good as the analytical solution in presence of bottom friction.

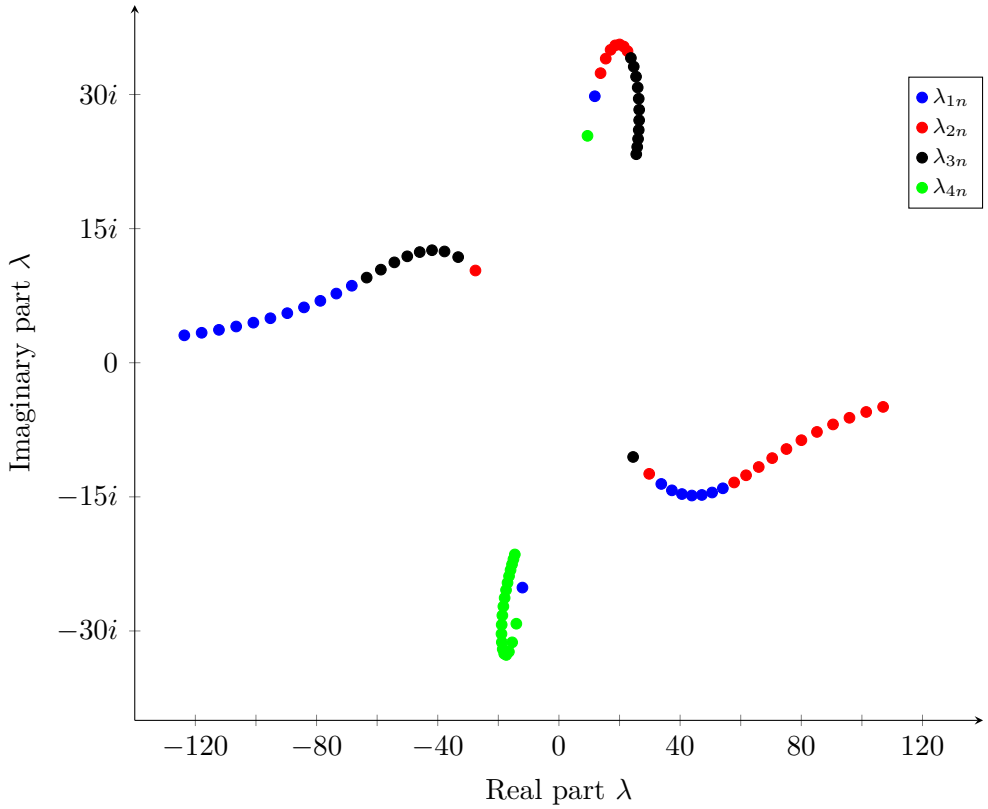

Figure 2.14: Argand plane. The roots λ_{jn} from (2.63) using $N = 20$.

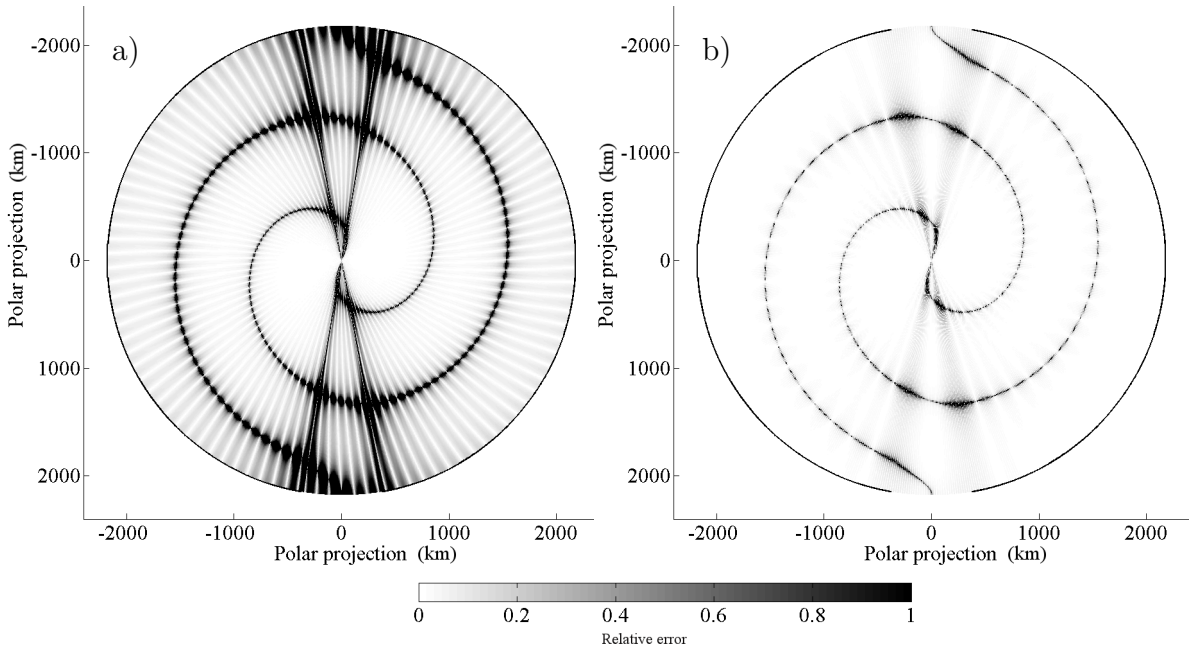

Figure 2.15: Convergence of the Fourier series (2.15) expressed as relative error. a) $|\psi(\varphi,\theta)_{50} - \psi(\varphi,\theta)_{350}|/\psi(\varphi,\theta)_{350}$ expressed in percentage; b) $|\psi(\varphi,\theta)_{300} - \psi(\varphi,\theta)_{350}|/\psi(\varphi,\theta)_{350}$ expressed in percentage. The streamlines denote isolines of flow transport in Sverdrups ($1Sv = 10^6\ m^3 s^{-1}$).

Figure 2.16 (a) shows the streamfunction calculated using the boundary layer approximation method. For comparison the solution using all the terms in the Laplacian operator is plotted in Figure 2.16 (b). The Imawaki and Takano (1974) solution was evaluated in the latter case using the analysis in their paper. The parameter values arein Table 2.1 and $N = 350$. As expected the solutions in Figure 2.16 were almost identical, underlying how well the boundary layer approximation worked. The flow enters the polar basin from the bottom gap and leaves through the top gap. The inlet flow turns westward (eastward) as soon as it is inside the basin in the North (South) Hemisphere. Hereafter, part of the flow diverges to the right forming two strong boundary currents; one anticyclonic and the other cyclonic.

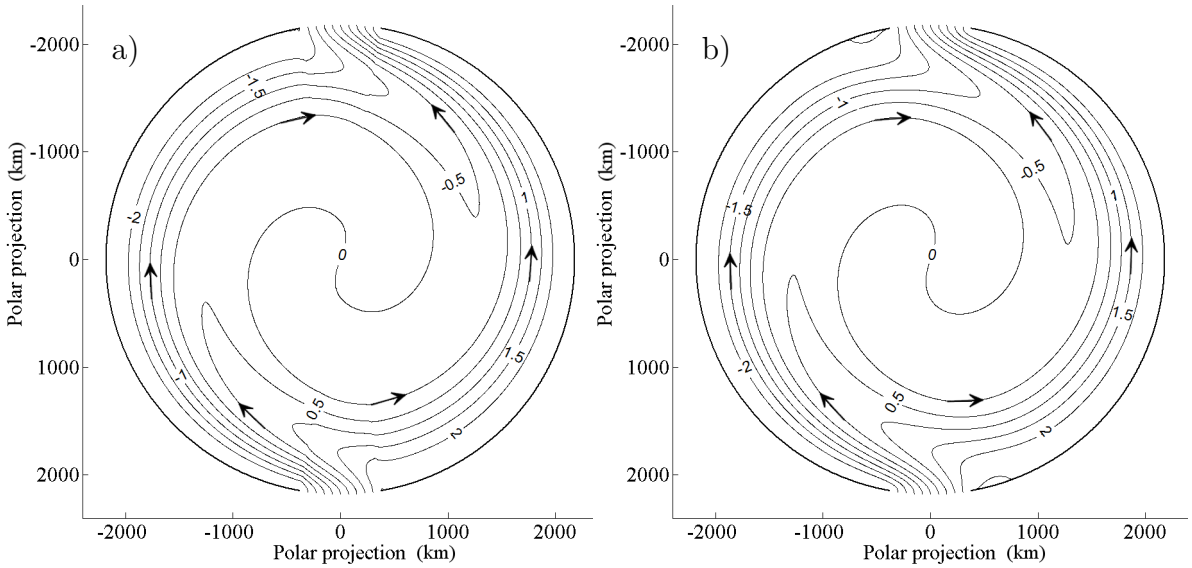

Figure 2.16: Source-sink planetary geostrophic circulation in presence of lateral friction. a) Lateral boundary layer approximation; b) Full Laplacian eddy viscosity operator evaluated from the Imawaki and Takano (1974) solution. The streamlines denote isolines of flow transport in Sverdrups ($1Sv = 10^6\ m^3 s^{-1}$).

The dependence of the solutions on the magnitude of A_H is shown in Figure 2.17 (a) and (b). As A_H increases the diffusive circulation occupies the entire domain. Figure 2.17 (c) and (d) once again demonstrate the solutions are insensitive to the values of θ_f. However, this method of solutions fails when $\theta \to 0$ because the coefficients P_1, P_2, P_3 and $P_4 \to \infty$.

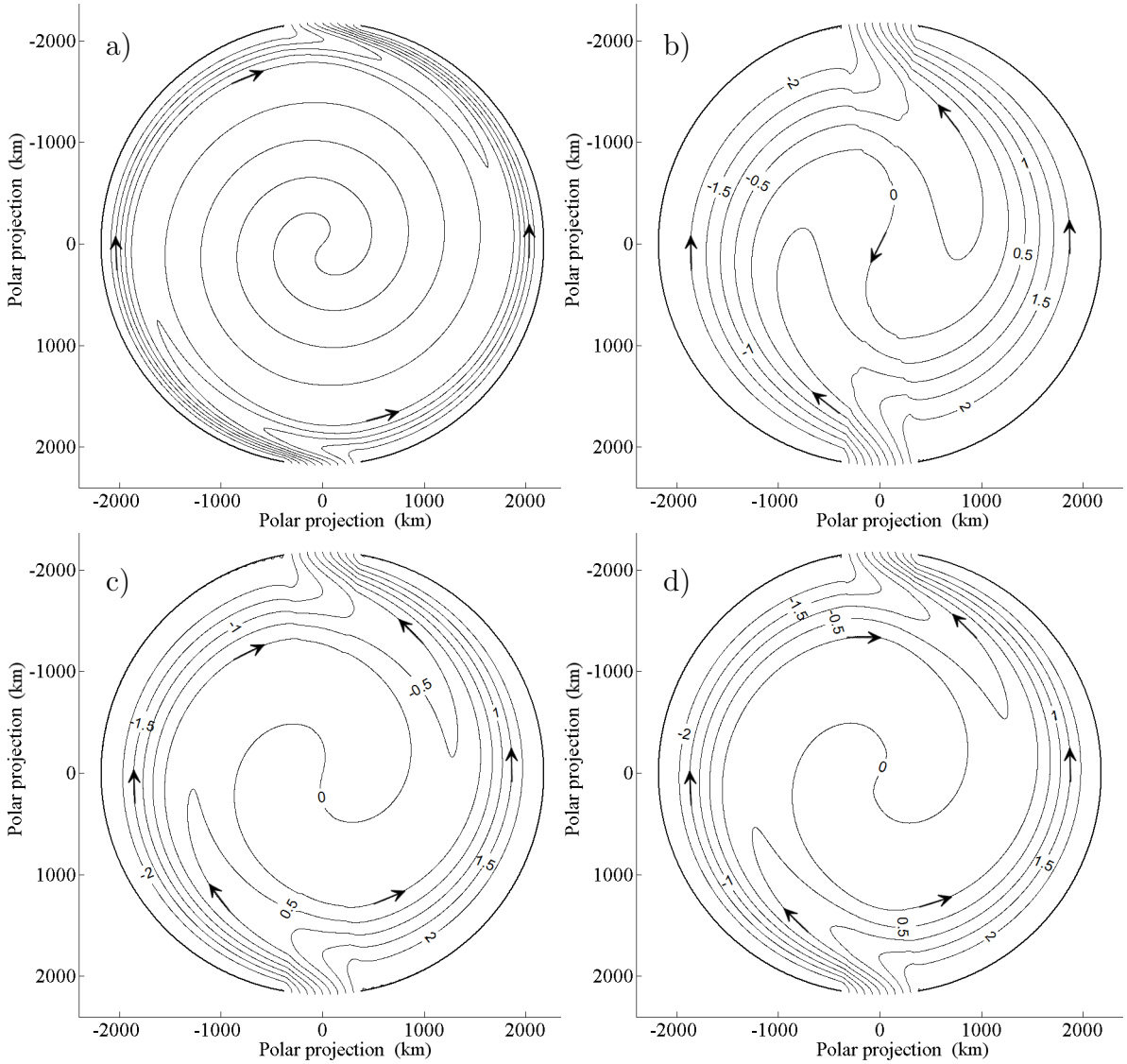

Figure 2.17: As in Figure 2.16 except, a) $A_H = 500\ m^2 s^{-1}$; b) $A_H = 5 \times 10^4\ m^2 s^{-1}$; c) $\theta_f = 0.25\theta_B$ and $N = 80$; d) $\theta_f = \theta_B$. The streamlines denote isolines of flow transport in Sverdrups ($1Sv = 10^6\ m^3 s^{-1}$).

b Step shelf

The method of solution in the previous section can be extended to a polar basin with a uniform width step-shelf defined in (2.36) as shown schematically in Figure 2.10.

Let ψ_j $(j = 1, 2)$ denote the streamfunction on the shelf and deep basin, respectively. Then ψ_j satisfies (2.56), noting that P_j $(j = 1, .., 5)$ are depth independent. On the boundary of the basin we require that (2.11), (2.58) and at the pole we impose again (2.59).

To complete the specification of the problem we impose four matching conditions at the shelf edge:

$$\left.\begin{aligned} [\psi_\theta] = [\psi_\varphi] &= 0 \\ \left[fu + \frac{A_H}{R^2} v_{\theta\theta}\right] &= 0 \\ \left[-fv + \frac{A_H}{R^2} u_{\theta\theta}\right] &= 0 \end{aligned}\right\} \quad \text{on} \quad \theta = \theta_S. \tag{2.65a}$$

(2.65b)

(2.65c)

Matching conditions (2.65a) ensure that the transports tangential and normal to the shelf edge are continuous, and (2.65b and c) ensure that the pressure, and its derivatives normal to the shelf edge, are continuous. In terms of ψ, (2.65b) becomes

$$\left[\frac{f}{HR}\psi_\theta + \frac{A_H}{R^2}\left(-\frac{1}{HR\sin\theta}\psi_\varphi\right)_{\theta\theta}\right] = 0 \quad \text{at} \quad \theta = \theta_S. \tag{2.66}$$

If we multiply (2.66) by HR^3/A_H and we expand the second term, we obtain

$$\left[\frac{fR^2}{A_H}\psi_\theta + \frac{-1-\cos^2\theta}{\sin^3\theta}\psi_\varphi + \frac{2\cos\theta}{\sin^2\theta}\psi_{\varphi\theta} - \frac{1}{\sin\theta}\psi_{\varphi\theta\theta}\right] = 0 \quad \theta = \theta_S. \tag{2.67}$$

Thus (2.67) becomes

$$\begin{aligned} &\frac{f_S R^2}{A_H}\psi_{1\theta_S} + \frac{-1-\cos^2\theta_S}{\sin^3\theta_S}\psi_{1\varphi} + \frac{2\cos\theta_S}{\sin^2\theta_S}\psi_{1\varphi\theta} - \frac{1}{\sin\theta_S}\psi_{1\varphi\theta\theta} = \\ &\frac{f_S R^2\hat{s}}{A_H}\psi_{2\theta_S} + \frac{\hat{s}\,(-1-\cos^2\theta_S)}{\sin^3\theta_S}\psi_{2\varphi} + \frac{\hat{s}2\cos\theta_S}{\sin^2\theta_S}\psi_{2\varphi\theta} - \frac{\hat{s}}{\sin\theta_S}\psi_{2\varphi\theta\theta}, \end{aligned} \tag{2.68}$$

where $\hat{s} = H_1/H_2$ and f_S is the Coriolis parameter evaluated at the shelf edge. In terms of ψ, (2.65c) becomes

$$\left[\frac{f}{HR\sin\theta}\psi_\varphi + \frac{A_H}{R^2}\left(\frac{1}{HR}\psi_\theta\right)_{\theta\theta}\right] = 0 \quad \theta = \theta_S, \tag{2.69}$$

which can be re-written as

$$\left[\frac{f}{H\sin\theta}\psi_\varphi + \frac{A_H}{HR^2}\psi_{\theta\theta\theta}\right] = 0 \quad \theta = \theta_S. \tag{2.70}$$

Expanding (2.70) in terms of ψ_j we obtain

$$\frac{f_S}{\sin\theta_S}\psi_{1\varphi} + \frac{A_H}{R^2}\psi_{1\theta\theta\theta} = \frac{\hat{s}f_S}{\sin\theta_S}\psi_{2\varphi} + \frac{\hat{s}A_H}{R^2}\psi_{2\theta\theta\theta}. \tag{2.71}$$

We seek solutions of (2.56) of the form (2.42), and follow the method of solution in section 2.2.2a. The general solutions for z_n and Z_n, as defined in section 2.2.1c, are given by

$$z_n = \sum_{j=1}^{4} k_{jn}\exp(\lambda_{jn}\theta) \quad \theta_S \le \theta \le \theta_B, \tag{2.72a}$$

$$Z_n = \sum_{j=1}^{4} K_{jn}\exp(\lambda_{jn}\theta) \quad 0 \le \theta \le \theta_S, \tag{2.72b}$$

where λ_{jn} are the roots of (2.63), noting that the coefficients P_j $(j = 1, .., 5)$ do not depend on the depth.

Once again, the definitions of a_n and A_n are self-contained within this subsection. The eight coefficients k_{jn}, K_{jn} $(j = 1..4)$ are determined by applying the boundary conditions (2.11), (2.58), (2.59) and the matching conditions (2.65a), (2.68) and (2.71).

In terms of Z_n and z_n, the boundary condition (2.11), (2.58), (2.59) can be re–written as

$$\left.\begin{aligned} z_n &= \hat{z}_n \\ \dot{z}_n &= 0 \end{aligned}\right\} \quad \text{at} \quad \theta = \theta_B \quad \text{and} \quad \left.\begin{aligned} Z_n &= 0 \\ \dot{Z}_n &= 0 \end{aligned}\right\} \quad \text{at} \quad \theta = 0, \tag{2.73a}$$

and the matching conditions (2.65a), (2.68) and (2.71) become

$$\left.\begin{aligned} \dot{z}_n &= \dot{Z}_n \\ z_n &= Z_n \end{aligned}\right\} \quad \text{at} \quad \theta = \theta_S, \tag{2.73b}$$

$$\begin{aligned} \dot{z}_n + \frac{inA_H\,(1+\cos^2\theta_S)}{f_S R^2 \sin^3\theta_S} z_n - \frac{inA_H}{R^2\Omega\sin^2\theta_S}\dot{z}_n + \frac{inA_H}{f_S R^2\sin\theta_S}\ddot{z}_n = \\ \hat{s}\dot{Z}_n + \frac{in\hat{s}A_H\,(1+\cos^2\theta_S)}{f_S R^2\sin^3\theta_S} Z_n - \frac{inA_H\hat{s}}{\Omega\sin^2\theta_S}\dot{Z}_n + \frac{inA_H\hat{s}}{f_S R^2\sin\theta_S}\ddot{Z}_n \quad \theta = \theta_S, \end{aligned} \tag{2.73c}$$

and

$$-\frac{inf_S}{\sin\theta_S} z_n + \frac{A_H}{R^2}\dddot{z}_n = -\frac{in\hat{s}f_S}{\sin\theta_S} Z_n + \frac{\hat{s}A_H}{R^2}\dddot{Z}_n \quad \theta = \theta_S. \tag{2.73d}$$

In (2.73) the superscripts on z_n, Z_n denote derivatives with respect to θ. Finally, substituting (2.72) into (2.73) yields

$$\hat{Z}_n = k_{1n}e^{\lambda_{1n}\theta_B} + k_{2n}e^{\lambda_{2n}\theta_B} + k_{3n}e^{\lambda_{3n}\theta_B} + k_{4n}e^{\lambda_{4n}\theta_B}, \tag{2.74a}$$

$$0 = \lambda_{1n}k_{1n}e^{\lambda_{1n}\theta_B} + \lambda_{2n}k_{2n}e^{\lambda_{2n}\theta_B} + \omega_{3n}k_{3n}e^{\lambda_{3n}\theta_B} + \lambda_{4n}k_{4n}e^{\lambda_{4n}\theta_B}, \tag{2.74b}$$

$$0 = K_{1n} + K_{2n} + K_{3n} + K_{4n}, \tag{2.74c}$$

$$0 = \lambda_{1n}K_{1n} + \lambda_{2n}K_{2n} + \lambda_{3n}K_{3n} + \lambda_{4n}K_{4n}, \tag{2.74d}$$

$$\begin{aligned} 0 = {} & k_{1n}e^{\lambda_{1n}\theta_S} + k_{2n}e^{\lambda_{2n}\theta_S} + k_{3n}e^{\lambda_{3n}\theta_S} + k_{4n}e^{\lambda_{4n}\theta_S} \\ & - K_{1n}e^{\lambda_{1n}\theta_S} - K_{2n}e^{\lambda_{2n}\theta_S} - K_{3n}e^{\lambda_{3n}\theta_S} - K_{4n}e^{\lambda_{4n}\theta_S}, \end{aligned} \tag{2.74e}$$

$$
\begin{aligned}
0 = {} & \lambda_{1n} k_{1n} e^{\lambda_{1n}\theta_S} + \lambda_{2n} k_{2n} e^{\lambda_{2n}\theta_S} + \lambda_{3n} k_{3n} e^{\lambda_{3n}\theta_S} + \lambda_{4n} k_{4n} e^{\lambda_{4n}\theta_S} \\
& - \lambda_{1n} K_{1n} e^{\lambda_{1n}\theta_S} + \lambda_{2n} K_{2n} e^{\lambda_{2n}\theta_S} + \omega_{3n} K_{3n} e^{\lambda_{3n}\theta_S} + \lambda_{4n} K_{4n} e^{\lambda_{4n}\theta_S},
\end{aligned} \tag{2.74f}
$$

$$
\begin{aligned}
0 = {} & k_{1n}\left(\gamma\lambda_{1n}(n)^3 - in\right) e^{\lambda_{1n}\theta_S} + k_{2n}\left(\gamma\lambda_{2n}(n)^3 - in\right) e^{\lambda_{1n}\theta_S} \\
& + k_{3n}\left(\gamma\lambda_{3n}(n)^3 - in\right) e^{\lambda_{3n}\theta_S} + k_{4n}\left(\gamma\lambda_{4n}(n)^3 - in\right) e^{\lambda_{4n}\theta_S} \\
& - K_{1n}\hat{s}\left(\gamma\lambda_{1n}(n)^3 - in\right) e^{\lambda_{1n}\theta_S} - K_{2n}\hat{s}\left(\gamma\lambda_{2n}(n)^3 - in\right) e^{\lambda_{2n}\theta_S} \\
& - K_{3n}\hat{s}\left(\gamma\lambda_{3n}(n)^3 - in\right) e^{\lambda_{3n}\theta_S} - K_{4n}\hat{s}\left(\gamma\lambda_{4n}(n)^3 - in\right) e^{\lambda_{4n}\theta_S},
\end{aligned} \tag{2.74g}
$$

$$
\begin{aligned}
0 = {} & k_{1n}\left(\lambda_{1n}(n) - i\mathcal{F}n\lambda_{1n}(n) + in\mathcal{E} + \lambda_{1n}(n)^2 in\mathcal{G}\right) e^{\lambda_{1n}\theta_S} \\
& + k_{2n}\left(\lambda_{2n}(n) - i\mathcal{F}n\lambda_{2n}(n) + in\mathcal{E} + \lambda_{2n}(n)^2 in\mathcal{G}\right) e^{\lambda_{2n}\theta_S} \\
& + k_{3n}\left(\lambda_{3n}(n) - i\mathcal{F}n\lambda_{3n}(n) + in\mathcal{E} + \lambda_{3n}(n)^2 in\mathcal{G}\right) e^{\lambda_{3n}\theta_S} \\
& + k_{4n}\left(\lambda_{4n}(n) - i\mathcal{F}n\lambda_{4n}(n) + in\mathcal{E} + \lambda_{4n}(n)^2 in\mathcal{G}\right) e^{\lambda_{4n}\theta_S} \\
& - K_{1n}\hat{s}\left(\lambda_{1n}(n) - i\mathcal{F}n\lambda_{1n}(n) + in\mathcal{E} + \lambda_{1n}(n)^2 in\mathcal{G}\right) e^{\lambda_{1n}\theta_S} \\
& - K_{2n}\hat{s}\left(\lambda_{2n}(n) - i\mathcal{F}n\lambda_{2n}(n) + in\mathcal{E} + \lambda_{2n}(n)^2 in\mathcal{G}\right) e^{\lambda_{2n}\theta_S} \\
& - K_{3n}\hat{s}\left(\lambda_{3n}(n) - i\mathcal{F}n\lambda_{3n}(n) + in\mathcal{E} + \lambda_{3n}(n)^2 in\mathcal{G}\right) e^{\lambda_{3n}\theta_S} \\
& - K_{4n}\hat{s}\left(\lambda_{4n}(n) - i\mathcal{F}n\lambda_{4n}(n) + in\mathcal{E} + \lambda_{4n}(n)^2 in\mathcal{G}\right) e^{\lambda_{4n}\theta_S},
\end{aligned} \tag{2.74h}
$$

where the constants γ, $\mathcal{E}$, $\mathcal{F}$ and $\mathcal{G}$ in (2.74) are defined as

$$
\gamma \equiv \frac{A_H \sin\theta_S}{f_S R^2}, \quad \mathcal{E} \equiv \frac{A_H\left(1+\cos^2\theta_S\right)}{\sin^3\theta_S R^2 f_S}, \quad \mathcal{F} \equiv \frac{A_H}{\sin^2\theta_S R^2 \Omega}, \quad \mathcal{G} \equiv \frac{A_H}{f_S R^2 \sin\theta_S}.
$$

As in the previous section, the roots of (2.63) were obtained using the roots algorithm from MATLAB. Subsequently, the roots were plotted to observe if the algorithm generated any imprecision and correct them, if it were necessary, using the Newton method. Hereafter, the K_{jn} and k_{jn} in (2.72) were numerically obtained from (2.74) using the *linsolve* function from MATLAB (source code Appendix A.3.3). Streamfunction (2.42) can be evaluated using the coefficients a_n, b_n, A_n and B_n obtained from (2.72).

Figure 2.18 shows the streamfunction (2.42) using the control parameters in Table 2.1 and $N = 350$. We observe that the circulation is confined to the shelf within the "Munk-type" boundary layers or boundary layers given by the Laplacian diffusion.

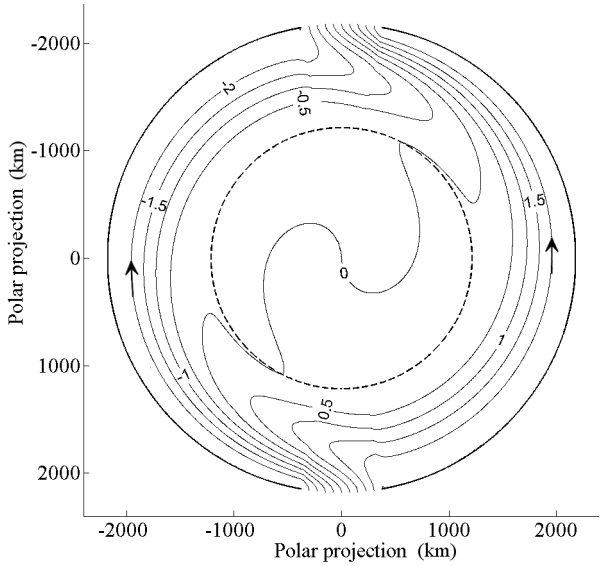

Figure 2.18: Steady source–sink planetary geostrophic circulation in a step-shelf domain in presence of lateral friction. The shelf break is denoted by a dashed line. The streamlines denote isolines of flow transport in Sverdrups ($1Sv = 10^6\ m^3 s^{-1}$).

2.2.3 Basin with three gaps

In the previous sections the basin has two, diametrically opposed gaps. As a modest step towards a more realistic Arctic basin application we generalise the basin to one with three gaps, across which source/sinks are prescribed which sum to zero (i.e. no net fluid enters the domain). The gap size and location varies depending on the geographic position and extension of the real straits of the Arctic Ocean basin at co-latitude 20^o. Thus, we consider the Davis Strait (650 km wide), the Bering Strait (620km wide) and the GINs straits (1660 km wide). Figure 2.19 shows a schematic of the idealised Arctic domain and Table 2.2 presents the parameter values used in this section. Across the Bering Strait an inflow is prescribed, while across the Davis Strait an outflow is prescribed. At the GINs strait we prescribe an inflow (North Atlantic Current) across part of the strait and an outflow (East Greenland Current through the Fram Strait) across the remaining part of the strait. The magnitude proposed represents the mean annual transport across the straits (see Table 2.2) following different studies (Tsubouchi *et al.*, 2012; Beszczynska-Möller *et al.*, 2012). Mathematically, we define ψ_B to represent the transports through the three gaps:

$$\psi(\varphi,\theta_B) \equiv \psi_B(\varphi) = \begin{cases} 4.5\varphi/\varphi_1 & if \quad 0 \le \varphi \le \varphi_1, \\ 4.5 & if \quad \varphi_1 \le \varphi \le \varphi_2, \\ 4.5 + 1\left[\varphi - \varphi_2\right] / \left[\varphi_3 - \varphi_2\right] & if \quad \varphi_2 \le \varphi \le \varphi_3, \\ 5.5 & if \quad \varphi_3 \le \varphi \le \varphi_4, \\ 5.5 - 2.1\left[\varphi - \varphi_4\right] / \left[\varphi_5 - \varphi_4\right] & if \quad \varphi_4 \le \varphi \le \varphi_5, \\ 3.4 & if \quad \varphi_5 \le \varphi \le \varphi_6, \\ 3.4 - 5.4\left[\varphi - \varphi_6\right] / \left[\varphi_7 - \varphi_6\right] & if \quad \varphi_6 \le \varphi \le \varphi_7, \\ -2 + 2\left[\varphi - \varphi_7\right] / \left[2\pi - \varphi_7\right] & if \quad \varphi_7 \le \varphi \le 2\pi. \end{cases} \tag{2.75}$$

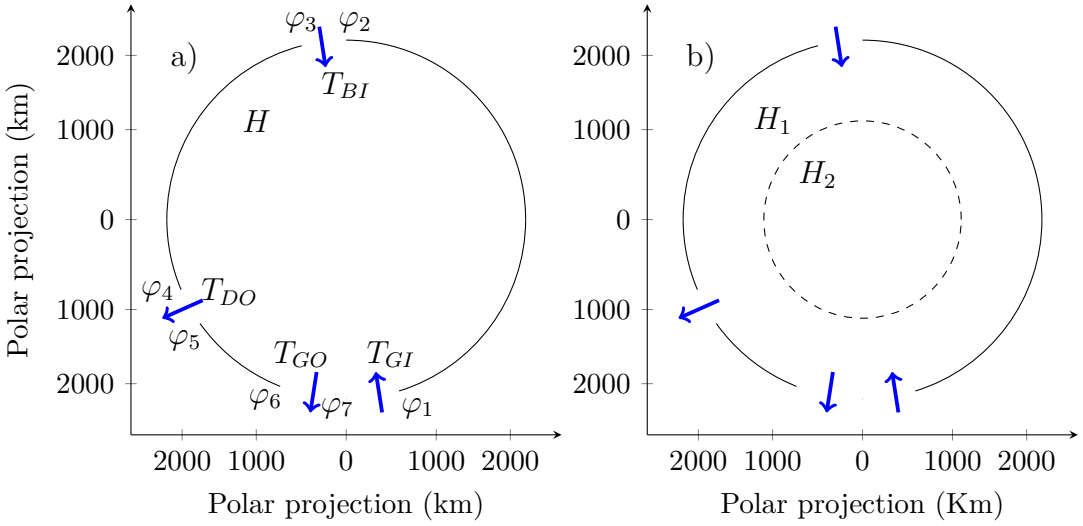

Figure 2.19: Idealised Arctic domain; a) flat bottom domain, b) step-shelf domain. The arrows represent the inflow and outflow across the straits.

The Fourier representation of the streamfunction (2.75) is written in Appendix A.4 and plotted as dashed blue line Figure 2.20. We can note that $\hat{a}_0 \neq 0$ but the analytical solutions from section 2 were based on the assumption that $\hat{a}_0 = 0$. Therefore, we transposed the function to a different level in the y–axis resulting in $\hat{a}_0 = 0$. This new function is shown as continuous blue line.

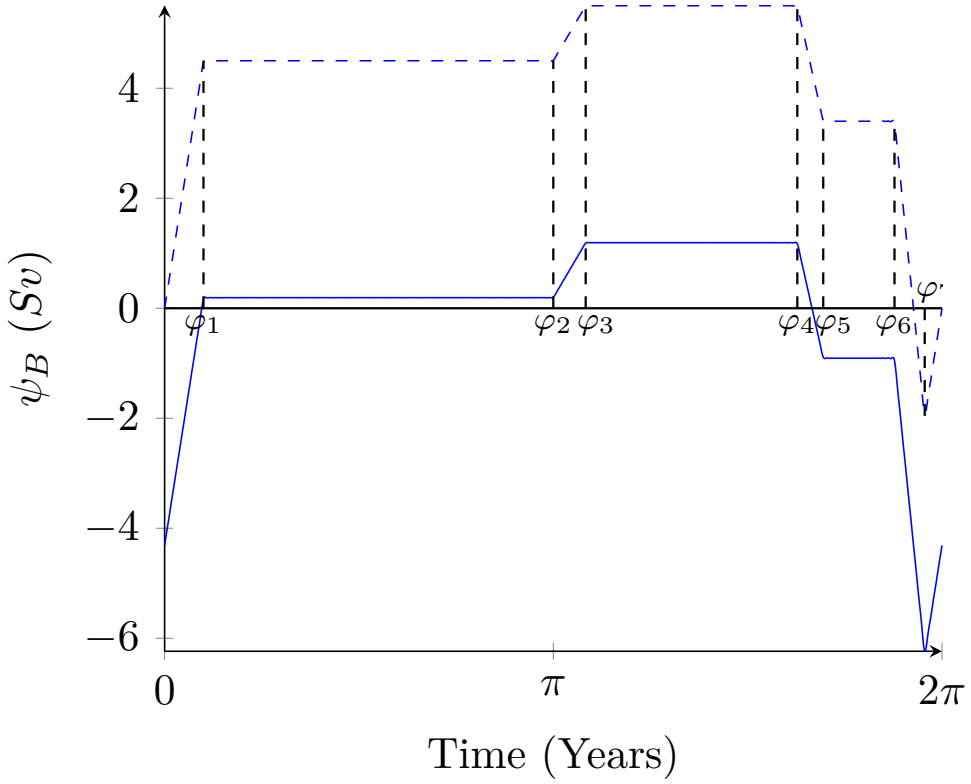

Figure 2.20: Plot of the streamfunction 2.75. Dashed and continuous lines denote the function defined in (2.75) together with its transpose satisfying $\hat{a}_0 = 0$, respectively.

Figures 2.21 (a) and (b) show the solution for a flat bottom basin in presence of linear bottom friction and Laplacian eddy viscosity, respectively. The parameters used to calculate the streamfunctions are given in Table 2.2 and the number of terms used in summation of (2.15) is $N = 150$. The inlet flow from the GINs strait is deflected to the left where the majority of it recirculates leaving the domain through the same place (see panels (c) and (d) which show the neighbourhood of the GINs strait enlarged). The remaining part of the flow circulates towards the Davis Strait where it merges with the Bering Strait inflow before exiting the basin. Qualitatively the solutions plotted in Figure 2.21 (a) and (b) are similar, with the exception of the closed anticyclonic gyre in the latter plot, close to the GINs strait.

The sensitivity of both solutions to θ_f is addressed in Figure 2.21 (e) and 2.21 (f). The dashed and black lines show the difference between solutions using $\theta_f = 0.25\theta_B$ and $\theta_f = \theta_B$, respectively. The solution in presence of linear bottom friction does not show a significant change with the of θ_f (see Figure 2.21 (e)). However, the lateral friction solution reveals important changes in the structure of the anticyclonic closed circulation (Figure 2.21 (f)). Also, we can observe the formation of another closed circulation near the Davis Strait.

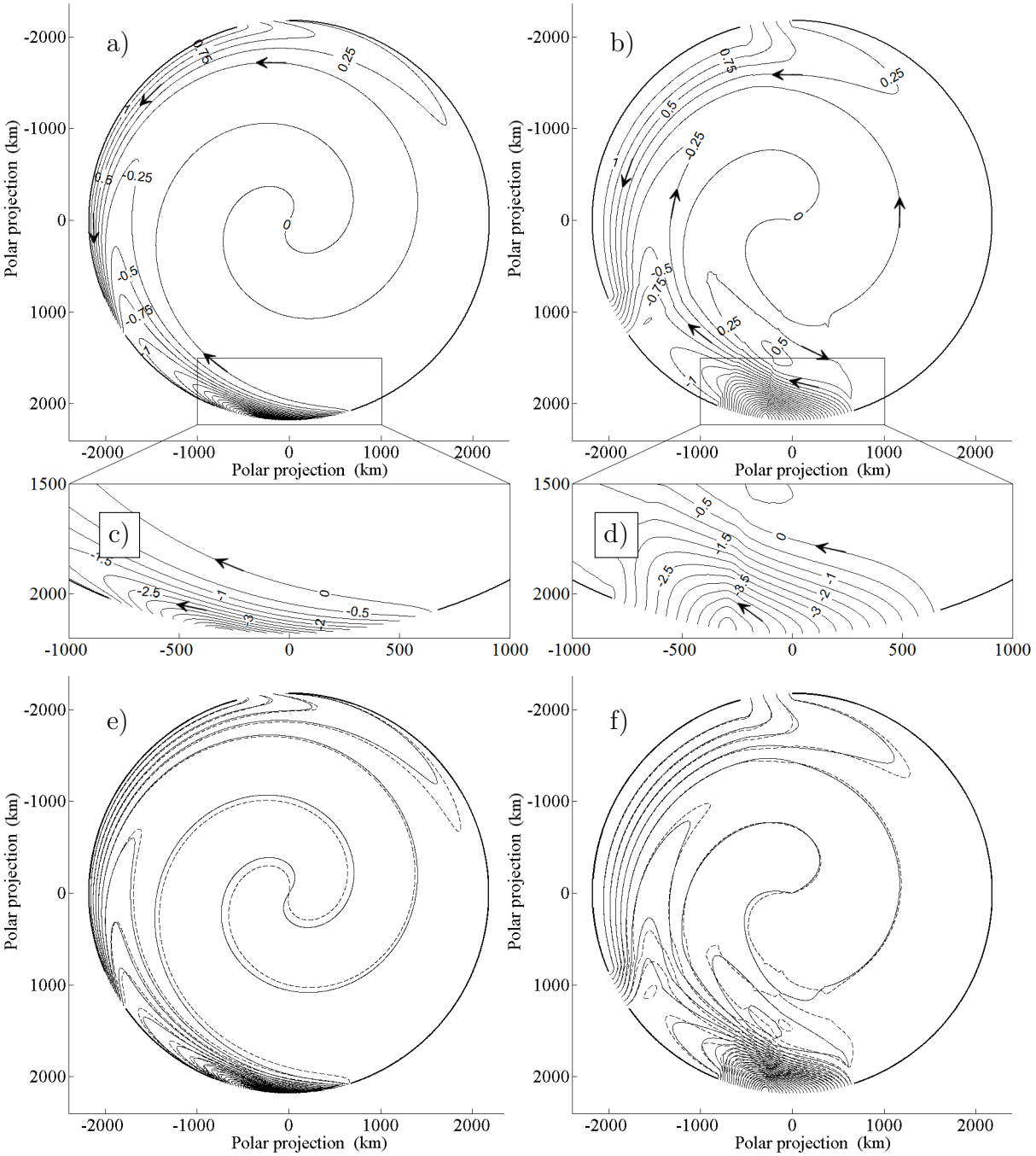

Figure 2.21: Steady source–sink planetary geostrophic flow in an idealised flat bottom Arctic basin. a) bottom friction solution; b) lateral friction solution; c) enlarge area of (a) denoted by a square; d) enlarge area of (b) denoted by a square; e) sensitivity of the solution to the value of θ_f; f) same as (e) but in presence of lateral friction. The dashed line and the black line denote $\theta_f = 0.25\theta_B$ and $\theta_f = \theta_B$, respectively. The streamlines denote isolines of flow transport in Sverdrups ($1Sv = 10^6\ m^3 s^{-1}$).

We now consider how the addition of a step–shelf alters the circulation in a basin with three straits. Figures 2.22 (a) and (b) show the streamfunction (2.42) using the a_n, b_n, A_n and B_n obtained from (2.45) and (2.72), respectively. The parameter values used

are presented in Table 2.2. The flow enters the basin from the GINs and Bering Strait. Most of the GINs inflow exits as soon as it enters the basin (recirculation); the remaining part flows anticyclonically on the shelf exiting through the Davis Strait, together with the circulation from the Bering Strait. The deep basin remains stagnant. Even though both solutions are qualitatively similar, the Laplacian friction solution reveals a cyclic circulation on the step–shelf close to the Nordic gap (see Figure 2.22 (b)).

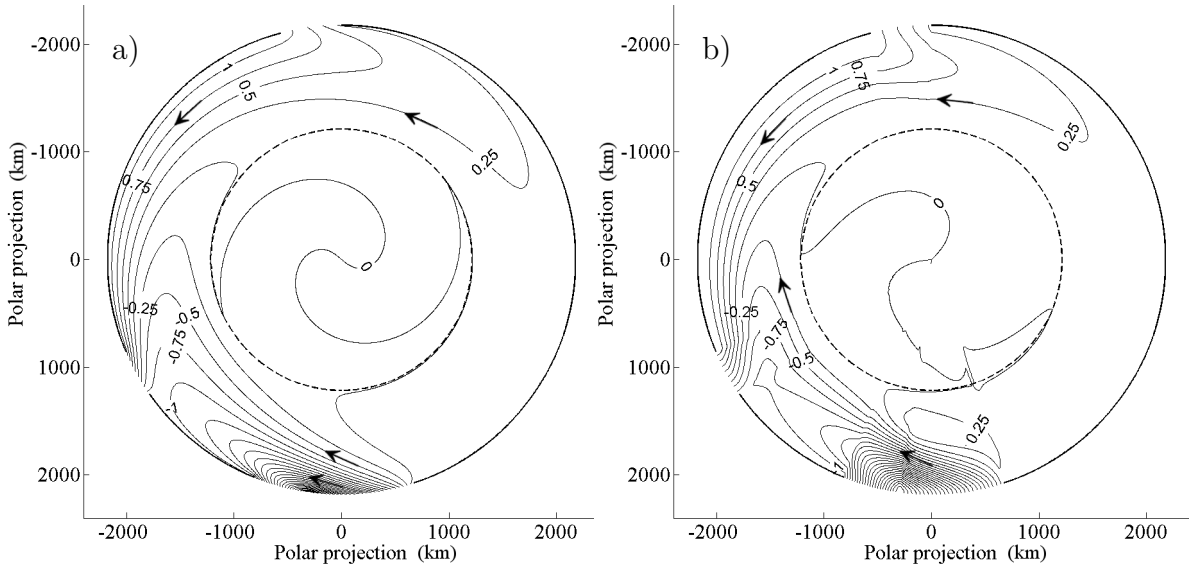

Figure 2.22: Steady source–sink planetary geostrophic flows Arctic basin in an idealised step-shelf with three gaps; a) bottom friction solution; b) lateral friction solution. The streamlines denote isolines of flow transport in Sverdrups ($1Sv = 10^6\ m^3 s^{-1}$).

Finally, we consider how the circulation is altered on a narrower step–shelf in comparison with Figure 2.22. The Arctic Ocean has a wide continental shelf limiting the Amerasian and Eurasian basin on the east. However, Canadian and Alaskan continental shelves are narrower in comparison to the Eurasian shelf. In fact, in some areas of the Alaskan continental shelf, the shelf break is located less than 100 km from the coastline as it is the case in the Beaufort Sea region. In section 2.2.2b we saw that a narrow shelf leads to ageostrophic cross–shelf circulation as long as it is smaller than the frictional boundary layer width. The frictional boundary layer was computed in section 2.2.1b for a basin with depth 250 m giving approximately 114 km width. The continental shelf from the Canadian archipelago has a depth average of 100 m, thus the frictional boundary layer in this region is wider than in section 2.2.1b. The frictional boundary layer width in the Canadian archipelago, $W \sim (\mu_0/f_0)^{1/2}\, r_b$ obtaining that $\mu_0 \equiv \mu/H_1 = 10^{-6}\ s^{-1}$ and $W \sim 180\ km$. It can be noted that the frictional boundary layer almost twice the size is

some areas of the Alaskan shelf.

Figure 2.23 shows the streamfunction (2.42) using the values in Table 2.2, $\theta_S = 18\pi/180$, a the linear bottom friction of $\mu = 5 \times 10^{-4}\ ms^{-1}$ and $H_1 = 100\ m$ giving the frictional boundary layer width to 300 km. As in Figure 2.22 (a) most of the circulation is given in the western area of the basin, although a small portion of the inlet is deflected to the East. The Bering and the Nordic branches are constrained by the shelf to form strong boundary currents. The deep basin remains stagnant, only two deep currents are observed close to the shelf break.

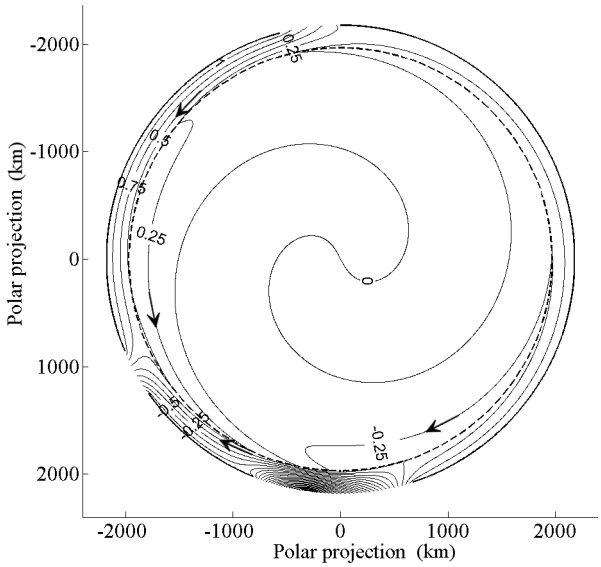

Figure 2.23: As in Figure 2.22 (a) with a narrower step–shelf of width 200 km ($\theta_S = 0.9\theta_B$) and $\mu = 5 \times 10^{-4}\ ms^{-1}$. The streamlines denote isolines of flow transport in Sverdrups ($1Sv = 10^6\ m^3 s^{-1}$).

Table 2.2: Parameters values for an Arctic basin with three straits.

Symbol	Variable(Unit)	Value
φ_1	- (rad)	$\pi/10$
φ_2	- (rad)	π
φ_3	- (rad)	$39\pi/36$
φ_4	- (rad)	$293\pi/180$
φ_5	- (rad)	$61\pi/36$
φ_6	- (rad)	$169\pi/90$
φ_7	- (rad)	$88\pi/45$
T_{GI}	GIN inflow (Sv)	6.5
T_{GO}	GIN outflow (Sv)	5.4
T_{BI}	Bering Strait (Sv)	1
T_{DO}	Davis Strait (Sv)	2.1
H	Depth (m)	1000
H_1	Step shelf depth (m)	250
H_2	Deep basin (m)	3000
n	numbers of Fourier terms	150
μ	Bottom friction (ms^{-1})	10^{-4}
A_H	Eddy viscosity (m^2s^{-1})	10000
θ_B	Co-latitude at the boundary (rad)	$\pi/9$
θ_S	Shelf Edge (rad)	$0.55\theta_B$

2.3 Conclusions

This chapter develops analytical models for a steady planetary geostrophic circulation driven by source/sink boundary flows in a polar basin with simple topography. Analytic solutions are obtained using the "beta–sphere" approximation first proposed by Imawaki and Takano (1974).

Firstly, a source–sink driven circulation in the presence of bottom friction is examined in section 2.2.1. In a circular basin without bathymetry, the circulation was characterised by two strong boundary currents which in the presence of small linear bottom friction, $\mu = 10^{-5}\ ms^{-1}$, is constrained to isolines of planetary vorticity except in the frictional boundary layer adjacent to the basin wall. This characteristic flow was due to the geostrophic behaviour of the flow away from the frictional boundary layer. However, Figure 2.6 (a) showed how this balance could be "broken" with much high values of bottom friction (i.e. $\mu = 10^{-2}\ ms^{-1}$) producing a nearly symmetrical transpolar circulation. Next, the circulation in a flat bottom basin driven by a sheared inflow and uniform outflow is considered. There is no observed change in the planetary geostrophic circulation in this case because the relative vorticity is much smaller than the planetary vorticity. These results disagree with Yang (2005) who observed a changed in the direction of the circulation due to a change in the PV balance. In addition, the analytic model is extended to a basin with a step–shelf. The circulation was constrained on the shelf leaving the deep basin stagnant, although large values of bottom friction (i.e. $\mu = 10^{-2}\ ms^{-1}$) allowed the flow to cross the shelf break forming a deep basin circulation. This circulation was revealed to be irrotational by an integral constraint analysis. A similar outcome was also obtained by setting the shelf width narrower than the frictional boundary layer. Same effect was also observed by Willmott and Luneva (2015) on source–sink boundary flows in a polar basin with one strait.

The analytic model is modified to incorporate lateral viscosity (2.5) using a boundary layer approximation which keeps the leading order cross–boundary layer derivative term of the Laplacian eddy viscosity operator (i.e. $A_H\nabla^2\boldsymbol{u}$). Such a boundary layer approximation is familiar in the literature for determining the approximate mid–latitude (Munk) western boundary layer dynamics (Pond and Pickard, 1983, Chapter 9). Qualitatively, the boundary layer approximation reproduced the same circulation as that observed with linear bottom friction. In addition, this circulation was compared with that calculated by Imawaki and Takano (1974) which retained the full expression $A_H\nabla^2\boldsymbol{u}$. Both proved to

be indistinguishable showing that the boundary layer approximation captures the exact circulation in a polar basin.

Finally, we considered a circular polar basin with three gaps representing the three main "corridors" connecting the Arctic Ocean to its marginal seas. The flat bottom solution exhibits an anticyclonic circulation in the basin. Two strong boundary currents connect the Bering and the GINs strait with the Davis Strait.

The addition of a step–shelf in the domain confines the flow circulation to the step–shelf. Also, we considered the circulation in a basin with a narrow shelf typical of that in the Canadian Archipelago. We observed the presence of deep currents close to the shelf edge.

In Chapter 4 we will introduce a "community" numerical global ocean model called NEMO. We will compare the approximate analytical and equivalent numerical solutions assessing the accuracy of the former. In addition, NEMO will enable us to consider circulations in basins with more complex (i.e. realistic) bathymetries that cannot be solved by the analytical methods.

Chapter 3

Planetary and gravity waves in a polar basin on the "β-sphere"

3.1 Introduction

In Chapter 2 we saw that planetary waves are responsible for the spin–up of source–sink driven flow in a polar basin. We now consider the dynamics of freely–propagating barotropic waves of this type in this Chapter. Once again the "beta sphere" approximation is employed to derive an approximate form for the wave dispersion relation.

The analytical treatment of divergent barotropic planetary and gravity waves in a polar basin is clearly complicated by the non-uniform meridional gradient of the Coriolis parameter. Nevertheless, LeBlond (1964) solved the governing unsteady, barotropic circulation on a tangent plane to the spherical Earth at the pole. LeBlond (1964) obtained the barotropic planetary wave dispersion relation in a polar basin using a "polar β-plane" approximation in cylindrical polar coordinates. As we saw in Chapter 2 and in comparison with the "β-plane" approximation of mid latitudes, the "polar β-plane" projects a tangential plane on the North Pole. On that plane the β coefficient of the Taylor expansion of the Coriolis parameter is dependent on the r (see 2.2b) whereas on the "β-plane" is constant. Subsequently, LeBlond (1964) contrasted the planetary waves eigenfrequencies from "polar β-plane" approximation with the "β-plane" approximation (Longuet-Higgins, 1968) revealing a good agreement between them. In related meteorological studies, Haurwitz (1975) and Bridger and Stevens (1980) use cylindrical polar coordinates to study freely propagating waves in a high-latitude atmosphere. The concept of the δ–plane approximation for quasi-geostrophic dynamics at high latitudes was devel-

oped by Harlander (2005). Harlander (2005) demonstrates that the high-latitude δ-plane model can be consistently derived from spherical geometry. On the δ-plane Harlander (2005) demonstrates that high-latitude Rossby waves energy rays are curved, which is not the case on the β-plane.

In contrast with studies of free-waves in a polar basin there is a considerable body of literature on free-waves in a thin layer of fluid on the entire rotating earth. For example, Paldor *et al.* (2013) and Paldor (2015) obtain solutions for zonally propagating planetary and inertial-gravity (i.e. Poincaré) waves on the entire rotating earth, extending the solutions in the seminal work of Longuet-Higgins (1968).

In this chapter we present a new approximate method for obtaining the dispersion relation for freely propagating barotropic gravity and planetary waves in a polar basin. The computationally efficient dispersion relation is derived using "β–sphere" approximation, first proposed by Imawaki and Takano (1974), in their analysis of steady source-sink driven planetary geostrophic dynamics in a polar basin. In comparison to a more accurate approximation as LeBlond (1964), the linearised spherical shallow water equations are used to derive the barotropic vorticity equation, and thereafter the co-latitude is fixed in the coefficients of this partial differential equation, as in Chapter 2. How well does the "β-sphere" approximation capture the dynamics of planetary waves in a polar basin? This question is addressed in this chapter which is structured as follows. Section 3.2 derives the eigenvalue problem for gravity and planetary waves using the "β-sphere" approximation. Subsequently, planetary waves are discussed in Section 3.3 and gravity waves are discussed in Section 3.4, followed by conclusions in Section 3.5. The majority of the results in this chapter have been published (Willmott and Gavilan Pascual-Ahuir, 2017). In addition, we present the eigenfunctions and discuss the cut–off period associated to the planetary waves.

3.2 Formulation of the eigenvalue problem

We consider an ocean of uniform density on a polar cap with centre located at the pole. As spherical polar coordinates system is adopted where θ and φ denote the co-latitude and longitude angles, respectively. Let θ_B denote the co-latitude of the boundary of the polar basin. Then, $\theta \in [0, \theta_B)$ and $\varphi \in [0, 2\pi)$. The unit vectors $\left\{\mathbf{k}, \hat{\boldsymbol{\theta}}, \hat{\boldsymbol{\varphi}}\right\}$ form a right-handed triad, where

$$\mathbf{k} \wedge \hat{\boldsymbol{\theta}} = \hat{\boldsymbol{\varphi}},$$

and **k** is a unit vector in the (outward) radial direction (see Figure 2.1). With respect to this coordinates system the linearised shallow water equations for inviscid homogeneous dynamics in the polar cap take the form

$$u_t + fv = -\frac{g}{R\sin\theta}\eta_\varphi, \tag{3.1a}$$

$$v_t - fu = -\frac{g}{R}\eta_\theta, \tag{3.1b}$$

$$\eta_t + \frac{1}{R\sin\theta}\left[(Hu)_\varphi + (Hv\sin\theta)_\theta\right] = 0, \tag{3.1c}$$

where the velocity $\boldsymbol{u} = u\hat{\boldsymbol{\varphi}} + v\hat{\boldsymbol{\theta}}$, η is the free surface elevation, H is the undisturbed depth of the ocean, g is the gravitational acceleration, $f = 2\Omega\cos\theta$, where Ω is the angular frequency of the rotation of the Earth and R is the radius of the Earth. We seek azimuthally propagating waves solutions of (3.1) of the form

$$\left.\begin{aligned} u &= U(\theta)\, exp\left[i\left(m\varphi - \omega t\right)\right], \\ v &= V(\theta)\, exp\left[i\left(m\varphi - \omega t\right)\right], \\ \eta &= F(\theta)\, exp\left[i\left(m\varphi - \omega t\right)\right], \end{aligned}\right\} \tag{3.2}$$

where $\omega > 0$ is the angular wave frequency, m is the azimuthal integer wave number (i.e $m = \pm1, \pm2, \pm3, ..$) and U, V and F are amplitude functions. Substituting (3.2) in (3.1) we obtain

$$-i\omega U + fV = -\frac{img}{R\sin\theta}F, \tag{3.3a}$$

$$-i\omega V - fU = -\frac{g}{R}F', \tag{3.3b}$$

$$-i\omega F + \frac{1}{R\sin\theta}\left[imHU + (HV\sin\theta)_\theta\right] = 0, \tag{3.3c}$$

where $F' \equiv dF/d\theta$. First, we multiply (3.3a) and (3.3b) by f and $i\omega$, respectively, to obtain

$$-i\omega fU + f^2V = -\frac{imgf}{R\sin\theta}F, \tag{3.4a}$$

$$\omega^2 V - i\omega fU = -\frac{gi\omega}{R}F', \tag{3.4b}$$

Subtracting (3.4b) from (3.4a) gives a expression for V in terms of F and its first derivative.

$$V\left(f^2 - \omega^2\right) = \frac{ig\left(\omega F' - \frac{mf}{\sin\theta}F\right)}{R}. \tag{3.5}$$

A similar approach is used to obtain an expression for U. In summary,

$$U = \frac{g\left(fF' - \frac{m\omega}{\sin\theta}F\right)}{RD}, \tag{3.6a}$$

$$V = \frac{ig\left(\omega F' - \frac{mf}{\sin\theta}F\right)}{RD}, \tag{3.6b}$$

where $D \equiv f^2 - \omega^2$. Upon substituting (3.6) into (3.3c), we obtain

$$\begin{aligned} -i\omega F + \frac{1}{R\sin\theta}\Bigg[imH\frac{g\left(fF' - \frac{m\omega}{\sin\theta}F\right)}{RD} \\ + \left(\left(\frac{ig\left(\omega F' - \frac{mf}{\sin\theta}F\right)}{RD}\right)H\sin\theta\right)_\theta\Bigg] &= 0. \end{aligned} \tag{3.7}$$

Expanding (3.7) and multiplying by R^2H^{-1},

$$\begin{aligned} -\frac{i\omega R^2}{H}F + \frac{ig}{\sin\theta}\Bigg[m\frac{\left(fF' - \frac{m\omega}{\sin\theta}F\right)}{D} + \left(\frac{\left(\omega F' - \frac{mf}{\sin\theta}F\right)}{D}\right)_\theta\sin\theta \\ + \frac{\left(\omega F' - \frac{mf}{\sin\theta}F\right)}{D}\cos\theta\Bigg] &= 0. \end{aligned} \tag{3.8}$$

We expand again the partial derivative and we get,

$$\begin{aligned} -\frac{i\omega R^2}{H}F + \frac{ig}{\sin\theta}\Bigg[m\frac{\left(fF' - \frac{m\omega}{\sin\theta}F\right)}{D} + \frac{\sin\theta}{D^2}\Bigg(4\Omega f\sin\theta\left(\omega F' - \frac{mf}{\sin\theta}F\right) \\ + D\left(wF'' - \frac{mf}{\sin\theta}F' + \frac{2\Omega m}{\sin^2\theta}F\right)\Bigg) + \frac{\left(\omega F' - \frac{mf}{\sin\theta}F\right)}{D}\cos\theta\Bigg] &= 0. \end{aligned} \tag{3.9}$$

If we multiply (3.9) by $D\left(ig\omega\right)^{-1}$ we obtain

$$\begin{aligned} -\frac{R^2D}{gH}F + \frac{1}{\omega\sin\theta}\Bigg[m\left(fF' - \frac{m\omega}{\sin\theta}F\right) + \frac{\sin\theta}{D}\Bigg(4\Omega f\sin\theta\left(\omega F' - \frac{mf}{\sin\theta}F\right) \\ + D\left(wF'' - \frac{mf}{\sin\theta}F' + \frac{2\Omega m}{\sin^2\theta}F\right)\Bigg) + \left(\omega F' - \frac{mf}{\sin\theta}F\right)\cos\theta\Bigg] &= 0, \end{aligned} \tag{3.10}$$

(3.10) can be simplified to

$$\begin{aligned} F'' + \frac{\cos\theta}{\sin\theta}F' + \frac{4\Omega f\sin\theta}{D}F' - \frac{4\Omega f^2 m}{\omega D}F \\ + \frac{2\Omega m}{w\sin^2\theta}F - \frac{R^2D}{gH}F - \frac{m^2}{\sin^2\theta}F - \frac{mf\cos\theta}{\omega\sin^2\theta}F &= 0. \end{aligned} \tag{3.11}$$

Defining the dimensionless wave frequency, $\sigma = \omega\left(2\Omega\right)^{-1}$

$$\begin{aligned} F'' + \frac{\cos\theta}{\sin\theta}F' + \frac{2\cos\theta\sin\theta}{\cos^2\theta - \sigma^2}F' - \frac{2f^2m}{\sigma D}F \\ + \frac{m}{\sigma\sin^2\theta}F - \frac{R^2D}{gH}F - \frac{m^2}{\sin^2\theta}F - \frac{m\cos^2\theta}{\sigma\sin^2\theta}F &= 0. \end{aligned} \tag{3.12}$$

Rearranging (3.12), we obtain

$$F'' + \frac{\cos\theta}{\sin\theta}F' + \frac{2\cos\theta\sin\theta}{\cos^2\theta - \sigma^2}F' - \frac{2\cos^2\theta m}{\sigma\left(\cos^2\theta - \sigma^2\right)}F + \frac{m}{\sigma}F - \frac{R^2 D}{gH}F - \frac{m^2}{\sin^2\theta}F = 0. \tag{3.13}$$

Finally, we obtain the wave amplitude equation for freely-propagating waves in polar cap:

$$F'' + \left\{\frac{\sin 2\theta}{\cos^2\theta - \sigma^2} + \cot\theta\right\}F' - \left\{\frac{m}{\sigma}\left(\frac{\cos^2\theta + \sigma^2}{\cos^2\theta - \sigma^2}\right) + \frac{m^2}{\sin^2\theta} + \left(\frac{R}{r_e}\right)^2\left(\cos^2\theta - \sigma^2\right)\right\}F = 0, \tag{3.14}$$

where

$$r_e^2 = \frac{gH}{4\Omega^2},$$

where r_e is the external Rossby radius of deformation.

On the basin wall we demand that there is no normal flow:

$$V = 0 \quad \text{on} \quad \theta = \theta_B,$$

which can be expressed as

$$F' - \frac{m}{\sigma}\cot\theta_B F = 0, \quad \text{on} \quad \theta = \theta_B, \tag{3.15}$$

upon using (3.6b). At the pole (3.14) reduces to

$$F(0) = 0. \tag{3.16}$$

We now invoke the "beta-sphere approximation" and let $\theta = \theta_f$, where $0 < \theta_f < \theta_B$, in the coefficients of (3.14) thereby obtaining a constant coefficient second order ordinary differential equation. Typically, we let $\theta_f = 0.5\theta_B$, but the sensitivity of the free-wave dispersion relations to this angle will be discussed later. Equation (3.14) together with boundary conditions (3.15) and (3.16) form a Sturm-Liouville eigenvalue problem for σ.

Before solving this eigenvalue problem in the subsequent sections, it is interesting to consider how the amplitude equation (3.14) is affected when variations of f with co-latitude are neglected. An approximation of this type in a spherical polar basin would be valid for small wavelength waves in the meridional direction. When $f = 2\Omega$, the amplitude equation simplifies to

$$F'' + \cot\theta F' - \left\{\frac{m^2}{\sin^2\theta} + \left(\frac{R}{r_e}\right)^2\left(\cos^2\theta - \sigma^2\right)\right\}F = 0. \tag{3.17}$$

Comparing (3.17) with (3.14) we observe that

$$\frac{\sin 2\theta}{\cos^2\theta - \sigma^2} \quad ; \quad \frac{m}{\sigma}\left(\frac{\cos^2\theta + \sigma^2}{\cos^2\theta - \sigma^2}\right),$$

arise from the variation of the Coriolis parameter with co-latitude. On the "f-sphere", we noted that $f = 2\Omega$ (retaining the first term in the Maclaurin expansion in powers of θ) which leads to the modification of the term involving r_e in (3.14). The full derivation for a "f-sphere" can be found in Appendix B.1.

3.3 Planetary waves ($\sigma^2 \ll 1$)

For these low frequency waves (3.14) can be approximated as

$$F'' + AF' - BF = 0, \tag{3.18}$$

where

$$A \equiv 2\tan\theta_f + \cot\theta_f > 0,$$

and

$$B \equiv \frac{m}{\sigma} + \frac{m^2}{\sin\theta_f} + \left(\frac{R}{r_e}\right)^2 \cos^2\theta_f.$$

We observe that if the meridional structure of these wave modes is to be oscillatory then we require $m < 0$. The general solution of (3.18) will then take the form:

$$F = e^{-\frac{A\theta}{2}}\left(c_1 e^{i\kappa\theta} + c_2 e^{-i\kappa\theta}\right), \tag{3.19}$$

where

$$\kappa^2 = -B - (1/4)\,A^2, \tag{3.20}$$

and c_1, c_2 are arbitrary constants. Notice that since $m < 0$, (3.2) reveals that the phase velocity of the waves is westward (i.e. in the negative φ sense) as expected for planetary waves. Application of (3.16) into (3.19) yields.

$$c_1 + c_2 = 0,$$

and thus (3.19) can be re-written as

$$F = c_3 e^{-A\theta/2}\sin(\kappa\theta), \tag{3.21}$$

where c_3 is an arbitrary constant. Applying (3.21) in (3.15) gives

$$-\frac{A}{2}\sin(\kappa\theta_B) + \kappa\cos(\kappa\theta_B) - \frac{m}{\sigma}\cot\theta_B\sin(\kappa\theta_B) = 0, \tag{3.22}$$

which simplifies to

$$\kappa = \left[\frac{m}{\sigma}\cot\theta_B + \frac{1}{2}A\right]\tan\left(\kappa\theta_B\right). \tag{3.23}$$

Equation (3.23) is the dispersion equation for divergent barotropic planetary waves in a spheric cap using the "beta-sphere approximation". For a given value of $m < 0$ the discrete set of roots $\sigma_{m,n}\,(n = 1, 2, 3, ..)$ can be determined numerically from (3.23). However, approximate values of the roots are readily obtained from (3.23) upon noting that when $\sigma \ll 1$ the dispersion relation can be approximated by

$$m\cot\theta_B\tan\left(\kappa\theta_B\right) = 0,$$

whence

$$\kappa_n \approx \frac{n\pi}{\theta_B}, \qquad n = 1, 2, \ldots \quad . \tag{3.24}$$

The approximate roots (3.24) together with (3.20) yield the approximate values for $\sigma_{m,n}$:

$$\frac{|m|}{\sigma_{m,n}} = \left(\frac{n\pi}{\theta_B}\right)^2 + \frac{m^2}{\sin^2\theta_f} + \left(\frac{R}{r_e}\right)^2\cos^2\theta_f + \sec^2\theta_f + (1/4)\cot^2\theta_f. \tag{3.25}$$

It is instructive to compare the eigenfrequencies given explicitly by (3.25) and implicitly by the dispersion relation (3.23) with those calculated by LeBlond (1964). Table 3.1 lists the parameter values used by LeBlond (1964). We note that LeBlond requires the radius of the polar basin, r_B to calculate the planetary wave frequencies on a polar β-plane. In contrast, (3.23) and (3.25) require the colatitude of the boundary of the basin, θ_B, rather than r_B. However, $r_B = R\sin\theta_B$ and using the parameter values in Table 3.1 we find that $r_B = 1424km$. Table 3.2 lists the eigenfrequencies given by (3.25), and for comparison Table 3.3 list the eigenfrequencies calculated from (3.23).

The eigenfrequencies from (3.25) are displayed in Table 3.2. They can be readily computed using MATLAB (Appendix B.2 includes the MATLAB script). However, the eigenfrequencies obtained from the dispersion equation (3.23) required careful treatment because they can only be obtained using an initial value of $\sigma_{m,n}$. Therefore, the roots in Table 3.2 were used as initial approximation for the numerical technique used to solve the roots (3.23). Subsequently, the Newton–Raphson method was employed (Appendix B.3) to find the exact eigenvalues for the dispersion equation.

Table 3.1: Parameter values used by LeBlond (1964) and also employed in this study.

Symbol	Variable(Unit)	Value
Ω	Angular velocity of the Earth (s^{-1})	7.292×10^{-5}
R	Radius of the Earth (m)	6.370×10^{6}
g	Gravitational acceleration (ms^{-2})	9.8
H	Depth of the basin (m)	5753
θ_B	Co-latitude at the boundary $(degrees)$	12.92

We observe that the eigenfrequencies (3.25) listed in Table 3.2 are identical to those in Table 3.3 with the exception of $\sigma_{-1,1}$ and $\sigma_{-2,2}$ which differ in the last decimal place.

Table 3.2: Eigenfrequencies $\sigma_{m,n}$ given by (3.25).

$m =$	-1	-2	-3	-4
$n = 1$	0.00324	0.00367	0.00319	0.00268
2	0.00112	0.00177	0.00197	0.00193
3	0.00054	0.00095	0.00120	0.00131
4	0.00031	0.00058	0.00078	0.00091
5	0.00020	0.00038	0.00054	0.00065

Table 3.3: Eigenfrequencies $\sigma_{m,n}$ given by (3.23).

$m =$	-1	-2	-3	-4
$n = 1$	0.00325	0.00367	0.00319	0.00268
2	0.00112	0.00178	0.00197	0.00193
3	0.00054	0.00095	0.00120	0.00131
4	0.00031	0.00058	0.00078	0.00091
5	0.00020	0.00038	0.00054	0.00065

Table 3.4 shows the absolute error between the "β-sphere" approximation and the polar plane dispersion of LeBlond (1964) using the parameters Table 3.1. We observe that the low order planetary waves modes are accurately represented using the "beta-sphere" approximation. More specifically, $\sigma_{-1,n}\,(n = 1, ..., 5)$ and $\sigma_{-2,1}$ satisfying (3.23) are within 11% of the equivalent frequencies calculated by LeBlond (1964). We also observe increasing discrepancies between the eigenfrequencies determined by LeBlond (1964) and the "beta-sphere" approximation as the azimuthal and meridional wavelengths decrease, corresponding to increasing $|m|$ and n. This discrepancy reflects the fact that as the wavelengths of the modes decrease, their structure becomes more sensitive to the choice of the co-latitude θ_f in the dispersion relation. In practice, forced planetary waves generally have most of their energy in the lowest modes for which (3.25) gives accurate predictions for the wave periods.

Table 3.4: Relative error of eigenfrequencies. % Error= $|\sigma_{BSm,n} - \sigma_{LEm,n}|/\sigma_{BSm,n}$ where BS and LE refer to "β-sphere" and "polar plane" approximation, respectively.

$m =$	-1	-2	-3	-4
$n = 1$	0.47	0.42	13.38	28.00
2	11.03	21.33	20.75	15.76
3	10.81	22.78	26.76	26.55
4	9.73	21.34	27.05	29.21
5	8.73	19.54	25.85	29.22

Figure 3.1 displays the relative error as a function of depth for lowest modes. In general, we observe the differences between solutions remain constant for deep basin ($H > 1000\ m$). As the basin becomes shallower the discrepancy decreases for $\sigma_{m,2}$ but it increases slightly for the eigenfrequencies $\sigma_{m,1}$.

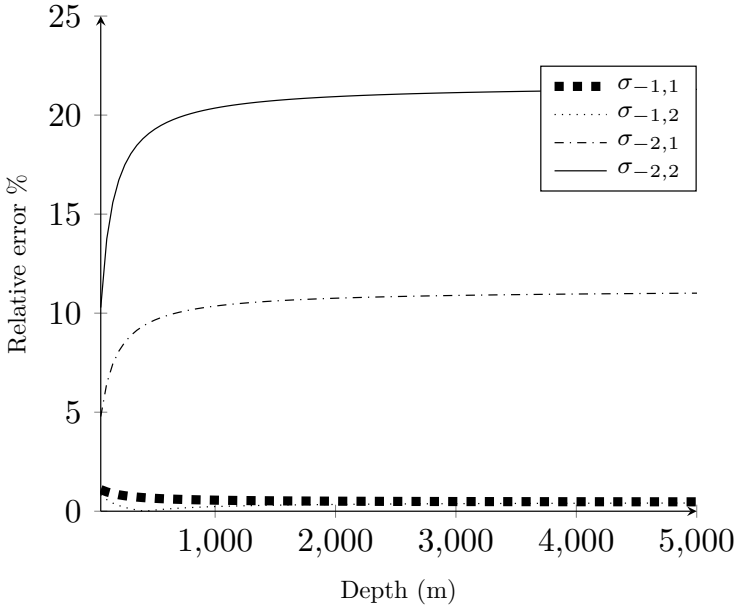

Figure 3.1: Plot of the relative error between "β-sphere" and "Polar plane" approximation as a function of depth.

In addition, we can obtain the sea surface elevation associated with the lowest modes of the planetary waves from the real part of (3.2) and computing the normalised amplitude, $F(\theta)$, from (3.21) using ($c_3 = 1$). Figure 3.2 shows the sea surface displacement corresponding to the eigenfrequencies from Table 3.3. $\sigma_{m,n}$ has $n-1$ nodal circles of amplitude, and m nodal diameters.

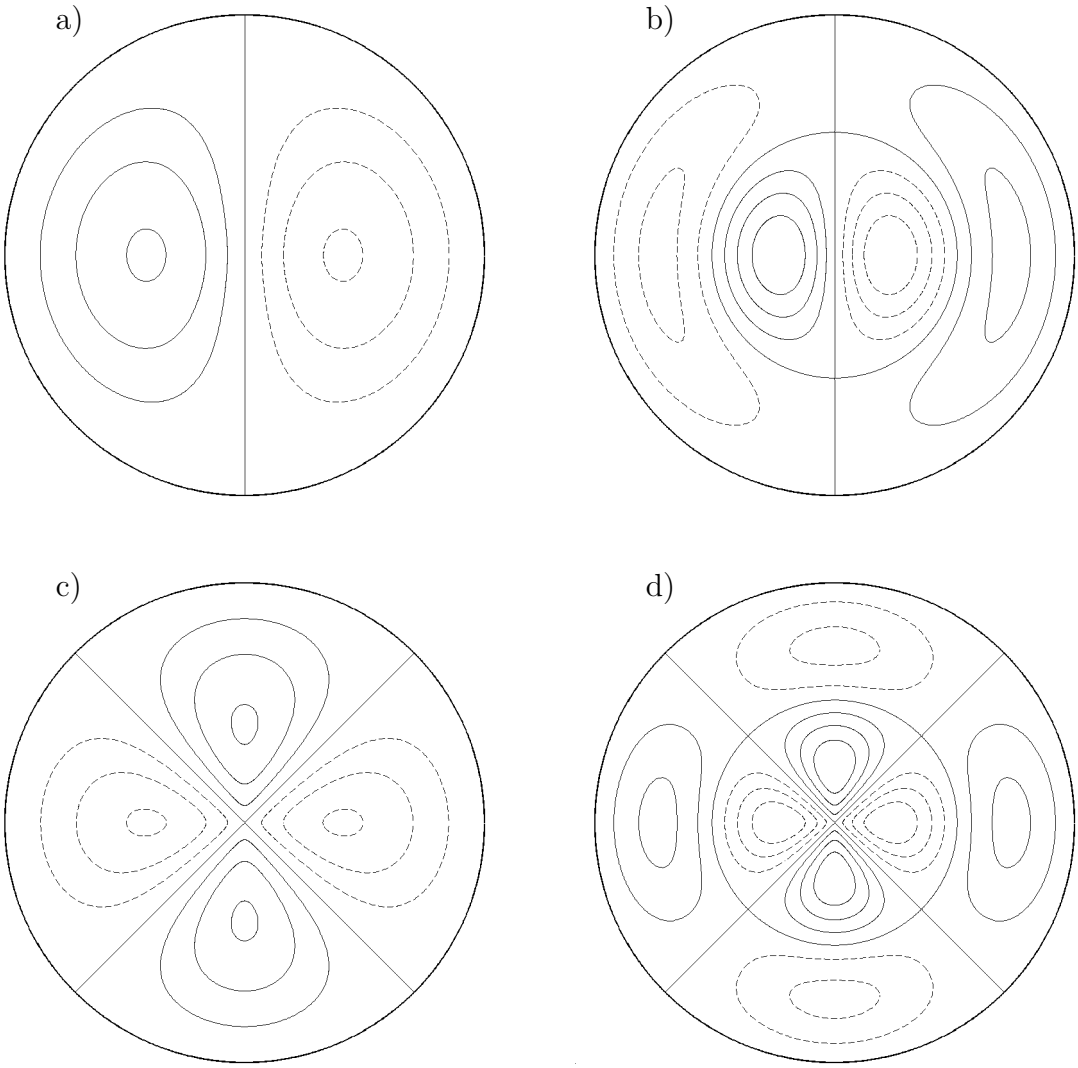

Figure 3.2: Eigenfunctions associated with planetary wave modes. The dashed (solid) line represent negative (positive) values of sea surface elevation. a) $\sigma_{-1,1}$; b) $\sigma_{-1,2}$; c) $\sigma_{-2,1}$; d) $\sigma_{-2,2}$. The patterns rotate clockwise for $m \leq -1$.

Figure 3.3 shows a plot of $\sigma_{-1,n}$ $(n = 1, .., 5)$ as a function of $\epsilon^2 = (r_e/R)^2$, when $\theta_f = 0.5\theta_B$. Varying ϵ is equivalent to varying the depth, H, of the ocean basin. The planetary wave frequencies in a polar basin are monotonic functions of ϵ. Similar qualitative behaviour for the planetary wave eigenfrequencies on a sphere was noted by Longuet-Higgins (1968). Note that the asymptotic values of the eigenfrequencies $\sigma_{-1,n}$, in the limit of large H, are given by

$$\sigma_{-1,n} \to \left[\left(\frac{n\pi}{\theta_B}\right)^2 + \frac{1}{\sin^2\theta_f} + \sec^2\theta_f + (1/4)\cot^2\theta_f\right]^{-1}.$$

Also, the same figure reveals the behaviour of another propriety which is the "cut–off" period for planetary wave. The "cut–off" period is the minimum period for which planetary waves can be propagated. For example, Table 3.5 displays the wave period associated with the wave frequencies Table 3.3. As we can observe the shortest waves that can be generated are $\sigma_{-2,1}$. Referring back to Figure 3.3 reveals that cut–off periods are longer in shallow basins but shorter in deep basins.

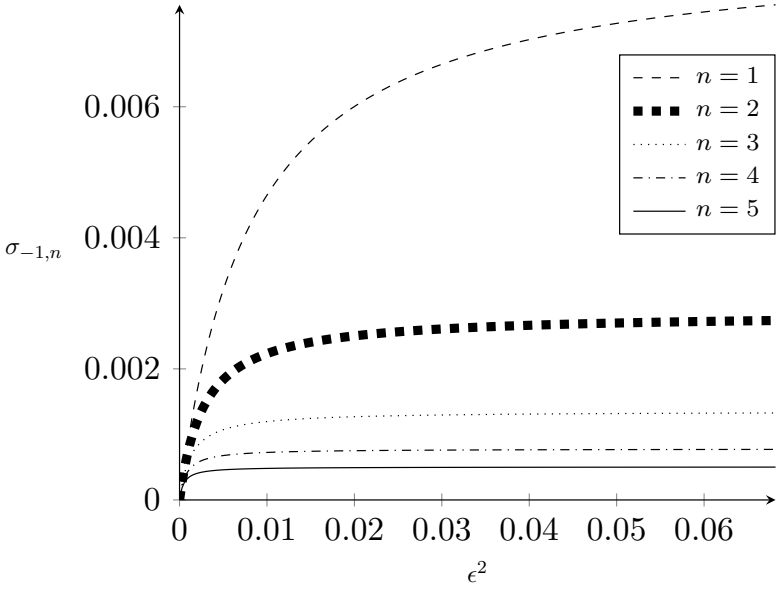

Figure 3.3: Plot of the planetary waves frequencies $\sigma_{-1,n}$ $(n = 1, .., 5)$ as a function of $\epsilon^2 = (r_e/R)^2$ when $\theta_f = 0.5\theta_B$.

Table 3.5: Equivalent wave periods (in days) of the eigenfrequencies $\sigma_{m,n}$ from (3.23).

$m =$	-1	-2	-3	-4
$n = 1$	153	136	156	186
2	443	281	253	259
3	927	523	414	380
4	1,605	862	640	549
5	2,476	1,297	930	767

How sensitive are the eigenfrequencies given by dispersion relation (3.23) to the value of θ_f? It is clear from (3.25) that for "large" $|m|$ and n the sensitivity of the eigenfrequencies to the values of these modal numbers will be small. To quantify this assertion Table 3.6 shows $|\sigma_{m,n}(0.75\theta_B) - \sigma_{m,n}(0.5\theta_B)|/\sigma_{m,n}(0.5\theta_B)$, expressed as a percentage. Entries below the principal diagonal in Table 3.6 show decreasing sensitivity of the eigenvalues to the value of θ_f. In practice, we are interested in the sensitivity of $\sigma_{-1,n}\,(n = 1, ..., 5)$ and $\sigma_{-2,1}$ to θ_f, because they are a good approximation to the exact values. Clearly, the gravest mode eigenfrequency given by (3.25) provides an accurate approximation to the exact value when $\theta_f = 0.5\theta_B$. Other values of $\theta_f \in (0, \theta_B]$ reduce the accuracy of this frequency. On the other hand, $\sigma_{-1,4}$ and $\sigma_{-1,5}$ are relatively insensitive to θ_f and provide acceptable approximations to their exact values. A final remark about the choice of θ_f is that an alternative measure of frequency sensitivity to this angle is $|\sigma_{m,n}(0.25\theta_B) - \sigma_{m,n}(0.5\theta_B)|/\sigma_{m,n}(0.5\theta_B)$. However, (3.25) shows that as $\theta_f \to 0$ the dispersion relation will become singular. The simple message is to therefore, "stay away from the pole", using the "β-sphere" approximation.

Table 3.6: Sensitivity of the eigenfrequencies $\sigma_{m,n}$ calculated from (3.23) to the co–latitude θ_f in percentage.

$m =$	-1	-2	-3	-4
$n = 1$	21.85	51.95	75.58	90.77
2	6.59	19.80	36.24	52.09
3	3.04	9.74	19.39	30.44
4	1.73	5.69	11.74	19.25
5	1.12	3.71	7.79	13.06

3.4 Gravity waves ($\sigma > 1$)

For the high frequency gravity modes we re-write the amplitude equation (3.14) as

$$F'' + PF' + QF = 0, \tag{3.26}$$

where

$$P \equiv \frac{\sin 2\theta_f}{\cos^2\theta_f - \sigma^2} + \cot\theta_f,$$

and

$$Q \equiv \left(\frac{R}{r_e}\right)^2 \left(\sigma^2 - \cos^2\theta_f\right) - \frac{m^2}{\sin^2\theta_f} - \frac{m}{\sigma}\left(\frac{\cos^2\theta_f + \sigma^2}{\cos^2\theta_f - \sigma^2}\right).$$

The meridional structure of the gravity modes is determined by the sign of $\{(1/4)\,P^2 - Q\}$. For given m, there exists σ_m^c such that

$$\begin{aligned}\mu^2 &\equiv (1/4)\,P^2 - Q \\ &= \frac{1}{4}\left[\frac{\sin 2\theta_f}{\cos^2\theta_f - \sigma^2} + \cot\theta_f\right]^2 - \left(\frac{R}{r_e}\right)^2\left(\sigma^2 - \cos^2\theta_f\right) \\ &\quad + \frac{m^2}{\sin^2\theta_f} + \frac{m}{\sigma}\left(\frac{\cos^2\theta_f + \sigma^2}{\cos^2\theta_f - \sigma^2}\right) > 0,\end{aligned}$$

when $1 < \sigma \leq \sigma_m^c$. When $\sigma > \sigma_m^c$ the sign of μ^2 becomes negative.

3.4.1 Gravity waves with a frequency $1 < \sigma \leq \sigma_m^c$

Following the method of solution in the previous section, we see that the general solution for (3.26), for $\mu^2 > 0$, has the form:

$$F = e^{-\frac{P\theta}{2}}\left(k_1 e^{\mu\theta} + k_2 e^{\mu\theta}\right), \tag{3.27}$$

where

$$\mu^2 = (1/4)\,P^2 - Q, \tag{3.28}$$

and k_1, k_2 are arbitrary constants. Application of (3.16) into (3.26) yields.

$$k_1 + k_2 = 0,$$

and thus, (3.27) can be rewritten as

$$F = k_3 e^{-P(\theta)/2}\sinh(\mu\theta), \tag{3.29}$$

where k_3 is an arbitrary constant. Finally, using (3.29) in (3.15) gives the dispersion relation for divergent barotropic gravity waves in spherical cap using the "β-sphere" approximation.

$$-\frac{P}{2}\sinh(\mu\theta_B) + \mu\cosh(\mu\theta_B) - \frac{m}{\sigma}\cot\theta_B\sinh(\mu\theta_B) = 0$$

$$\mu = \left[\frac{1}{2}P + \frac{m}{\sigma}\cot\theta_B\right]\tanh(\mu\theta_B), \tag{3.30}$$

3.4.2 Gravity waves with a frequency $\sigma_m^c < \sigma$

When $\sigma > \sigma_m^c$ the general solution for (3.26) for $\mu^2 < 0$ has the form:

$$F = e^{-\frac{P\theta}{2}}\left(k_4 e^{i|\mu|\theta} + k_5 e^{-i|\mu|\theta}\right), \tag{3.31}$$

where

$$\mu^2 = (1/4)\,P^2 - Q, \tag{3.32}$$

and k_4, k_5 are arbitrary constants. Application of (3.16) into (3.26) yields.

$$k_4 + k_5 = 0,$$

and thus,

$$F = k_6 e^{-P\theta/2}\sin(|\mu|\theta), \tag{3.33}$$

where k_6 is an arbitrary constant. Applying boundary condition (3.15) in (3.33) yields

$$-\frac{P}{2}\sin(|\mu|\theta_B) + \mu\cos(|\mu|\theta_B) - \sin(|\mu|\theta_B) = 0,$$

which upon re–arrangement yields

$$|\mu| = \left[\frac{1}{2}P + \frac{m}{\sigma}\cot\theta_B\right]\tan(|\mu|\theta_B). \tag{3.34}$$

In the limit when $\sigma \gg 1$, $P \sim \cot\theta_f$ and $Q \sim (R/r_e)^2\,\sigma^2$ and

$$\mu^2 \sim \left(\frac{1}{4}\right)\cot^2\theta_f - \left(\frac{R}{r_e}\right)^2\sigma^2 \sim -\left(\frac{R}{r_e}\right)^2\sigma^2.$$

The dispersion relation (3.34) can then be approximated, in this high frequency limit, by

$$X = \frac{1}{2}\cot\theta_f\tan(X\theta_B), \tag{3.35}$$

where $X \equiv \sigma\,(R/r_e)$. This high frequency gravity wave limit is, of course, captured by the "f-sphere" amplitude equation (3.17). We observe from (3.35) that the gravity wave frequencies become independent of m in this limit.

The values of σ from (3.30) and (3.34) were obtained using MATLAB (see Appendix B.4). In contrast with the previous section, there is not an approximate set of explicit roots for which it can be refined numerically. Therefore, (3.30) and (3.34) are evaluated for different values of σ which is then plotted to determine the approximate location of the roots. Thereafter, the bisection method is used to refine the value of any root of particular interest.

Table 3.7 presents the gravity wave mode eigenfrequencies using the basin parameters listed in Table 3.1. Table 3.7 indeed reveals that as $|m|$ increases the eigenfrequencies converge, namely, $\sigma_{m,n} \sim \sigma_{-m,n}$ as predicted by (3.35). The sensitivity of the gravity wave frequencies to θ_f is again found to decrease with increasing meridional modal number n (see Tables 3.7 and 3.8).

Figure 3.4 shows the normalised eigenfunctions proportional to the surface displacement for low order gravity wave modes, $\sigma_{m,n}$ has $n-1$ nodal circles of amplitude, and m nodal diameters. The displacement field associated with the modes $\sigma_{m,1}$ ($m = \pm 1, \pm 2, ..$) resembles a coastal trapped wave, with amplitude monotonically decreasing towards the centre of the basin, although in contrast with vorticity waves, their propagation is not restricted towards the west in the Northern Hemisphere. $\sigma_{1,2}$ and $\sigma_{2,2}$ are not displayed because there were indistinguishable with $\sigma_{-1,2}$ and $\sigma_{-2,2}$. This is because of the convergence of the eigenfrequencies with the increase of m.

Table 3.7: Gravity wave eigenfrequencies $\sigma_{m,n}$ calculated from (3.30) and (3.34) using the basin parameters in Table 3.1 when $\theta_f = 0.5\theta_B$.

$m =$	-4	-3	-2	-1	1	2	3	4
$n = 1$	9.2962	7.0887	4.9374	2.9452	2.3853	4.5943	6.8493	9.1133
2	10.575	8.6947	7.0442	5.817	5.7392	6.9381	8.5907	10.481
3	12.744	11.232	10.008	9.1886	9.1578	9.9558	11.17	12.68
4	15.44	14.217	13.272	12.668	12.652	13.243	14.178	15.396
5	18.433	17.422	16.66	16.184	16.174	16.642	17.396	18.402

Table 3.8: Gravity wave eigenfrequencies $\sigma_{m,n}$ calculated from (3.30) and (3.34) using the basin parameters in Table 3.1 when $\theta_f = 0.25\theta_B$.

$m =$	-4	-3	-2	-1	1	2	3	4
$n = 1$	18.221	13.708	9.2169	4.8105	4.553	9.0825	13.617	18.153
2	18.961	14.677	10.603	7.1093	7.0626	10.561	14.644	18.935
3	20.254	16.312	12.769	10.057	10.032	12.739	16.283	20.229
4	22.052	18.497	15.463	13.311	13.297	15.441	18.474	22.031
5	24.243	21.061	18.453	16.693	16.683	18.438	21.043	24.226

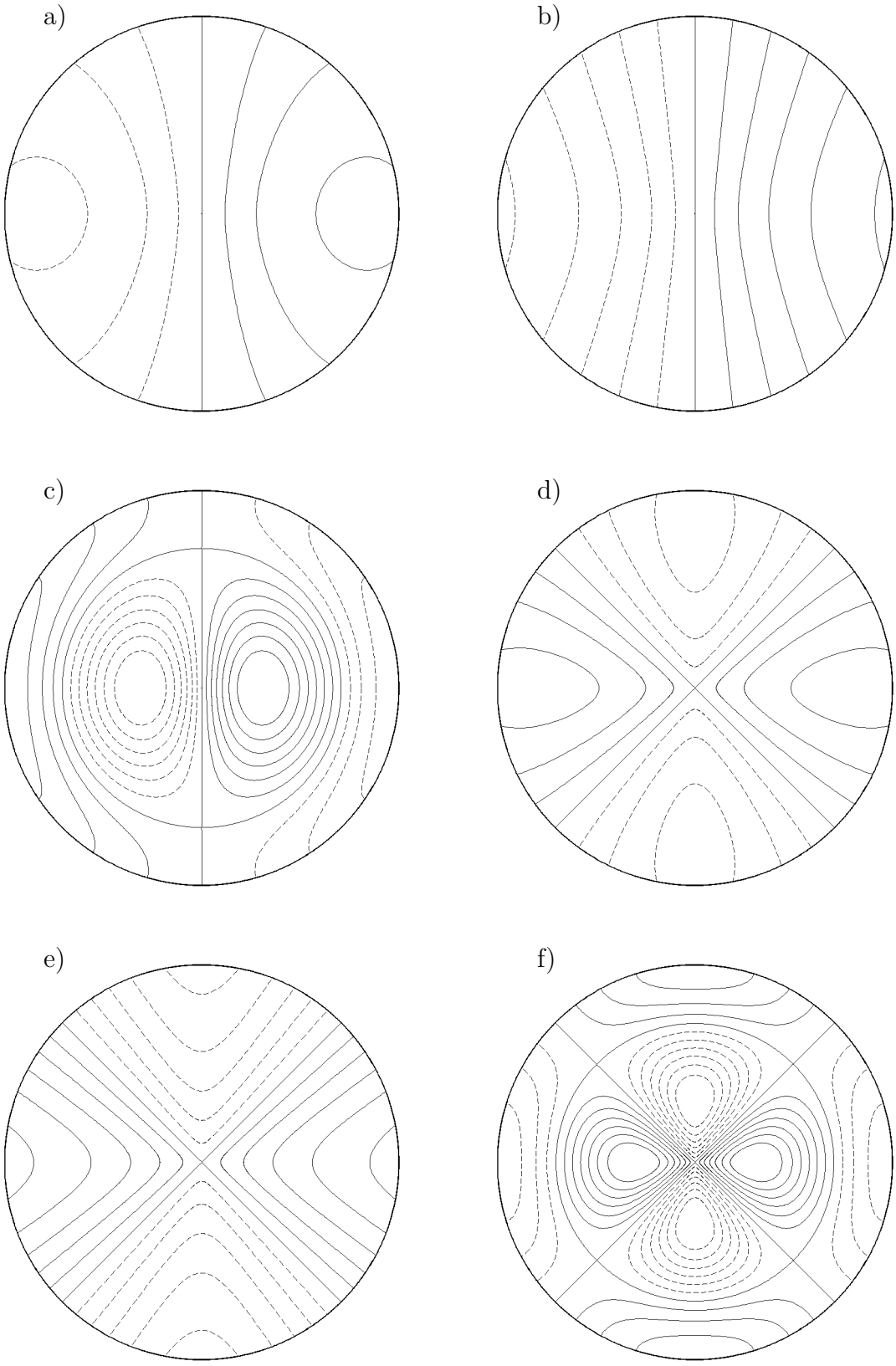

Figure 3.4: Normalised eigenfunctions for the sea surface displacement associated with gravity waves. a) $\sigma_{-1,1}$; b) $\sigma_{1,1}$; c) $\sigma_{-1,2}$; d) $\sigma_{-2,1}$; e) $\sigma_{2,1}$; f) $\sigma_{-2,2}$. The patterns rotate counter–clockwise (clockwise) for $m \geq 1\,(m \leq -1)$.

Interestingly, the asymptotic behaviour of the gravity wave frequencies when n is large can be deduced from the amplitude equation (3.12) without invoking the "β-sphere" approximation. First, observe that when $\sigma \gg 1$ (3.12) can be approximated by

$$F'' + \cot\theta F' + \left(\frac{\sigma R}{r_e}\right)^2 F = 0, \tag{3.36}$$

The change of independent variable $z = \cos\theta$ transforms (3.36) into the ordinary differential equation

$$\left(1 - z^2\right) F'' + 2zF' + \left(\frac{\sigma R}{r_e}\right)^2 F = 0, \tag{3.37}$$

where $F'(z) = dF(\theta)/dz$. In deriving (3.37), we observe that

$$\begin{aligned} \frac{dF}{d\theta} &= \frac{dF}{dz}\frac{dz}{d\theta}, \\ &= -\sin\theta \frac{dF}{dz}. \end{aligned}$$

Differentiating again with respect to θ we find that

$$\begin{aligned} \frac{d^2F}{d\theta^2} &= -\cos\theta\frac{dF}{dz} - \sin\theta\frac{d^2F}{dz^2}\frac{dz}{d\theta}, \\ &= -\cos\theta\frac{dF}{dz} + \sin^2\theta\frac{d^2F}{dz^2}. \end{aligned}$$

Substituting into (3.36) we find that

$$-z\frac{dF}{dz} + \left(1 - z^2\right)\frac{d^2F}{dz^2} + -\cot\theta\sin\theta\frac{dF}{dz} + \left(\frac{\sigma R}{r_e}\right)^2 F = 0. \tag{3.38}$$

which can be re–arranged to give (3.37). Equation (3.37) is the Legendre equation and it is well known that it supports bounded solutions on $[-1, 1]$ only when (see Abramowitz and Stegun, 1965, Chapter 22).

$$\left(\frac{\sigma_n R}{r_e}\right)^2 = n(n+1). \tag{3.39}$$

In other words, the gravity wave eigenfrequencies become independent of m when $\sigma^2 \gg 1$, and (3.39) shows that

$$\sigma_n \sim \frac{r_e}{R} n \qquad n \gg 1. \tag{3.40}$$

Similar asymptotic behaviour for σ_n follows immediately from (3.35) where $\sigma_n \sim (r_e/R)(n\pi/\theta_B)$, noting that the difference in the constant of proportionality between this expression and (3.40) is due to the "β-sphere" approximation.

3.5 Conclusions

In this chapter we have derived the governing amplitude equation for azimuthally propagating gravity and divergent planetary waves modes in a spherical cap, retaining full spherical geometry. Thereafter, we adopt the "β-sphere" approximation first advanced by Imawaki and Takano (1974), and fixed the co-latitude in the coefficients of the governing wave amplitude equation, thereby allowing analytical techniques to be used to solve the eigenvalue problem.

The planetary wave frequencies calculated from the computationally efficient dispersion relation show acceptable agreement with their equivalent counterparts in LeBlond (1964) for relatively long azimuthal and meridional wavelength eigenfunctions. As these wavelengths decrease the departure between the eigenfrequencies in LeBlond (1964) and in this study, increase. This reflects the fact that short wavelength modes are more sensitive to the fixed value of the co-latitude in the "β-sphere" approximation. We have found the gravest mode planetary wave eigenfrequency, which is accurately predicted by the dispersion relation derived using the "β-sphere" approximation, is sensitive to the choice of the co-latitude, θ_f. Values of θ_f other that $0.5\theta_B$ reduce the accuracy of this mode. The sensitivity of $\sigma_{m,n}$ to θ_f reduces for $m = -1\,(n = 2, .., 5)$, and for these frequencies the "β-sphere" approximation produces an acceptable estimate of their exact value.

The eigenfrequencies and eigenfunctions (corresponding to the surface displacement) for gravity waves modes in a spherical polar cap are also calculated in this study. For a fixed azimuthal wavenumber, $|m|$, there is a clockwise and counterclockwise propagating gravity wave mode, in contrast with the planetary waves. For fixed low values of m and n (the meridional wavenumber index) $\sigma_{-m,n} \neq \sigma_{m,n}$. However, as $|m|$ increases the frequencies of the clockwise and counterclockwise propagating modes converge in value, as predicted analytically in this study. Further, as n increases, $\sigma_{m,n}$ increases and the dependence of $\sigma_{m,n}$ on m becomes weak. Asymptotically, we find that when $\sigma \gg 1$, $\sigma_{m,n} \propto n$, with dependence on m becoming weak.

The high degree of accuracy of the "β-sphere" approximation in representing steady-state planetary flows in a spherical cap has been established by Kitauchi and Ikeda (2009). However, we are unaware of any study that addresses how well the "β-sphere" approximation captures freely propagating gravity and vorticity wave dynamics in a spherical cap which is the purpose of this study. By fixing θ in the wave amplitude equation on a sphere, we are effectively assigning a fixed representative value of the meridional gradient

of the Coriolis parameter. The resulting free-wave dynamics are in qualitative agreement with the planetary waves on a sphere, and for low modes there is also good quantitative agreement. For gravity modes at high frequencies (i.e. $\sigma \gg 1$) we demonstrate that σ is asymptotically in agreement, as a function of the meridional wavenumber n, with the equivalent expression derived using full spherical geometry. We anticipate that the low order (long wavelength) planetary wave modes in a layered or a continuously stratified ocean in a polar cap will also be accurately represented using the "β-sphere" approximation.

It appears that the wave amplitude equation (3.14) for freely propagating waves in a polar cap together with the boundary conditions (3.15) and (3.16) has not been numerically solved for gravity and planetary wave frequencies. Such an exercise is not straight forward because the eigenvalue, σ, appears in both governing equations and the boundary conditions (3.15). Nevertheless, a worthwhile extension of this chapter would be to determine the exact eigenfrequencies of these two classes of waves retaining the full spherical geometry represented in (3.14).

Chapter 4

Source-sink driven planetary flows in a polar basin; numerical experiments

4.1 Introduction

Chapter 2 developed an analytic model for steady barotropic planetary geostrophic circulation driven by boundary flows in a polar flat bottom and step–shelf basin. However, more complex scenarios such as a basin with a non–uniform width shelf or the addition of a transpolar ridge are not amendable to analytic treatment. Therefore, this chapter indeed utilises the community global ocean circulation model, NEMO, to study the circulation in basins with more complex topography.

There is a wide spectrum of numerical modelling studies on Arctic Ocean circulation. These use high resolution atmospheric–ocean–sea ice models to predict the sea ice extent, water mass formation and propagation, freshwater balance etc..To a first approximation the Arctic Ocean basin can be viewed as circular, with a wide Euro–Asian (eastern shelf) shelf and the narrower North American shelf (western basin). The transpolar Lomonosov ridge spans the basin (see Figure 1.2). If one argues that topography steers the quasi–steady (geostrophic) circulation then it comes as no surprise that shelf edge (rim) currents are ubiquitous. These are observed in numerical studies (Zhang and Steele, 2007; Aksenov *et al.*, 2011; Spall, 2013) and in the field (Pnyushkov *et al.*, 2013; Pnyushkov *et al.*, 2015). However, it is interesting to note that established global ocean circulation models do not all agree on the direction of rim currents in the Arctic basin, even when using the same model forcing parameters (Yang, 2005). Yang (2005) using a simple bowl shape circular basin demonstrated the importance of the strait depth setting the boundary current direction.

Yang (2005) suggested that the relative vorticity generated in the Fram Strait was one of the factors that caused the switching of the rim current direction. The importance of Yang (2005) lies in the elucidation of the physics that controls the direction of barotropic Arctic rim currents. Zhang and Steele (2007) also investigated the same problem but they claimed that the direction of these currents was controlled by buoyancy changes in the case of a stratified ocean. This idea was further studied numerically by Spall (2013). Using an idealised domain representative of the Arctic basin, Spall (2013) reproduced the cyclonic rim current of the Arctic basin and the anticyclonic current in the Canadian basin, driven by a buoyancy flux.

Such idealised Arctic Ocean process modelling studies are uncommon in the literature. Sakai and Imawaki (1981a) employed a barotropic ocean model in spherical coordinates to study a planetary circulation driven by a source–sink boundary flow in a circular polar basin with two topographic "walls" or "peninsulas" to allow the formation of western boundary currents. The steady–state circulation revealed western boundary currents against the eastern side of the peninsulas. Weakly nonlinear effects on steady-state planetary flows were later investigated numerically by Sakai and Imawaki (1981b). In a flat bottom polar cap the source-sink driven flows take the form of cyclonic and anti–cyclonic boundary currents. More recently, Taniguchi and Yamada (2012) numerically investigated the transition of the boundary currents connecting the source and sink in a polar cap to a western boundary layer circulation as the latitude of the centre of the basin migrates equatorward. Luneva *et al.* (2012) considered a polar geostrophic adjustment problem in the spirit of Gill (1982) in the polar cap. They employed the NEMO ocean model to investigate the spin–up of a barotropic geostrophic flow in a closed basin forced by different initial SSH fields.

First, we investigate the adjustment of a planetary flow in a flat bottom polar basin. Second, the approximate (i.e. beta–sphere) analytical solutions in Chapter 2 are compared with the equivalent numerical NEMO simulations. NEMO is then used to study source–sink circulation in a polar basin with a step–shelf and a ridge. Third, we study source–sink planetary circulation driven in a basin with three gaps which represent the main connections of the Arctic Ocean basin to its marginal seas. Finally we briefly study the impact of dynamic sea ice in the steady circulation.

4.2 NEMO model description

We consider numerical solutions of a barotropic ocean in a circular polar basin driven by prescribed sources/sink on the boundary of the basin. All the numerical simulations discussed in this chapter employed the nonlinear three-dimensional ocean circulation Ocean PArallelise or OPA model from NEMO (Madec, 2008). Following Luneva *et al.* (2012) we use a filtered non-linear free surface algorithm, which is stable with relatively large time steps but damps the fast gravity and inertia-gravity waves. Planetary waves, are however, permitted using this algorithm. Three basin configurations will be used; (i) uniform depth; (ii) step–shelf and (iii) step–shelf with a top–hat ridge. Several of the numerical experiments discussed in this chapter are the analogues of the analytical problems discussed in Chapter 2. Thus, we are able to assess the accuracy of the beta–sphere analytical solutions by comparing them with the equivalent NEMO simulations.

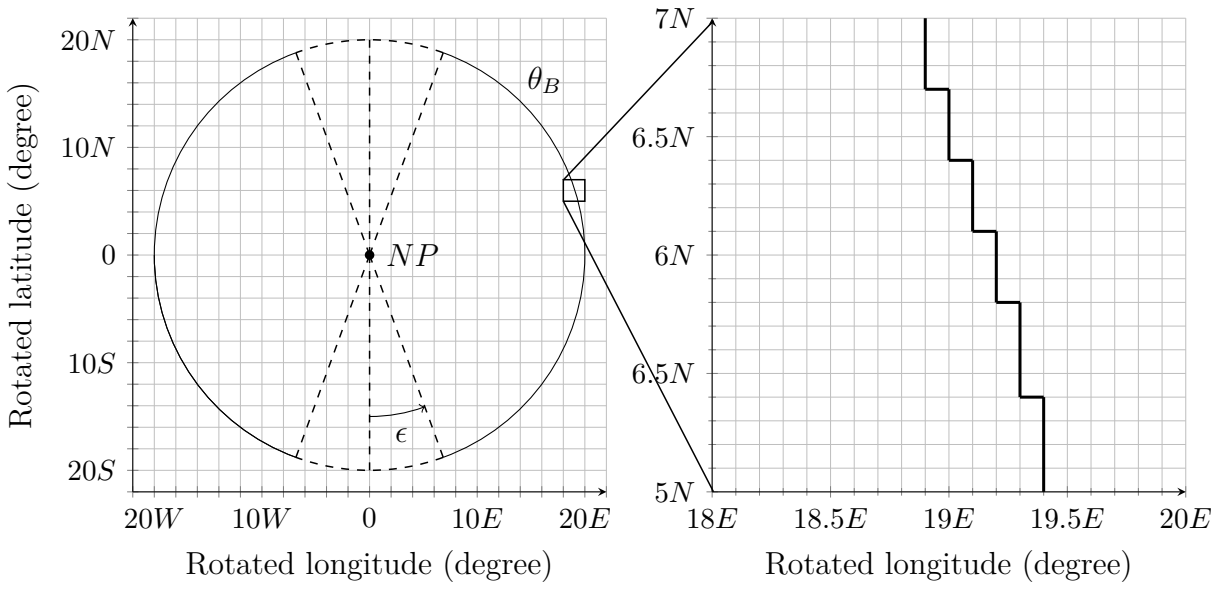

Figure 4.1: Computational domain of NEMO: a) Rotated grid where NP is the North Pole; b) enlarged area of section (a)

The geographical domain is a circular basin where the North Pole is located in the centre and the basin boundary co–latitude corresponds to $\theta_B = \pi/9$ (i.e. 20^o). However, the computational domain is defined by the rotation of geographical coordinates placing the North Pole in the equator (see Figure 4.1(a) and (b)). This method is widely used in high latitudes to avoid the loss of grid integrity and/or the coordinate singularity at the North Pole (Gerdes and Küberle, 1999; Prange and Gerdes, 2006; Itkin *et al.*, 2014). The rotated grid was set with a horizontal resolution of $0.1^o \times 0.1^o$. This can be easily set in

namelist_cfg from NEMO, but the Coriolis parameter had to be calibrated to the rotated grid domain. This transformation was done by the rotation Euler angles. The Euler angles represent the angle of rotation of a vector or scalar field from original coordinate frame. There are multiple options to perform this transformation, here we chose the ZYZ rotation which is used in the AOMIP grid (Uotila *et al.*, 2006). Following the ZYZ or Y convention, the Euler angles are α, β, γ for the counter clockwise rotation of Z, Y, and Z axis, respectively (see Figure 4.2). In a sphere, the Z axis goes through the poles and the X axis goes through the prime meridian. The remaining axis orientation can be determined using the right hand rule.

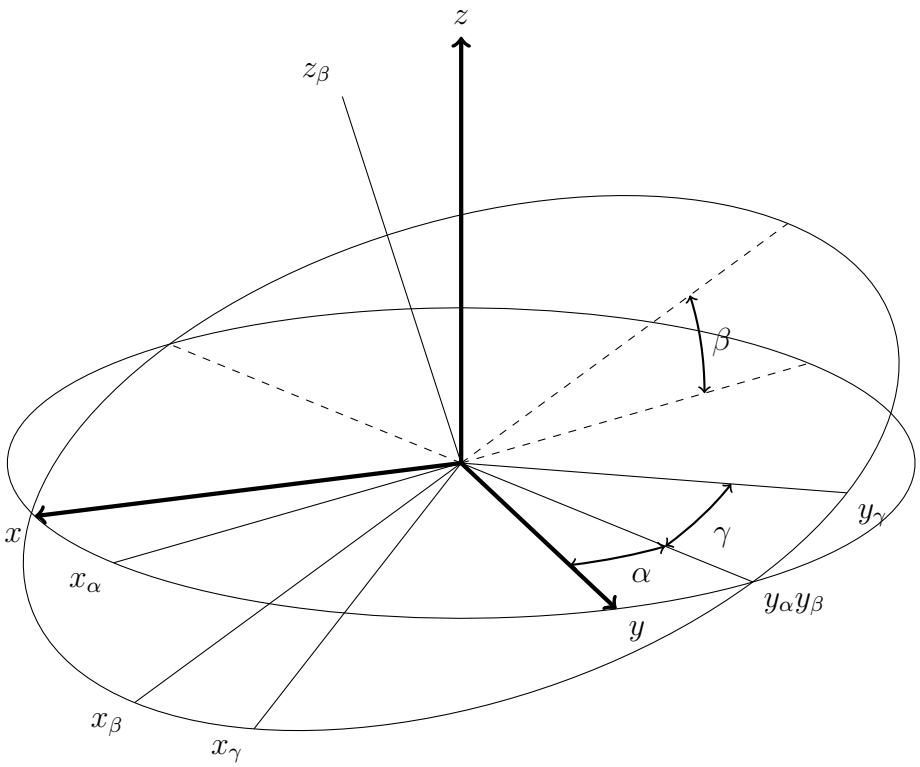

Figure 4.2: Rotation of coordinates following the proper Euler angles (ZYZ rotation)

Here, we set the Euler angles to $\alpha = 0$, $\beta = 90^o$ and $\gamma = 0$. Thus, the rotation is given only by the $Y-$axis

$$\mathbf{R}_y = \begin{bmatrix} \cos\beta & 0 & -sin\beta \\ 0 & 1 & 0 \\ \sin\beta & 0 & \cos\beta \end{bmatrix} \tag{4.1}$$

If we rotate the geographical domain $\beta = 90^o$. The rotated grid in spherical coordinates

is,

$$\mathbf{R}_y \times \boldsymbol{x} = \begin{bmatrix} 0 & 0 & -1 \\ 0 & 1 & 0 \\ 1 & 0 & 0 \end{bmatrix} \times \begin{bmatrix} R\cos\phi\cos\varphi \\ R\cos\phi\sin\varphi \\ R\sin\phi \end{bmatrix} = \begin{bmatrix} -R\sin\phi_r \\ R\cos\phi_r\sin\varphi_r \\ R\cos\phi_r\cos\varphi_r \end{bmatrix}_r \tag{4.2}$$

where ϕ is the latitude; φ is the longitude; ϕ_r rotated latitude and φ_r is the rotated longitude. Let us remind the reader that the analytic solution was given in terms of co–latitude and longitude whereas NEMO works in geographical latitude and longitude. Therefore, the Coriolis parameter which is represented as $2\Omega\cos\theta$ in the analytical model, is defined as $2\Omega\sin\phi$ in the geographical grid and transformed into $2\Omega\cos\phi_r\cos\varphi_r$ in the rotated grid.

The vertical grid varies depending on values in the sections *namcfg, namzgr* and *namdom* of the *namelist_cfg*. In particular, the bathymetry profile is selected by the value of *nn_bathy* and the number of vertical levels, coordinates and resolution are set by *jpkdta, ln_zco, ppacr, ppa0, ppa1, ppkth* and *pphmax*. These variables are then used in the subroutine *domzgr.F90* to make the grid.

Figure 4.3 displays the four different basins used in this chapter, all of which have two diametrically opposed straits. They were parametrised following the FORTRAN script in Appendix C.1 (see ntopo= $2, 3, 4$ in the script) using the ocean basin parameters in Table 4.1. The vertical grid was set in z-coordinates (i.e. *ln_zco=.true.*) and uniform grid resolution (i.e. *ppkth*= 0). Upon setting *ppkth*= 0, the variables *ppacr, ppa0* and *ppa1* are not needed and the vertical cells depend only on *jpkdta* and *pphmax*. The number of vertical levels (*jpkdta-1*) varied with the scenario. The flat bottom (Figure 4.3 (a)) basin had two levels a depth interval of $500m$. The vertical levels of the remaining basins were increased to eight in order to allow the addition of extra elements at different depths giving an interval of $125m$. This type of distribution generated a maximum depth of 1000 m in the deep basin.

The addition of unstructured open boundaries is only available when the configuration is compiled with *key_bdy* and its setting is given in the section *nambdy* of *namelist_cgf*. NEMO requires the values of temperature, salinity, density, SSH and velocity components of the boundary flow. Among these, temperature, salinity and density are called *tracers* and they can be set as the initial conditions or supplied in an external netCDF file. NEMO then uses the boundary condition called *frs* scheme to incorporate these tracers into the computational domain. The remaining variables determine the volume transport across the strait. They are handled in the subroutine *bdydyn2d.F90* or *bdydyn3d.F90* and

bdydyn.F90 where the velocity components of the boundary flow vary depending on the boundary conditions.

Unless stated otherwise two open boundaries, or straits, were prescribed in the basin with their arc length given by $R \sin 2\epsilon$ (see Figure 4.1). Across one gap a uniform barotropic inflow is prescribed (i.e. a source) and across the opposite gap, an equal but opposite outflow (i.e. a sink) is prescribed (see Figure 4.3). The scalar components of the flow (temperature,salinity and density) were set as the initial condition (i.e. nn_tra_dta= 0) and the volume transport was input as external netCDF file (i.e. nn_dyn2d_dta= 1). For a barotropic flow, NEMO employs the Flather (1994) boundary condition to adjust the volume transport to the interior. However, this algorithm modifies the inflow and outflow producing a shear in the flow. Therefore, the subroutines *bdydyn2d.F90* and *bdydyn.F90* were modified to reproduce a uniform constant flux (see Appendix C.2 and C.3).

The initial conditions for salinity, SSH, temperature and velocity are computed in *istate.F90*. We set salinity and temperature to 35.5 psu and 2^oC, respectively, and noting that these variables do not change with time because the boundary flow has the same properties as the initial condition. The initial velocity field and the SSH are set to zero.

Finally, the wind stress is handled by the section *namsbc* of *namelist_cgf*. This chapter does not include wind stress but NEMO always requires the specification of a wind stress parametrisation. Therefore, the simulations were run with the analytical scheme (i.e. *ln_ana=.true.*) setting *rn_utau0, rn_utau0, rn_qns0, rn_qsr0* and *rn_emp0* to zero.

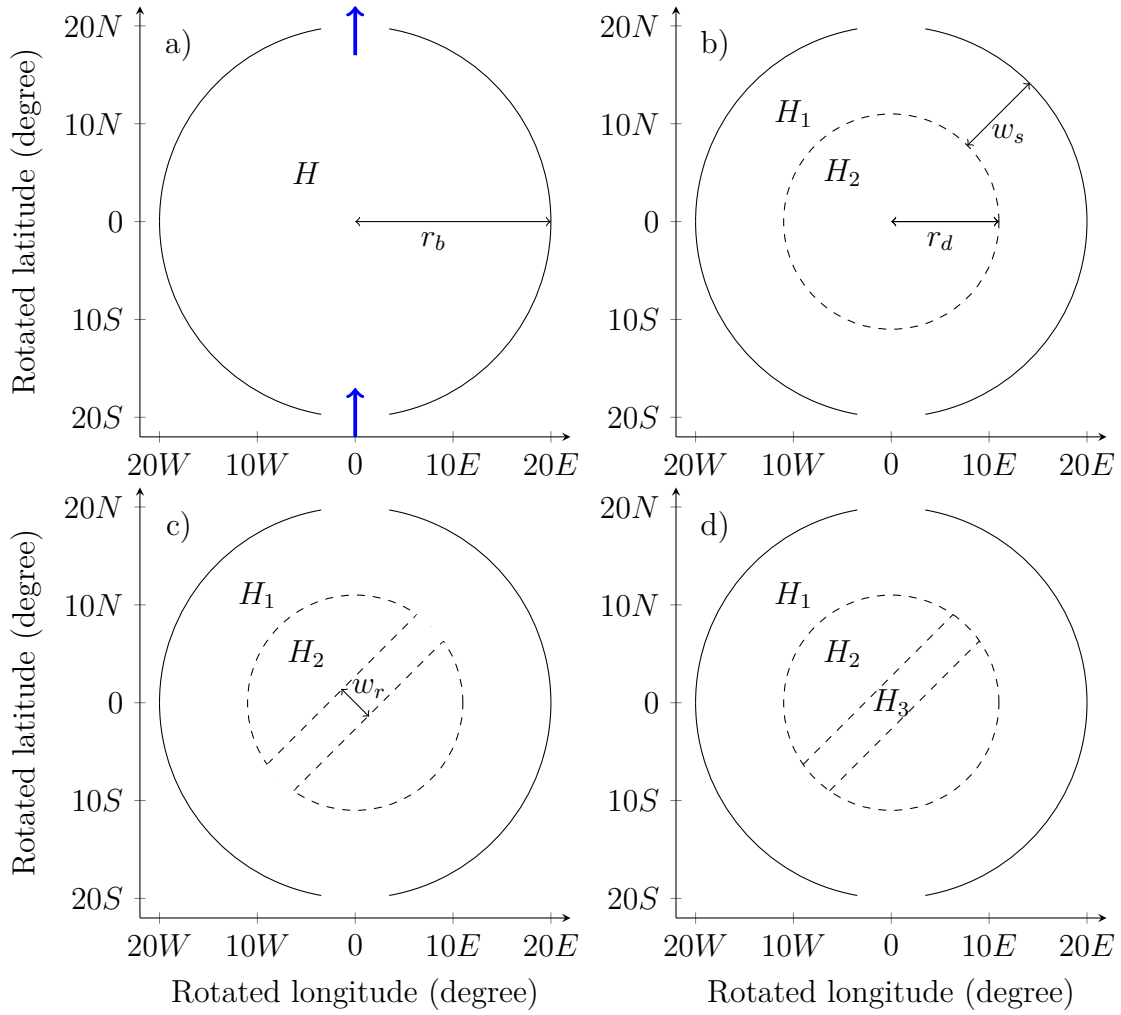

Figure 4.3: Schematic of a) flat bottom basin; b) step–shelf basin; c) step–shelf and top–hat transpolar ridge where the ridge top is at the same depth as the shelf; d) as in (c) except the top of the ridge is deeper than the shelf. Note r_b is the radius of the basin, r_d is the radius of the deep basin, w_s is the width of the step–shelf, w_r is the ridge width, H is the depth of the basin, H_1 is the step–shelf depth, H_2 is deep basin depth and H_3 is the depth of the ridge.

Table 4.1: NEMO model control parameters used in the numerical experiments, unless otherwise stated.

Symbol	NEMO variable	Variable(Unit)	Value
-	ppe1_deg, ppe2_deg	Horizontal resolution (*degrees*)	0.1 x 0.1
-	e3w_1d	Vertical resolution (m)	250-500
-	rn_rdt	Time step (s)	1200
A_H	rn_ahm_0_lap	Horizontal Laplacian eddy viscosity ($m^2 s^{-1}$)	500
-	rn_avm0	vertical eddy viscosity ($m^2 s^{-1}$)	1.2×10^{-4}
-	rn_avt0	vertical eddy diffusivity ($m^2 s^{-1}$)	1.2×10^{-5}
-	rn_bfri1	Bottom Drag Coefficient ($m s^{-1}$)	5×10^{-4}
-	-	Strength of the prescribed source/sink (*Sverdrups*)	5
H	pphmax	Undisturbed depth (m)	1000
H_1	-	Step-shelf depth (m)	250
H_2	pphmax	Deep basin depth (m)	1000
H_3	-	Ridge depth (m)	250
2ϵ	-	Longitudinal extent of the straits (*degrees*)	20^o
θ_B	-	Geographical co–latitude at the boundary (*degrees*)	20^o
r_b	-	Longitudinal extent of the basin (*degrees*)	20^o
r_d	-	Longitudinal extent of the deep basin (*degrees*)	9^o
w_s	-	Ridge width (m)	400

4.3 The spin-up regime

This section briefly investigates the spin-up of boundary forced circulation in a flat bottom basin. This process describes adjustment of the circulation from an initial rest–state to a steady spun–up state. Figure 4.4 shows the spin-up of a source-sink driven circulation in a flat bottom polar basin using the NEMO model. Table 4.1 lists the model parameter values used in this NEMO experiment, noting that the bottom friction coefficient used in this simulation is $10^{-4} ms^{-1}$. Figure 4.4 (a) shows a time series of the SSH at an interior point in the domain defined by $\theta = 10^o$, $\varphi = 304^o$ (see Figure 4.4 (c)). The results in reveal that the period of the planetary waves is approximately 100 days. Figure 4.4 (b) shows contours of SSH in the time-longitude domain defined by $\theta = 10°$, and they reveal the presence of westward propagating planetary waves. Chapter 3 derived an approximate expression for the planetary wave dispersion relation in a polar basin (3.25) which we re–state below for convenience:

$$\frac{|m|}{\sigma_{m,n}} = \left(\frac{n\pi}{\theta_B}\right)^2 + \frac{m^2}{\sin^2\theta_0} + \left(\frac{R}{r_e}\right)^2 \cos^2\theta_0 + \sec^2\theta_0 + (1/4)\cot^2\theta_0. \tag{4.3}$$

In (4.3) the dimensional wave frequency $\omega_{m,n}$ is related to its non-dimensional counter-part $\sigma_{m,n}$ by $\omega_{m,n} = 2\Omega\sigma_{m,n}$, where Ω is the angular velocity of the Earth. In (4.3), m is the azimuthal wave number ($m = -1, -2, -3, ..$); $n = 1, 2, 3, ..$ is the integer characterising the meridional structure of the waves; $0 < \theta_0 < \theta_B$ is a fixed co-latitude, which for most applications, including here, is given by $\theta_0 = 0.5\theta_B$. We find that the propagation characteristics of the waves in Figure 4.4 (c) are captured by the gravest planetary wave mode in this basin for which $|m| = 1 = n$. The period of this mode $T_{-1,1} = \pi\left(\Omega\sigma_{-1,1}\right)^{-1} =$ 101 days which compares well with the wave period observed in Figure 4.4 (b). The phase velocity of the waves described by (4.3) is $\omega_{m,n}/|m|$, which for gravest mode is simply $\omega_{-1,1} = 0.00491 s^{-1}$. This values compares well with the slope of the line in Figure 4.4 (c), namely $0.004997 s^{-1}$.

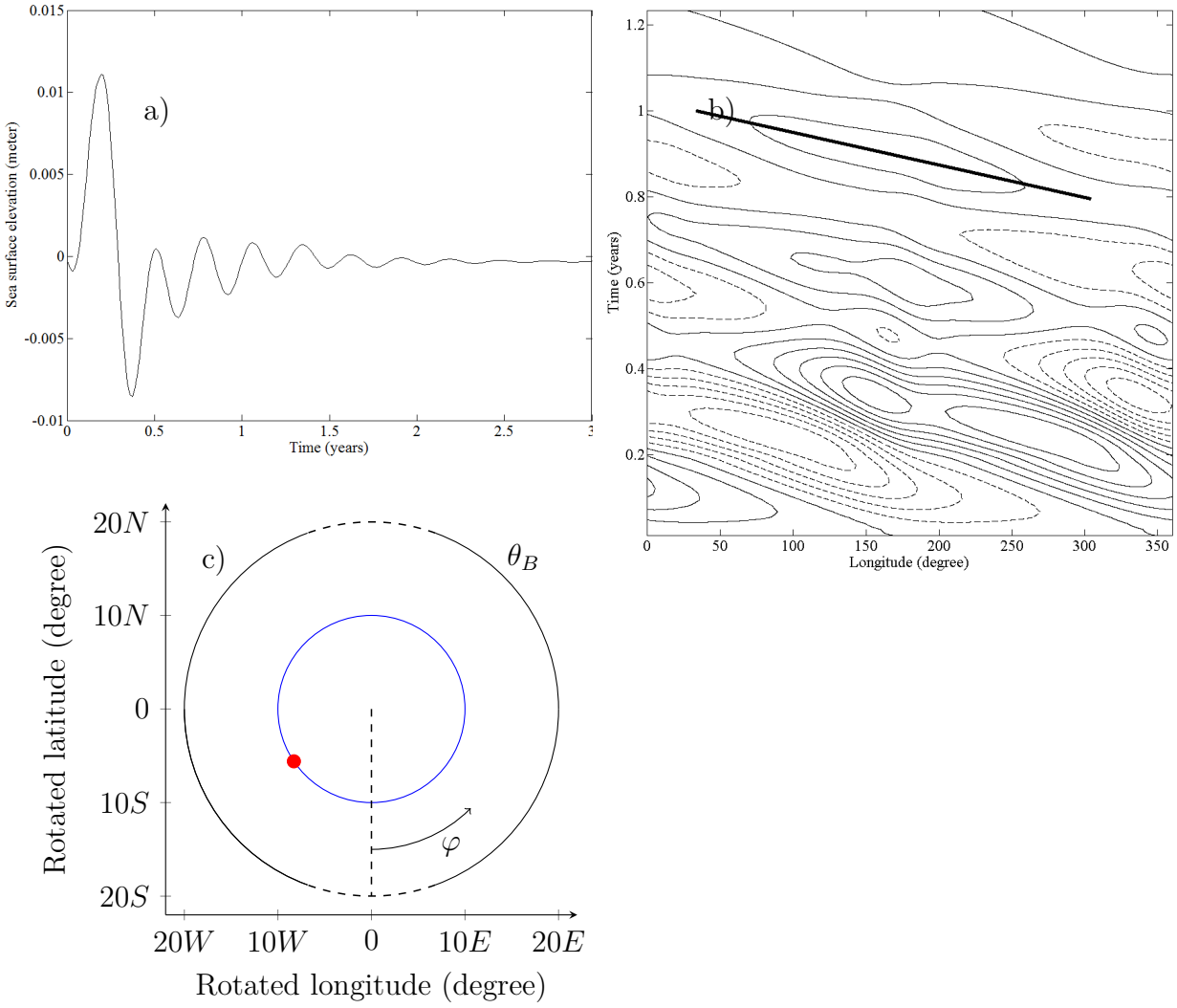

Figure 4.4: Spin-up of a source-sink driven barotropic flow in a polar basin using the NEMO model. a) time series of the SSH at the point $\theta = 10°$, $\varphi = 304°$; b) contours of SSH in the longitude–time plane defined by $\theta = 10°$; c) Rotated computational domain. Note the blue line and red dot denote the vertical section in (b) and the location of the time series in (a), respectively. Dashed and continuous contours correspond to negative and positive of SSH, respectively. Bold line in (b) shows the wave crest used to estimate the phase speed of planetary waves.

4.4 Comparison of NEMO simulations with the equivalent analytical solutions

Section 4.3 discussed the spin–up of a source–sink driven planetary geostrophic circulation in terms of planetary waves. Here, we study the circulation once it reaches the steady state. We will first assess how accurately the beta–sphere analytical solutions reproduce

the source–sink circulation by comparing them with NEMO simulations. Of course, the NEMO modelling system allows us to determine source–sink driven flows in basin with more complicated (and realistic) geometry where analytical results are not available.

The analytical solutions of Chapter 2 were given in terms of streamfunction. Contours of streamfunction are streamlines for the barotropic volume transport. In a steady state, isolines of SSH are, in most regions, a barotropic streamfunction. The exceptions are where the dissipation is important (e.g. in the frictional boundary layer). Qualitatively, the streamfunction and SSH contours will therefore coincide where the flow is geostrophic. A quantitative comparison can be made between the analytical solutions of Chapter 2 and the spun-up NEMO simulations, by examining their relative vorticity fields.

The relative vorticity in spherical polar coordinates is given by

$$\hat{\boldsymbol{k}} \cdot \nabla \times \boldsymbol{u} = \frac{1}{R \sin\theta} \left[(\sin\theta u)_\theta - v_\varphi \right], \tag{4.4}$$

where R is the radius of the Earth, H is the depth, θ is the co–latitude, φ is the longitude and $\hat{\boldsymbol{k}}$ is the unit vector in the radial direction. In Chapter 2 (section 2), we saw that the velocity components were given by

$$u = \frac{1}{HR} \frac{\partial \psi}{\partial \theta}, \tag{4.5a}$$

$$v = -\frac{1}{HR \sin\theta} \frac{\partial \psi}{\partial \varphi}. \tag{4.5b}$$

In terms of ψ, (4.4) becomes

$$\hat{\boldsymbol{k}} \cdot \nabla \times \boldsymbol{u} = \frac{1}{R \sin\theta} \left[\left(\frac{\sin\theta}{HR} \frac{\partial \psi}{\partial \theta} \right)_\theta - \left(-\frac{1}{HR \sin\theta} \frac{\partial \psi}{\partial \varphi} \right)_\varphi \right].$$

If we expand the derivatives we get

$$\hat{\boldsymbol{k}} \cdot \nabla \times \boldsymbol{u} = \frac{1}{R \sin\theta} \left[\frac{\cos\theta}{HR} \psi_\theta + \frac{\sin\theta}{HR} \psi_{\theta\theta} + \frac{1}{HR \sin\theta} \psi_{\varphi\varphi} \right],$$

and re–arranging we obtain

$$\hat{\boldsymbol{k}} \cdot \nabla \times \boldsymbol{u} = \frac{1}{\sin^2\theta HR^2} \left[\cos\theta \sin\theta \psi_\theta + \sin^2\theta \psi_{\theta\theta} + \psi_{\varphi\varphi} \right]. \tag{4.6}$$

Thus given ψ, (4.6) can be analytically evaluated for the vertical component of the relative vorticity of the steady planetary geostrophic circulation.

The relative vorticity from the numerical simulations is obtained following a different approach. NEMO output includes velocity field components and the size of grid cells in the rotated grid. Assuming that the size of cells barely changes, the relative vorticity can

be obtained in a Cartesian plane. Therefore, we can rewrite (4.4) in terms of Cartesian coordinates where the relative vorticity is given by

$$\hat{\boldsymbol{k}} \cdot \nabla \times \boldsymbol{u} = \frac{\partial v}{\partial x} - \frac{\partial u}{\partial y}, \tag{4.7}$$

where $\partial/\partial y$ and $\partial/\partial x$ are the partial derivative of the rotated latitude and longitude, respectively. Here, we computed (4.7) using central finite differences. As a MATLAB algorithm the above expression can be written as,

```
for  l=2:jpj-1
 for  m=2:jpi-1
  rv(l,m)=(v(l,m+1)-v(l,m-1))/(e1t(l,m)+e1t(l,m-1)) ...
                -(u(l+1,m)-u(l-1,m))/(e2t(l-1,m)+e2t(l,m));
 end
end
```

where the $e1t$ and $e2t$ are the size (in meters) of x and y in the grid cell, respectively. jpj and jpi are the total rotated latitude and longitude grid points.

4.4.1 Planetary geostrophic flows in presence of linear bottom friction

In Chapter 2, section 2.2, we discussed the analytical solution for a barotropic steady-state planetary geostrophic circulation in a circular basin in presence of linear bottom friction. The bottom friction in the NEMO ocean model is set in the section *nambfr* of the namelist_cfg. The NEMO ocean model cannot run without horizontal eddy viscosity, but it can be set small enough to ensure that dissipation is dominated by linear bottom friction. Wallcraft *et al.* (2005) investigated the limits of the horizontal eddy viscosity in terms of stability. They concluded that the horizontal eddy viscosity cannot be smaller than the square root of the grid spacing, thus for a grid resolution of 10 km the $A_H \geq 100$ $m^{-2}s^{-1}$.

The expression for the relative vorticity (4.6) can be further simplified for the analytical solutions in presence of linear bottom friction. Using (2.9) in (4.6) we obtain

$$\hat{\boldsymbol{k}} \cdot \nabla \times \boldsymbol{u} \equiv -\frac{2\Omega}{\mu R^2}\psi_\varphi. \tag{4.8}$$

Figure 4.5 (a) shows the SSH with the barotropic velocity vectors from NEMO simulation after 10 years of model integration. The ocean basin parameters used in Figure 4.5 are

listed in Table 4.1 and a linear bottom friction coefficient $10^{-4}\ ms^{-1}$ is specified. Upon entering the basin the flow is deflected in a clockwise direction, whence it bifurcates into a cyclonic and anticyclonic current. The numerical solution is qualitatively the same as that shown in Figure 2.5 (a). The sensitivity of the analytical solution compared with the numerical solution is shown in Figure 4.5 (c) and (e). Figure 4.5 (c) shows the relative error between the relative vorticity of the analytical solution with $\theta_f = 0.5\theta_B$ and the numerical simulation. Overall, there is good agreement between the analytical and the numerical solutions. The differences on the boundary could be explained by the interpolation and the central difference at the boundary where one of the points is outside the domain giving errors in the computation of relative vorticity. Figure 4.5 (e) is the same as (c) except $\theta_f = \theta_B$ in the analytic solution. Here, relative error between models increases more than 50% in the centre of the basin. This difference reveals the importance of the value of θ_f in (2.10).

The addition of a step–shelf is studied in Figure 4.5 (b), (d) and (f). Figure 4.5 (b) shows the contours of SSH using the ocean basin parameters of Table 4.1. The addition of a shelf constrains the flow, leaving the interior deep basin almost stagnant. An almost identical result is observed in the analytical solution shown in Figure 2.11. The relative error of the relative vorticity is again assessed in Figure 4.5 (d) and (f). Figure 4.5 (d) and (f) shows the relative error between the relative vorticity of numerical solution and analytical solution using $\theta_f = 0.5\theta_B$ and $\theta_f = \theta_B$, respectively. In general, there is a good agreement in the step–shelf, in particular when the analytical solution uses $\theta_f = \theta_B$ in (2.10). However, the relative vorticity in the deep basin motion is not well captured by the numerical solution. This difference could be due to the Laplacian diffusion present in the numerical solutions and the representation of the step–shelf in the numerical model. In the analytical model at the shelf break, the deep basin and the step–shelf have the same coordinate depth point (see Figure 4.6 (a)) because the shelf break is a vertical wall whereas in NEMO there is a single depth for each coordinate point (see Figure 4.6 (b)).

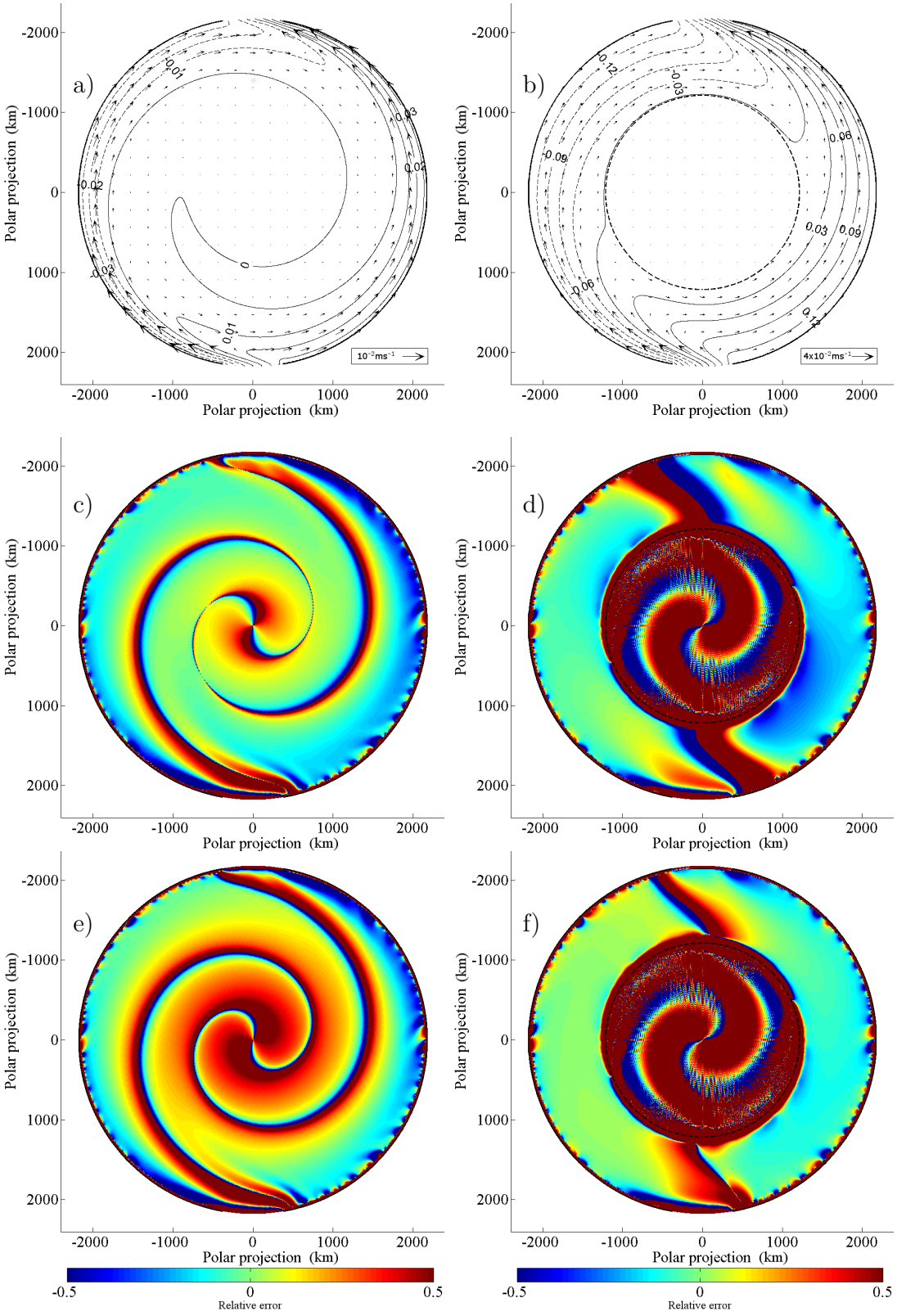

Figure 4.5: Source sink planetary geostrophic flows model comparisons in presence of linear bottom friction calculated by NEMO. a) Sea surface elevation in a flat bottom basin; b) same as (a) but in a step–shelf basin; c) relative error of the relative vorticity between the analytical and the numerical solution where $Error = (\xi_{NEMO} - \xi_{ana}) / \xi_{NEMO}$ using $\theta_f = 0.5\theta_B$ in a flat bottom basin; d) same as (c) but in a step–shelf basin; e) same as (c) except $\theta_f = \theta_B$; f) same as (d) except $\theta_f = \theta_B$.

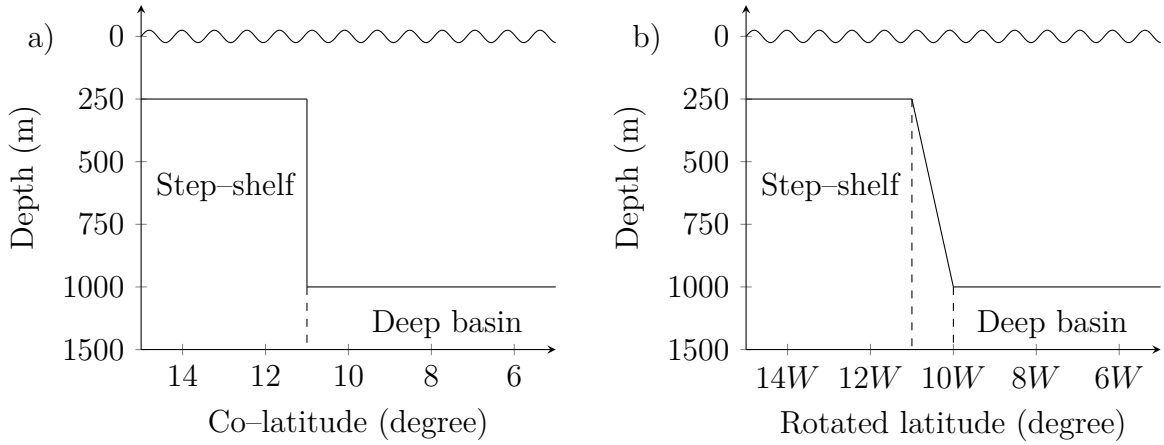

Figure 4.6: Schematic of the shelf and shelf-break topography in; a) the analytic model at $\varphi = 180$; b) the NEMO ocean model at $\phi_r = 0$.

4.4.2 Planetary geostrophic flows in presence of lateral diffusion

Chapter 2 derived an approximate analytical solution for a barotropic steady-state planetary geostrophic circulation in a circular basin in presence of eddy diffusion as the dissipation mechanism. We consider the equivalent numerical simulations using NEMO by setting the linear bottom friction to zero. This is achieved in the NEMO code by setting *nn_bfr=0* in *namelist_cfg*.

Figure 4.7 (a) shows the contours of SSH and barotropic velocity vectors calculated by NEMO after ten years of model integration. The ocean basin parameters used are in Table 4.1 and $A_H = 10^4\ m^{-2}s^{-1}$. As in Figure 4.5, the numerical simulation is qualitatively able to reproduce the flow circulation given in the analytic solution (see Figure 2.16). However, the comparison between the relative vorticity of both solutions, using $\theta_f = 0.5\theta_B$ in the analytic model, reveals strong differences (see Figure 4.7 (c)). This could be a consequence of the boundary layer approximation which only keeps the highest order terms of the Laplacian operator whereas NEMO parametrises the entire operator. A similar result is observed when $\theta_f = \theta_B$ (not shown).

The addition of a step–shelf is studied in Figure 4.7 (b) and (d). Figure 4.7 (b) shows contours of the SSH field and the barotropic velocity vectors, and is compared with the corresponding analytical solution (Figure 2.18). The numerical solution is able to reproduce the same characteristic circulation on the shelf, but we observe once more a discrepancy in the relative error (see Figure 4.7 (d)). This is due, once again, to the different step–shelf representation and the different parametrisation of the Laplacian

operator in the analytical model and NEMO ocean model.

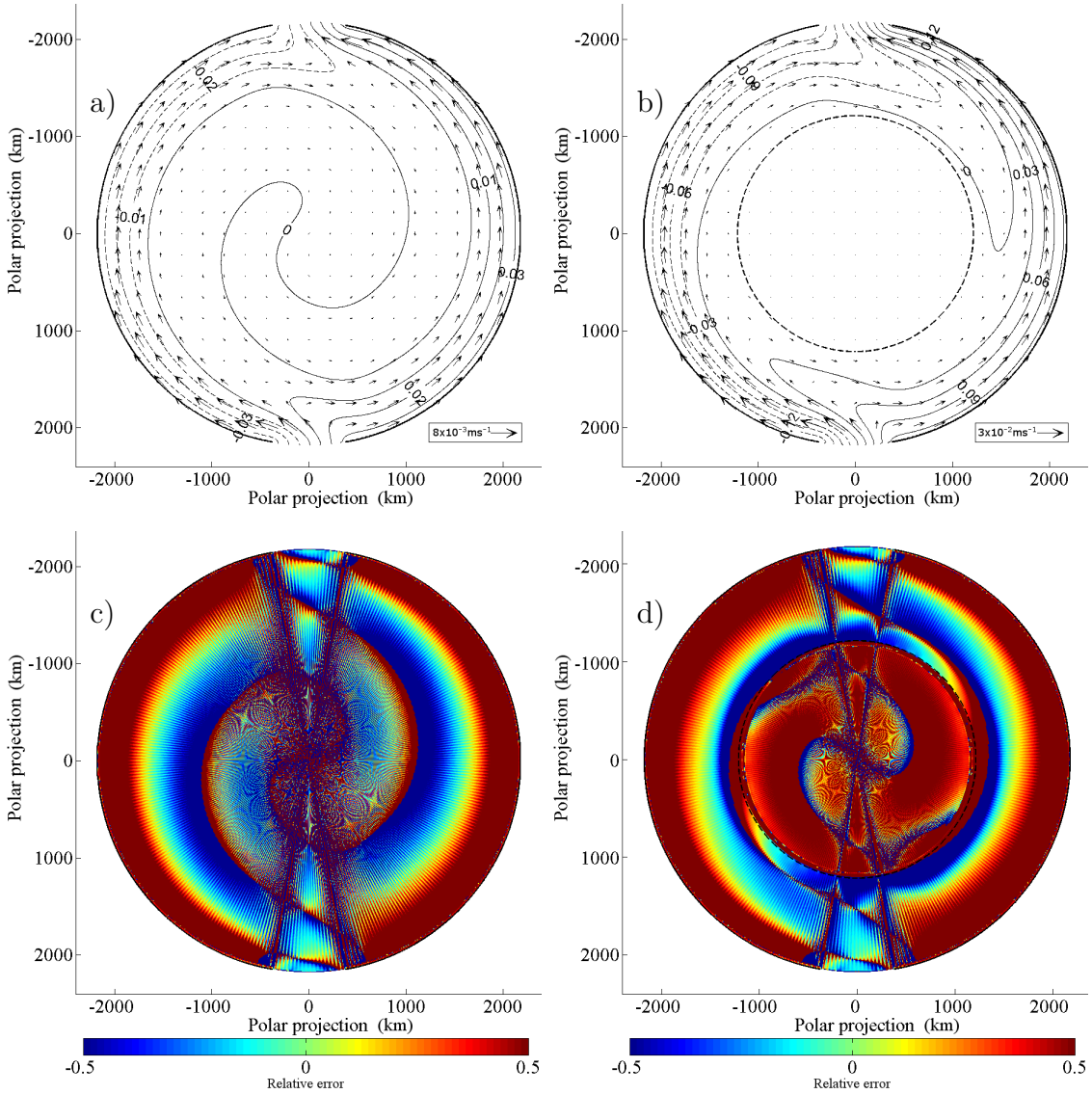

Figure 4.7: Source sink planetary geostrophic flow in the presence of Laplacian horizontal diffusion calculated by NEMO. a) Sea surface elevation in a flat bottom basin; b) same as (a) but in a step–shelf basin; c) relative error of the relative vorticity between the analytical and the numerical solution where $Error = (\xi_{NEMO} - \xi_{ana})/\xi_{NEMO}$ using $\theta_f = 0.5\theta_B$ in the analytical solution; d) same as (c) but in a step–shelf basin.

4.5 Basin with a step–shelf and a trans–polar ridge

In this section we explore the impact on the circulation caused by the addition of a trans–polar ridge in a basin with a step–shelf. This leads to two isolated deep basins in the domain interior. Ridges have a strong impact on barotropic and weakly stratified geostrophic/quasi–geostrophic ocean circulation because of topographic steering (Jiang and Garwood, 1998; Cushman-Roisin and Beckers, 2011). The deep basins are found to support isolated gyres as observed in the Amundsen and Makarov basins (Björk *et al.*, 2018).

Figure 4.8 shows schematically the four basin topographies used in these source–sink driven circulation experiments. Firstly, we investigate the impact of the ridge orientation in a basin with step–shelf of width 900 km (see Figure 4.8 (a) and (b)). Secondly, we define a "narrow" step–shelf whose width is smaller than the frictional boundary layer. As we saw in Chapter 2, the frictional boundary layer, $W \sim (\mu_0/f_0)^{1/2}\, r_b$, adjacent to the basin boundary, where f_0 is the Coriolis parameter evaluated at the pole, μ_0 is the coefficient of the bottom friction with dimensions s^{-1} and r_b is the radius of the polar basin. For $\mu = 5\times10^{-4}\ ms^{-1}$ and a step–shelf of depth 250 m the effective bottom friction parameter $\mu_0 \equiv \mu/H = 2\times10^{-6}\ s^{-1}$ and $W \sim 260\ km$. Therefore, we set the width of the narrow shelf to be 200 km (see Figure 4.8 (c) and (d)). Finally in this subsection, we study the influence on the circulation by a ridge whose top is below the step–shelf.

Figure 4.9 shows the steady–state circulation in a step–shelf basin with two different ridge orientations. The ocean basin parameters used in this simulation are given in Table 4.1 and the simulations were run for 10 years. In Figure 4.9 (a) we observe that upon entering the basin the flow bifurcates into three branches each of which exits at the sink strait. The anticyclonic and cyclonic (i.e. western and eastern branches) shelf currents support a volume fluxes of 1.98 and 1.87 Sv calculated normal to the sections $\overline{AB}$ and $\overline{EF}$, respectively. The third branch, which is comparably weaker, crosses the ridge forming a transpolar current with a volume flux of magnitude 1.06 Sv (measured across the section $\overline{CD}$). It is interesting to observe connected weak "Stommel–type" western boundary currents on the ridge (see Figure 4.9 (b)). "Stommel–type" western boundary currents are frictional boundary layer currents near to a western boundary (only if bottom friction is considered). They of course cross from one side of the ridge to the other in the neighbourhood of the pole (i.e. to be adjacent to the effective "dynamical western boundary"). The deep basin circulation is characterised by weak counter–rotating gyres

each with a magnitude of 0.05 Sv in each basin. We choose not to visualise this circulation because the velocity vectors are very much smaller in comparison with those on the shelf. Rotation of the ridge relative to the gaps does not qualitatively change the circulation as shown in Figure 4.9 (c). There is slight decrease in the transpolar transport on the ridge of 0.1 Sv which is re–distributed in the shelf currents.

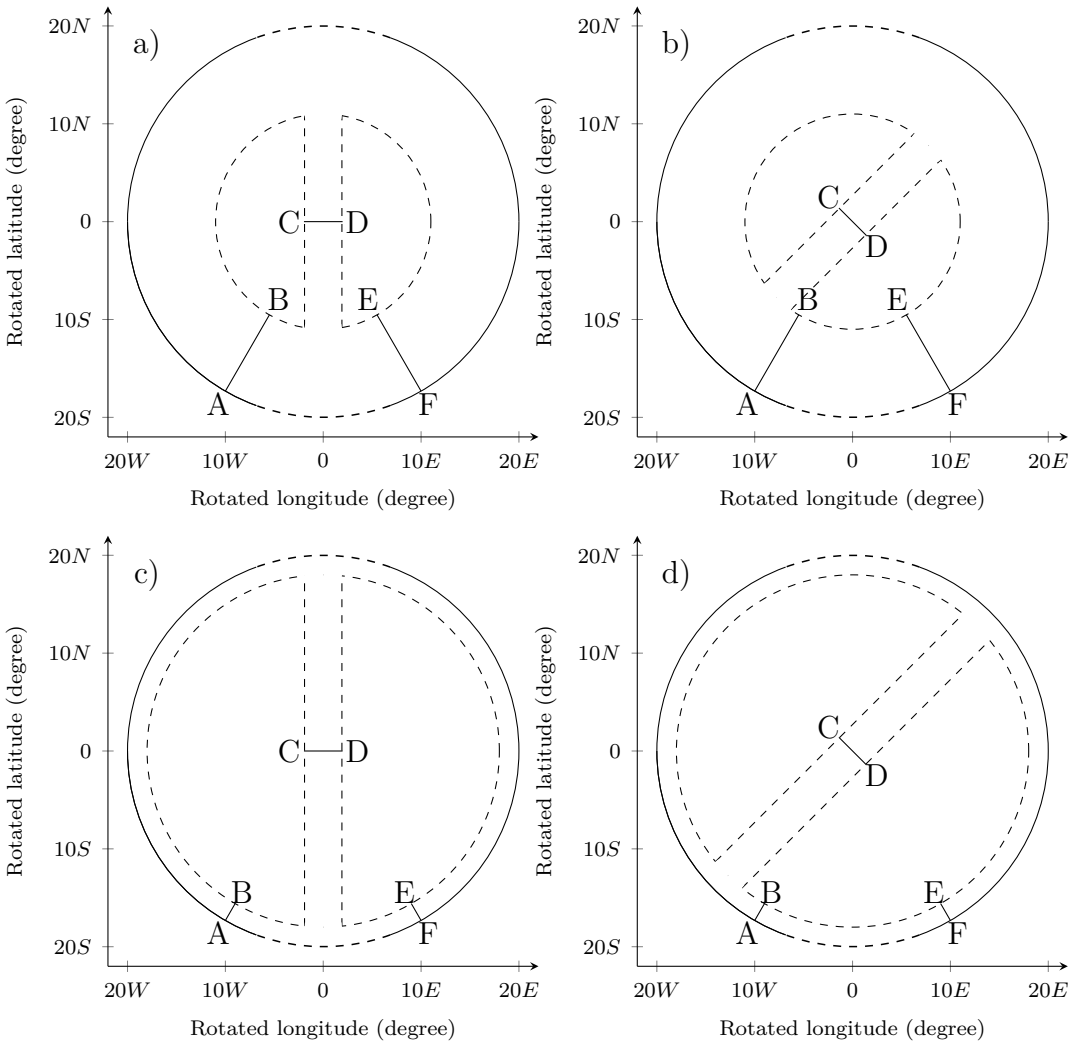

Figure 4.8: Schematic of the basin geometry used in the numerical Arctic Ocean experiments; a) step–shelf with a ridge aligned with the gaps; b) step–shelf with a rotated ridge; c) same as (a) but with a narrower step–shelf; d) same as (b) but with a narrower step–shelf. Sections $\overline{AB}$, $\overline{CD}$ and $\overline{EF}$ denote where the volume transport was computed.

Figure 4.10 shows the circulation in two basins analogous to those in Figure 4.9, except in a "narrow width shelf". The solutions plotted in Figure 4.10 have reached steady–state which is achieved in a simulated 10 years of model integration. Comparing Figure 4.9 (a) and 4.10 (a) reveals a different partitioning of the inflow between the cyclonic/anti–cyclonic shelf currents and the ridge current. Across the sections $\overline{AB}$ and

$\overline{EF}$ the transports are 0.77 Sv (c.f. 1.98 Sv in the wide shelf) and 1.18 Sv (c.f. 1.87 Sv in the wide shelf), respectively, in Figure 4.10 (a). This decrease in the transport along the narrow shelf with respect to Figure 4.9 (a) leads to a much larger fraction of the inflow crossing the ridge forming a transpolar current with a magnitude of 2.72 Sv (c.f. 1.06 Sv in the wide shelf). The remaining 0.33 Sv crosses the shelf break forming counter rotating circulations in the deep basins (see Figure 4.10 (b)).

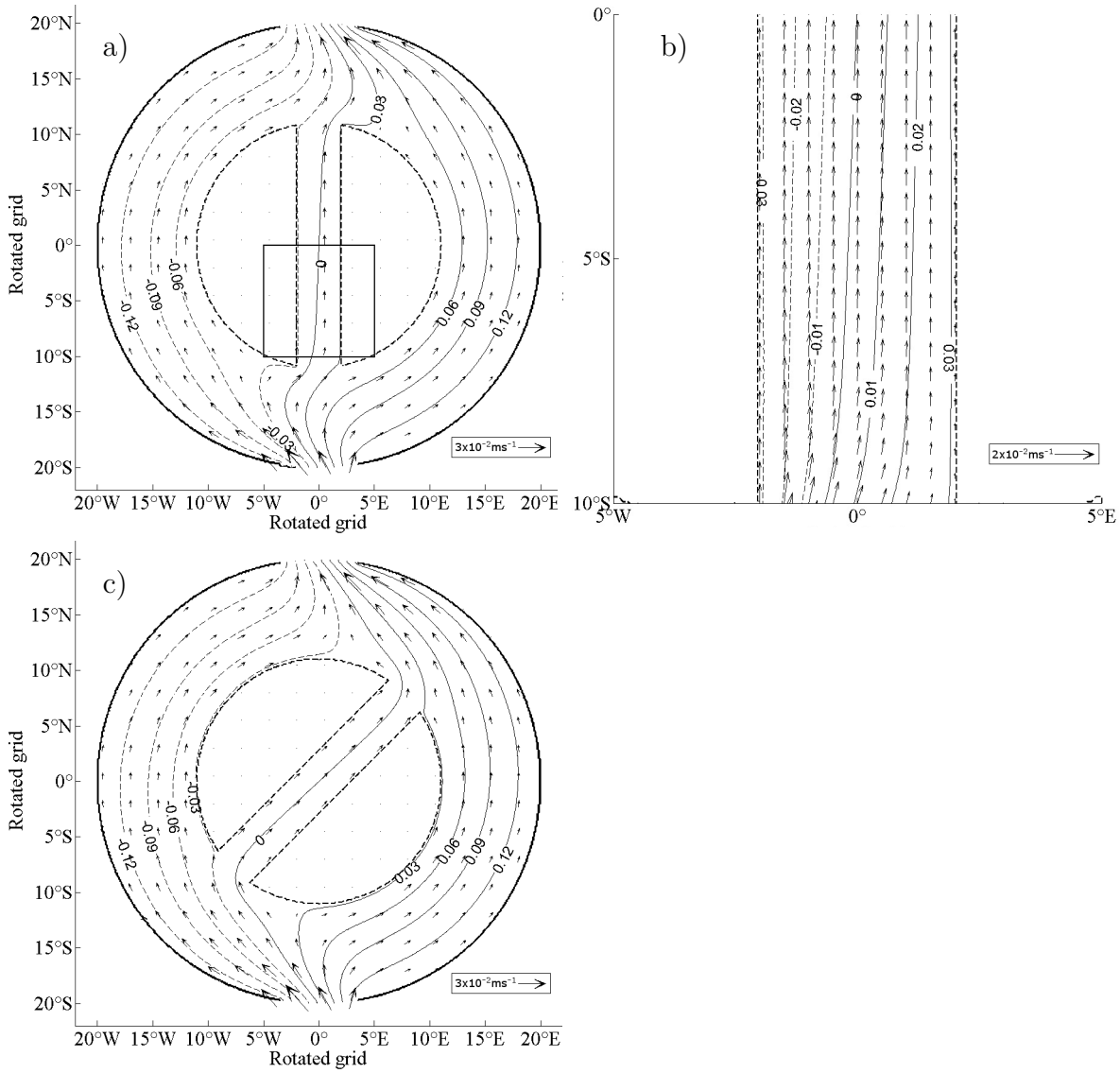

Figure 4.9: Numerical model results for a source–sink planetary geostrophic flow in a basin with a step–shelf and ridge. a) SSH and barotropic velocities in a basin with a step–shelf and ridge aligned with the gaps; b) Enlarged area of a sub–domain of (a) denoted by a black square; c) SSH and barotropic velocities in a basin where the ridge is oriented 45^o with respect to the diameter joining the centre of the gaps.

The change of the ridge orientation greatly alters the partition of the flow in the boundary currents (see Figure 4.10 (c)). The anti–cyclonic current with a volume trans-

port of 3.13 Sv (across the section $\overline{AB}$) is split in two sub–branches at the ridge where it forms a transpolar current of magnitude 1.84 Sv (measured transport across section $\overline{CD}$). The cyclonic current with magnitude 1.91 Sv, measured across section $\overline{EF}$, circulates on the shelf and merges with the transpolar drift current before exiting across the sink strait. The apparent inconsistency of the total mass balance across sections $\overline{AB}$ and $\overline{EF}$ (i.e. $3.13 + 1.91 > 5$) is due to the fact that the fluid crosses the shelf edge. For example, we observe near the strait, re–circulation of the fluid on the shelf and the deep basin (see Figure 4.10 (d)).

In the final numerical experiment, the top of ridge is located 250 meters below the step–shelf (i.e. the ridge depth is 500 m). Figure 4.11 (a) shows contours of the SSH with the barotropic velocity vectors for a step–shelf of width 900 km and a ridge with axis oriented 45^o with respect to the diameter joining the mid–points of the straits. The current circulates on the step–shelf with a magnitude 2.38 Sv across sections $\overline{AB}$ and $\overline{EF}$. There is essentially no ridge transport because of the discontinuity in the bathymetry where the ridge intersects the shelf. This depth discontinuity forms a barrier to geostrophic flow. The deep basin and the ridge remain almost stagnant supporting transports of 0.16 Sv and 0.06 Sv, respectively. The equivalent plot for a ridge aligned with the gaps is not shown because the flow distribution was almost identical, except that the transport across the ridge is slightly stronger. Figure 4.11 (b) displays contours of SSH for a narrower shelf (shelf width $\sim$ 200 km) with a ridge whose axis is aligned with the diameter joining the mid–points of the straits. Two strong boundary currents are observed on the step–shelf. The clockwise and anticlockwise boundary currents have a magnitude of 1.47 Sv and 2.27 Sv (measured across the sections $\overline{AB}$ and $\overline{EF}$), respectively. Continuity of mass would demand that the remaining 1.26 Sv are partitioned between the transpolar ridge and the deep basins. In fact at the section $\overline{CD}$ the transport is 1.20 Sv and the deep basins have extremely weak circulation (driven by cross–shelf transport in the frictional boundary layers) that closes the mass balance.

The impact of changing the ridge orientation on the circulation is addressed in Figure 4.11 (c). As in Figure 4.11 (b), the cyclonic boundary current branch is more intense than the anticyclonic revealing a transport of 2.6 Sv (measured across section $\overline{EF}$) whereas the anticyclonic is 2.3 Sv, measured across section $\overline{AB}$. The remaining 0.1 Sv crosses the shelf edge forming the deep basin circulation. Once the anticyclonic branch meets the ridge, it bifurcates forming a transpolar current of 0.72 Sv measured across section $\overline{CD}$.

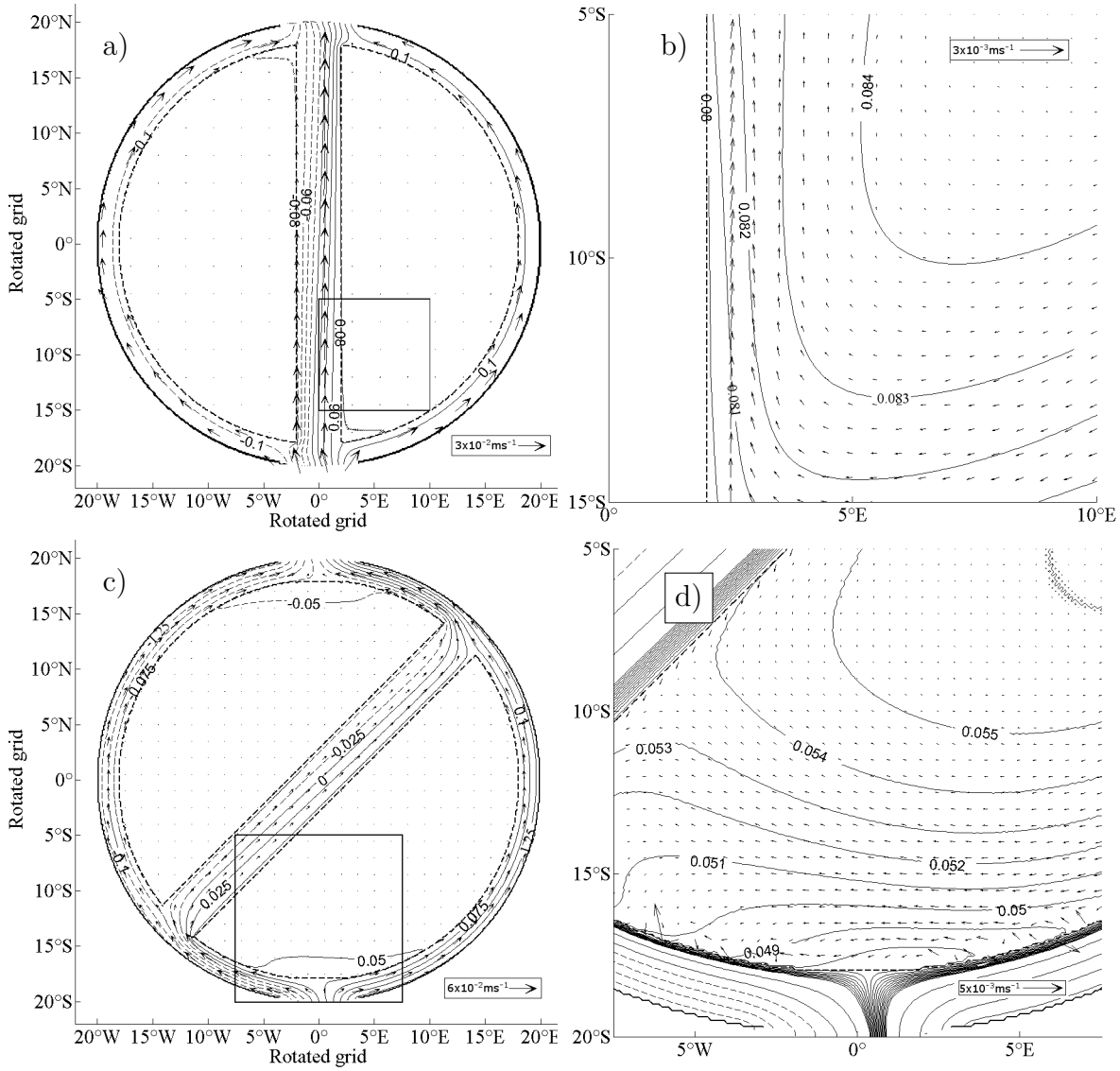

Figure 4.10: Same as Figure 4.9 except the width of the step–shelf is narrower than the "Stommel–type" frictional boundary layer; a) SSH and barotropic velocities in a basin with a step–shelf and ridge aligned orthogonal to the gaps; b) enlarged section of the ridge in (a) denoted by a black square; c) SSH and barotropic velocities in a basin with a step–shelf and ridge rotated 45^o to the diameter joining the mid–points of the gaps (straits); d) enlarged area of (c) denoted by a black square.

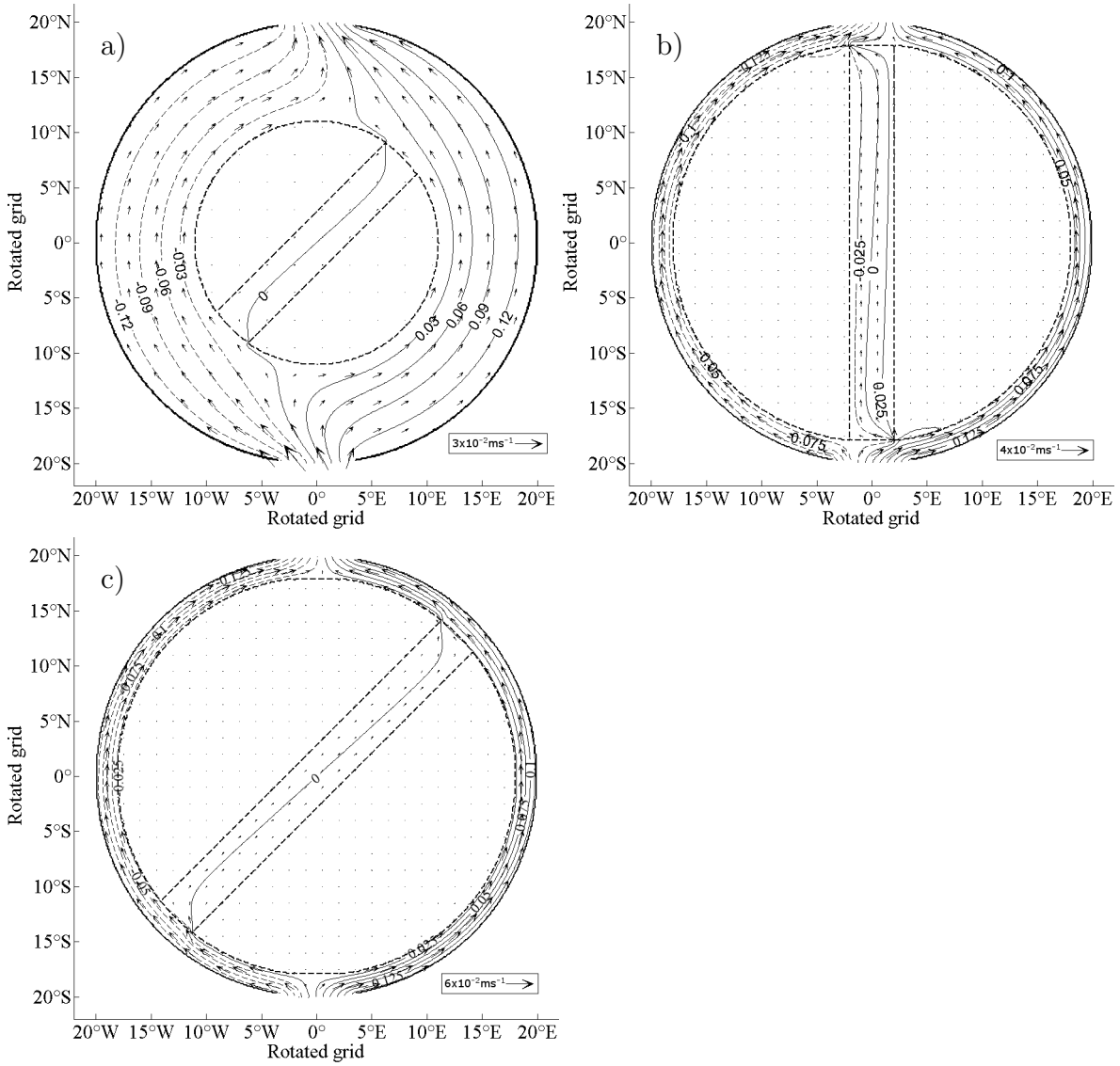

Figure 4.11: Numerical model simulations of source–sink planetary geostrophic flow in a basin with a ridge whose top is below the step–shelf. a) Contours of SSH and velocity vectors in a basin with a step–shelf and a ridge whose axis is rotated 45^o with respect of the axis joining the gaps; b) as in (a) except the ridge is aligned with the gaps and the step–shelf width is narrower. c) same as (a) except the step–shelf is narrower.

4.6 Source–sink driven circulation in a more realistic representation of the Arctic Ocean basin.

In this section we numerically determine the steady state source–sink driven circulation specified across three straits in a polar basin with a regular and irregular width step–shelf and a transpolar ridge, as shown schematically in Figure 4.12. The basin in Figure 4.12 (b) captures the fact that the continental shelf in the western Arctic (along the

coast of Greenland, Canada and USA) is much narrower (not exceeding $100km$) than the continental shelf in the eastern Arctic (Euro–Asian shelf). The top–hat ridge is a simple representation of the Lomonosov Ridge. Clearly, it is not possible to obtain analytical solutions for the planetary geostrophic circulation in the basins shown in Figure 4.12.

The top of the transpolar ridge in Figure 4.12 is $250m$ below the level of the shelf (see Table 4.1). The bathymetry of Figure 4.12 (a) can be set–up in the NEMO model in the subroutine *domzgr.F90* using a variation of Appendix C.1. Figure 4.12 (b) was coded in MATLAB (see Appendix C.4) and imposed as a external netCDF file (i.e. *nn_bathy*= 1 in *namelist_cfg*).

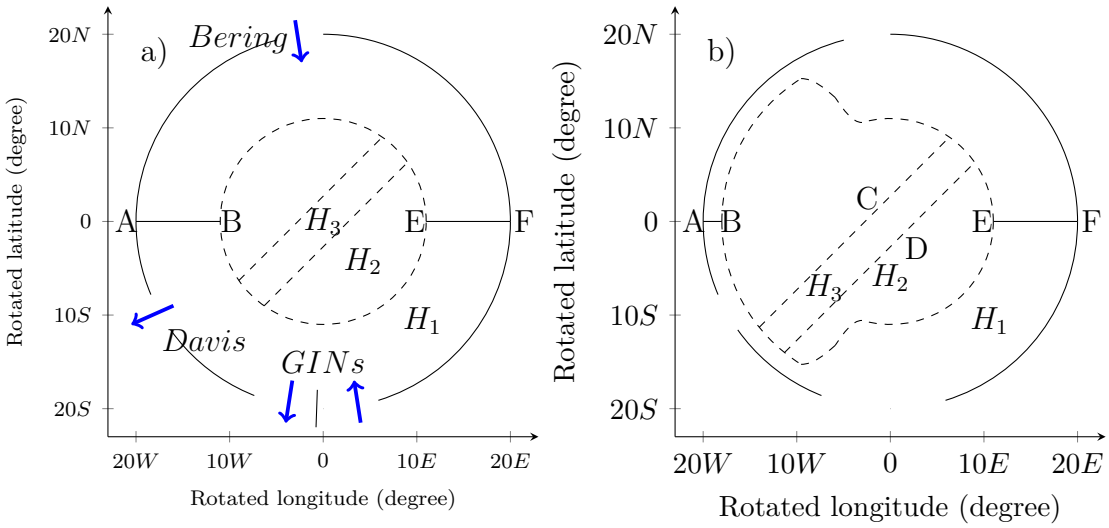

Figure 4.12: Schematic of a basin with three gaps and a ridge the top of which is below the step–shelf. a) Uniform width step–shelf with a ridge top below the shelf; b) same as (a) except that the shelf width is narrower in the "western side" of the basin. The shelf edge and ridge are denoted with dashed lines. Sections $\overline{AB}$, $\overline{CD}$ $\overline{EF}$ and $\overline{GH}$ denote where the volume transports were computed.

Three gaps (or straits) are prescribed at the boundary of the basin representing the Bering and the Davis Straits and the GINs as shown in Figure 4.12. Across the Bering and Davis Strait we prescribe an inflow and outflow, respectively. Across the GINs strait, we prescribe an inflow and an outflow. Therefore, across the first half of the strait an outflow is prescribed and across the remaining strait an inflow is prescribed. To be more precise, the azimuthal extent of the inflow is bigger than the outflow regions across the GINs strait. For consistency the magnitude of the boundary flows is set–up as in Chapter 2 (see Table 2.2). The implementation of these open boundaries follows the methodology in section 4.2.

Figure 4.13 (a) shows a contour plot of the steady state SSH field and the barotropic velocity field for the basin shown in Figure 4.12 (a). The inflow across the GINs strait splits into three branches. Two of them are deflected to the left; one branch flows towards the Davis Strait merging with the Bering branch before exiting the domain. The other, and more intense branch, recirculates leaving the domain through the GINs strait. At the GINs strait there is also a branch which flows cyclonically on the shelf with a (small) magnitude of 0.31 Sv measured across section $\overline{EF}$. This current merges with the Bering Strait inflow to form a cyclonic shelf current which has a volume transport of 1.12 Sv across section $\overline{AB}$ and which exits the Davis Strait. There is a small amount of drainage of the shelf currents into the deep basin that feeds weak cyclonic deep basin gyres.

Figure 4.13 (b) shows contours of the steady–state SSH and the barotropic velocity vectors for the basin shown in Figure 4.12 (b). We again observe that the inflow across the GINs strait bifurcates into three branches, as in Figure 4.13 (a). The cyclonic branch increases in magnitude (0.99 Sv at the section $\overline{EF}$) in comparison with Figure 4.13 (a). Subsequently, the GIN cyclonic branch bifurcates into two branches. The first branch crosses the ridge producing a transpolar drift current of 0.89 Sv (measured transport at the section $\overline{CD}$). The second merges with the Bering inflow flowing cyclonically along the narrow shelf with a magnitude of 0.85 Sv across section $\overline{AB}$. The remaining 0.25 Sv cross the shelf forming an anticyclonic boundary current in the deep basin (Figure 4.13 (c)).

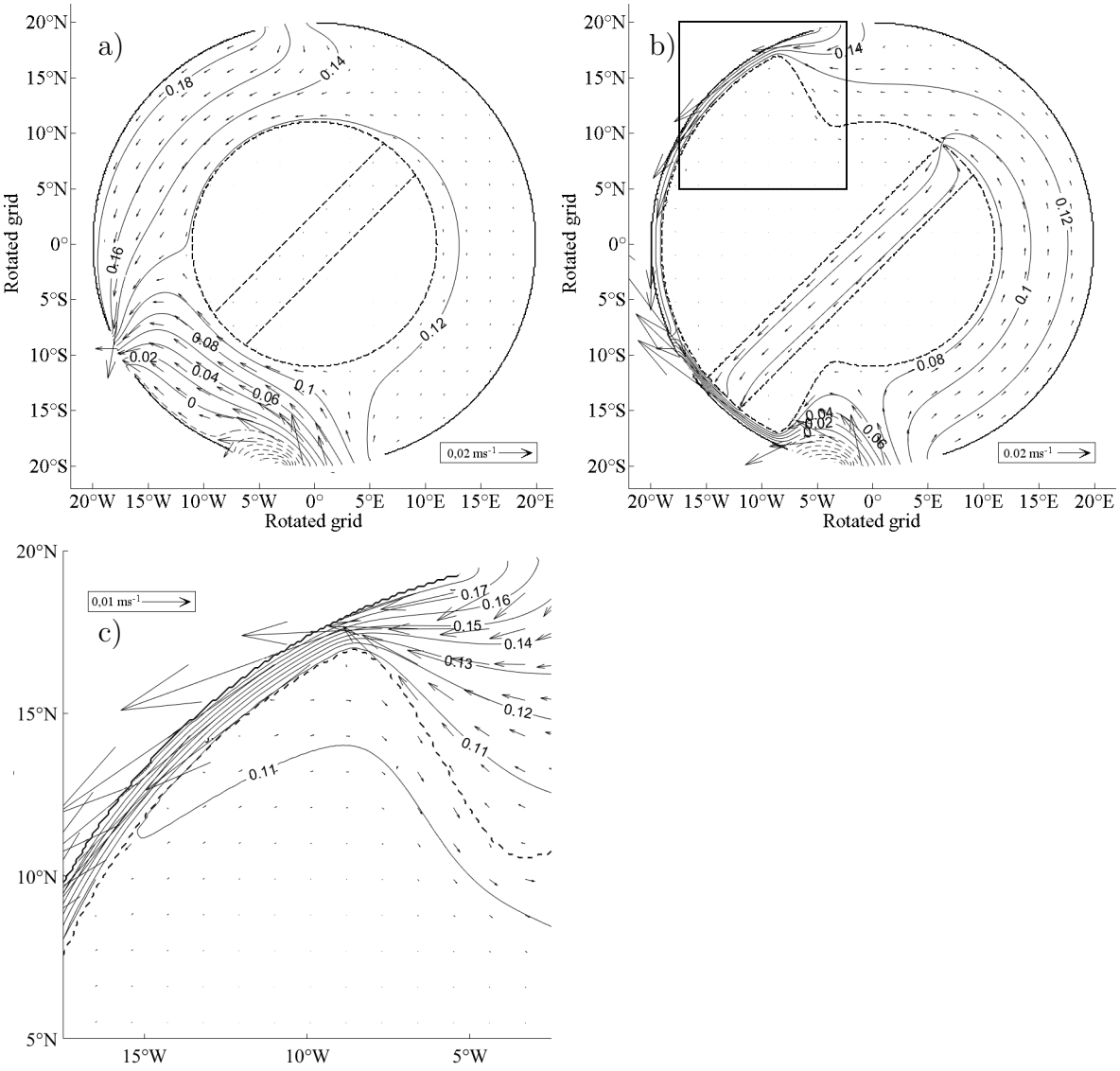

Figure 4.13: Steady source-sink planetary flows in the basins shown in Figure 4.12. a) Contours of SSH and barotropic velocities in the basin shown in Figure 4.12 (a); b) same as (a) except for the basin in Figure 4.12 (b); c) enlarged area of (b) within the black square. The shelf–break and ridge edge are denoted with dashed lines.

4.7 Impact of sea ice on the planetary geostrophic ocean circulation

This section calculates numerically the steady barotropic planetary circulation driven by a source–sink boundary flow in a polar basin covered by a layer of sea ice. The aim of this section is whether the ice–ocean shear stress leads to steady–state source–sink circulation that is significantly different from the ice–free state computed earlier. To simplify the study, sea ice thermodynamics are suppressed. Thus the sea ice depth and concentration

can only change by convergence and divergence of the sea ice velocity field. Such numerical ice dynamics experiments are uncommon in the refereed literature. Gray and Morland (1994) developed an idealised 1–dimensional time dependent analytical sea ice model neglecting thermodynamics and the Coriolis force. Their results demonstrated the sea ice converges and diverges in presence of a unidirectional wind stress. Schulkes *et al.* (1998) studied the sea ice dynamics in a 2–dimensional sea ice finite element model with four different rheology schemes and without diffusive terms. This model solved sea ice dynamics in spatial (Eulerian) coordinates. The sea ice velocity and numerical stability are shown to be sensitive to the use of free-slip and no-slip boundary conditions. In contrast to Schulkes *et al.* (1998), Morland and Staroszczyk (1998) employed a similar sea ice model but in material (Lagrangian) coordinates. They studied the sea ice dynamics using a viscous–elastic rheology scheme in presence of free–slip and no–slip boundary conditions. The use of material coordinates significantly improved the stability of the sea ice model despite the fact that the simulations became unstable after 5 days.

This section uses a coupled ocean–sea ice model, NEMO, in order to study the dynamical interaction between ocean and ice. The ocean model (OPA) implementation is similar to that in section 4.2 except the horizontal resolution is now set to $0.5^o \times 0.5^o$. Also, only two polar basins are considered, one without topography (see Figure 4.3 (a)) and one with a uniform width step shelf (see Figure 4.3 (b)).

The sea ice model in the NEMO modelling system is the Louvain-la-Neuve or LIM. LIM was developed as sea ice model but has been coupled to the OPA module of NEMO. LIM has three versions: LIM1D, LIM2 and LIM3. The implementation of sea ice model is specified in the *cpp_keys* and its parameters are in *namelist_ice_cfg*. All the experiments were performed using LIM2.

LIM incorporates routines which control the sea ice dynamics and thermodynamics. All the numerical experiments with sea ice retain ice dynamics only. In other words, the exclusion of sea ice thermodynamics implies that sea ice will not be created or melted. Thus the subroutine *limthd_2.F90* had to be modified to remove the thermodynamic processes (see Appendix C.5). Also, the Coriolis parameter is computed and had to be specified in the subroutine *limmsh_2.F90* to be consistent with the ocean model.

The ice open boundaries are controlled in the subroutine *bdyice_lim.F90*. As in the ocean module, open boundaries for sea ice can be imposed in the model using external forcing files which include the lead concentration, the snow and ice thickness. However, in the experiments reported in this section we did not use the latter external files. Instead, we

modified the *bdyice_lim.F90* subroutine in order to prescribe a constant sea ice velocity which has the same depth and ice concentration as the sea ice layer initially imposed. The outflow is configured to vary depending on the interior domain (see Appendix C.6).

The initial conditions for velocity, SSH, temperature and salinity were set as in section 4.2 and they remain constant during the computational integration. In addition, the polar basin is initially covered with sea ice of uniform depth and concentration which is at rest. The sea ice depth/concentration can change from their initial values due to sea ice velocity convergence/divergence. In all the numerical experiments the initial sea ice concentration is 1.0 and we consider two scenarios for the initial sea ice depth; $0.05m$ and $0.5m$.

Figure 4.14 (a) shows contours of SSH and the barotropic velocity vectors in a flat bottom basin initially covered by an ice layer of depth $0.05m$. Qualitatively, the polar circulation is the same as source–sink planetary flows without sea ice (see Figure 4.5 (a)). The difference between the ocean velocities and SSH fields in coupled ocean-ice model and the ocean only model are extremely small. This reflects the fact that the ocean velocities (and hence the ice–water shear stress) in the source–sink driven flow are small typically $< 0.01\ ms^{-1}$. Figure 4.14 (b) displays the sea ice thickness and the ice velocity vectors in the spin–up state for a basin initially covered by an ice layer of depth $0.05m$. There is a slight accumulation of ice near the outflow strait but in general the sea ice is motionless. The sea ice velocities and thickness in the spun–state, starting from an initial sea ice field of thickness $0.5m$, are shown in Figure 4.14 (c). Once again the sea ice is essentially motionless. The spun–up ocean state is almost identical to the equivalent ice–free experiments. Throughout most of the domain the small ocean velocities lead to an ice–ocean shear stress that is negligible. There is a tendency for modest ice accumulation in the neighbourhood of the outflow strait.

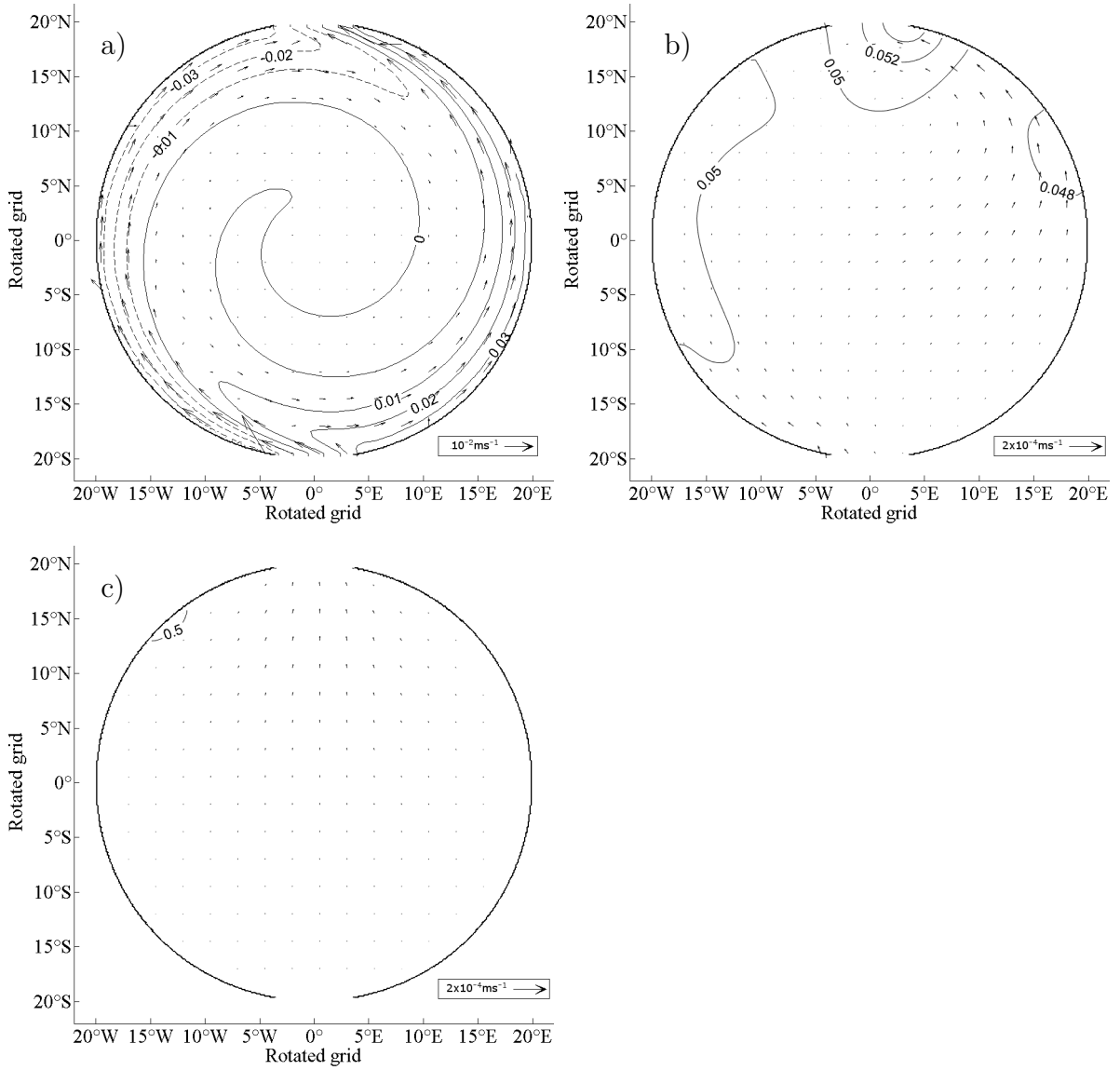

Figure 4.14: Source–sink planetary circulation coupled to dynamic sea ice in a flat bottom basin; a) contours of SSH and the barotropic velocity vectors; b) contours of sea ice thickness and sea ice velocity vectors. In (a) and (b) the initial sea ice depth was $0.05m$; c) as in (b), except the initial sea ice depth was $0.5m$.

Numerical experiments in a polar basin with the addition of a step–shelf are shown in Figure 4.15. Figure 4.15 (a) shows contours of the SSH and the barotropic velocity vectors in a step–shelf basin initially covered by sea ice with thickness of $0.05m$. The shelf circulation is indistinguishable to the equivalent solution without ice shown in Figure 4.5 (b). The sea ice drift is shown in Figure 4.15 (b). The presence of strong ocean velocities on the shelf alter considerably the sea ice distribution in the domain. In particular, we observe a convergence on the "western" side of the inflow and outflow straits due to the clockwise planetary wave propagation. Figure 4.5 (c) displays the sea ice thickness and

the sea ice velocity vectors for a step–shelf basin initially covered by sea ice of $0.5m$ thick. Once more, we observe a convergence of sea ice on the "western" side of the shelf whereas the "eastern" side reveals a divergence of sea ice.

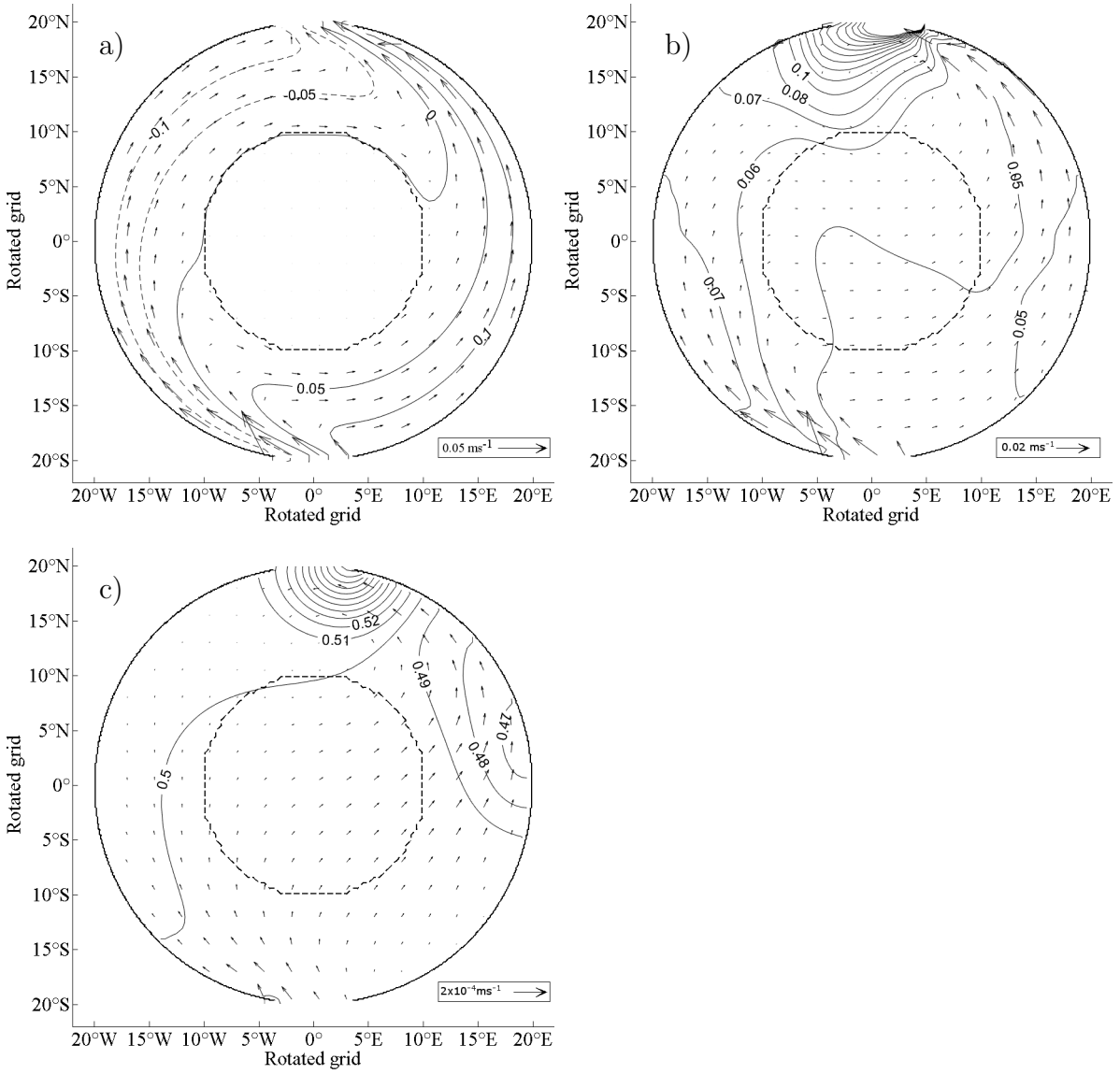

Figure 4.15: Source–sink planetary circulation coupled to dynamic sea ice in a step–shelf basin; a) contours of SSH and the barotropic velocity vectors; b) contours of sea ice thickness and sea ice velocity vectors. In (a) and (b) the initial sea ice depth was $0.05m$; c) as in (b), except the initial sea ice depth was $0.5m$.

4.8 Conclusions

First, the spin–up of source–sink driven circulation in a circular polar basin without topography shown in Figure 4.4 (a) is achieved by the generation of gravest mode planetary (Rossby) waves, in this case with a period of approximately 101 days. The spin–up takes a

simulated 3–years. We compared the wave phase speed from the numerical model with the phase speed given by the analytical dispersion relation in Chapter 3; it revealed that they are in good agreement. Therefore, we concluded that the beta-sphere approximation can successfully reproduce the dispersion properties of low–mode planetary wave dynamics in a polar basin.

Second, the comparison between the numerical simulations with the equivalent analytical results in Chapter 2 revealed qualitatively good agreement in the flat bottom basin. In particular, there was a better agreement between the linear bottom friction solutions than the Laplacian boundary layer approximation solutions. The latter revealed noticeable differences in relative vorticity due to different method to compute the Laplacian operator. The addition of a step–shelf in the domain revealed differences between the numerical ocean model and the analytic model in the relative vorticity of the deep basin. This could be related to the step–shelf representation in the analytic model.

Third, the addition of a transpolar ridge in the basin with step–shelf, where the top of the ridge has the same depth as the shelf, supports a transpolar current formation on the ridge. Overall, the ridge orientation did not have any noticeable impact in the wide step–shelf simulations. However, the strength of the boundary currents along the shelf proved to be sensitive to variation of the ridge orientation in the narrow step–shelf. Interestingly, this fact was not observed in the step–shelf basin with the top of ridge below the shelf where the "topographic barrier" at the intersection of the ridge and the shelf inhibits quasi–geostrophic flow crossing onto the ridge. The deep basin circulation remains stagnant except in the case of a "narrow" step–shelf. In particular, the deep basin displayed boundary currents close to the straits for a narrow step–shelf basin with a rotated ridge (Willmott and Luneva, 2015).

Fourth, the steady circulation in a circular step–shelf basin with a ridge and three gaps is studied with two different types of shelf geometry. The uniform width shelf supports steady shelf circulation similar to the analytical solution in Chapter 2 characterised by a strong recirculation in the GINs strait and an intense boundary current between the Bering Strait and the Davis Strait (Aksenov *et al.*, 2011). The irregular width shelf, which more closely resembles the topography of the Arctic basin, shows a similar circulation on the shelf except for shelf break current from the Canada shelf forming a deep basin circulation (see Figure 4.13 (c)). It is encouraging that this simulation qualitatively captures the numerically determined circulation of Spall (2013), although he used a stratified study forced by a buoyancy flux in the Canadian basin. The Canadian shelf is relatively narrow

(i.e. $\sim$ 100 km) and is adjacent to a deep basin depth (i.e.1000 m). Spall (2013) notes that the anticyclonic circulation in the deep basin was generated by mixing effects. In contrast, in this study frictional boundary layers enable fluid to cross isobaths, "breaking" the PV constraint.

Finally, we briefly consider source–sink circulation in basin covered by a layer of sea ice in a flat bottom and step–shelf basin. Sea ice thermodynamics is neglected preventing the formation and melt of sea ice. Ice thickness and concentration changes therefore are a result of sea ice convergence/divergence. Schulkes *et al.* (1998) and Morland and Staroszczyk (1998) used a "similar dynamic only sea ice modelling approach" to examine a proposed constitutive equation for sea ice. The calculated steady–states in this chapter reveal that sea ice at most perturbs the ice–free spun–up ocean circulation. This simply reflects the fact that the ice–ocean shear stress throughout the spin–up phase is negligible.

Chapter 5

Wind-driven planetary flows in a polar basin; analytical studies

5.1 Introduction

In the previous chapters we considered steady, barotropic, ocean circulation driven by a prescribed source–sink distributions on the boundary. As a step towards a more realistic model of Arctic ocean circulation, we consider wind–driven ocean circulation. The wind stress is of major significance in driving the Arctic circulation (Proshutinsky and Johnson, 1997; Rabe *et al.*, 2014; Proshutinsky *et al.*, 2015). In the literature there are very few *analytical* studies of wind–driven polar ocean circulation, due to the non–linear dependence of the Coriolis parameter with latitude. One exception is the study by Hart (1975) which develops a steady, non–linear, two–layer, wind–driven ocean circulation model in a circular polar basin in the presence of large amplitude idealised topography. The latter assumption means that "topography beta" dominates over planetary beta. In this model the layers are coupled by a mixing parametrisation represented by interfacial Laplacian friction. The circulation in the lower layer is found to be steered along bathymetric contours, while the upper layer circulation is "shielded" from the topography effects. More recently, Newton *et al.* (2006) evaluated steady, linear, two–layer, wind–driven ocean circulation on a $f-$plane using cylindrical coordinates. They studied the change of the pycnocline depth in response to a different azimuthal wind stress. Willmott and Luneva (2015) investigated barotropic ocean circulation driven by a double gyre wind stress curl on a closed polar plane using the "polar β-plane" approximation of LeBlond (1964).

This chapter utilises a circular polar domain with a simple bathymetry, following

Willmott and Luneva (2015). In contrast to the closed basin of Willmott and Luneva (2015), we consider a circular polar basin with two gaps. We obtain solutions for steady barotropic circulation using the "β-sphere" approximation in a flat bottom basin and a basin with a step-shelf of uniform width. After deriving the exact forced potential vorticity equation in spherical polar coordinates for planetary geostrophic flow in presence of linear bottom friction, we utilise the "β-sphere approximation" (Imawaki and Takano, 1974) to obtain a second order partial differential equation with constant coefficients which can be solved using classical methods.

5.2 Analytical approach

We consider an homogeneous ocean on a polar cap. A spherical polar coordinate system is adopted where θ and φ denote the co-latitude and longitude (i.e azimuthal) angle, respectively, and θ_B is the co-latitude of the boundary of the polar cap. Therefore, $\theta \in [0, \theta_B)$ and $\varphi \in [0, 2\pi)$. The unit vectors $\mathbf{k}, \hat{\boldsymbol{\theta}}, \hat{\boldsymbol{\varphi}}$ form a right-handed triad where

$$\mathbf{k} \wedge \hat{\boldsymbol{\theta}} = \hat{\boldsymbol{\varphi}},$$

and $\boldsymbol{k}$ is directed in the radial direction (see Figure 2.1) The steady-state linearised shallow water momentum equations take the form

$$f\boldsymbol{k} \times \mathbf{u} = -g\nabla\eta + -\frac{\mu}{H}\boldsymbol{u} + \frac{\boldsymbol{\tau}}{\rho H}, \tag{5.1}$$

where $\boldsymbol{u} = u\hat{\boldsymbol{\varphi}} + v\hat{\boldsymbol{\theta}}$, $f = 2\Omega\cos\theta$, $\boldsymbol{\tau}$ is the wind stress, ρ is the density, η is the dynamic free surface elevation and g is the gravitational acceleration. In chapter 2 we considered two types of dissipation, here we only explore the linear (Rayleigh) bottom friction where μ is the constant bottom friction parameter and H is the undisturbed ocean depth. A rigid-lid approximation is adopted allowing the introduction of a transport streamfunction $\psi(\varphi, \theta)$ where

$$Hu = \frac{1}{R}\psi_\theta, \qquad Hv = \frac{-1}{R\sin\theta}\psi_\varphi. \tag{5.2}$$

5.2.1 Flat bottom basin

In this subsection we derive solutions for steady-state planetary geostrophic circulation in a circular flat bottom basin where the North Pole is located in centre of the domain. The circulation is wind–driven by two opposite wind stress curl gyres which force an inflow/outflow across two open boundaries via the Sverdrup balance. Each gyre of the curl occupies a nearly semi–circular region. The diameter that forms the axis of symmetry of the two shaded wedge–shaped transition regions is defined by $\varphi = \hat{\varphi}_1$ and $\varphi = \hat{\varphi}_1 + \pi$ $(= \hat{\varphi}_2)$ as shown in Figure 5.1. Within each semi–circular domain the wind stress curl has a constant value except in a wedge transition region where the curl varies linearly with φ. This transition ensures a continuous change between the uniform values of each wind curl gyre. These wedge regions are shown as shaded in Figure 5.1. The open boundaries or gaps, lie at co-latitude θ_B and the mid-point of each strait lies on the diameter of $\varphi = 0$ and $\varphi = \pi$ (see Figure 5.1). The vorticity equation is obtained by taking the curl of (5.1).

$$-fu_\varphi - (fv\sin\theta)_\theta = \left(\mu\frac{u\sin\theta}{H}\right)_\theta - \left(\mu\frac{v}{H}\right)_\varphi + \frac{\left(\tau^\theta_\varphi - (\sin\theta\tau^\varphi)_\theta\right)}{\rho H} \tag{5.3}$$

In terms of ψ, defined by (5.2), the vorticity equations takes the form

$$-f\frac{1}{HR}\psi_{\varphi\theta} - \left(-\frac{f}{HR}\psi_\varphi\right)_\theta = \left(\mu\frac{\sin\theta}{H^2R}\psi_\theta\right)_\theta - \left(\mu\frac{-1}{H^2R\sin\theta}\psi_\varphi\right)_\varphi + \frac{\left(\tau^\theta_\varphi - (\sin\theta\tau^\varphi)_\theta\right)}{\rho H} \tag{5.4}$$

Expanding the partial derivatives we obtain

$$-\frac{2\Omega\sin\theta}{HR}\psi_\varphi = \frac{\mu}{H^2R}\left(\cos\theta\psi_\theta + \sin\theta\psi_{\theta\theta}\right) + \frac{\mu}{H^2R\sin\theta}\psi_{\varphi\varphi} + \frac{\left(\tau^\theta_\varphi - (\sin\theta\tau^\varphi)_\theta\right)}{\rho H} \tag{5.5}$$

We multiply equation (5.5) by $\mu^{-1}HR\sin\theta$ and rearrange:

$$\psi_{\varphi\varphi} + A\psi_{\theta\theta} + B\psi_\theta + C\psi_\varphi = \mu^{-1}R^2H\sin^2\theta\{\boldsymbol{k}\cdot\nabla\times\boldsymbol{\tau}/\rho\}, \tag{5.6}$$

The coefficients A, B and C in (5.6) are defined as

$$A \equiv \sin^2\theta, \qquad B \equiv \sin\theta\cos\theta, \qquad C \equiv 2\Omega H\mu^{-1}\sin^2\theta. \tag{5.7}$$

Notice that in the absence of bottom friction (5.6) reduces to the Sverdrup balance

$$\frac{2\Omega}{R^2}\psi_\varphi = \boldsymbol{k}\cdot\nabla\times(\boldsymbol{\tau}/\rho)\,, \tag{5.8}$$

where right hand side represents the wind stress curl

$$\{\underline{k}\cdot\nabla\times\underline{\tau}/\rho\} = \frac{\left((\sin\theta\tau^\varphi)_\theta - \tau^\theta_\varphi\right)}{R\sin\theta\rho} \equiv \sin\left(\pi\frac{\theta}{\theta^*}\right)W(\varphi)\,. \tag{5.9}$$

where wind stress curl vanishes at the pole and the constant angle θ^* determines its meridional structure across the polar basin. Note we are *assuming* that the wind stress curl has a separable form of the type given in (5.9).

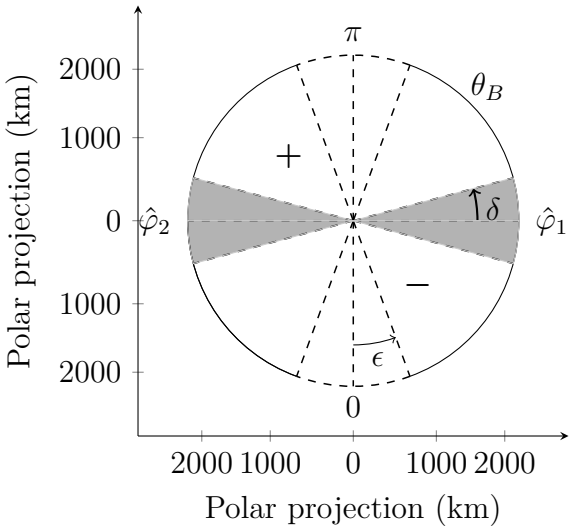

Figure 5.1: Schematic of a circular polar basin with diametrically opposed gaps (i.e. straits) on the boundary. A double gyre wind stress curl drives the circulation. The shaded wedges allow a continuous transition from a uniform positive value curl (indicated by the + sign) in the upper, near semi–circular region to a negative uniform value curl in the domain (indicated a − sign).

Hereafter, we apply the "beta-sphere approximation" and fix $\theta = \theta_f$ in (5.7), the typical value being mid-way between the pole and $\theta = \theta_B$. The sensitivity of the solutions to θ_f is considered later. Equation (5.6) then becomes a constant coefficient linear 2^{nd} order partial differential equation which can be solved using classical analytical techniques.

We impose two opposite wind stress curl gyres of the form,

$$W(\varphi) \equiv W_0 \begin{cases} -1 & \text{if } 0 \le \varphi \le \hat{\varphi}_1 - \delta, \\ -1 + [\varphi - (\hat{\varphi}_1 - \delta)]/\delta & \text{if } \hat{\varphi}_1 - \delta \le \varphi \le \hat{\varphi}_1 + \delta, \\ 1 & \text{if } \hat{\varphi}_1 + \delta \le \varphi \le \hat{\varphi}_2 - \delta, \\ 1 - [\varphi - (\hat{\varphi}_2 - \delta)]/\delta & \text{if } \hat{\varphi}_2 - \delta \le \varphi \le \hat{\varphi}_2 + \delta, \\ -1 & \text{if } \hat{\varphi}_2 + \delta \le \varphi \le 2\pi, \end{cases} \tag{5.10}$$

where $W_0 = \tau_0/(\rho R)$ and τ_0 is a typical wind stress magnitude. Figure 5.2 shows a contour plot of (5.9), scaled by W_0 using the parameter values list in Table 5.2 when $\hat{\varphi}_1 = \pi/2$ and $\hat{\varphi}_2 = 3\pi/2$.

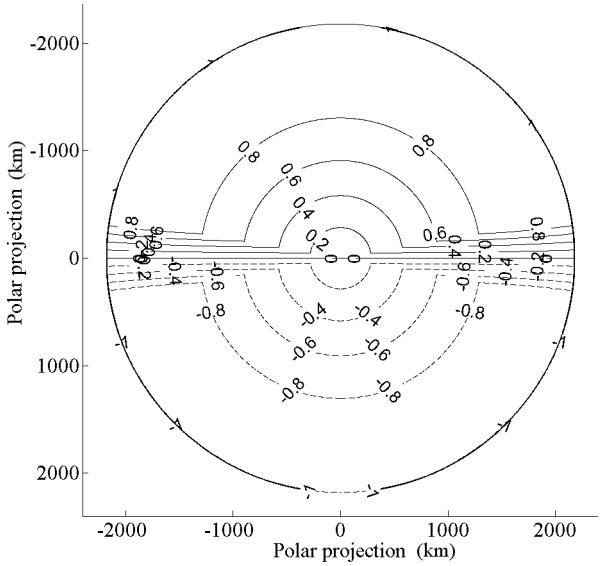

Figure 5.2: Contours of the wind stress curl (5.9) and (5.10) scaled by W_0. The continuous/dashed lines denote positive and negative values, respectively.

On the boundary of the basin the streamfunction must satisfy

$$\psi(\varphi, \theta_B) \equiv \psi_B(\varphi) = \psi_0 \begin{cases} -\varphi/\epsilon & \text{if } |\varphi| \leq \epsilon, \\ -1 & \text{if } \epsilon \leq \varphi \leq \pi - \epsilon, \\ -1 + [\varphi - (\pi - \epsilon)]/\epsilon & \text{if } \pi - \epsilon \leq \varphi \leq \pi + \epsilon, \\ 1 & \text{if } \pi + \epsilon \leq \varphi \leq 2\pi - \epsilon. \end{cases} \tag{5.11}$$

where

$$\psi_0 = \frac{\epsilon R^2 W_0}{2\Omega} \sin\left(\pi \frac{\theta_B}{\theta^*}\right). \tag{5.12}$$

Clearly (5.11) describes steady transport between straits: $[-\epsilon, \epsilon]$ and $[\pi - \epsilon, \pi + \epsilon]$. The direction of the flow across the straits (5.11) is determined by the sign of $\sin(\pi\theta_B/\theta^*)$ in (5.12). Figure 5.3 shows a plot $\sin(\pi\theta_B/\theta^*)$ for various values of θ^* over the latitudinal extent of basin (i.e. $\theta_B = \pi/9$) and Table 5.1 presents values of ψ_0 as a function of θ^* in (5.12) using the parameters as given in Table 5.2. For $\theta^* > \pi/9$, at the boundary of the basin (i.e. $\theta_B = \pi/9$) there is an inflow across $[\pi - \epsilon, \pi + \epsilon]$ and a outflow through $[-\epsilon, \epsilon]$. For $\pi/18 < \theta^* < \pi/9$, the inflow and outflow change, there is inflow across $[-\epsilon, \epsilon]$ and outflow $[\pi - \epsilon, \pi + \epsilon]$. Note that if the value of θ^* is $\pi/18$ or $\pi/9$, the transport across the strait vanishes.

Table 5.1: Source–sink position and values of ψ_0 depending on the θ^* following (5.12). The transport is given in Sverdrups and the negative sign indicates inflow.

Strait	$\theta^* = \pi/18$	$\theta^* = \pi/12$	$\theta^* = \pi/9$	$\theta^* = 2\pi/9$
$[\pi - \epsilon, \pi + \epsilon]$	0	0.64	0	-0.75
$[-\epsilon, \epsilon]$	0	-0.64	0	0.75

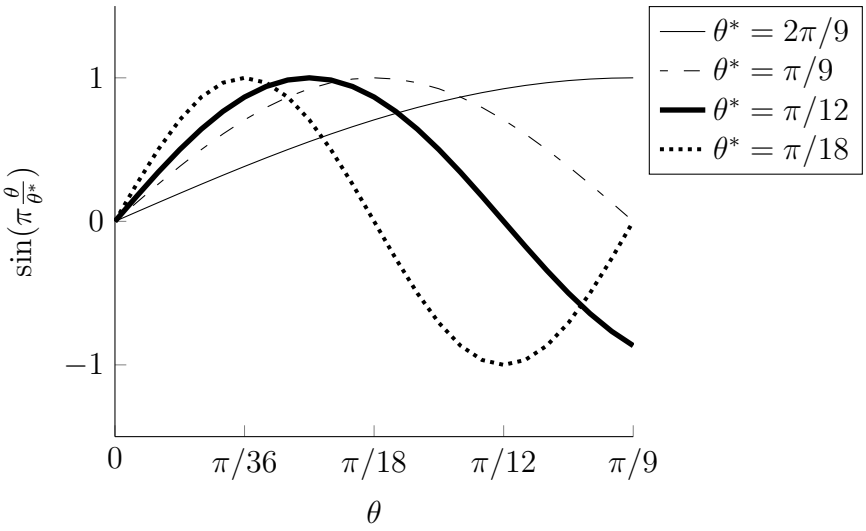

Figure 5.3: Plot of $\sin(\pi\theta/\theta^*)$ for various values of θ^*.

At the pole (5.6) requires that

$$\psi_{\varphi\varphi} = 0 \quad \text{at} \quad \theta = 0. \tag{5.13}$$

We seek a solution of (5.6) of the form

$$\psi(\varphi, \theta) = a_0(\theta) + \sum_{n=1}^{N} \left[a_n(\theta) \cos n\varphi + b_n(\theta) \sin n\varphi\right], \tag{5.14}$$

and therefore we decompose $W(\varphi)$ into a Fourier series:

$$W(\varphi) = p_0 + \sum_{n=1}^{N} \left[p_n \cos n\varphi + q_n \sin n\varphi\right]. \tag{5.15}$$

where p_0, p_n and q_n are the Fourier coefficients. With $W(\varphi)$ prescribed by (5.10) we find that

$$p_n = \frac{2W_0}{\pi n^2 \delta} \sin(n\delta) \left(\sin(n\hat{\varphi}_2) - \sin(n\hat{\varphi}_1)\right) \quad n = 1, 2, .. \tag{5.16a}$$

$$q_n = \frac{2W_0}{\pi n^2 \delta} \sin(n\delta) \left(\cos(n\hat{\varphi}_2) - \cos(n\hat{\varphi}_1)\right) \quad n = 1, 2, .. \tag{5.16b}$$

and $p_0 = 0$ $(n = 1, 2, ..)$. Substituting (5.14), (5.15) and (5.9) into (5.6) and collecting the coefficients of $\cos(n\varphi)$ and $\sin(n\varphi)$ we obtain

$$\left.\begin{aligned} -a_n n^2 + A\ddot{a}_n + B\dot{a}_n + Cb_n n &= \frac{R^2 H \sin^2\theta \sin\left(\pi\frac{\theta}{\theta^*}\right) p_n}{\mu} \\ -b_n n^2 + A\ddot{b}_n + B\dot{b}_n - Ca_n n &= \frac{R^2 H \sin^2\theta \sin\left(\pi\frac{\theta}{\theta^*}\right) q_n}{\mu} \end{aligned}\right\} \quad n \geq 1 \tag{5.17a}$$

and

$$A\ddot{a}_0 + B\dot{a}_0 = \frac{R^2 H \sin^2\theta \sin\left(\pi\frac{\theta}{\theta^*}\right) p_0}{\mu} \tag{5.17b}$$

We introduce the complex functions

$$Z_n = a_n + ib_n, \quad ; \quad W_n = p_n + iq_n \quad n \geq 1, \tag{5.18}$$

in which case (5.17a) can be combined in a single equation for Z_n, namely

$$A\ddot{Z}_n + B\dot{Z}_n - Z_n\left(n^2 + Cin\right) = \mu^{-1} R^2 H \sin^2\theta \sin\left(\pi\frac{\theta}{\theta^*}\right) W_n, \quad n = 1, 2, .. \tag{5.19}$$

The general solution of (5.19) takes form

$$Z_n = Z_{nCF} + Z_{nPI}, \tag{5.20}$$

The complimentary function Z_{nCF} is the solution of the homogeneous form of (5.19),

$$Z_{nCF} = R_n e^{\lambda_1\theta} + S_n e^{\lambda_1\theta}, \tag{5.21}$$

where R_n and S_n are arbitrary constants; λ_1 and λ_2 are calculated from the auxiliary equation

$$A\lambda^2 + B\lambda^2 - \left(n^2 + inC\right) = 0, \tag{5.22}$$

Clearly,

$$\left.\begin{matrix}\lambda_1 \\ \lambda_2\end{matrix}\right\} = \frac{-B}{2A} \pm \frac{1}{2A}\{B^2 + 4A\left(n^2 + inC\right)\}^{1/2}. \tag{5.23}$$

Note that λ_1 and λ_2 are functions of n, although we have not shown this explicitly in the notation.

To obtain the particular integral of (5.19) we re–write the right hand side of the equation as

$$\begin{aligned} A\ddot{Z}_n + B\dot{Z}_n - Z_n\left(n^2 + Cin\right) = \frac{R^2 H}{\mu}\Bigg(&\frac{\sin\left(\pi\frac{\theta}{\theta^*}\right) W_n}{2} - \frac{\sin\left(\left(2 + \frac{\pi}{\theta^*}\right)\theta\right) W_n}{4} \\ &+ \frac{\sin\left(\left(2 - \frac{\pi}{\theta^*}\right)\theta\right) W_n}{4}\Bigg), \end{aligned} \tag{5.24}$$

Therefore, the particular integral Z_{nPI} will be the linear combination of

$$Z_{nPI} = \sum_{j=1}^{3} \left[\alpha_{jn} \cos\left(\gamma_j \theta\right) + \beta_{jn} \sin\left(\gamma_j \theta\right)\right], \quad \text{where} \quad \begin{bmatrix} \gamma_1 \\ \gamma_2 \\ \gamma_3 \end{bmatrix} = \begin{bmatrix} \pi \frac{\theta}{\theta^*} \\ 2 + \frac{\pi}{\theta^*} \\ 2 - \frac{\pi}{\theta^*} \end{bmatrix} \tag{5.25}$$

and α_{jn} and β_{jn} are constants to be determined. Using (5.25) in (5.24) and collecting the coefficients of $\cos\left(\gamma_j \theta\right)$ and $\sin\left(\gamma_j \theta\right)$ we obtain

$$\begin{aligned}
&-\alpha_{1n}\gamma_A^2 + \beta_{1n}\gamma_1 B - \alpha_{1n}\left(n^2 + Cin\right) = 0 \\
&-\beta_{1n}\gamma_1^2 A - \alpha_{1n}\gamma_1 B - \beta_{1n}\left(n^2 + Cin\right) = \frac{R^2 H W_n}{2\mu} \\
&\alpha_{2n}\gamma_{2n}^2 A - \beta_{2n}\gamma_2 B + \alpha_{2n}\left(n^2 + Cin\right) = 0 \\
&\beta_{2n}\gamma_{2n}^2 A + \alpha_{2n}\gamma_2 B + \beta_{2n}\left(n^2 + Cin\right) = -\frac{R^2 H W_n}{4\mu} \\
&-\alpha_{3n}\gamma_{3n}^2 A + \beta_{3n}\gamma_2 B - \alpha_{3n}\left(n^2 + Cin\right) = 0 \\
&-\beta_{3n}\gamma_{3n}^2 A - \alpha_{3n}\gamma_2 B - \beta_{3n}\left(n^2 + Cin\right) = \frac{R^2 H W_n}{4\mu}.
\end{aligned} \tag{5.26}$$

Firstly we solve for β_j, therefore rearranging (5.26)

$$\begin{aligned}
&\alpha_{1n}\left(\gamma_1^2 A + \left(n^2 + Cin\right)\right) = \beta_{1n}\gamma_1 B \\
&-\alpha_{1n}\gamma_1 B - \beta_{1n}\left(\gamma_1^2 A + \left(n^2 + Cin\right)\right) = \frac{R^2 H W_n}{2\mu} \\
&\alpha_{2n}\left(\gamma_2^2 A + \left(n^2 + Cin\right)\right) = 4\mu\beta_{2n}\gamma_2 B \\
&\alpha_{2n}\gamma_2 B + \beta_{2n}\left(\gamma_2^2 A + \left(n^2 + Cin\right)\right) = -\frac{R^2 H W_n}{4\mu} \\
&\alpha_{3n}\left(\gamma_3^2 A + \left(n^2 + Cin\right)\right) = \beta_{3n}\gamma_3 B \\
&-\alpha_{3n}\gamma_3 B - \beta_3\left(\gamma_3^2 A + \left(n^2 + Cin\right)\right) = \frac{R^2 H W_n}{4\mu},
\end{aligned} \tag{5.27}$$

Substituting α_j in (5.27) yields

$$-\left(\frac{\beta_{1n}\gamma_1 B}{(\gamma_1^2 A + (n^2 + Cin))}\right)\gamma_1 B - \beta_{1n}\left(\gamma_1^2 A + \left(n^2 + Cin\right)\right) = \frac{R^2 H W_n}{2\mu}$$

$$\left(\frac{\beta_{2n}\gamma_2 B}{(\gamma_2^2 A + (n^2 + Cin))}\right)\gamma_2 B + \beta_{2n}\left(\gamma_2^2 A + \left(n^2 + Cin\right)\right) = -\frac{R^2 H W_n}{4\mu} \tag{5.28}$$

$$-\left(\frac{\beta_{3n}\gamma_3 B}{(\gamma_3^2 A + (n^2 + Cin))}\right)\gamma_3 B - \beta_{3n}\left(\gamma_3^2 A + \left(n^2 + Cin\right)\right) = \frac{R^2 H W_n}{4\mu}.$$

We multiply (5.28) by $\left(\gamma_j^2 A + (n^2 + Cin)\right)$ $(j = 1, 2, 3)$ to obtain

$$\beta_{1n} = -\frac{R^2 HW_n \left(\gamma_1^2 A + (n^2 + Cin)\right)}{2\mu\left(\gamma_1^2 B^2 + \left(\gamma_1^2 A + (n^2 + Cin)\right)^2\right)}$$

$$\beta_{2n} = \frac{R^2 HW_n \left(\gamma_2^2 A + (n^2 + Cin)\right)}{4\mu\left(\gamma_2^2 B^2 + \left(\gamma_2^2 A + (n^2 + Cin)\right)^2\right)} \tag{5.29}$$

$$\beta_{3n} = -\frac{R^2 HW_n \left(\gamma_3^2 A + (n^2 + Cin)\right)}{4\mu\left(\gamma_3^2 B^2 + \left(\gamma_2^3 A + (n^2 + Cin)\right)^2\right)}.$$

Now, we can obtain α_{jn} using the β_{jn}'s from (5.29) in (5.27):

$$\alpha_{1n} = -\frac{R^2 HW_n B\gamma_1}{2\mu\left(\gamma_1^2 B^2 + \left(\gamma_1^2 A + (n^2 + Cin)\right)^2\right)}$$

$$\alpha_{2n} = \frac{R^2 HW_n B\gamma_2}{4\mu\left(\gamma_2^2 B^2 + \left(\gamma_2^2 A + (n^2 + Cin)\right)^2\right)} \tag{5.30}$$

$$\alpha_{3n} = -\frac{R^2 HW_n B\gamma_3}{4\mu\left(\gamma_3^2 B^2 + \left(\gamma_2^3 A + (n^2 + Cin)\right)^2\right)}.$$

Thus the general solution (5.20) can be rewritten as

$$\begin{aligned} Z_n \;=\; & R_n e^{\lambda_1\theta} + S_n e^{\lambda_1\theta} + \alpha_{1n}\cos\left(\pi\frac{\theta}{\theta^*}\right) + \beta_{1n}\sin\left(\pi\frac{\theta}{\theta^*}\right) \\ & + \alpha_{2n}\cos\left[\left(2 + \frac{\pi}{\theta^*}\right)\theta\right] + \beta_{2n}\sin\left[\left(2 + \frac{\pi}{\theta^*}\right)\theta\right] \\ & + \alpha_{3n}\cos\left[\left(2 - \frac{\pi}{\theta^*}\right)\theta\right] + \beta_{3n}\sin\left[\left(2 - \frac{\pi}{\theta^*}\right)\theta\right] \end{aligned} \tag{5.31}$$

To determine R_n, S_n, we first decompose (5.11) into a Fourier series:

$$\psi_B = \hat{a}_0 + \sum_{n=1}^{N}\left[\hat{a}_n\cos n\varphi + \hat{b}_n\sin n\varphi\right], \tag{5.32}$$

noting that $\hat{a}_0 = 0$. Then

$$Z_n(\theta_B) \equiv \hat{Z}_n = \hat{a}_n + i\hat{b}_n, \tag{5.33}$$

where

$$\left.\begin{aligned} \hat{a}_n &= \frac{1}{\pi}\int_0^{2\pi}\psi_B\cos(n\varphi)\,\mathrm{d}\varphi, \\ &= 0 \\ \hat{b}_n &= \frac{1}{\pi}\int_0^{2\pi}\psi_B\sin(n\varphi)\,\mathrm{d}\varphi, \\ &= \frac{2\psi_B}{\pi n^2\epsilon}\sin(n\varphi)\left(1 - \cos(n\pi)\right) \end{aligned}\right\} \quad n \geq 1 \tag{5.34a}$$

At the pole Z_n satisfies (5.13) which yields

$$Z_n = 0 \qquad \text{at} \qquad \theta = 0, \tag{5.35}$$

Application of (5.33) and (5.35) yields

$$0 = R_n + S_n + \alpha_{1n} + \alpha_{2n} + \alpha_{3n} \tag{5.36a}$$

$$\begin{aligned} \hat{Z}_n = {} & R_n e^{\lambda_1 \theta_B} + S_n e^{\lambda_1 \theta_B} + \alpha_{1n} \cos\left(\pi \frac{\theta_B}{\theta^*}\right) + \beta_{1n} \sin\left(\pi \frac{\theta_B}{\theta^*}\right) \\ & + \alpha_{2n} \cos\left[\left(2 + \frac{\pi}{\theta^*}\right)\theta_B\right] + \beta_{2n} \sin\left[\left(2 + \frac{\pi}{\theta^*}\right)\theta_B\right] \\ & + \alpha_{3n} \cos\left[\left(2 - \frac{\pi}{\theta^*}\right)\theta_B\right] + \beta_{3n} \sin\left[\left(2 - \frac{\pi}{\theta^*}\right)\theta_B\right] \end{aligned} \tag{5.36b}$$

Turning to $a_0(\theta)$ we note that the solution of (5.17b) will be of the form $a_0 \equiv a_0(\theta)$ which corresponds to a "swirling flow" (i.e. the $\hat{\boldsymbol{\varphi}}$–direction) independent of longitude. Now across the gaps the Sverdrup balance is imposing inflow/outflow in the "$\hat{\boldsymbol{\theta}}$–direction". Across the gaps there is no circulation component in the "$\hat{\boldsymbol{\varphi}}$–direction" and therefore $a_0(\theta) \equiv 0$.

Note that (5.36) is a system of linear algebraic equations for the coefficients R_n, S_n. Using a MATLAB script (see Appendix) it is straightforward to solve (5.36). Then, we obtain $\psi(\varphi, \theta)$ from (5.14) using the coefficients a_n and b_n that are computed from (5.31). Using the basin parameters in Table 5.2, we noted that $\psi(\varphi, \theta)$ converges relatively fast giving a smooth behaviour with $N = 50$. Figure 5.4 (a) displays the relative error between $\psi(\varphi, \theta)$ using $N = 50$ and $N = 300$. We note that the relative error is not bigger than 0.1% or in streamfunction units 0.001 Sv. However, increasing to $N = 150$, we obtain a relative error of 0.001% or 10^{-5} Sv (see Figure 5.4 (b)).

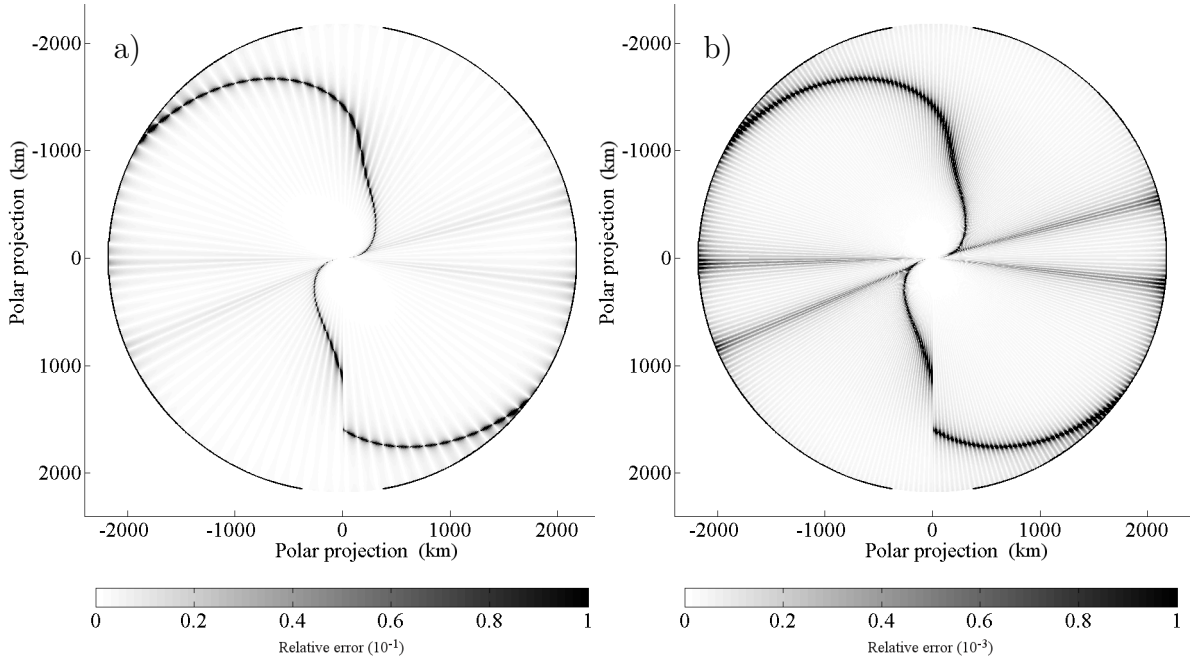

Figure 5.4: Convergence of the Fourier series (5.14) expressed in relative error. a) $|\psi(\varphi,\theta)_{50} - \psi(\varphi,\theta)_{300}|/\psi(\varphi,\theta)_{300}$ expressed in percentage; b) $|\psi(\varphi,\theta)_{150} - \psi(\varphi,\theta)_{300}|/\psi(\varphi,\theta)_{300}$ expressed in percentage.

Table 5.2: Parameter values used to calculate the wind–driven circulation.

Symbol	Variable(Unit)	Value
τ_0	Magnitude of the wind stress (Nm^{-2})	0.1
R	Radius of the Earth (m)	6.37×10^6
θ^*	Angle that controls the meridional structure of the curl$(radians)$	$2\pi/9$
ρ	Density $(kg\ m^{-3})$	1025
H	Depth (m)	1000
H_1	Step shelf depth (m)	250
H_2	Deep basin (m)	1000
μ	Control value of bottom friction (ms^{-1})	10^{-4}
2ϵ	Source-sink gap size $(radians)$	$\pi/9$
2δ	Wind stress curl transition region size $(radians)$	$\pi/9$
θ_B	Co-latitude at the boundary $(radians)$	$\pi/9$
θ_f	Fixed co-latitude in the coefficients of the governing PDEs $(radians)$	$\pi/18$
θ_S	Co-latitude at the shelf edge $(radians)$	$\pi/18$

Figure 5.5 (a) shows the contour plot of the streamfunction (5.14) using $N = 150$. The flow circulation is characterised by two gyres; cyclonic and anticyclonic. Both gyres are separated by a circulation which connects the inlet (top gap) with the outlet (bottom gap). The value $\theta* = 2\pi/9$ produces the maximum Sverdrup driven transport through the straits, as seen in Figure 5.5 (b). The sense of the circulation can be easily obtained from Figure 5.5 (b) and the Sverdrup balance (5.8). Noting that $\sin(\pi\theta_B/\theta) > 0$ at the boundary, the transport across the top and bottom gap is negative (inflow) and positive (outflow), respectively. The inflow is deflected to the right forming a strong boundary current, then it spreads and flows following the limit of the counter–rotating gyres. Once the flow reaches the bottom part of the domain, it is deflected again to the right forming another boundary current before exiting the domain.

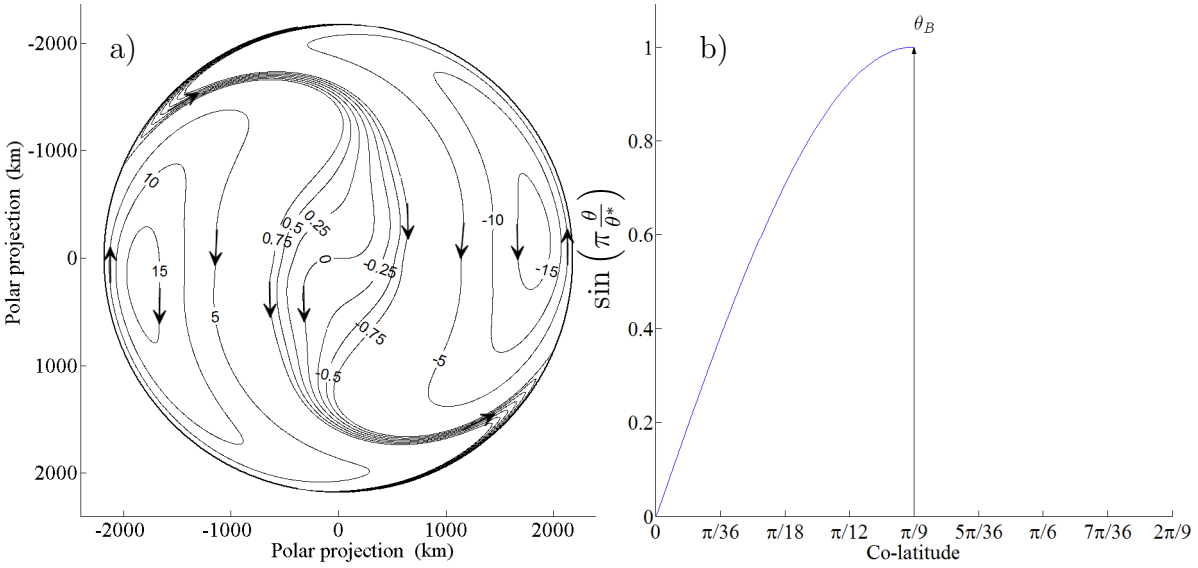

Figure 5.5: Planetary geostrophic circulation driven by the wind stress curl (5.9) in a) a flat bottom domain where the contour labels are in units of Sverdrups; b) plot of meridional variation of the wind stress curl, $\sin(\pi\theta/\theta^*)$, when $\theta^* = 2\pi/9$.

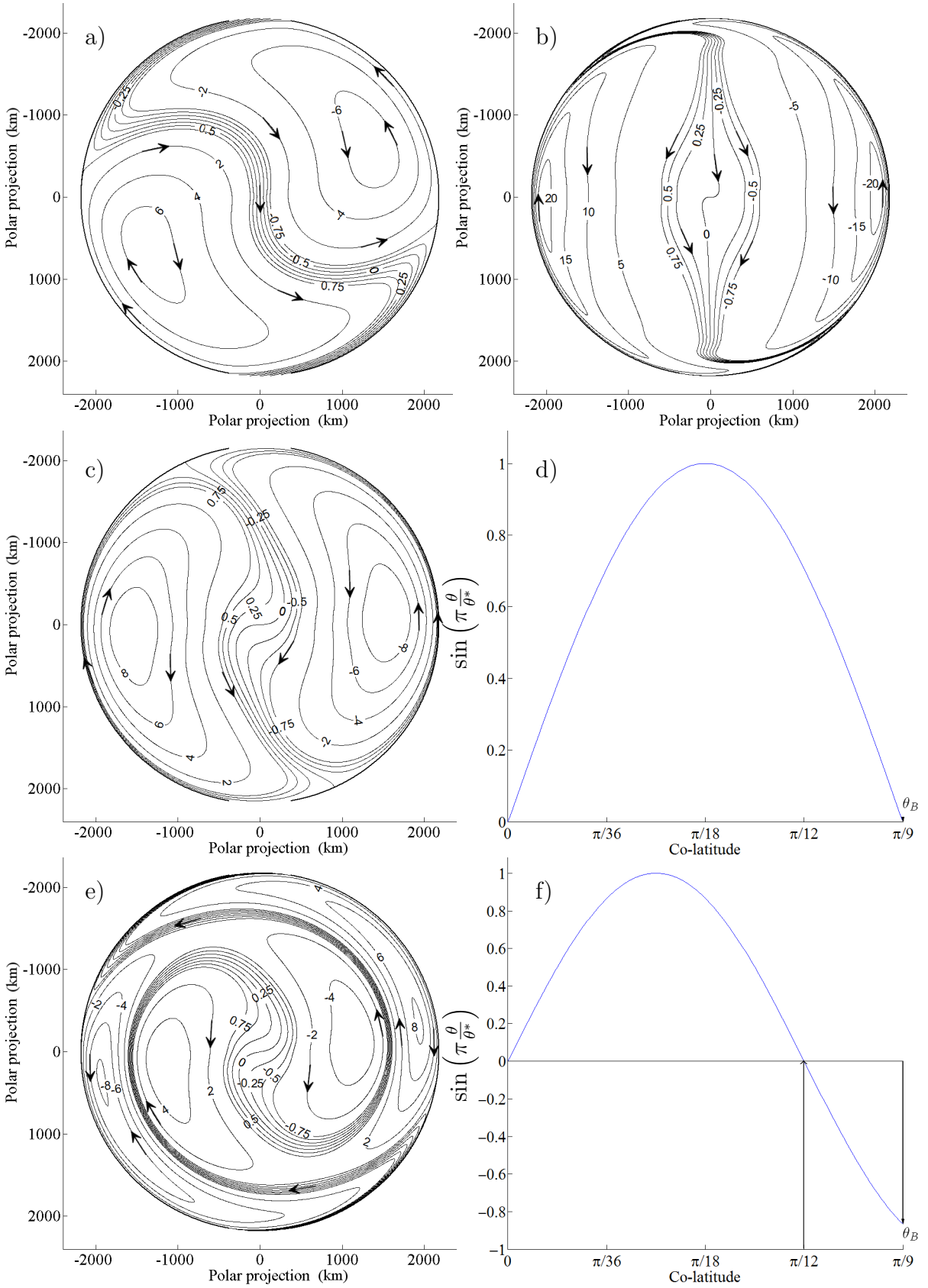

Figure 5.6: As in Figure 5.5 except, a) $\mu = 10^{-3}\ ms^{-1}$; b) $\mu = 10^{-5}\ ms^{-1}$; c) ocean circulation when $\theta^* = \pi/9$; d) Meridional variation of the wind stress curl, $\sin(\pi\theta/\theta^*)$, for $\theta^* = \pi/9$; e) ocean circulation when $\theta^* = \pi/12$, resulting in four gyres; f) same as (d) except for $\theta^* = \pi/12$. The contour labels are in units of Sverdrups.

The effect of the magnitude of the bottom friction on the circulation is studied in Figure 5.6 (a) and (b). The Figure 5.6 (a) shows the contour plot of the streamfunction computed from (5.14) using the ocean parameters from Table 5.2 and a linear bottom friction coefficient $\mu = 10^{-3}\ ms^{-1}$, whereas in Figure 5.6 (b), $\mu = 10^{-5}\ ms^{-1}$. Higher values of bottom friction rotate the counter–rotating gyres while lower values have the opposite effect. This rotation can be explained by the Sverdrup balance. When bottom friction is small (Figure 5.6 (b)) the flow is inviscid except in the frictional boundary layer adjacent to $\theta = \theta_B$. Thus, on the basin diameter defined by $\varphi = \pi/2$ and $\varphi = 3\pi/2$ the Sverdrup balance (5.8) requires $\psi_\varphi = 0$, except in the frictional boundary layer adjacent to $\theta = \theta_B$. Thus, $v = 0$ on this diameter and the streamlines are therefore orthogonal to this diameter.

As shown previously, the flow across the straits is given by (5.11) where the magnitude and direction of the inflow and outflow can be altered by the value of θ^* which controls the meridional structure of the wind stress curl (5.9). Figure 5.6 (c) and (e) display the streamfunction calculated from (5.14) using $\theta^* = \pi/9$ and $\theta^* = \pi/12$, respectively. The other basin parameters are given in Table 5.2. When $\theta^* = \pi/9$, the wind stress curl vanishes at the boundary (see Figure 5.6 (d)). Therefore, there is no Sverdrup driven transport through the straits which is clearly seen in Figure 5.6 (c). Figure 5.6 (e) displays a source–sink wind–driven circulation with four cells. Here, the formation of a second pair of gyres in the basin is a consequence of the meridional change of sign in the wind stress curl (see Figure 5.6 (f)). Also, we notice that the inflow and outflow have reversed positions due to the change of sign of (5.12) at the boundary.

Figure 5.7 (a) and (b) investigate how the circulation depends on the solid–body rotation of the wind stress curl field. Figure 5.7 (a) shows the contour plot of the streamfunction (5.14) using $\hat{\varphi}_1 = 3\pi/4$ and $\hat{\varphi}_2 = 7\pi/4$ in (5.10). Once again, we keep the other parameters as in Figure 5.5. Notice that the centre of the gyres have been rotated counter–clockwise generating strong boundary current in the inflow and outflow. The opposite scenario is given in Figure 5.7 (b) where $\hat{\varphi}_1 = \pi/4$ and $\hat{\varphi}_2 = 5\pi/4$. Here, the centre of the cells rotate clockwise positioning close to the gap from the opposite sign. We can see that the inflow is deflected to the left crossing the centre of the basin and turning to the left again before exiting the domain.

The sensitivity of the solution to a change in the value of the fixed co–latitude θ_f is addressed in Figure 5.8 where $\theta_f = \pi/9$. Comparison with the control solution in Figure 5.5, reveals that the counter–rotating gyres are weaker in Figure 5.8. Also, the

inlet–outlet cross–basin current is more diffusive. This aspect will be again investigated in Chapter 6 where NEMO will be employed to perform the equivalent scenario. In fact, we will observe that $\theta_f = \pi/9$ reproduces a more realistic representation of wind-driven circulation.

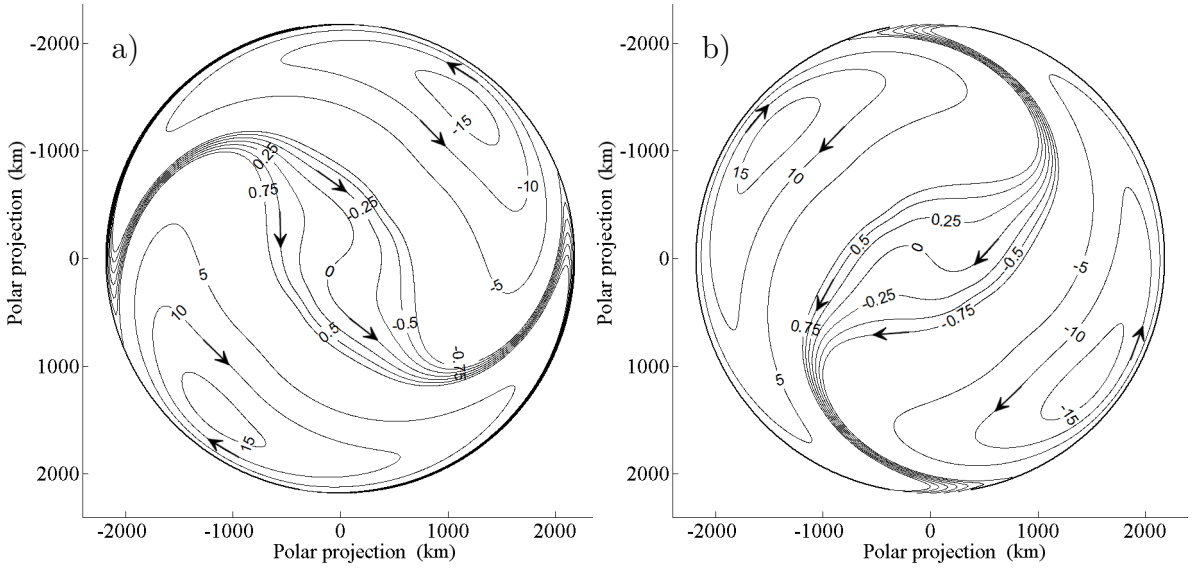

Figure 5.7: Planetary geostrophic circulation driven by the wind stress curl; a) wind–stress curl with $\hat{\varphi}_1 = 3\pi/4$ and $\hat{\varphi}_2 = 7\pi/4$; b) wind–stress curl with $\hat{\varphi}_1 = \pi/4$ and $\hat{\varphi}_2 = 5\pi/4$. The contour labels are in units of Sverdrups.

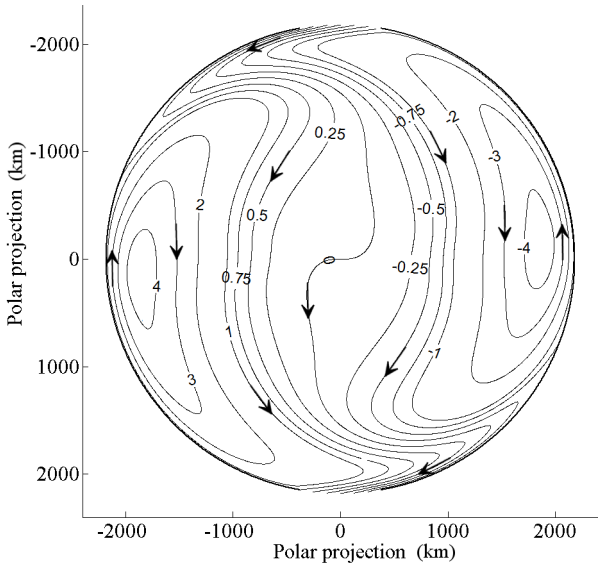

Figure 5.8: Planetary geostrophic circulation driven by the wind stress curl (5.9) when $\theta_f = \pi/9$. The contour labels are in units of Sverdrups.

5.2.2 Step shelf

The method of solution in the previous section can be extended to a polar basin with a uniform width step-shelf shown schematically in Figure 5.9. The topography is given by

$$H(\theta) = \begin{cases} H_1 & \text{if } \theta_S \le \theta \le \theta_B, \\ H_2 & \text{if } 0 \le \theta \le \theta_S, \end{cases} \tag{5.37}$$

where $H_1 < H_2$.

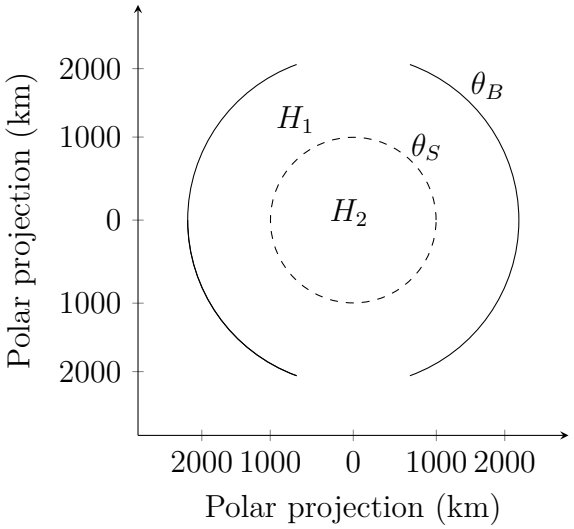

Figure 5.9: Schematic of a basin with a step-shelf and two straits.

Let $\psi_1(\varphi, \theta)$ and $\psi_2(\varphi, \theta)$ denote the streamfunction on the shelf $\theta_S \le \theta \le \theta_B$ and in the deep basin $0 \le \theta \le \theta_S$, respectively. On the shelf and in the deep basin the vorticity equation takes the form

$$\psi_{1\varphi\varphi} + A\psi_{1\theta\theta} + B\psi_{1\theta} + C_1\psi_{1\varphi} = \frac{R^2 H_1 \sin^2\theta\{\underline{k}\cdot\nabla\times\underline{\tau}/\rho\}}{\mu}, \tag{5.38a}$$

$$\psi_{2\varphi\varphi} + A\psi_{2\theta\theta} + B\psi_{2\theta} + C_2\psi_{2\varphi} = \frac{R^2 H_2 \sin^2\theta\{\underline{k}\cdot\nabla\times\underline{\tau}/\rho\}}{\mu}, \tag{5.38b}$$

where

$$C_j \equiv 2\Omega H_j \mu^{-1}\sin^2\theta, \qquad (j = 1, 2).$$

As in the flat bottom solution, ψ_2 must satisfy boundary condition (5.13) and ψ_1 must satisfy boundary condition (5.11). At the shelf edge we demand continuity of the meridional transport and pressure. The former matching condition is satisfied provided

$$\psi_1 = \psi_2 \quad \text{at} \quad \theta = \theta_S. \tag{5.39}$$

Using (5.1), the latter matching condition requires that

$$\left[fv + \mu \frac{u}{H} - \frac{\tau^{\varphi}}{\rho H} \right] = 0, \quad \text{at} \quad \theta = \theta_S. \tag{5.40}$$

Notice that the introduction of the step-shelf gives rise to the presence of the azimuthal wind stress component $\tau^{\varphi}(\varphi, \theta)$ in (5.40). Since the wind stress patterns in the Arctic Ocean are predominantly anticlockwise or clockwise (Proshutinsky and Johnson, 1997), we can hypothesise that the wind stress curl (5.9) is associated with a purely azimuthal wind stress in which case

$$\frac{(\sin\theta\tau^{\varphi})_{\theta}}{\rho R \sin\theta} = \sin\left(\frac{\pi\theta}{\theta^*}\right) W(\varphi).$$

Upon integrating with respect to θ we obtain

$$\tau^{\varphi} \sin\theta = \int \rho R \sin\theta \sin\left(\pi \frac{\theta}{\theta^*}\right) W(\varphi)\, \mathrm{d}\theta. \tag{5.41}$$

Expanding the integrand in (5.41) yields

$$\tau^{\varphi} = \frac{R\rho W(\varphi)}{\sin\theta} \int \frac{1}{2} \left(\cos\left(\theta - \frac{\pi\theta}{\theta^*}\right) - \cos\left(\theta + \frac{\pi\theta}{\theta^*}\right) \right) \mathrm{d}\theta \tag{5.42}$$

which allows (5.42) to be evaluated to yield

$$\tau^{\varphi}(\varphi, \theta) = \frac{\rho R W(\varphi)}{2\sin\theta} \left[\frac{\sin\left(\theta - \frac{\pi\theta}{\theta^*}\right)}{(1 - \pi/\theta^*)} - \frac{\sin\left(\theta + \frac{\pi\theta}{\theta^*}\right)}{(1 + \pi/\theta^*)} \right]. \tag{5.43}$$

Figure 5.10 shows a plot of the azimuthal wind stress field given by (5.43) using the parameters of Table 5.2.

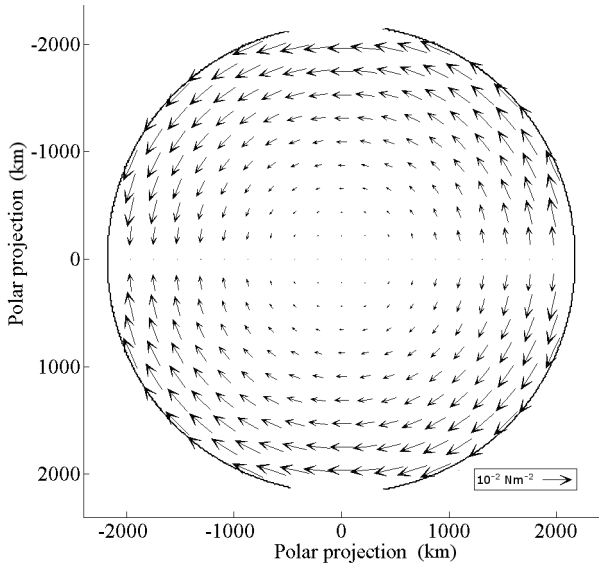

Figure 5.10: Plot of the azimuthal wind stress vectors given by (5.43).

Now we rewrite (5.40) in terms of ψ:

$$\left[-\frac{f}{HR\sin\theta}\frac{\partial\psi}{\partial\varphi}+\frac{\mu}{H^2R}\frac{\partial\psi}{\partial\theta}-\frac{\tau^{\varphi}}{\rho H}\right]=0,\quad \text{at}\quad \theta=\theta_S, \tag{5.44}$$

Expanding this jump condition yields

$$\frac{f}{RH_1\sin\theta}\psi_{1\varphi}+\frac{\mu}{H_1^2R}\psi_{1\theta}-\frac{\tau^{\varphi}}{\rho H_1}=\frac{f}{RH_2\sin\theta}\psi_{2\varphi}+\frac{\mu}{H_2^2R}\psi_{2\theta}-\frac{\tau^{\varphi}}{\rho H_2},\quad \text{at}\quad \theta=\theta_S, \tag{5.45}$$

We multiply (5.45) by RH_1^2 to obtain

$$\frac{-fH_1\psi_{1\varphi}}{\sin\theta}+\mu\psi_{1\theta}-\frac{RH_1\tau^{\varphi}}{\rho}=\frac{-fH_1^2\psi_{2\varphi}}{H_2\sin\theta}+\frac{\mu H_1^2\psi_{2\theta}}{H_2^2}-\frac{RH_1^2\tau^{\varphi}}{\rho H_2},\quad \text{at}\quad \theta=\theta_S, \tag{5.46}$$

Once again, we seek solutions of (5.38) of the form

$$\psi_1(\varphi,\theta)=a_0(\theta)+\sum_{n=1}^{N}\left[a_n(\theta)\cos n\varphi+b_n(\theta)\sin n\varphi\right], \tag{5.47a}$$

$$\psi_2(\varphi,\theta)=A_0(\theta)+\sum_{n=1}^{N}\left[A_n(\theta)\cos n\varphi+B_n(\theta)\sin n\varphi\right], \tag{5.47b}$$

where the coefficients a_n, b_n, A_n and B_n are self-contained within each subsection (i.e. a_n's are distinct from those in the previous solution). Substituting (5.47) into (5.46) and collecting the coefficients of $\cos(\theta)$ and $\sin(\theta)$ we obtain

$$\begin{aligned}&-\frac{H_1f_S}{\sin\theta_S}nb_n+\mu\dot{a}_n-\frac{H_1R^2p_n}{2\sin\theta_S}\left(\frac{\sin\left(\theta_S-\pi\frac{\theta_S}{\theta^*}\right)}{\left(1-\frac{\pi}{\theta^*}\right)}-\frac{\sin\left(\theta_S+\pi\frac{\theta_S}{\theta^*}\right)}{\left(1+\frac{\pi}{\theta^*}\right)}\right)=\\&-\frac{H_1\hat{s}f_S}{\sin\theta_S}nB_n+\hat{s}^2\mu\dot{A}_n-\frac{\hat{s}H_1R^2p_n}{2\sin\theta_S}\left(\frac{\sin\left(\theta_S-\pi\frac{\theta_s}{\theta^*}\right)}{\left(1-\frac{\pi}{\theta^*}\right)}-\frac{\sin\left(\theta_S+\pi\frac{\theta_S}{\theta^*}\right)}{\left(1+\frac{\pi}{\theta^*}\right)}\right)\quad n\geq 1\end{aligned} \tag{5.48a}$$

$$\begin{aligned}&\frac{H_1f_S}{\sin\theta_S}na_n+\mu\dot{b}_n-\frac{H_1R^2q_n}{2\sin\theta_S}\left(\frac{\sin\left(\theta_S-\pi\frac{\theta_S}{\theta^*}\right)}{\left(1-\frac{\pi}{\theta^*}\right)}-\frac{\sin\left(\theta_S+\pi\frac{\theta_S}{\theta^*}\right)}{\left(1+\frac{\pi}{\theta^*}\right)}\right)=\\&\frac{H_1\hat{s}f_S}{\sin\theta_S}nA_n+\hat{s}^2\mu\dot{B}_n-\frac{\hat{s}H_1R^2q_n}{2\sin\theta_S}\left(\frac{\sin\left(\theta_s-\pi\frac{\theta_S}{\theta^*}\right)}{\left(1-\frac{\pi}{\theta^*}\right)}-\frac{\sin\left(\theta_S+\pi\frac{\theta_S}{\theta^*}\right)}{\left(1+\frac{\pi}{\theta^*}\right)}\right)\quad n\geq 1\end{aligned} \tag{5.48b}$$

$$\begin{aligned}&\mu\dot{a}_0-\frac{H_1R^2p_0}{2\sin\theta_S}\left(\frac{\sin\left(\theta_S-\pi\frac{\theta_S}{\theta^*}\right)}{\left(1-\frac{\pi}{\theta^*}\right)}-\frac{\sin\left(\theta_S+\pi\frac{\theta_S}{\theta^*}\right)}{\left(1+\frac{\pi}{\theta^*}\right)}\right)=\\&\hat{s}^2\mu\dot{A}_0-\frac{\hat{s}H_1R^2p_0}{2\sin\theta_S}\left(\frac{\sin\left(\theta_s-\pi\frac{\theta_s}{\theta^*}\right)}{\left(1-\frac{\pi}{\theta^*}\right)}-\frac{\sin\left(\theta_S+\pi\frac{\theta_S}{\theta^*}\right)}{\left(1+\frac{\pi}{\theta^*}\right)}\right)\end{aligned} \tag{5.48c}$$

where $\hat{s}=H_1/H_2$, $f_S=2\Omega\cos\theta_S$ and p_n, q_n are given by (5.16).

Let

$$z_n = a_n + ib_n, \quad Z_n = A_n + iB_n, \quad \text{and} \quad W_n = p_n + iq_n \quad n \geq 1,$$

In terms of these complex functions (5.48) take the form

$$\begin{aligned} &\frac{H_1 f_S}{\sin\theta_S} in z_n + \mu \dot{z}_n - \frac{H_1 R^2 W_n \Theta(\theta_S)}{2\sin\theta_S} = \\ &\frac{H_1 \hat{s} f_S}{\sin\theta_S} in Z_n + \hat{s}^2 \mu \dot{Z}_n - \frac{\hat{s} H_1 R^2 W_n \Theta(\theta_S)}{2\sin\theta_S}, \quad \text{at} \quad \theta = \theta_S \quad n \geq 1 \end{aligned} \tag{5.49}$$

where Θ is defined by

$$\Theta(\theta) \equiv \left[\frac{\sin\left(\theta\left(1 - \frac{\pi}{\theta^*}\right)\right)}{(1 - \pi/\theta^*)} - \frac{\sin\left(\theta\left(1 + \frac{\pi}{\theta^*}\right)\right)}{(1 + \pi/\theta^*)} \right]. \tag{5.50}$$

Now z_n satisfies (5.19) with C replaced by C_1. Similarly Z_n satisfies (5.19) with C replaced by C_2. Their general solutions are given

$$z_n = f_n e^{\lambda_1 \theta} + g_n e^{\lambda_2 \theta} + z_{nPI}, \tag{5.51a}$$

$$Z_n = F_n e^{\omega_1 \theta} + G_n e^{\omega_2 \theta} + Z_{nPI}, \tag{5.51b}$$

where λ_1, λ_2, ω_1 and ω_2 are given by (5.23) noting that C is substituted by C_1 and C_2 forλ_1, λ_2 and ω_1, ω_2, respectively. The particular integrals z_{nPI} and Z_{nPI} have the same form as (5.25) noting that H and C in α_{jn} and β_{jn} for $(j = 1..3)$ are replaced by H_1 and C_1 in the step-shelf and by H_2 and C_2 in the deep basin.

The coefficients f_n, g_n, F_n and G_n are to be determined by applying boundary and matching conditions. Application of (5.13), (5.11) and (5.49) yields:

$$F_n + G_n + Z_{nPI}(0) = 0 \tag{5.52a}$$

$$f_n e^{\lambda_1 \theta_B} + g_n e^{\lambda_2 \theta_B} + z_{nPI}(\theta_B) = \hat{z}_n \tag{5.52b}$$

$$f_n e^{\lambda_1 \theta_S} + g_n e^{\lambda_2 \theta_S} + z_{nPI}(\theta_S) = F_n e^{\omega_1 \theta_S} + G_n e^{\omega_2 \theta_S} + Z_{nPI}(\theta_S), \tag{5.52c}$$

$$\begin{aligned} &\left(\frac{H_1 f_S}{\sin\theta_S} in + \mu\lambda_1\right) f_n e^{\lambda_1 \theta_S} + \left(\frac{H_1 f_S}{\sin\theta_S} in + \mu\lambda_2\right) g_n e^{\lambda_2 \theta_S} + \frac{H_1 f_S}{\sin\theta_S} in z_{nPI}(\theta_S) + \mu \dot{z_{nPI}}(\theta_S) \\ &= \left(\frac{H_1 \hat{s} f_S}{\sin\theta_S} in + \mu\hat{s}^2\omega_1\right) F_n e^{\omega_1 \theta_S} + \left(\frac{H_1 \hat{s} f_S}{\sin\theta_S} in + \mu\hat{s}^2\omega_2\right) G_n e^{\omega_2 \theta_S} + \frac{H_1 \hat{s} f_S}{\sin\theta_S} in Z_{nPI}(\theta_S) \end{aligned} \tag{5.52d}$$

$$+ \mu\hat{s}^2 \dot{Z_{nPI}}(\theta_S) + \frac{H_1 R^2 W_n \Theta(\theta_S)}{2\sin\theta_S}(1 - \hat{s}).$$

It is straightforward to solve (5.52) for the coefficients f_n, g_n, F_n and G_n and subsequently we compute the coefficients a_n, A_n, b_n and B_n in (5.47) using (5.51). Note that the axi-symmetric swirling flow component associated with the coefficients a_0 and A_0 is again set to zero following the arguments in section 5.2.1. Equations (5.52) are a system of linear algebraic equations for the coefficients f_n, g_n, F_n and G_n. Using a MATLAB code it is straightforward to solve (5.52) by writing the equations in matrix form and then using *linsolve* algorithm as previously was done in Chapter 2. The model parameters used to obtain ψ_1 and ψ_2 are given in Table 5.2 unless otherwise stated. We use $N = 150$ in (5.47) for the reasons as given in 5.2.1.

Figure 5.11 shows contours of the streamfunction of (5.47). The shelf edge is shown by the dashed line. The ocean circulation is characterised by two strong counter–rotating cells on the step-shelf. The Sverdrup–driven flow enters the polar basin from the strait located on the top part of the domain and it flows between the two cells forming strong currents near the shelf edge. Subsequently, the water leaves the domain through the bottom gap. In the deep basin, there is a weak circulation decoupled from the step-shelf driven by the wind stress curl.

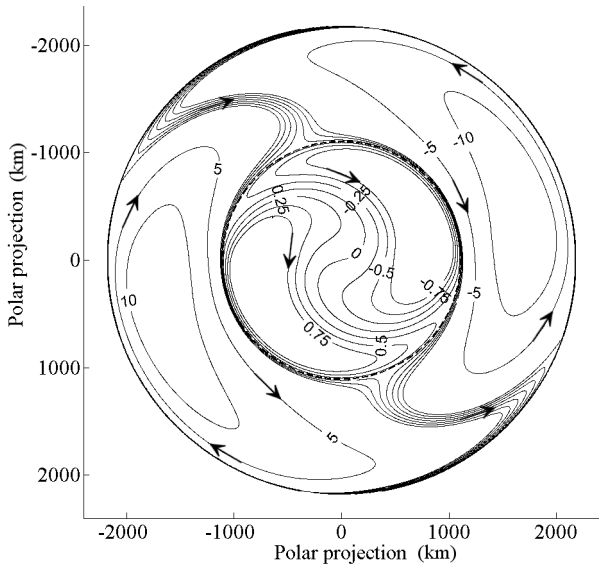

Figure 5.11: Steady wind–driven planetary geostrophic flow in a basin with a step-shelf and two straits. The contour labels are in units of Sverdrups.

The influence of the bottom friction on the circulation is studied in Figure 5.12 (a) and (b). As μ increases (see Figure 5.12(a)), both gyres migrate counter–clockwise as was previously shown in the flat bottom solutions. The circulation evolves to one which is almost symmetric above the diameter joining $\varphi = 0$ to $\varphi = \pi$ (i.e. joining the mid–points

of the two straits). On the other hand, lower values of μ (see Figure 5.12(b)) lead to a clockwise rotation of the cells placing their centres at $\varphi = \pi/2$ and $\varphi = 3\pi/2$ forming two symmetric cyclic circulations. The reason for this orientation of the cells was described earlier. The Sverdrup balance which now holds over most of the domain interior requires v to vanish along the line of zero wind stress curl. As a result, the gyres adopt an orientation such that the streamlines are orthogonal to the diameter joining $\varphi = \pi/2$ and $\varphi = 3\pi/2$. The deep basin circulation displays an increase in strength.

Figure 5.12(c) and 5.12(d) investigate varying the width of the shelf (equivalent to varying θ_S) on the circulation. Figure 5.12(c) shows a narrow step-shelf compared with Figure 5.11. On the step-shelf the gyres are compressed between the shelf edge and boundary wall producing larger gradients of the streamfunction. The deep basin displays an increase of ocean circulation strength. Figure 5.12(d) show a step-shelf where its width is thinner than the frictional boundary layer width. Here, the bottom friction was increased to $5\times10^{-4}\ ms^{-1}$ to ease the visualisation of the frictional boundary layer effect (as in Chapter 2). The frictional boundary layer for this polar basin, $W \sim (\mu/(H_1 2\Omega))^{1/2} R\sin\theta$, is approximately 255 km. On the shelf, the ocean circulation is dominated by frictional boundary currents whereas in the deep basin there are two counter–rotating gyres driven by a combination of the wind stress curl and the pressure gradient at the shelf edge.

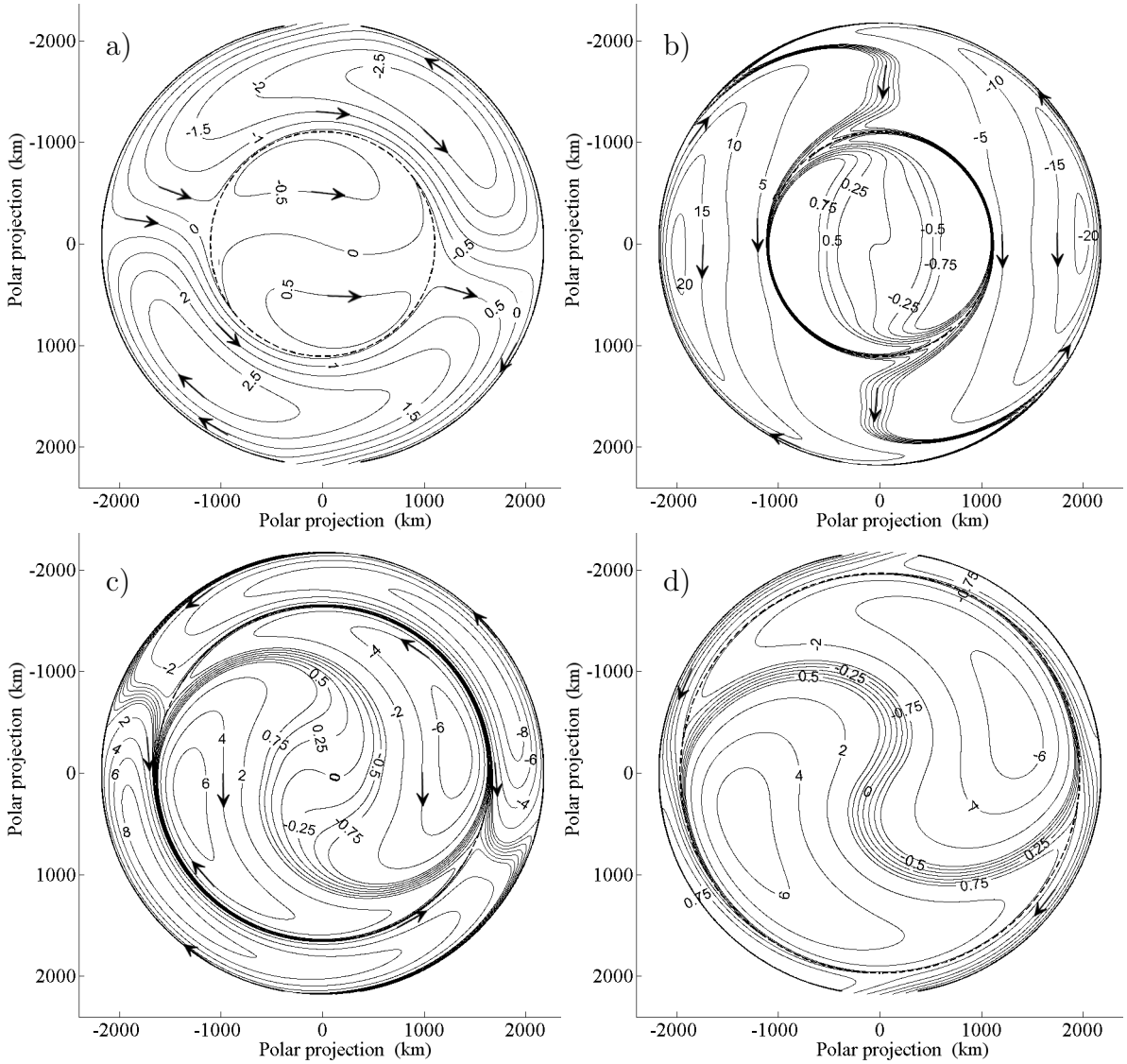

Figure 5.12: Steady wind–driven planetary geostrophic flow in a a basin with a step-shelf and two straits. a) bottom friction coefficient $\mu = 10^{-3}\ ms^{-1}$; b) bottom friction coefficient $\mu = 10^{-5}\ ms^{-1}$; c) step-shelf width approximately 500 km; d) step-shelf width approximately 200 km. The contour labels are in units of Sverdrups.

5.2.3 Integral constraints on the circulation in a basin with step-shelf

Using same method as in Chapter 2, we can further study the dynamics of the steady–state circulation shown in Figure 5.11 by integrating the curl of the momentum equation (5.1) over the deep basin.

$$\iint_S \nabla \times \left(f\hat{\boldsymbol{k}} \times \mathbf{u}\right) \cdot \mathrm{d}\boldsymbol{S} = -\frac{\mu}{H_2} \iint_S (\nabla \times \boldsymbol{u}) \cdot \mathrm{d}\boldsymbol{S} + \frac{1}{\rho H_2} \iint_S \nabla \times \boldsymbol{\tau} \cdot \mathrm{d}\boldsymbol{S}, \tag{5.53}$$

where ρ, H and μ are constants and $\mathrm{d}\boldsymbol{S} = \hat{\boldsymbol{k}}\,\mathrm{d}S$ is the area element (see Figure 2.13). Application of Stokes' theorem to left hand side of (5.53) yields

$$\iint_S \nabla \times \left(f\hat{\boldsymbol{k}} \times \mathbf{u}\right) \cdot \mathrm{d}\boldsymbol{S} = \oint_{\mathcal{C}} \left(f_S\hat{\boldsymbol{k}} \times \mathbf{u}\cdot\right) \mathrm{d}\boldsymbol{l}, \tag{5.54}$$

where $\mathrm{d}\boldsymbol{l} = \hat{\boldsymbol{\varphi}}\,\mathrm{d}l$. Substituting (5.54) in (5.53)

$$\oint_{\mathcal{C}} \left(f_S\hat{\boldsymbol{k}} \times \mathbf{u}\right) \cdot \mathrm{d}\boldsymbol{l} = -\frac{\mu}{H_2} \iint_S \nabla \times \boldsymbol{u} \cdot \mathrm{d}\boldsymbol{S} + \frac{1}{\rho H_2} \iint_S \nabla \times \boldsymbol{\tau} \cdot \mathrm{d}\boldsymbol{S}. \tag{5.55}$$

Upon using commutativity of the scalar and triple product, (5.55) can be re–arranged

$$\oint_{\mathcal{C}} \mathbf{u} \cdot \left(\hat{\boldsymbol{\varphi}} \times f_S\hat{\boldsymbol{k}}\right) \mathrm{d}l = -\frac{\mu}{H_2} \iint_S (\nabla \times \boldsymbol{u}) \cdot \hat{\boldsymbol{k}}\,\mathrm{d}S + \frac{1}{\rho H_2} \iint_S (\nabla \times \boldsymbol{\tau}) \cdot \hat{\boldsymbol{k}}\,\mathrm{d}S. \tag{5.56}$$

Noting that $\left(\hat{\boldsymbol{\varphi}} \times \hat{\boldsymbol{k}}\right) = \hat{\boldsymbol{\theta}}$ and $(\nabla \times \boldsymbol{u})\cdot\hat{\boldsymbol{k}}$ is the vertical component of the relative vorticity. (5.56) can be re-written

$$\oint_{\mathcal{C}} f_S\mathbf{u} \cdot \hat{\boldsymbol{\theta}}\,\mathrm{d}l = -\frac{\mu}{H_2} \iint_S \xi\,\mathrm{d}S + \frac{1}{\rho H_2} \iint_S (\nabla \times \boldsymbol{\tau}) \cdot \hat{\boldsymbol{k}}\,\mathrm{d}S. \tag{5.57}$$

Finally, noting that $\mathbf{u} \cdot \hat{\boldsymbol{\theta}}$ is the velocity component in the meridional direction (i.e. v, normal to the shelf break) (5.57) becomes

$$f_S \oint_{\mathcal{C}} v\,\mathrm{d}l = -\frac{\mu}{H_2} \iint_S \xi\,\mathrm{d}S + \frac{1}{\rho H_2} \iint_S (\nabla \times \boldsymbol{\tau}) \cdot \hat{\boldsymbol{k}}\,\mathrm{d}S. \quad \theta = \theta_S \tag{5.58}$$

In the steady state $\oint_{\mathcal{C}} v\,\mathrm{d}l = 0$ (otherwise, the deep basin will empty or fill), thus the surface integral of the relative vorticity in the deep basin has to be cancelled by the surface integral of the wind curl. Upon knowing that the surface integral of the wind curl is equal to zero, the surface integral of the relative vorticity has to be also equal to zero. This can be seen in Figure 5.11 where relative vorticity associated to the circulation in one part is cancelled by the opposite part of the deep basin.

5.3 Conclusion

The thrust of this chapter was to develop an analytical approach to solve steady, barotropic planetary geostrophic flow driven by two opposite signed wind stress curl gyres in a polar basin with two diametrically opposed straits using the mathematical methods introduced in Chapter 2. The analytical model developed in this chapter is an extension of the one that is used in Chapter 2. Here, the transport across the straits is determined by Sverdrup balance.

In the flat bottom basin, we observed two counter–rotating gyres which are separated by a cross–basin current connecting the inflow to the outflow strait. The flow enters the basin from the top and is forced to circulate between the cyclonic and anticyclonic gyres crossing the centre of the domain. Subsequently, the water exits through the bottom strait. Higher values of bottom friction rotate the ocean gyres counter clockwise whereas lower values locate the centre of the ocean gyres in the diameter of the zero wind stress curl. These solutions are qualitatively similar to Willmott and Luneva (2015) in a closed basin where two counterrotating ocean gyres were present. In addition, we saw a strong transpolar current connecting the source with the sink. It is interesting to observe the strong impact of the θ_f in (5.7) compared with the Chapter 2. In Chapter 2 we saw little sensitivity between the solutions when we varied θ_f in (2.10). However, in this chapter we observed the strength of the gyres was greatly diminished when $\theta_f = \pi/9$. This will be further investigated in Chapter 6, where the NEMO ocean circulation model is used to study wind–driven circulation in a variety of polar basins.

The addition of a step-shelf, adding an extra degree of realism (and of course, complexity in the analysis) into the model is also considered in this chapter. The circulation is characterised by 4 gyres; two on the step-shelf and two in the deep basin which its total relative vorticity vanished as it was proved by the constraint analysis. Also the counter–rotating cells force the flow to cross the domain forming two boundary currents near the shelf edge. In general the step-shelf circulation is stronger than the deep basin circulation. However, this structure varied when the shelf width was smaller than the frictional boundary layer width. The ocean gyres on the step-shelf vanished forming boundary currents whereas the deep basin circulation is driven by two ocean gyres.

The solutions presented in this chapter only address simple shelf topography whereas in Chapter 6 we will use the numerical model NEMO to investigate more complex, and realistic, scenarios.

Chapter 6

Wind–driven planetary flows in a polar basin; numerical experiments

6.1 Introduction

In Chapter 5 we obtained approximate analytical solutions for wind–driven steady, barotropic, planetary flow circulation using the "beta sphere" approximation. Here, we use the "community" NEMO ocean model to consider wind–driven circulation in polar basins with more realistic topography; problems which cannot be solved analytically.

As pointed out in the introduction, the wind stress is one of the forcing mechanisms that drives the barotropic circulation in the Arctic Ocean. In fact, Aksenov *et al.* (2016) showed how the pathway of the Bering inflow into Arctic basin varies depending on the wind stress regime, albeit in a numerical ocean model that includes stratification. In a series of papers (Proshutinsky and Johnson, 1997; Proshutinsky *et al.*, 2002) the case is made for the wind stress being the dominating factor in driving the barotropic ocean circulation in the Arctic. This hypothesis is supported in a one–dimensional baroclinic idealised multi–box ocean–atmospheric–ice coupled model which includes the central Arctic and the GINs (Dukhovskoy *et al.*, 2006). Even though this simple mechanistic model does not include a realistic representation of the Arctic basin, nevertheless it explains the ocean thermodynamic mechanisms which control the periodicity of wind stress regimes observed by Proshutinsky and Johnson (1997). It is intriguing that such a simplistic model can explain a complex relationship between ocean and atmosphere. Another idealised study by Sugimura (2008) explores the influence of different wind stress regimes on source–sink boundary circulation in a circular polar basin. These experiments were an extension of

the source–sink numerical experiments by Yang (2005). In addition, Sugimura (2008) evaluates the impact of a ridge with different orientations on the wind–driven circulation.

More recently, there are several studies about the dynamics of the Beaufort Gyre due to an anomalous trapping of the freshwater storage (Rabe *et al.*, 2014). Yang *et al.* (2016) studied the potential vorticity balance in the Beaufort Gyre. They argued that the lack of $\beta-$gradient, or meridional gradient of the Coriolis parameter, in the Arctic basin produces an imbalance in the potential vorticity field. Thus, an anticyclonic wind–driven circulation was forced on a idealised bowl–shape polar basin using a baroclinic wind–driven nonlinear ocean model on a $\beta-$plane. Yang *et al.* (2016) observed the importance of baroclinic eddies in the spinning–up. Furthermore, the impact of vorticity associated baroclinic eddies in the PV balance was more significant than the vorticity formed by the $\beta-$gradient. Although Yang *et al.* (2016) found that the effect of the baroclinic eddies in the PV balance decreases in the presence of topography walls such as ridges or meridional boundaries. Similar experiments in the presence of anticyclonic wind stress in a closed polar basin performed by Manucharyan and Spall (2016) suggested that the mesoscale eddy dynamics control the adjustment of the Beaufort Gyre.

In chapter 4 we briefly considered numerical coupled ocean–ice model simulations driven by boundary flows. In these experiments sea ice thermodynamics were suppressed. Numerical studies that utilise a dynamical sea ice model are relatively uncommon in the referred literature, being focused mainly on "process studies" (Morland and Staroszczyk, 1998). There are several numerical studies that address how the sea ice modifies the shear stress acting in the sea ice–ocean system. At one extreme if the sea ice is land–fast and rigid it "shields" the underlying ocean from the wind stress. Martin *et al.* (2014) used a coupled ocean–ice model, PIOMAS, to study the impact of the sea ice in the transference of momentum between the atmosphere and the ocean. The study showed that in the presence of winter land–fast ice, the wind stress is greatly diminished to the ocean whereas in summer the opposite happens. Davis *et al.* (2014) also studies the influence of the sea ice in the effective wind stress on the ocean. Davis *et al.* (2014) used a baroclinic ocean model in a idealised circular polar basin with one strait. In these experiments they used an anticyclonic wind stress regime with two different magnitudes to simulate the effect of the sea ice stress during the year. Their results suggested that the decline of sea ice in the Arctic basin is strengthening the Beaufort Gyre by enhancing the wind stress effect in the ocean.

Here, we first compare the analytic solutions of Chapter 5 with their equivalent numer-

ically derived counterparts using the NEMO modelling system. Secondly, we numerically determine the steady planetary geostrophic circulation in a polar basin with more realistic Arctic topography, such as a step–shelf with a "top–hat" transpolar ridge. Thirdly, we introduce more realistic representations of the Arctic basin wind stress in the aforementioned numerical experiments with a view to capturing the dominant features of the observed surface circulation in this basin. Finally, we study the impact of the sea ice on a wind–driven circulation in a closed polar basin.

6.2 NEMO model description

We consider numerical solutions of a barotropic ocean in a circular polar basin driven by steady wind stress fields. The numerical simulations use the nonlinear three-dimensional ocean circulation model NEMO (Madec, 2008). As mentioned in Chapter 4, we use a filtered non-linear free surface algorithm for same reasons as in Chapter 4. Three basin configurations will be used; (a) uniform depth; (b) step–shelf and (c) step–shelf with a transpolar top–hat ridge. The first series of the numerical experiments discussed in this chapter are the analogues of the analytical problems discussed in Chapter 5. Thus, we can assess the ability of the NEMO model to reproduce wind–driven planetary geostrophic flows in a polar basin.

The computational domain is a circular polar basin with two diametrically opposed straits (Figure 4.1). The North Pole is located in the centre of the grid. The horizontal resolution is $0.1^o \times 0.1^o$ which can be easily set in *namelist_cgf* file from NEMO. The Coriolis parameter was calibrated following the same approach as in Chapter 4.

The configuration of the bathymetry and the vertical resolution follow the same approach as in Chapter 4. Therefore, we use the same algorithm to reproduce the bathymetries of Figure 6.1 using the ocean basin parameters in Table 4.1. The vertical levels, coordinates and resolution are set in the sections *namcfg*, *namzgr*, *namdom* of *namelist_cfg*. All the simulations were performed using z-coordinates with uniform vertical resolution. As previously mentioned, the number of vertical levels in the flat bottom simulation was set to two. For the basins with a step–shelf and a step–shelf with ridge, the levels were increased to eight following the methodology in Chapter 4.

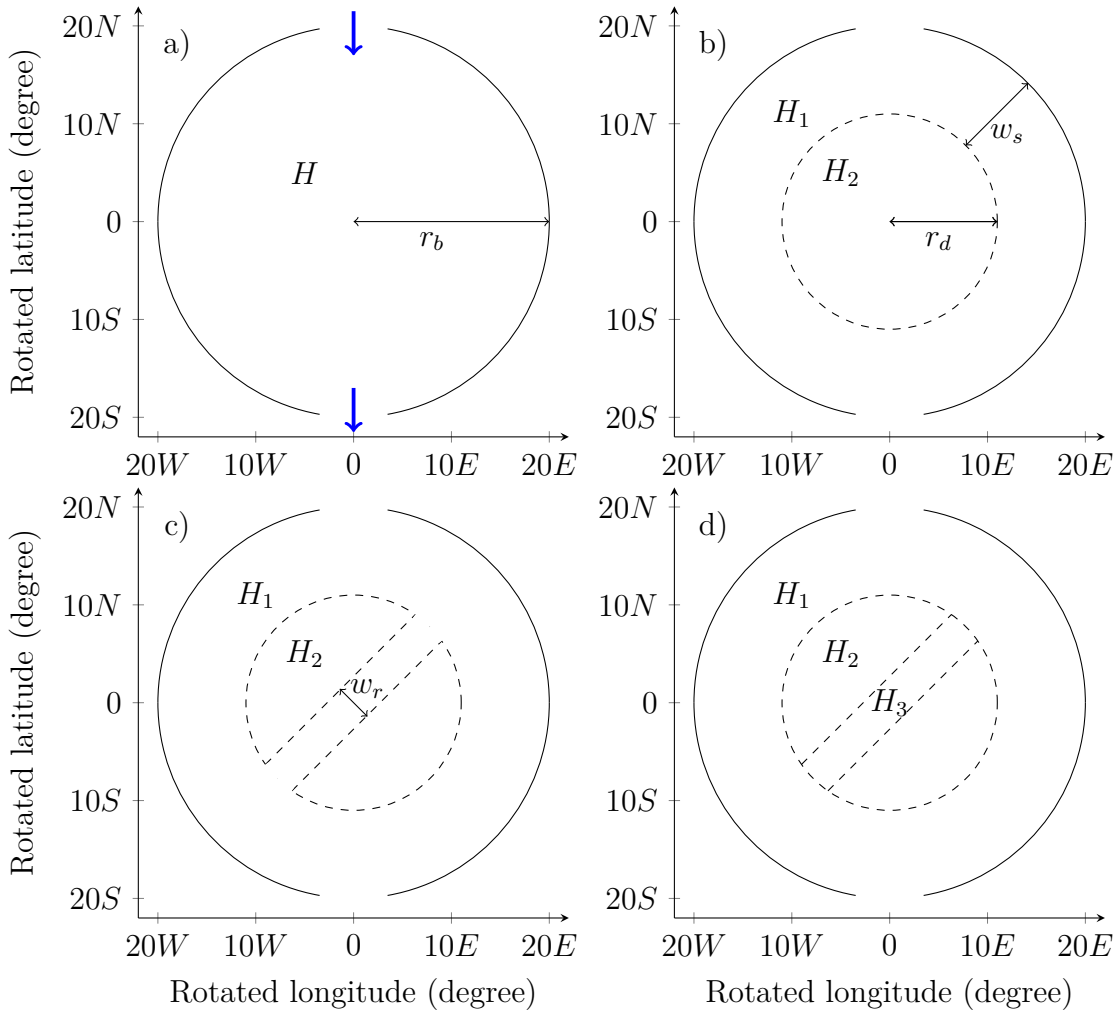

Figure 6.1: Schematic of the topography in a polar basin; a) flat bottom basin; b) step–shelf basin; c) step–shelf with ridge. Note r_b is the radius of the basin, r_d is the radius of the deep basin, w_s is the width of the step–shelf, w_r is the ridge width, H is the depth of the basin, H_1 is the deep basin depth, H_2 is the step–shelf depth and H_3 is the depth of the ridge.

The wind stress can be added into the model as a surface boundary condition which is found in the section *namsbc* of the *namelist_cfg*. We chose a wind stress which was given by the flux scheme (i.e. *ln_flux=.true.*). This scheme uses external files to input the wind stress. In particular, the model requires the wind stress components in the τ^{φ_r} (*rn_utau0*) and τ^{ϕ_r} (*rn_vtau0*) direction, freshwater budget (*rn_emp0*), total heat flux (*rn_tot*) and the solar radiation (*rn_qsr*). Among them, the total heat flux, the solar radiation and the freshwater budget were set to zero. These forcing files are imposed in the model in the routine *sbcflux.F90*. For this study, we initially impose the same wind stress that was considered in Chapter 5, namely an azimuthal wind stress

$$\tau^{\varphi}(\varphi,\theta) = \frac{R\rho W(\varphi)}{2\sin\theta}\left[\frac{\sin\left(\theta-\frac{\pi\theta}{\theta^*}\right)}{(1-\pi/\theta^*)} - \frac{\sin\left(\theta+\frac{\pi\theta}{\theta^*}\right)}{(1+\pi/\theta^*)}\right], \tag{6.1}$$

where R is the radius of the Earth, ρ is the density, $W(\varphi)$ is azimuthal structure of the wind stress which was defined in Chapter 5, θ is the co–latitude, and θ^* is the angle that controls the meridional structure of the wind stress. The above expression describes an azimuthal mode of wind stress which decays to zero in the centre of the grid and along the axis of symmetry in the transition area where the wind stress curl changes sign (see dashed line in Figure 6.2 (b)). In the rotated grid this can be parametrised using the following expression

$$\tau^{\varphi_r} = \tau^{\varphi}\cos\varphi, \tag{6.2}$$

$$\tau^{\phi_r} = \tau^{\varphi}\sin\varphi. \tag{6.3}$$

Note φ and τ^{φ} were interpolated onto the rotated grid using the WEIGHT tools from the NEMO ocean model (see Figure 6.2 (a)). The Figure 6.2 (b) displays the wind stress vectors forced by NEMO using the above expression in the rotated grid.

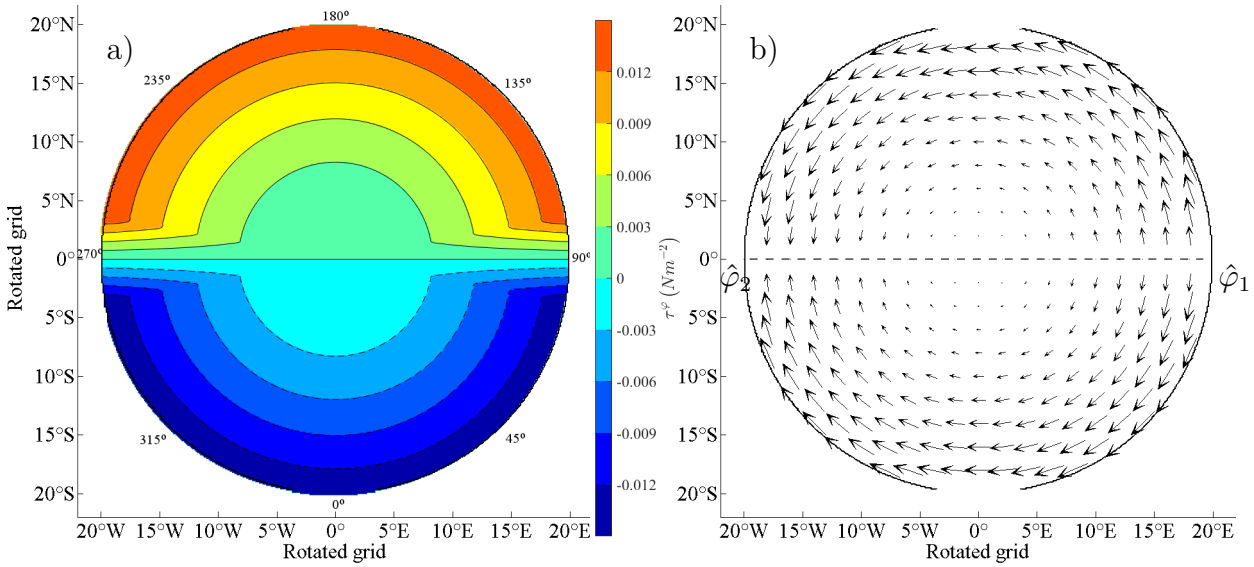

Figure 6.2: Azimuthal wind stress; a) obtained by the interpolation of the analytic expression (6.1). Dashed line denotes negative values of wind stress; b) wind stress vectors generated by NEMO. Dashed line denotes zero wind stress curl.

The implementation of open boundaries follow the same methodology as Chapter 4. Thus two open boundaries, or straits, were prescribed in the basin (see Figure 6.1). The forcing files were different to those in Chapter 4 because the magnitude and direction of flow across the strait is determined by the Sverdrup balance (5.8). Table 5.1 shows

different source–sink positions and magnitudes of ψ_0 for different wind stress curls. Also, we remind the reader that the total transport across the strait in the analytic model is given by $2\psi_0$ (see Chapter 2). These experiments were set using the control wind stress values of Chapter 5 (see Table 5.2) giving approximately a boundary transport of 1.5 Sv (see third column of Table 5.1).

The initial conditions for salinity, SSH, temperature and velocity are computed in *istate.F90*. We set salinity and temperature to 35.5 psu and 2^oC, respectively and they remain constant throughout the numerical integration. The initial velocity field and the SSH are set to zero.

6.3 Comparison of numerical and analytical solutions

This section compares the approximate analytical solutions of Chapter 5 with the numerical results from the NEMO ocean model. We note that NEMO cannot run in the absence of lateral diffusion because a certain amount of diffusion is required to preserve numerical stability. Therefore, we decrease the Laplacian eddy diffusivity ($100m^2s^{-1}$) to a level which retains numerical stability, thereby allowing the dominant dissipation mechanism to be linear bottom friction.

First, we compare the steady state isolines of SSH with the analytical streamfunction. Qualitatively, the streamfunction and SSH elevation contours will coincide where the flow is geostrophic. In the frictional boundary layer(s) the isolines of η and ψ differ. In addition a quantitative comparison is made between the analytical solutions of Chapter 5 and the spun-up NEMO simulations, by examining their relative vorticity fields.

Chapter 4 derived the relative vorticity in spherical polar coordinates (4.6) which we restate below for convenience:

$$\hat{\boldsymbol{k}} \cdot \nabla \times \boldsymbol{u} \equiv \frac{1}{\sin^2\theta H R^2}\left[\cos\theta \sin\theta \psi_\theta + \sin^2\theta \psi_{\theta\theta} + \psi_{\varphi\varphi}\right]. \tag{6.4}$$

Equation (6.4) can be further simplified by using (5.6) to yield,

$$\hat{\boldsymbol{k}} \cdot \nabla \times \boldsymbol{u} \equiv \frac{1}{\sin^2\theta H R^2}\left[-2\Omega H \mu^{-1}\sin^2\theta \psi_\varphi + \mu^{-1} R^2 H \sin^2\theta\{\boldsymbol{k} \cdot \nabla \times \boldsymbol{\tau}/\rho\}\right]. \tag{6.5}$$

Using the definition of the wind stress curl (5.8), (6.5) can be further simplified to

$$\hat{\boldsymbol{k}} \cdot \nabla \times \boldsymbol{u} \equiv \frac{1}{\mu R^2}\left(-2\Omega\psi_\varphi + R^2 \sin\left(\pi\frac{\theta}{\theta^*}\right) W(\varphi)\right), \tag{6.6}$$

where $W(\varphi)$ is given by (5.10). Note that for the analytic model ψ_φ can be obtained analytically.

The relative vorticity from the numerical model output was obtained using the same approach as in Chapter 4 and subsequently the relative vorticity field is interpolated to the geographical grid.

Figure 6.3 (a) shows the contour plot of SSH together with the barotropic velocity vectors from NEMO simulation after 10 years of simulation in a flat bottom basin. The ocean basin parameters used are in Table 4.1 and the bottom friction coefficient was 10^{-4} ms^{-1}. Across the source strait the inflow is given by the Sverdrup balance, which crosses the basin to exit at the sink strait. The inlet-outlet circulation is trapped between two ocean gyres, forcing the flow to cross the domain interior. This result is qualitatively similar to Figure 5.5 (a), although Figure 5.5 (a) displays a stronger current crossing the centre of the domain. In addition, Figure 6.3 (a) displays small wedges in the transition area where the wind stress curl decays to zero whereas in Figure 5.5 (a) these are absent. This could be a consequence of the discretization of the wind stress curl in the transition area or the effect of the Laplacian eddy diffusion of the numerical model.

The sensitivity of the analytical solution to a change in θ_f is compared with numerical solution and shown in Figure 6.3 (b) and (c). The Figure 6.3 (b) shows the relative error between the relative vorticity of analytical solution using $\theta_f = \pi/18$ and the numerical simulation. Unlike Chapter 4, there is a large difference between the results. Interestingly, the increase of θ_f significantly decreases the error between solutions on the boundary (see Figure 6.3 (c)).

The impact of a step–shelf on the circulation is studied in Figure 6.4 (a), (b) and (c). Figure 6.4 (a) shows contours of the SSH and barotropic velocity vectors superposed, from the NEMO ocean model. The ocean basin parameters used are in Table 4.1 and the bottom friction coefficient was 10^{-4} ms^{-1}. The addition of a shelf generates two pairs of ocean gyres; on the step–shelf and in the deep basin. The inflow enters the basin from the top strait and flows across the step–shelf forming two strong rim currents on the shelf. Subsequently, it leaves the basin from the bottom strait. The deep basin supports a weak circulation taking the form of two counter–rotating ocean gyres in agreement with the approximate analytical solution of shown in Figure 5.11. Note the total relative vorticity in the deep basin is nearly zero since the relative vorticity of the ocean gyres nearly balance out as it was proved in the integral constraint analysis. Figure 6.4 (b) and (c) shows the relative error between the relative vorticity of numerical solution and analytical solution in Chapter 5 using $\theta_f = \pi/18$ and $\theta_f = \pi/9$, respectively. In the step–shelf, there are strong differences when $\theta_f = \pi/18$ whereas $\theta_f = \pi/9$ provides a good agreement between

the solutions. In the deep basin, we observe the opposite situation, $\theta_f = \pi/18$ solution shows a better agreement than $\theta_f = \pi/9$. As in Chapter 4, the differences in the deep basin circulation are likely to be due to the representation of the shelf break topography and the presence of Laplacian eddy diffusion in the numerical model.

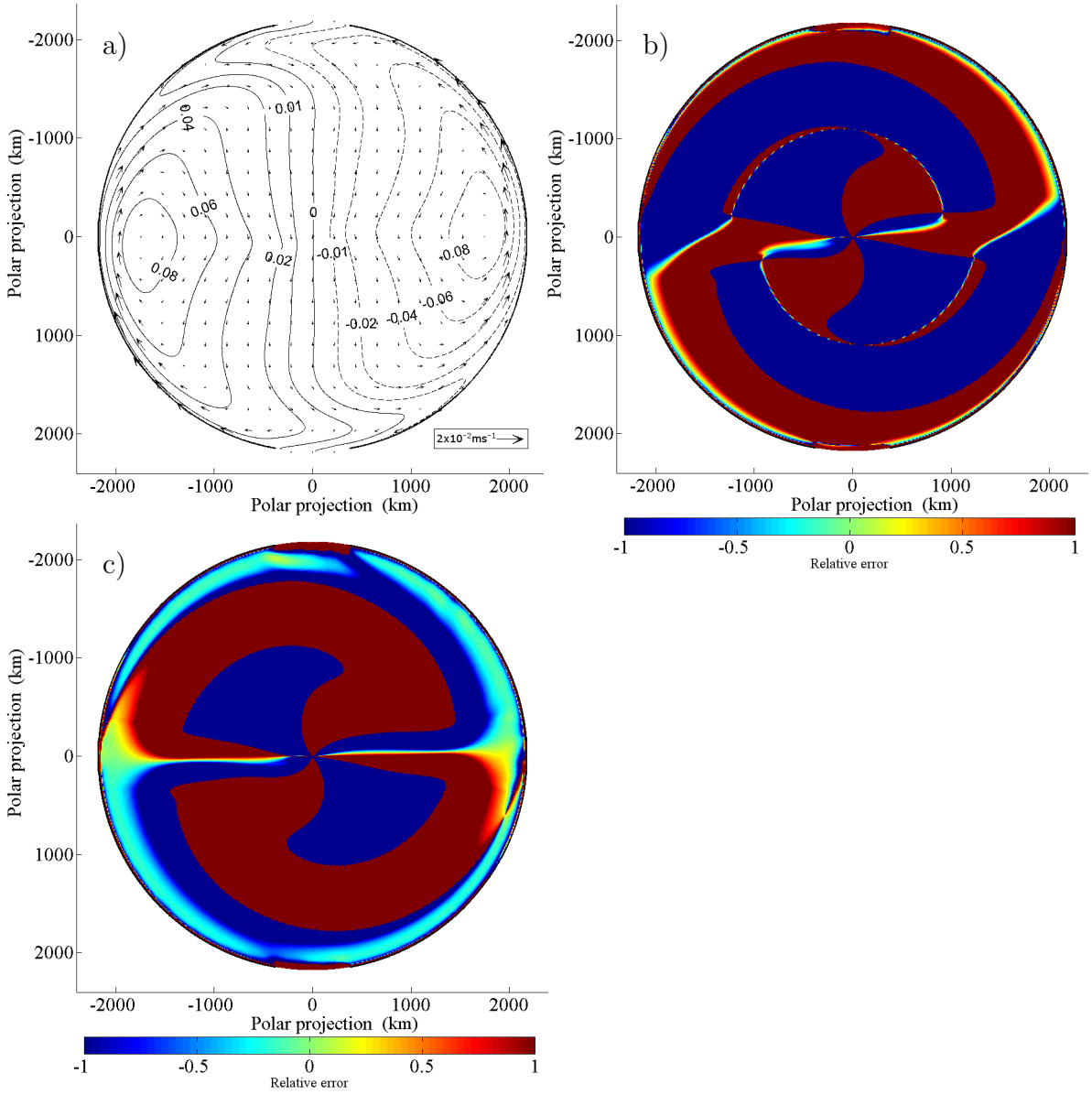

Figure 6.3: Wind–driven planetary geostrophic flows in a polar basin with two diametrically opposed straits. a) Contours of SSH and barotropic velocity vectors in a flat bottom basin; b) relative error of the relative vorticity between the analytical and the numerical solution where $Relative \quad Error = (\xi_{NEMO} - \xi_{ana})/\xi_{NEMO}$ using $\theta_f = \pi/18$ in a flat bottom basin; c) same as (b) except $\theta_f = \pi/9$.

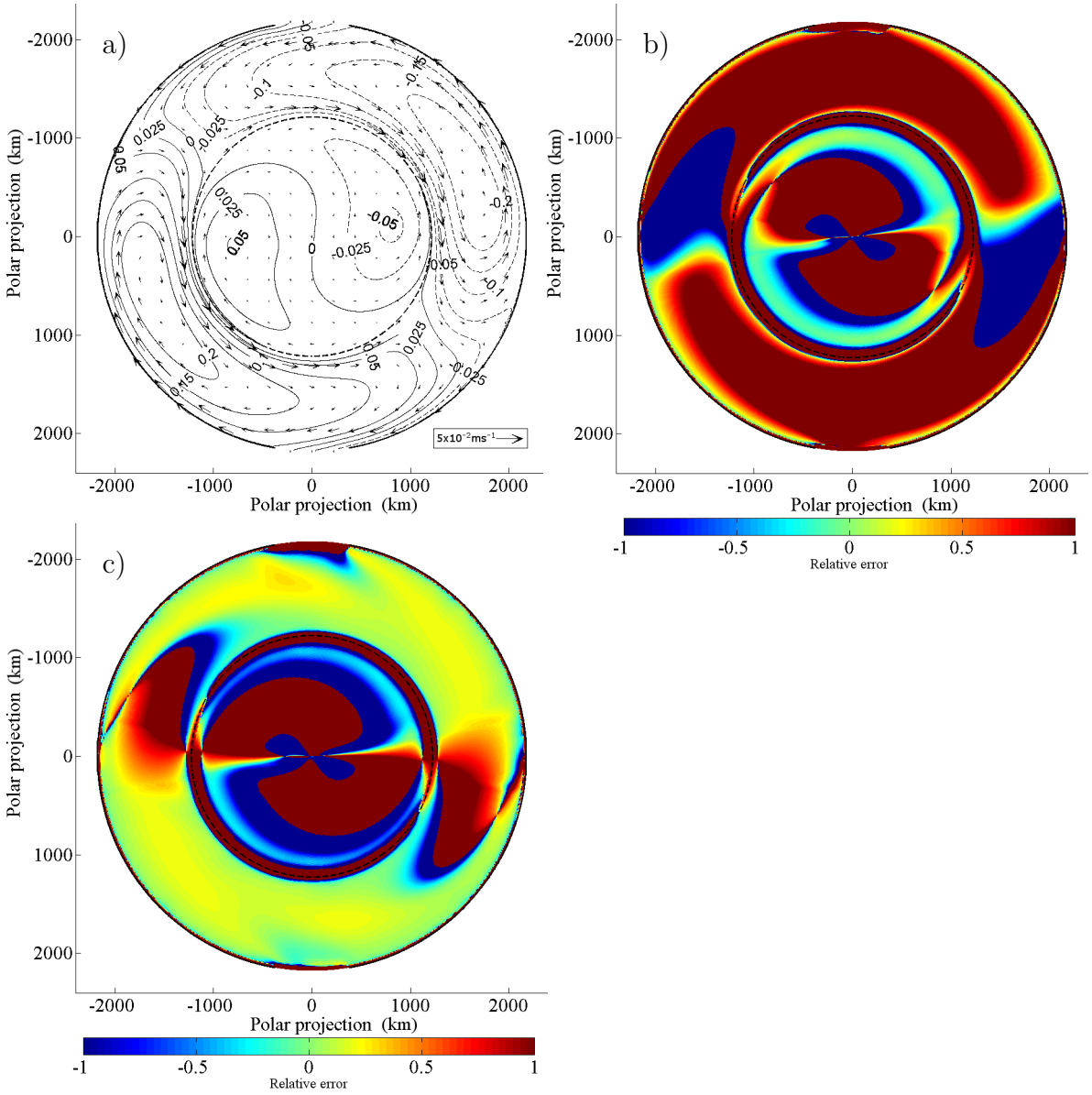

Figure 6.4: Wind–driven planetary geostrophic flows in a polar basin with a step–shelf and two diametrically opposed straits. a) Contours of SSH and barotropic velocity vectors; b) relative error of the relative vorticity between the analytical and the numerical solution where $Relative \quad Error = (\xi_{NEMO} - \xi_{ana}) / \xi_{NEMO}$ using $\theta_f = \pi/18$; c) same as (b) except $\theta_f = \pi/9$.

6.4 Step shelf with ridge

By analogy with Chapter 4, we study the influence of ridge orientation on the wind–driven ocean circulation using different basin configurations shown in Figure 6.5. Firstly, we evaluate the ridge orientation in a "wide" step–shelf of width 900 km (see Figure 6.5 (a) and (b)). The control parameters used in NEMO for this scenario are in Table 4.1. Subsequently, we used the same narrow step–shelf with a width of 200 km considered in Chapter 4 to study its impact on the circulation (see Figure 6.5 (c) and (d)). Finally, we investigate the impact of the ridge depth on the circulation.

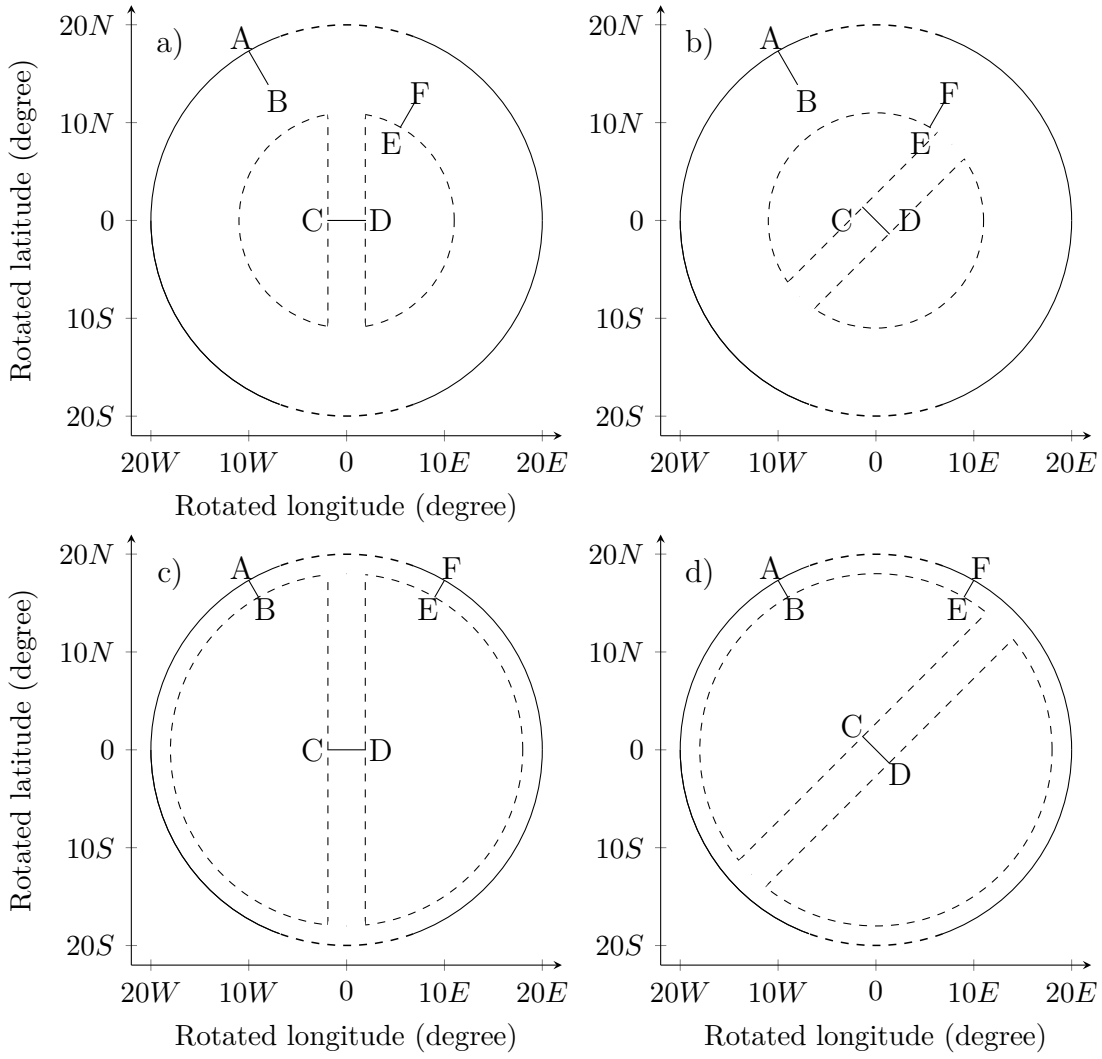

Figure 6.5: Schematic of the basin geometry used in the numerical experiments; a) step–shelf with a transpolar ridge whose axis joins the mid–points of the straits; b) same as (a) but with the transpolar ridge rotated clockwise of 45^o; c) same as (a) but with a narrow step–shelf; d) same as (b) but with a narrow step–shelf. Sections $\overline{AB}$, $\overline{CD}$ and $\overline{EF}$ denote where the volume transport was computed.

All the simulations were forced from rest and integrated for a simulated 10 years by which point the circulation is essentially steady. Figure 6.6 shows the time series of total kinetic energy in a basin with a wide shelf and a transpolar ridge whose axis of symmetry joins the mid–points of the straits. We observe that the simulation reaches the steady–state in the first year of integration.

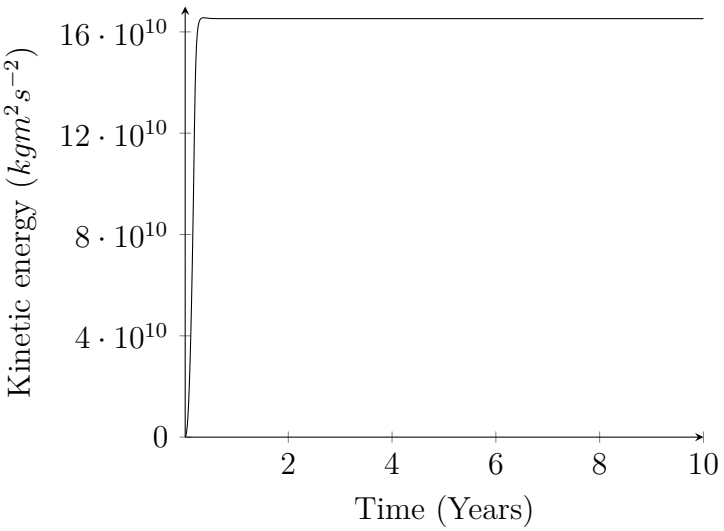

Figure 6.6: Time series of the total kinetic energy for a basin with a wide shelf width and a transpolar ridge whose axis joins the mid–points of the straits.

Figure 6.7 shows contour of the SSH and the barotropic velocity vectors associated with the steady circulation in a basin with a wide step–shelf and a ridge whose top is level with the shelf. The ocean basin parameters used in this simulation are in Table 4.1. In a basin with a wide step–shelf and ridge aligned with the straits (Figure 6.7 (a)), we observe two counter–rotating gyres on the shelf and four in the deep basins. Fluids entering the basin follows three distinct paths before exiting the basin at the diametrically opposite strait. The first pathway takes the form of a strong rim (cyclonic) current of magnitude 1.118 Sv (computed transport across section $\overline{AB}$) which is confined to the shelf break before exiting throughout the sink–strait. The second path is confined to the ridge, connecting the source–sink straits by a transpolar current of magnitude 0.595 Sv across $\overline{CD}$. A close-up of SSH and the velocity vectors on the ridge reveals a transpolar current which does not form "western boundary currents" (see Figure 6.7 (c)) as it was observed in Chapter 4 (see Figure 4.9 (b)). The third path is defined by an anticlockwise rim current of 0.947 Sv across $\overline{EF}$ that is partially confined to the shelf edge by the ocean gyre on the "NE" of the step–shelf. Note the total volume transport across section $\overline{EF}$ and $\overline{CD}$ is much larger than the difference between the inflow and the section $\overline{AB}$. This

inconsistency in the volume transport is due to two recirculations on the shelf produced by the ocean gyres (at "NW" and "NE").

Rotating the ridge (see Figure 6.7 (b)) dramatically changes the pathways of the source–sink trans–basin circulation. At the source strait the circulation bifurcates into two branches. The strongest is the cyclonically flowing branch (1.517 Sv across $\overline{AB}$) which, in turn, bifurcates into two branches at the neighbourhood of the junction where the ridge and the shelf meet. One branch flows as a "coupled western boundary current" across the ridge with a volume flux of magnitude 0.731 Sv across $\overline{CD}$ (see Figure 6.7 (d)). It is noteworthy that the rotation of the ridge reverses the transpolar ridge current direction. At the intersection of the shelf and the ridge the fluid that does not cross the ridge instead exits at the sink–strait. Returning to the source–strait, an anticyclonic shelf current of magnitude 0.912 Sv across $\overline{EF}$ merges with transpolar ridge current. Subsequently, this branch circulates as anticyclonic shelf current to exit the basin at the sink–strait. We observe in Figure 6.7 (b) that the overall gyre pattern configuration has not changed compared to the Figure 6.7 (a). In other words, there are two counter–rotating shelf gyres and in each deep basin two counter–rotating gyres.

Figures 6.8 (a) and (b) display the same ridge orientation configurations as Figure 6.7 (a) and (b), respectively, but with a narrow step–shelf width. In Figure 6.8 (a) we observe that the circulation on the shelf is reduced to a cyclonic and an anticyclonic boundary currents of magnitude 0.368 Sv (computed transport across section $\overline{AB}$) and 0.177 Sv (computed transport across section $\overline{EF}$), respectively. This structure resembles the analogous simulation in Chapter 4 (see Figure 4.10 (a)). In addition, we observe an intense current which crosses the ridge forming a transpolar current with a magnitude of 1.084 Sv across section $\overline{CD}$. Once more, western boundary currents are absent on the ridge (see Figure 6.8 (c)). This is a totally different structure to that observed in Chapter 4 where the same scenario revealed western boundary currents on both sides of the transpolar ridge. The circulation in the deep basin takes the form of a pair of gyres in each basin. The impact of the rotation of the ridge is displayed in Figure 6.8 (b). Once more, the circulation on the shelf is given by cyclonic and anticyclonic boundary current of magnitude 1.056 Sv (computed transport across section $\overline{AB}$) and 0.59 Sv (computed transport across section $\overline{EF}$), respectively. These branches flow along the shelf until the junction where the ridge and shelf intersect. Here, the current flows in and out forming a weak transpolar current with a magnitude of 0.017 Sv (see Figure 6.8 (d)). Subsequently, they leave the domain through the strait. Again the circulation in the deep basin takes

the form of two pairs of counter–rotating gyres in each basin.

Figure 6.9 shows contours of the SSH and the barotropic velocity vectors in a polar basin where the ridge top is 250 m below the step–shelf. Figure 6.9 (a) and (b) show the circulation in a basin with wide step–shelf and a ridge whose axis joins the mid–points of the straits and a rotated ridge, respectively. The circulation on the shelf is mainly controlled by the presence of two counter–rotating gyres. The deepening of the ridge forms a topographic barrier strengthening the shelf edge boundary currents. In particular, the boundary current on the "NE" side of the step–shelf reveals volume flow of 1.14 Sv (before 0.947 Sv) across section $\overline{EF}$. The change of ridge orientation does not alter this circulation. The deep basin circulation is controlled by two pairs of weak ocean gyres (one pair in each basin) although the basin with rotated ridge shows only one gyre in each sub–basin (see Figure 6.9 (b)). The transport across the aligned ridge is almost negligible (0.094 Sv) whereas the inclined ridge shows a transpolar drift of magnitude 0.212 Sv.

The impact of a narrow step–shelf is displayed in Figures 6.9 (c) and (d). Figure 6.9 (c) displays a similar circulation as Figure 6.8 (a), although the transpolar current magnitude decreases to 0.489 Sv (before it was 1.084 Sv) across $\overline{CD}$. This strengthens the cyclonic and anticyclonic boundary currents to 0.793 Sv across $\overline{AB}$ and 0.447 Sv across $\overline{EF}$, respectively. The change of ridge orientation does not have any significant impact on the shelf circulation (see Figure 6.9 (d)).

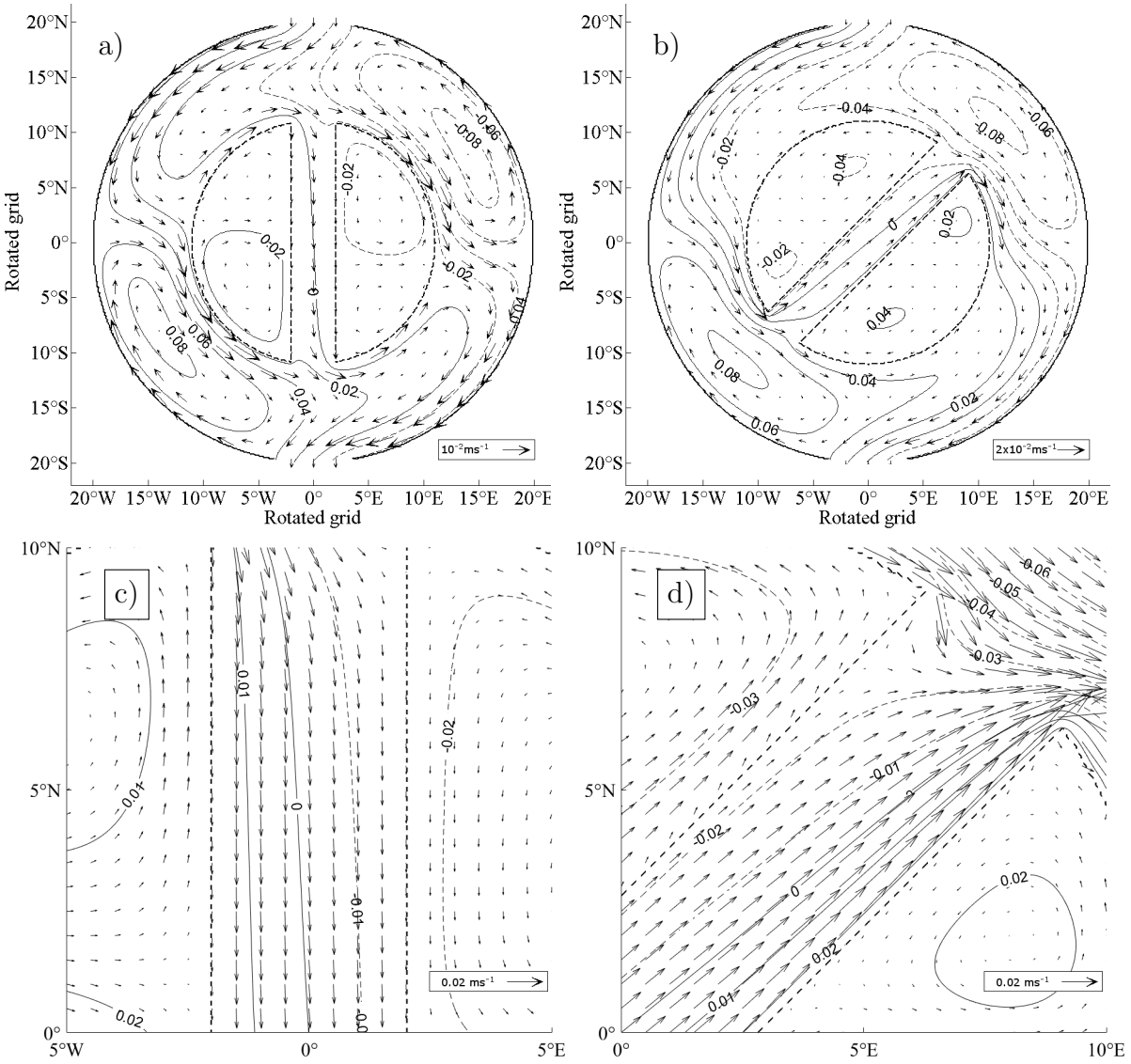

Figure 6.7: Planetary geostrophic wind–driven flows. a) Contours of SSH and barotropic velocities vectors in a wide step–shelf basin with ridge whose axis joins the mid–points of the straits; b) same as (a) but with a rotated ridge; c) enlarged area of (a); d) enlarged area of (b).

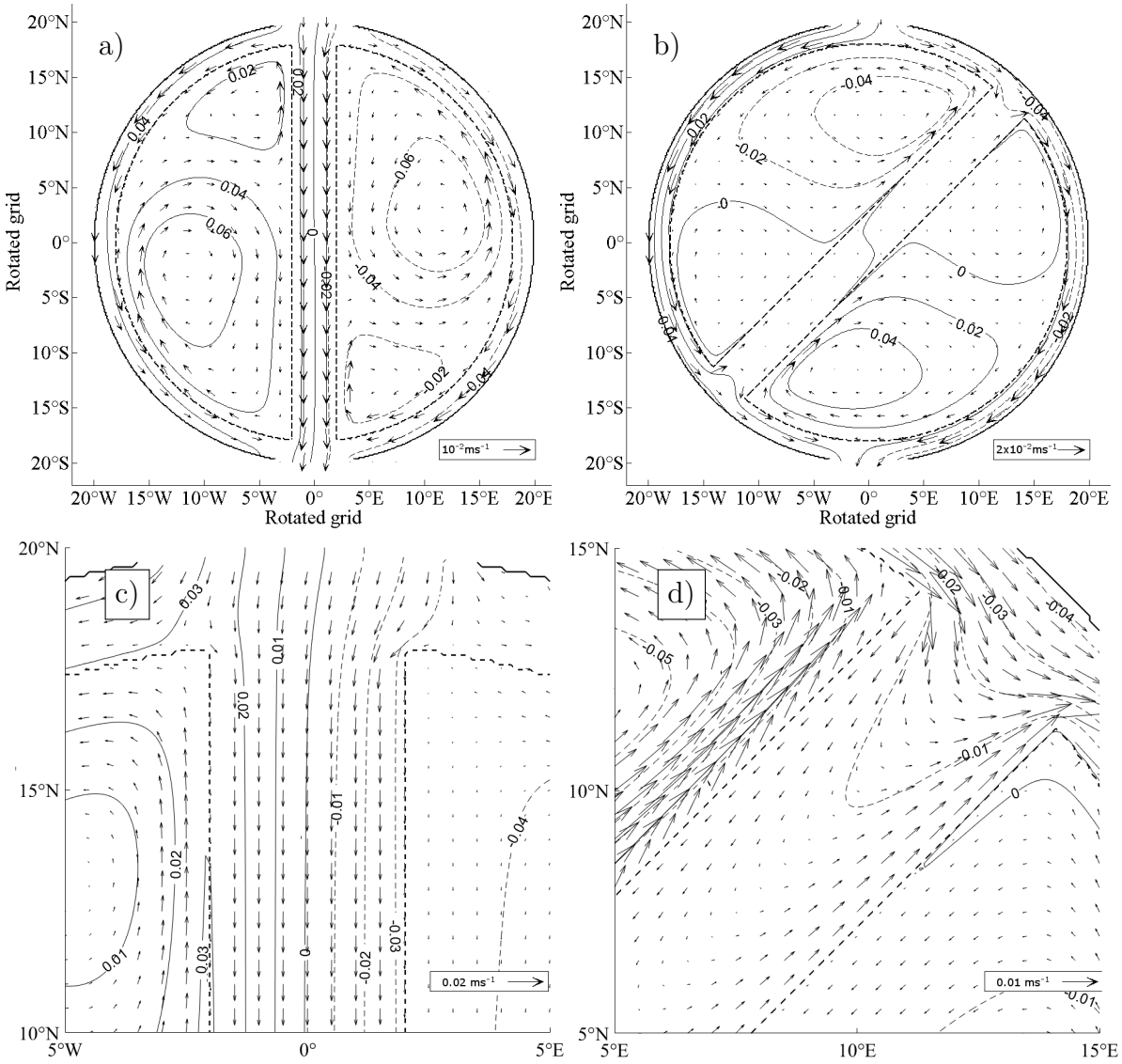

Figure 6.8: Planetary geostrophic wind–driven flows. a) Contours of SSH and barotropic velocities vectors in a narrow step–shelf basin with ridge whose axis joins the mid–points of the straits; b) same as (a) but with a rotated ridge; c) enlarged area of (a); d) enlarged area of (b).

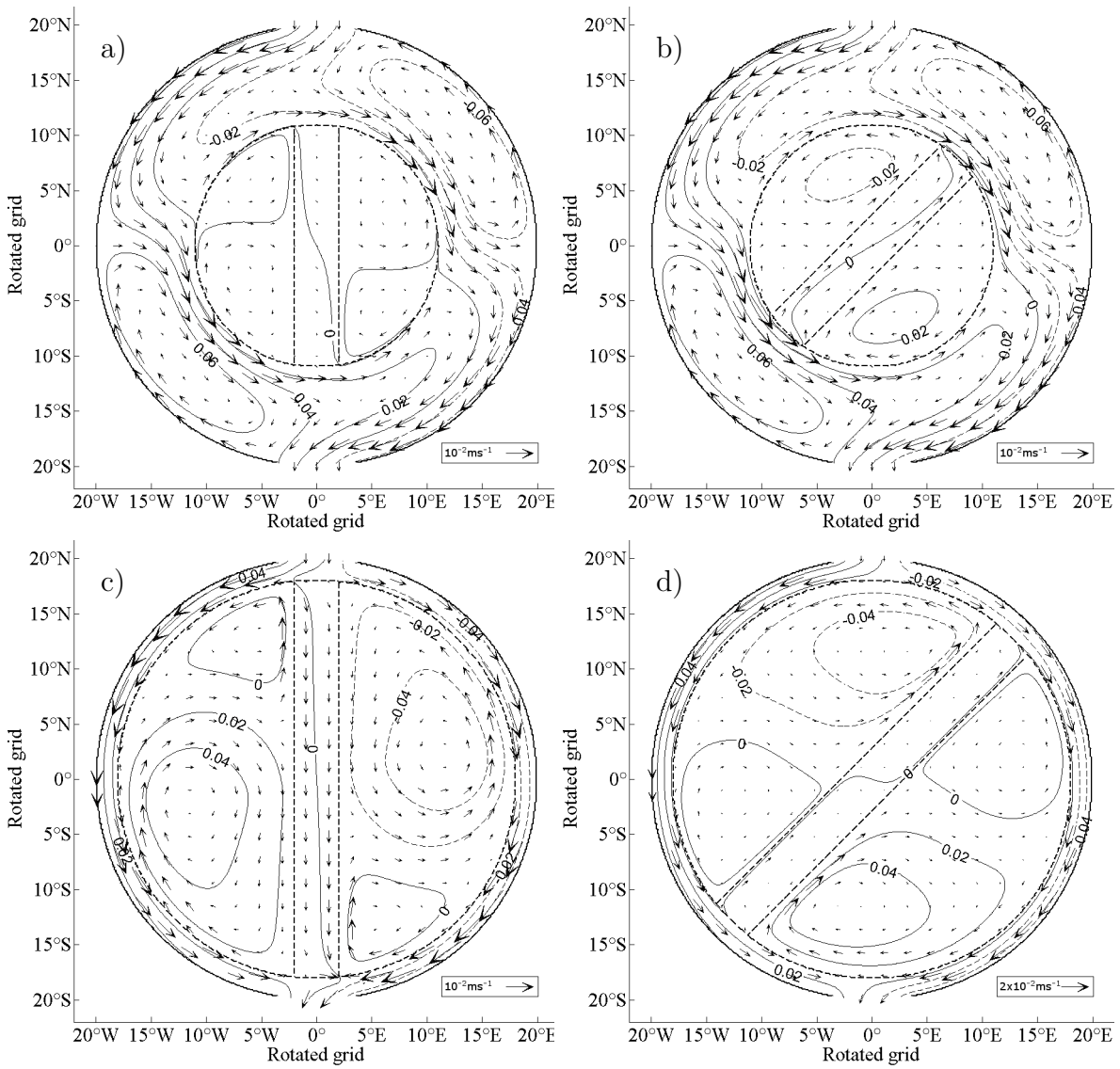

Figure 6.9: Planetary geostrophic wind–driven flows in a basin where the ridge top is below the step–shelf. a) Contours of SSH and barotropic velocities vectors in a step–shelf basin with ridge whose axis joins the mid–points of the straits; b) same as (a) but with a 45^o ridge with respect of the gaps; c) same as (a) but with a narrow step–shelf; d) same as (b) but with a narrow step–shelf.

6.5 Circulation driven by more realistic representations of the the Arctic Ocean wind stress

This section considers a barotropic Arctic Ocean circulation driven by a more realistic representation of the wind stress. Proshutinsky and Johnson (1997) using a barotropic coupled ocean–ice model driven by daily surface winds from NCAR, and demonstrated that the atmospheric circulation in the Arctic Ocean is dominated by two wind stress regimes; an intense anticyclonic and a cyclonic regime. The anticyclonic regime (see Figure 6.10 (b)) is characterised by a high pressure cell in the Beaufort Sea generating a clockwise circulation known as Beaufort Gyre producing a shift of the North Atlantic current from the central Arctic to the Barent and Kara Seas (see red arrow in Figure 6.10 (b)). During the cyclonic stage (Figure 6.10 (a)) there is a low pressure atmospheric cell in the Arctic Ocean decreasing the strength of the Beaufort Gyre and decreasing the strength of transpolar current allowing the North Atlantic current to propagate into the central Arctic (Proshutinsky *et al.*, 2015). These wind stress regimes alternate with a quasi–decadal time scale of 5-7 years (i.e. a cycle of 15 years). However, this cycle was interrupted from the early 2000s showing a continuous anticyclonic wind stress regime (Proshutinsky *et al.*, 2015) producing an anomalous accumulation of freshwater in the central Arctic (Rabe *et al.*, 2014).

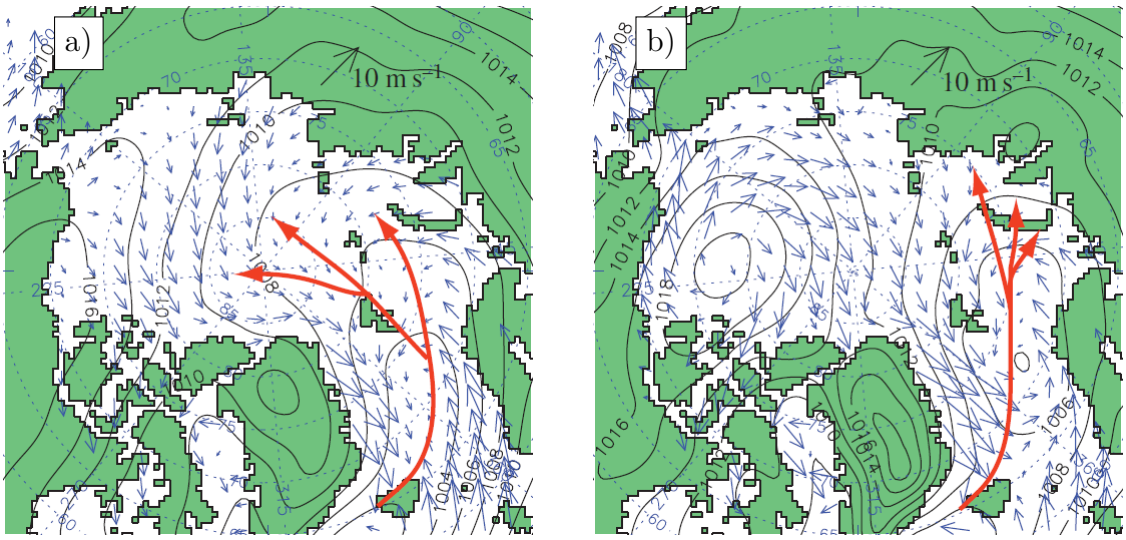

Figure 6.10: Wind stress regimes highlighted after Proshutinsky *et al.* (2015). a) Cyclonic wind stress regime in 1989; b) Anticyclonic wind stress regime in 2007. The blue arrows are the surface wind and the contour plot displays the sea level atmospheric pressure. The red arrows show the pathways of the North Atlantic water.

We study the wind–driven steady circulation associated with the anticyclonic wind stress regime shown in Figure 6.10 (b). Subsequently, the wind–stress changes linearly over 6 months becoming the cyclonic regime shown in Figure 6.10 (a). After a short period of time the circulation reaches a new steady state.

We consider polar basins with the different bathymetry configurations (Figure 6.11). First, we study the circulation driven by the two wind stress regimes in a closed basin with a step–shelf with and without a ridge (see Figure 6.11 (a) and (b)). Second, we repeat the same experiment but with three gaps (or straits) located in positions that are representative of the Bering Strait, Davis Strait and the GINs (see Figure 6.11 (c) and (d)).

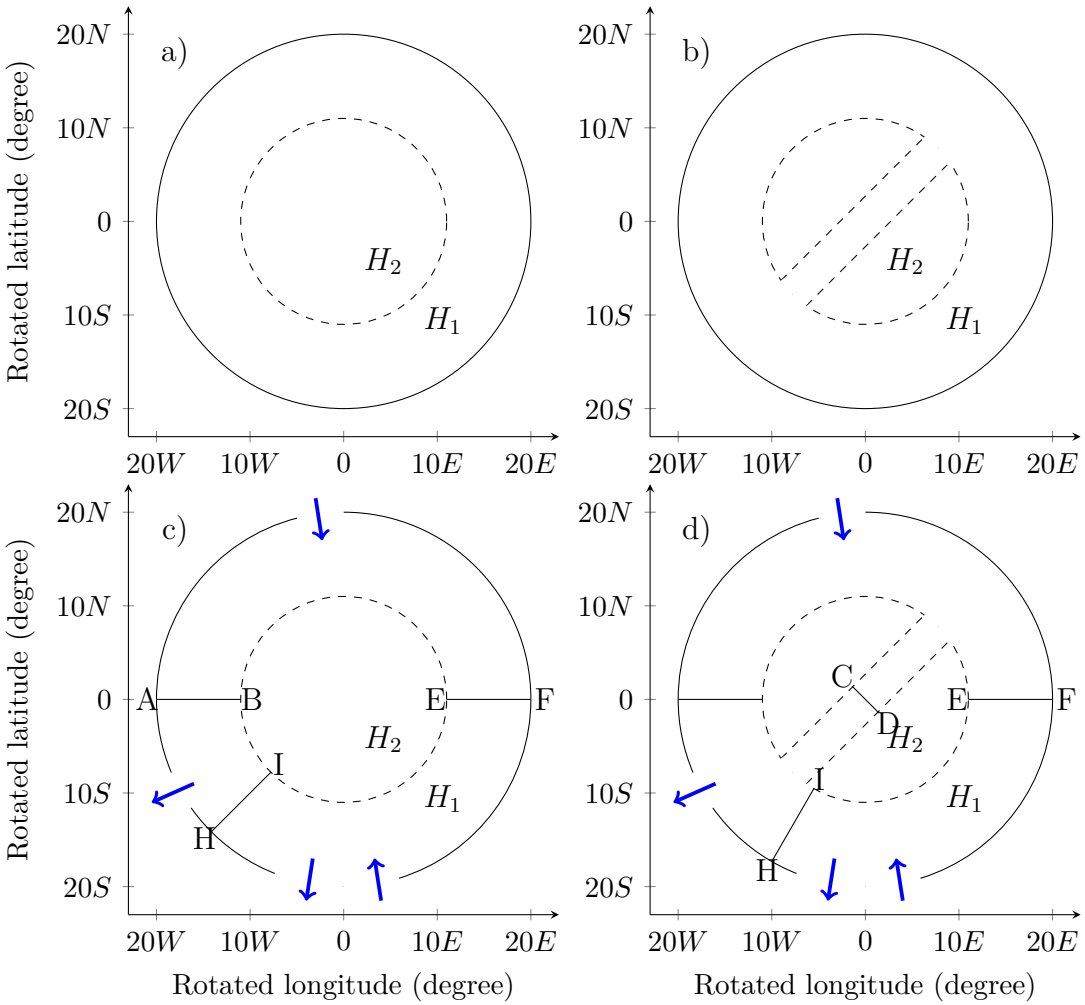

Figure 6.11: Schematic of a) closed basin with step–shelf and a ridge; b) as in (a) except with a ridge c) a step–shelf basin with three straits; d) as in (c) except with a ridge. Depths H_1 and H_2 are given in Table 4.1.

At the boundary of the basin with three straits (see Figure 6.11 (c) and (d)), we prescribe two inflows and two outflows as shown in Figure 6.11 (c). In the previous sections the prescribed source–sink flows were determined by the Sverdrup balance. Here, we instead employ the same volume transports as Chapter 4 since they represent the mean annual net flux across the main straits of the Arctic Ocean. The inflow via the Bering Strait is 1 Sv and remains constant over the entire model integration. The GINs and Davis straits are initially set as Table 6.1 (column two), but these boundary transports vary with time due to the Flather (1994) open boundary condition. The latter boundary condition was mentioned in Chapter 4 but not used because those experiments considered a constant source–sink flows across the straits. The Flather boundary allows gravity waves to leave the domain adjusting the boundary flows at each time step. Therefore, the steady transport across the straits will vary depending on the scenario (see Table 6.1). As pointed out in Chapter 4 the open boundaries are handled in *bdydyn2d.F90* and *bdydyn.F90*. The algorithm which computes the volume transport across the strait was modified in order to reproduce the boundary flows described for this section (see Appendix E.1 and E.2).

Figure 6.12 shows analytical representations of the cyclonic (Figure 6.12 (a)) and anticyclonic with stress regimes (Figure 6.12 (b)))

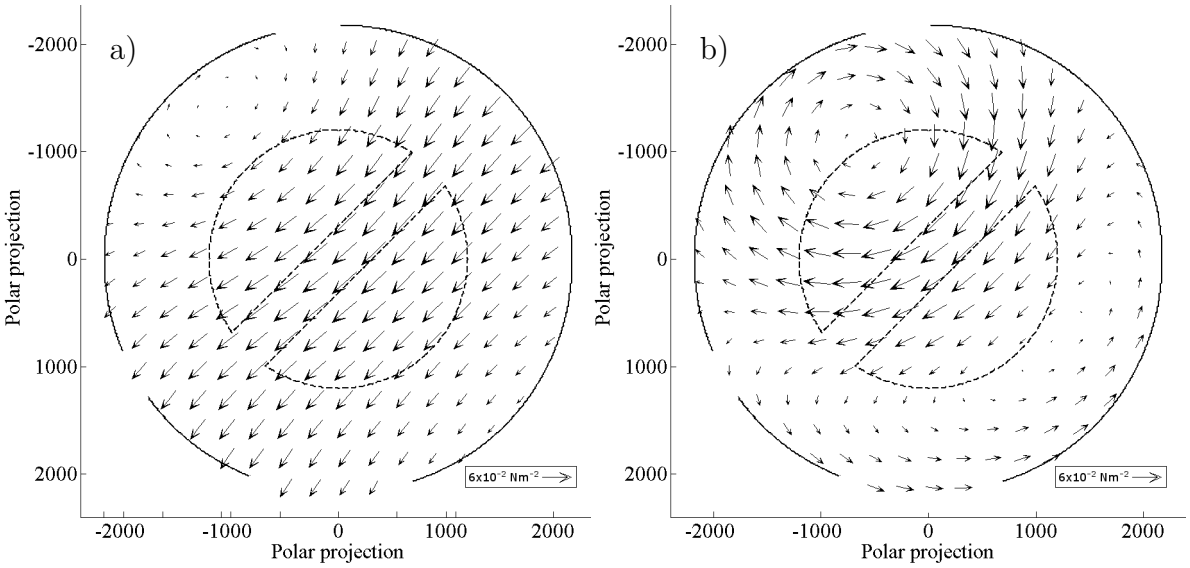

Figure 6.12: Plot of the wind stress vectors associated with the wind stress regimes identified by Proshutinsky *et al.* (2015). a) cyclonic wind stress regime typical of that in 1989; b) anticyclonic wind stress regime typical of that in 2007.

The wind stress vectors plotted in Figure 6.12 are obtained from analytical expressions which themselves are a linear superposition of two "building block" wind stress fields:

$$\tau^x = \alpha\tau^{x_1} + (1-\alpha)\,\tau^{x_2}, \tag{6.7a}$$

$$\tau^y = \alpha\tau^{y_1} + (1-\alpha)\,\tau^{y_2}, \tag{6.7b}$$

where the constant α for the anticyclonic and cyclonic wind stress regimes was set to 0.7 and 0.2, respectively. The transition from an anticyclonic steady wind–driven solution to a steady cyclonic wind–driven is achieved as follows. During the transition phase α varies linearly with time over a specified period T (i.e. 6 months):

$$\alpha\,(t) = 0.7 - 0.5t/T, \quad 0 \le t \le T.$$

The wind stress components τ^{x_1}, τ^{y_1} are referred to a Cartesian frame $O_1x_1y_1$ where O_1 is located at $[-500\text{km}, 900\text{km}]$ and O_1x_1 is parallel to Ox and O_1y_1 is parallel to Oy. The stress components are

$$\tau^{x_1} = \tau\frac{y_1}{r}\sin\left(\frac{r}{r_b}\pi\right), \tag{6.8a}$$

$$\tau^{y_1} = -\tau\frac{x_1}{r}\sin\left(\frac{r}{r_b}\pi\right), \tag{6.8b}$$

where r is distance from the origin O_1, r_b is the radius of the basin and $\tau = 0.07Nm^{-2}$. The wind stress (τ^{x_2}, τ^{y_2}) is a uni-directional wind stress field and is given by

$$\tau^{x_2} = -\frac{\tau}{\sqrt{2}}\sin\left(\frac{|y_2\text{km} - 2000\text{km}|}{5000\text{km}}\pi\right), \tag{6.9a}$$

$$\tau^{y_2} = 0, \tag{6.9b}$$

In (6.9a) the Cartesian frame Ox_2y_2 is obtained by a 45^o counter-clockwise rotation of frame Oxy and the coordinates are related by

$$x_2 = \frac{1}{\sqrt{2}}\,(x+y) \tag{6.10a}$$

$$y_2 = \frac{1}{\sqrt{2}}\,(-x+y)\,. \tag{6.10b}$$

Figure 6.13 (a) and (b) shows a time series of the kinetic energy for a closed basin with step–shelf and step–shelf basin with three straits. The dashed line denotes the change of the wind stress regime, and both scenarios reach a steady state in less than two years.

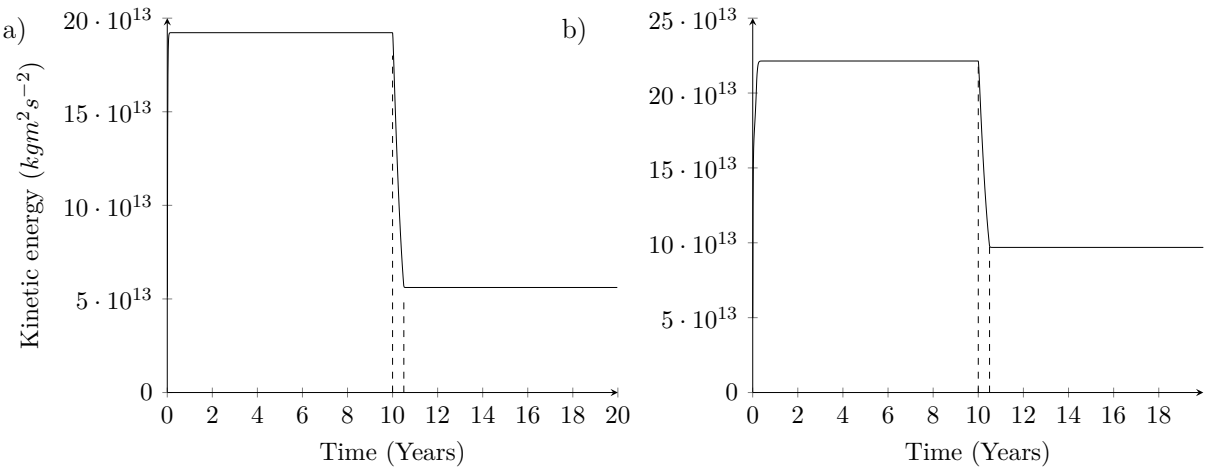

Figure 6.13: Time series of the total kinetic energy for a step–shelf basin with a) no gaps; b) three gaps (or straits). Dashed line denotes the change of wind stress regime.

Figure 6.14 shows the contour plot of the steady–state SSH and the barotropic velocities in a closed basin. Figures 6.14 (a) and (b) show the steady circulation in a basin with step–shelf, while Figure 6.14 (c) and (d) display the steady circulation in a basin with a step–shelf and a transpolar ridge. The NEMO ocean model parameters used to perform this simulation are given in Table 4.1, and the linear bottom friction was $3 \times 10^{-3}\ ms^{-1}$.

Figure 6.14 (a) shows the ocean circulation driven by the anticyclonic wind stress regime (Figure 6.12 (b)). This wind stress spins–up intense anticyclonic gyres on the shelf and the deep basin. On the eastern shelf a cyclonic boundary current, which changes its direction in the neighbourhood of the anticyclonic gyre, forms a clockwise shelf break boundary current which feeds into the anticyclonic gyre in the western basin. Even though the deep basin is dominated by a strong anticyclonic gyre, there is also a weak cyclonic gyre formed by shelf break currents from the eastern shelf. The impact of a change of wind stress regime is shown in Figure 6.14 (b). In comparison with Figure 6.14 (a), the anticyclonic gyres are considerably decreased in magnitude. The circulation on the eastern shelf is reduced to a weak anticyclonic current close to the shelf break which connects with the anticyclonic gyre on the western shelf.

Figures 6.14 (c) and (d) shows the impact of a trans–polar ridge on the circulation. One of the most striking features when comparing (a) and (c) is the absence of the shelf edge current adjacent to the deep basin. The ridge acts as a conduit for a transpolar current. Further, the anticyclonic gyre on the western shelf relies on the transpolar ridge current to close its circulation. Also, we note that the ridge acts like a wall constraining the anticyclonic gyre in the "NW" deep basin and leaving the other deep basin almost

motionless. The influence of the ridge on the circulation in the presence of a cyclonic wind stress regime is shown in Figure 6.14 (d). Again the ridge acts as a passage linking the "NE" and "SW" sides of the shelf reducing the magnitude of the boundary shelf edge currents on the eastern shelf. As observed in Figure 6.14 (b), the change of wind regime decreases the intensity of the ocean gyres in the shelf and the deep basin.

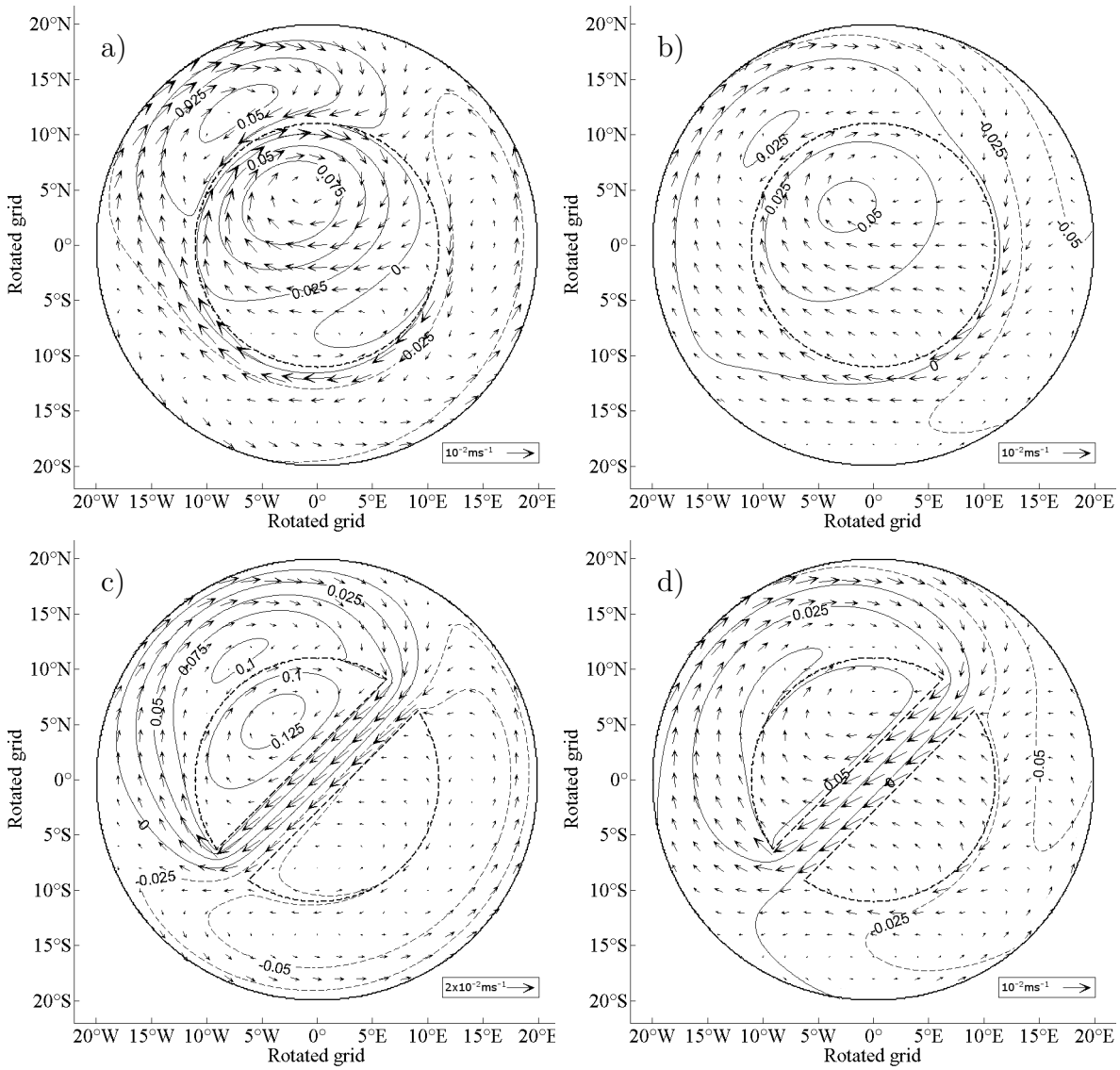

Figure 6.14: Planetary wind–driven flows in a closed basin. a) contours of SSH and barotropic velocity vectors in a step–shelf basin driven by an anticyclonic wind stress regime; b) same as (a) except for the cyclonic wind stress regime; c) same as (a), but in a step–shelf basin with ridge; d) same as (b), but in a step–shelf basin with ridge.

As a final step towards developing a more realistic process model for investigating the wind–driven Arctic Ocean circulation we introduce three gaps (i.e. straits) on the boundary of the basin representative of the Bering, Davis and GINs straits. Once again the circulation will be compared in basins with, and without, a transpolar ridge.

Figure 6.15 shows the contour plot of the SSH field and the barotropic velocities vectors in the steady–state in a basin with three gaps. Figures 6.15 (a) and (b) show the flow circulation in a step–shelf and Figures 6.15 (c) and (d) in a step–shelf with a ridge. The NEMO ocean model parameters used to perform this simulation are given in Table 4.1 and the magnitude of the linear bottom friction was $3 \times 10^{-3}\ ms^{-1}$.

Figure 6.15 (a) shows the steady circulation for the anticyclonic wind stress regime (Figure 6.12 (b)). The GINs inflow bifurcates into three branches. The first, and more intense, with a magnitude of 2.17 Sv recirculates exiting through the same strait (see Table 6.1). The second branch forms a cyclonic boundary current which resembles the North Atlantic current. The third flows towards the Davis Strait merging with the Bering inflow showing a magnitude of 3.183 Sv across section $\overline{HI}$. The cyclonic boundary current changes its direction on the "NE" side of the shelf flowing clockwise close to the shelf–edge. The presence of the anticyclonic gyre on the shelf and in the deep basin interrupts the communication between the Bering and the Davis Straits along the western shelf. A closer look on the "NW" side reveals Bering inflow crossing the shelf break to the deep basin "feeding" the anticyclonic deep ocean gyre. Subsequently, it circulates clockwise until it reaches again the shelf at the neighbourhood of the GINs strait where it crosses again merging with the GINs inflow.

Figure 6.15 (b) shows the steady circulation after changing to a cyclonic wind stress regime (Figure 6.12 (a)). The GINs inflow bifurcates forming two currents; the first, and more intense, recirculates and the second current flows towards the Davis Strait merging with the Bering inflow before exiting the domain. The Bering inflow bifurcates into two boundary currents which flow along the shelf until they reach the GINs current. It is interesting to note that the change of anticyclonic wind stress regime enables a direct link between the Bering and Davis Straits via the shelf (Aksenov *et al.*, 2016). In particular, the Canadian or western shelf supports a cyclonic boundary current with a magnitude of 0.261 Sv (computed transport across section $\overline{AB}$) and the Siberian or eastern shelf supports an anticyclonic branch with a volume transport of 0.504 Sv (computed transport across section $\overline{EF}$). The remaining 0.235 Sv cross the "NW" side of the shelf and merge with deep basin circulation which is governed by a single anticyclonic gyre.

Figure 6.15 (c) shows the steady circulation for an anticyclonic wind stress field in the presence of a ridge. Comparing this with Figure 6.15 (a), the cyclonic boundary current from the GINs strait meets the Bering inflow in the neighbourhood of the ridge and together they form a strong transpolar current with a magnitude of 2.32 Sv (computed

transport across section $\overline{CD}$). Also, we note that the deep basins circulation takes the form of two counter–rotating gyres similar to the ones found in the closed basin (Figure 6.14 (c)).

Figure 6.15 (d) shows the steady circulation for a cyclonic wind stress regime. We note the intensity of the transpolar current is greatly reduced to 1.3 Sv (computed transport across section $\overline{CD}$). Note the transport across the Bering Strait is 1 Sv. The inconsistency of the volume transport across the ridge is due to a cyclonic boundary current from the GINs strait. Even though this current is not visible, it has a magnitude of 0.4 Sv across section $\overline{EF}$. It is interesting that the Bering inflow does not circulate via the Canadian shelf with the change of wind regime as it was observed in the case of a step–shelf without ridge (see isolines in Figure 6.15 (b)). Finally, we briefly discuss the impact of the change of the wind stress from an anticyclonic to cyclonic regime on the transport across the straits (see Table 6.1). Overall we observe a similar behaviour in the step–shelf basin and step–shelf basin with ridge. The GINs inflow increases almost 0.2 Sv (0.215 Sv) whereas the GINS outflow decreases 0.109 Sv (0.121 Sv) in the step–shelf basin with ridge (step–shelf basin). The Davis outflow increase 0.309 Sv (0.374 Sv) in the step–shelf basin with ridge (a step–shelf basin). It is interesting how the variation in the wind stress regime affects differently the boundary flows with depending on the topography. In the presence of a step-shelf basin (see Figure 6.15 (a) and (b)), the strong anticyclonic gyre significantly decreases in magnitude with the change of wind regime. This suggests that there is an emptying of the step-shelf basin via Davis and GINs strait (see second and fourth column in Table 6.1). On the other hand, the change of wind stress in the step-shelf basin with ridge is shown in Figure 6.15 (c) and (d). Even though the outflows across the Davis and GINs strait change they are significantly lower than the step-shelf basin scenario (see third and fifth column in Table 6.1). This could be explained by a strong redistribution of the water between the deep basins.

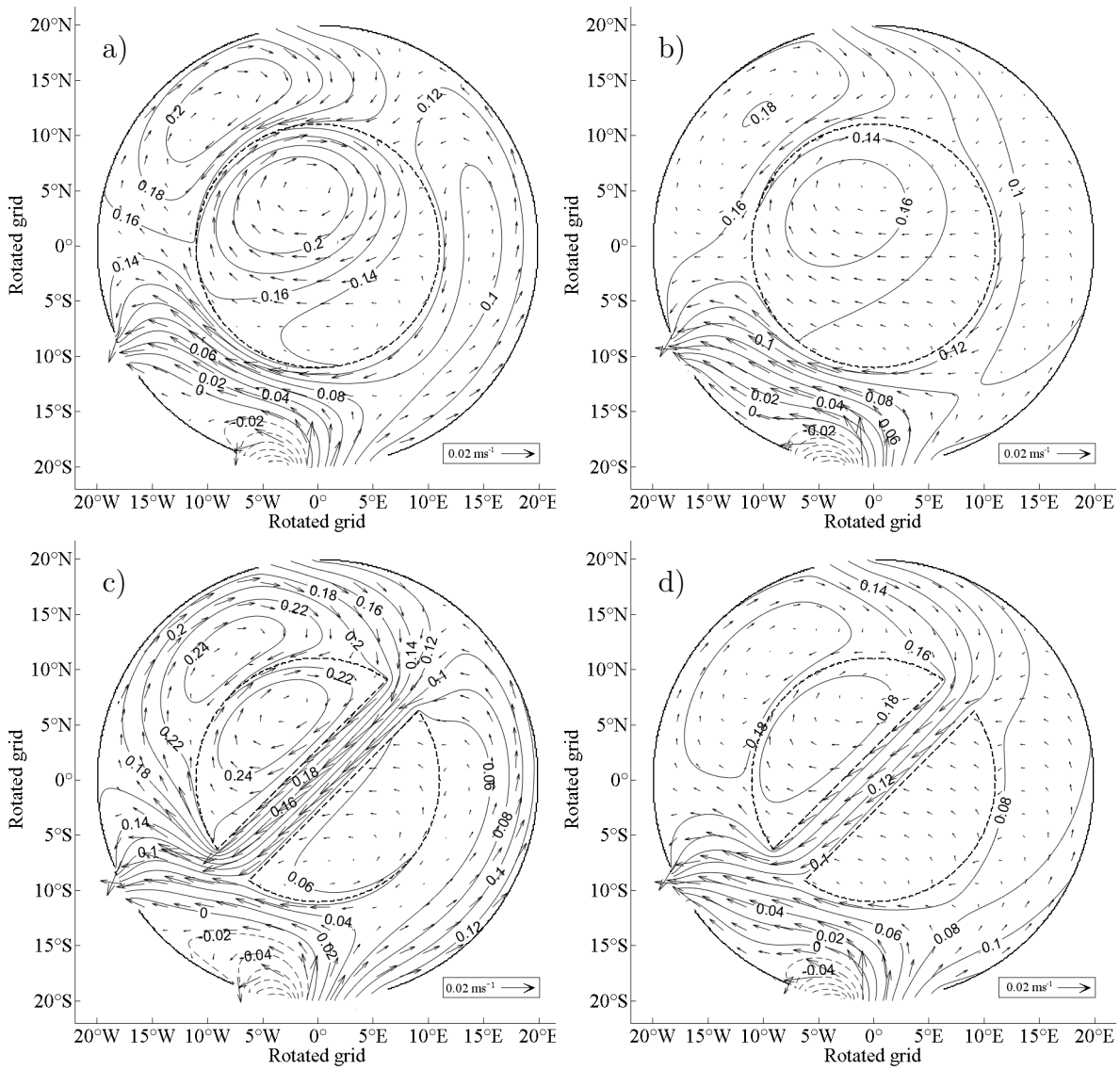

Figure 6.15: Planetary wind–driven flows in a basin with three gaps. a) contours of SSH and barotropic velocities vectors in a step–shelf basin driven by an anticyclonic wind stress; b) same as (a) except for cyclonic wind stress; c) same as (a), but in a step–shelf basin with ridge; d) same as (b), but in a step–shelf basin with ridge

Table 6.1: The transport boundary conditions initially imposed across the straits in the NEMO simulations. The Bering Strait transport is prescribed and held constant through the numerical integration. The transports across the Davis and Nordic Straits are allowed to adjust using a Flather open boundary condition. Note, the sign convection used to denote outflow from the basin is negative.

		Spun–up strait transport for the anticyclonic wind regime		**Spun–up strait transport for the cyclonic wind regime**	
Gap	**Intitial prescribed transport**	**step–shelf**	**step–shelf with ridge**	**step–shelf**	**step–shelf with ridge**
Bering inflow	1	1	1	1	1
Davis outflow	−2.1	−3.170	−3.314	−3.544	−3.623
Nordic inflow	6.5	4.752	4.868	5.005	5.068
Nordic outflow	−5.4	−2.582	−2.554	−2.461	−2.445

6.6 Impact of sea ice on the planetary geostrophic wind–driven ocean circulation

This section studies the dynamical effect of sea ice on wind–driven circulation in a polar basin. In contrast with Chapter 4, these experiments were performed in a closed basin. With sea ice present the shear stress at the ice–ocean interface will not always be equal to the air–ice shear stress. By definition these shear stresses are equal for sea ice in "free drift" except when the Coriolis term becomes significant (Maqueda and Willmott, 2000). In sea ice convergence regions these shear stresses will not be equal. This modification of the "effective shear stress" acting on the ocean will be considered in the closed basin experiments reported in this section.

As in Chapter 4, these experiments were performed using the couple ocean–ice model of NEMO (OPA–LIM2). The ocean model was set–up following methodology of section 6.2 except for the following modifications. The horizontal resolution was set to $0.5^o \times 0.5^o$. We only considered two basin geometries; flat bottom and step–shelf (see Figure 6.1 (a) and (b)).

The LIM2 ice model was also configured following the same methodology as Chapter 4 (see section 4.7). Therefore, the ice thermodynamics are absent and thus ice depth and concentration is only able to change due to convergence and divergence. Note that in a closed basin the total volume of ice is constant during the model integration.

The surface stresses such as the wind stress are incorporated differently when OPA is coupled to LIM2. There are only two available methods to implement the wind stress;*CLIO* and *CORE bulk formulae*. Between these two, the wind stress was imposed using CORE because it is more amendable than *CLIO*. *CORE* requires the wind velocity components (i.e. τ^{φ_r} (*sn_wndi*) and in τ^{ϕ_r} (*sn_wndj*)), incoming short wave radiation (*sn_qsr*), incoming long wave radiation (*sn_qlw*), the temperature of the air (*sn_tair*), humidity (*sn_humi*), total precipitation (*sn_prec*), solid precipitation (*sn_snow*). As can be seen *CORE* is a complex routine which determines the effective wind stress from different aspects. For these idealistic experiments, we consider the same wind stress curl as section 2 (see Figure 6.2 (b)). Therefore, the forcing files from section 2 were converted in terms of wind speed and the remaining atmospheric parameters were set zero. NEMO uses the routine *sbcblk_core.F90* to implement the wind stress. Since most of the parameters were set to zero, the latter routine had to be modified (see Appendix E.3).

The initial conditions for velocity, SSH, temperature and salinity were set as section 2 and they remain constant during the computational integration. In addition, the polar basin is initially covered with a uniform depth and concentration of sea ice which is at rest as specified. The sea ice depth/concentration can change from their initial values due to sea ice velocity convergence/divergence. In all the numerical experiments the initial sea ice concentration is 1.0 and we consider two scenarios for the initial sea ice depth; $0.05m$ and $0.5m$.

First we recall the steady circulation in a closed basin without sea ice because this problem was not previously investigated in this thesis. Figure 6.16 (a) and (b) shows the contours of SSH and the barotropic velocity vectors of a closed basin without topography and a basin with a step–shelf, respectively. We note that these figures are qualitative the same as their equivalent with two gaps shown in Figure 6.3 (a) and Figure 6.4 (a). The main difference occurs close to the straits where the flow enters/exits the basin. Also, the volume transport of the ocean gyres are qualitatively weaker in comparison with the basin with two diametrically opposed straits.

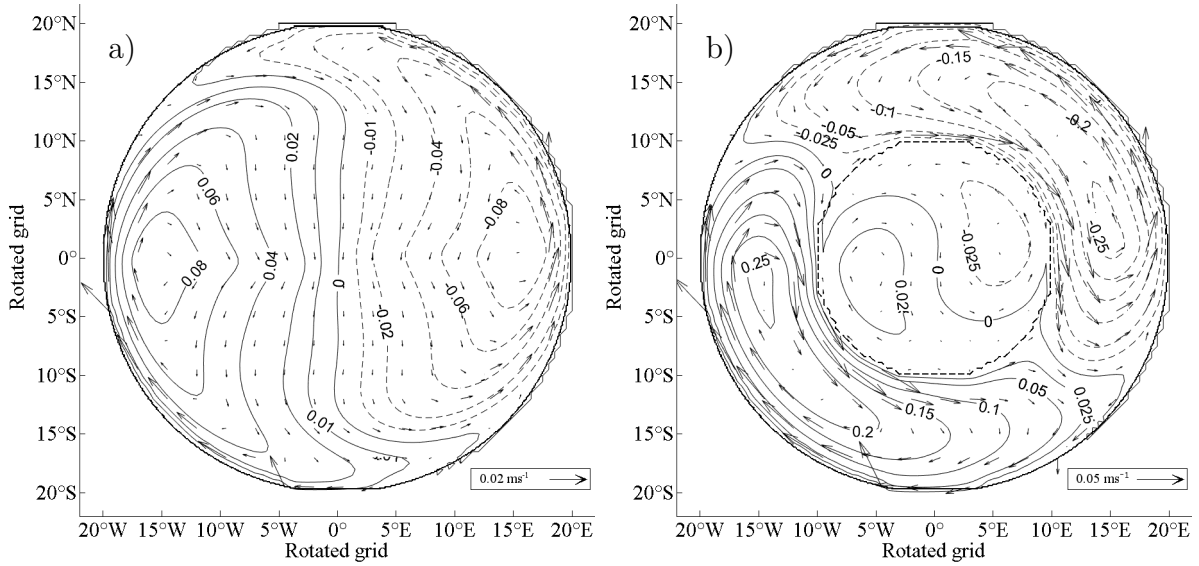

Figure 6.16: Wind–driven planetary circulation in a closed basin; a) contours of SSH and barotropic velocity vectors in flat bottom basin; b) contours of SSH and barotropic velocity vectors in step–shelf basin.

Figure 6.17 (a) shows contours of SSH and the barotropic velocity vectors for a flat bottom basin initially cover by a sea ice thickness of $0.05m$ and concentration of 1.0. The ocean circulation is qualitatively the same as in Figure 6.16 (a), although the shape of the "western" ocean gyre has been slightly altered by the convergence of the sea ice forming land-fast ice from the North Pole to the wall of the western domain (see Figure 6.17 (b)). Figure 6.17 (c) shows contours of SSH and the barotropic velocity vectors for a flat bottom basin initially covered by a sea ice depth of $0.5m$ and concentration of 1.0. We observe the steady ocean circulation has significantly changed showing a strong anticyclonic ocean gyre which covers almost the entire basin. The sea ice depth distribution is shown in Figure 6.17 (d). There is land–fast ice in the "Northern" side of the basin due to the wind and ocean interaction. In the "Southern" side of the basin, the clockwise wind stress regime is in the same direction as the ocean boundary currents. However, in the "Northern" side of the basin the wind stress regime is cyclonic and the ocean boundary current is anticyclonic. Therefore, the sea ice is being "piled–up" in the "Northern" side. In addition, we observe a sea ice convergence in the centre of the basin linked to land–fast ice by a narrow "bridge" located on the "western" side of the basin where the wind stress curl is zero.

The impact of a step–shelf on the steady planetary geostrophic ocean circulation is shown in Figures 6.18 and 6.19. Figure 6.18 (a) shows contours of SSH and barotropic velocity vectors in a basin initially covered by a sea ice depth of $0.05m$ and concentration

of 1.0. Visually, we cannot observe any difference with respect to Figure 6.16 (b). Figure 6.18 (b) displays the difference between Figures 6.18 (a) and in 6.16 (b). Note the contours of SSH are in millimetre units. As in the flat bottom scenario, there are subtle differences in the "western" side of basin or more specifically the "western" side of the step–shelf and part of the deep basin. This is probably a consequence of the sea ice convergence on the western shelf edge and deep basin (see Figure 6.18 (c)). The impact of an initial sea ice depth of $0.5m$ and concentration of 1.0 on the barotropic ocean circulation is shown in Figure 6.19 (a). The impact of the sea ice on the ocean circulation is not as pronounced as previously observed in the flat bottom scenario due to the high velocity currents on the shelf. Nevertheless, we observe some clear changes compared with Figure 6.18 (a). The western ocean gyre on the step–shelf is less intense than the eastern ocean gyre on the step–shelf. This interesting asymmetric structure could be explained by the location of land–fast ice in the step–shelf as shown in Figure 6.19 (b)). The "tongue" of land –fast ice could be the responsible for the single cyclonic gyre in the deep basin.

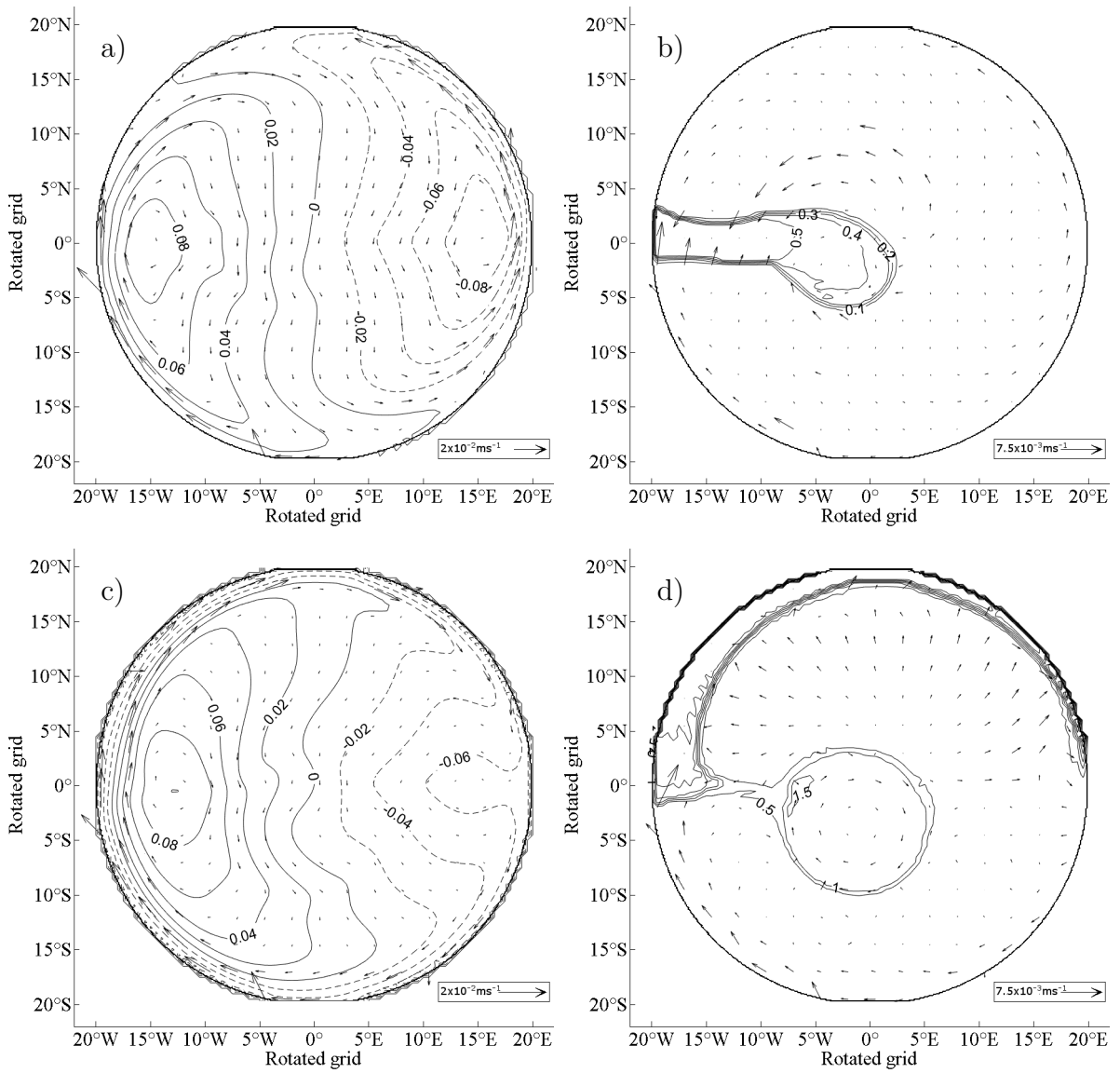

Figure 6.17: Wind–driven planetary circulation coupled to dynamic sea ice in a flat bottom basin; a) contours of SSH and the barotropic velocity vectors; b) contours of sea ice depth and sea ice velocity vectors. In (a) and (b) the initial sea ice depth was $0.05m$ and ice concentration of 1.0. c) As (a) except the initial sea ice depth was $0.5m$; d) As in (b) except the initial sea ice depth was $0.5m$.

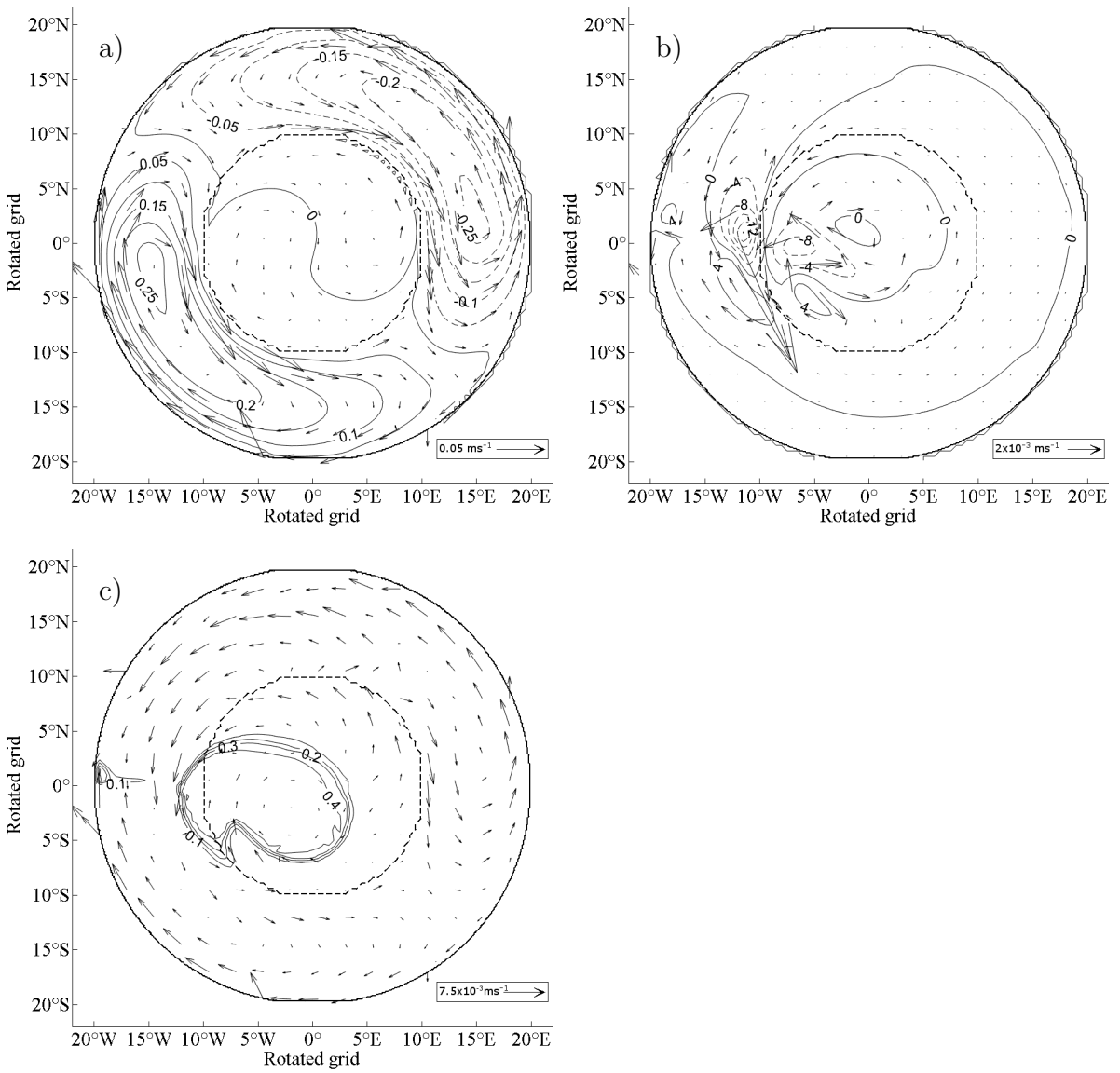

Figure 6.18: Wind–driven planetary circulation coupled to dynamic sea ice in a step–shelf basin; a) contours of SSH and the barotropic velocity vectors; b) anomaly SSH in mm and anomaly velocity vector between (a) and Figure 6.16 (b) c) contours of sea ice depth and sea ice velocity vectors. Note the initial sea ice depth was $0.05m$ and ice concentration of 1.0.

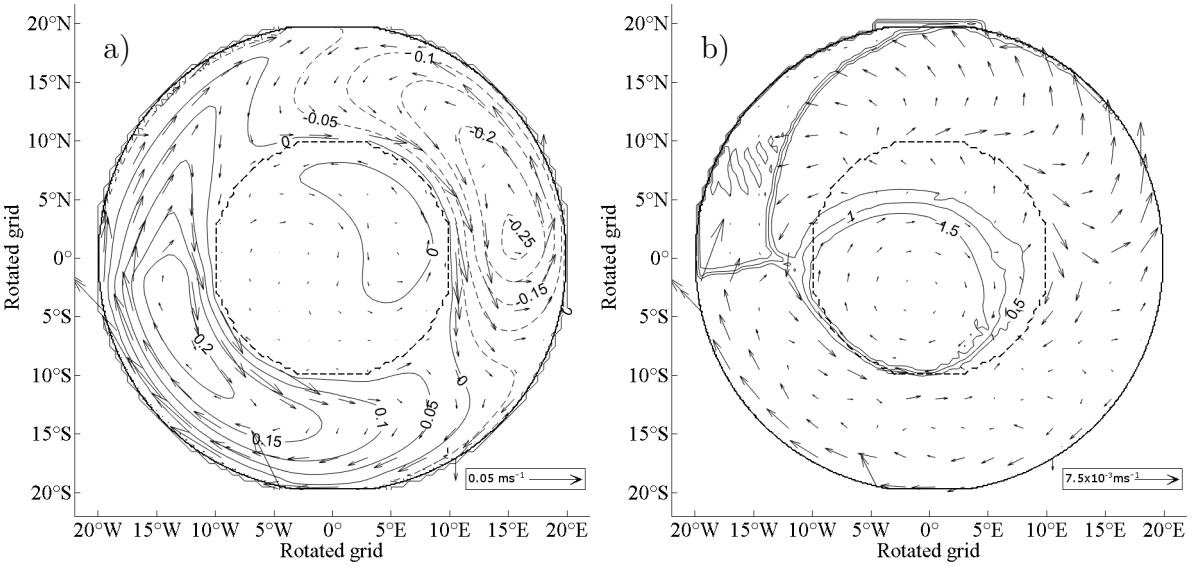

Figure 6.19: Wind–driven planetary circulation coupled to dynamic sea ice in a step–shelf basin; a) contours of SSH and the barotropic velocity vectors; b) contours of sea ice depth and sea ice velocity vectors. Note the initial sea ice depth was $0.5m$ and ice concentration of 1.0.

6.7 Conclusions

In this chapter we studied wind–driven circulation in a polar basin using the ocean global numerical model NEMO. The aim of this chapter was to evaluate the accuracy of the approximate analytic solution discussed in Chapter 5 by comparison with the equivalent NEMO simulations. The versatility of the NEMO model is then used to explore the wind–driven circulation in a basin with a step–shelf and a transpolar ridge. These experiments are conducted in (i) a closed polar basin (ii) in a basin with three straits representative of the Bering, Davis and GINs straits.

First, we have compared the analytical solutions with the numerical simulations. Both solutions were qualitatively very similar except for the flat bottom basin. NEMO simulation displayed a wedge in the transition area where the wind stress curl changes sign. This structure was not observed in the analytical solutions. We also saw quantitatively that the analytic solutions had a better agreement with the numerical simulations when the the fixed colatitude, θ_f, in coefficients of the potential vorticity equation (5.6) was set to θ_B (i.e. the colatitude at the basin boundary).

Second, the addition of ridge had a strong impact on the steady circulation. In particular in the deep basin the presence of a ridge leads to two pairs of counter–rotating gyres.

The ridge orientation played an important role in the formation of connected western boundary currents on the ridge. Also, we note on the narrow step–shelf basin that the cyclonic shelf branch is always stronger that the anticyclonic branch whereas in Chapter 4 we saw their magnitude was highly dependent on the orientation of the ridge.

Third, we examined more realistic wind stress regimes representative of those observed in the Arctic Ocean in closed and three gap basins. Overall cyclonic boundary currents are developed in the Siberian shelf in the presence of the anticyclonic wind stress whereas these currents are greatly diminished by the effect of the cyclonic wind regime (see Figure 6.14). The addition of gaps reveals the importance of the wind regime in the communication between Bering and Davis Strait in the step–shelf basin. In particular, we observed that the Bering–Davis branch via the Canadian shelf is interrupted in the presence of the anticyclonic wind stress regime. The change of wind stress regime produces a cyclonic current from the Bering strait via the western shelf. The switch of the Davis–Bering current direction agrees with the numerical experiments performed with realistic topography by Aksenov *et al.* (2016). The addition of a ridge also has a strong effect on the shelf circulation, forming an intense transpolar current linking the Bering with the Davis Strait.

Finally, we considered a closed basin in presence of a sea ice with different initial ice depths. The presence of sea ice can dramatically affect the transfer of the momentum associated with the wind (Davis *et al.*, 2014). In presence of thick sea ice (initially $0.5m$), the steady circulation in the flat bottom basin is reduced to a single anticyclonic ocean gyre forming a strong clockwise boundary current. In the case of a step–shelf basin, the impact of the sea ice on the steady circulation is only significant when the initial sea ice depth is of the order of $0.5m$. In particular, the western gyres on the shelf and in the deep basin decrease in magnitude due to the land–fast ice on the shelf.

Chapter 7

SSH anomalies driven by unsteady volume transports through straits

7.1 Introduction

The previous chapters have studied the source/sink–driven circulation in an idealised polar basin. Up to this point the prescribed sources and sinks were steady. In this chapter we investigate the structure of SSH anomalies driven by prescribed fluctuating transport across one, or more, of the gaps (i.e.straits) on the polar basin boundary.

The volume transport through the straits connecting the Arctic Ocean to its marginal seas undergo variability across a wide range of time scales. For example, the Bering Strait transport variability spans time scales ranging from hours to interannual driven by the combination of wind stress, the pressure head associated with the along-strait SSH difference and remotely forced shelf waves (Danielson *et al.*, 2014). Within the Arctic basin the SSH anomalies calculated from dynamic topography reveal complex behaviour (Koldunov *et al.*, 2014). These authors show that in the 2000s the SSH anomalies in the Arctic Ocean interior are out of phase with the equivalent shelf anomalies, but in phase (i.e. co–oscillating) in the following decade.

With the advent of Cryosat 2 altimeter data (Wingham *et al.*, 2006) the structure of the SSH field in the Arctic is beginning to be revealed (Jin *et al.*, 2012; Gray *et al.*, 2015; Armitage *et al.*, 2016). Given that the SSH anomaly field in the Arctic can be routinely calculated using a combination of satellite and hydrographic data (increasingly collected by autonomous vehicles such as gliders) this may open the possibility of performing an inverse problem to determine volume transport through the Bering, Canadian Archipelago

and Greenland–Iceland–Norwegian Sea straits.

We first calculate the SSH anomalies forced by a prescribed unsteady (harmonic) source and sink which are exactly in phase. Subsequently, across one strait at a time varying transport (again harmonic) into the domain is prescribed (source) while an open boundary condition is employed at the other strait. In this type of experiment the ocean dynamics are responsible for determining the outflow. Finally as a step towards a more realistic representation of the Arctic basin, we consider a basin with three straits of the type firstly described in Chapter 2.

7.2 NEMO model description

We consider numerical solutions of a barotropic ocean in a circular polar basin driven by sources/sink flows. As in previous chapters, the numerical simulations use the ocean circulation model NEMO (Madec, 2008) retaining the filtered non-linear free surface algorithm. As in previous chapters we consider circular basin where the North Pole is located in the centre of the grid. The horizontal resolution was set to $0.1^o \times 0.1^o$. The vertical grid employed varies with the configuration of the bathymetry. The flat bottom scenario had two levels of 500 m each whereas the step-shelf and step-shelf with ridge had eight levels with a resolution of 125 m. These levels produce a total depth of 1000 m in the deep basin. Figure 7.1 shows the bathymetries used in this chapter for a basin with two gaps.

The implementation of the NEMO model with unstructured open boundaries varied depending on the section. For the first set of experiments a basin with two open boundaries, or straits, is considered (see Figure 7.1 (a)). The ocean circulation is spun–up to a steady–state by a prescribed steady source (inflow) and sink (outflow), which takes a simulated 3 years. We then prescribed a time periodic transport anomaly of the form $a \sin(\omega t)$ across each strait where a is the amplitude, ω is the angular velocity and $T = 2\pi\omega^{-1}$ is the anomaly period. In this experiment there is no net change in the volume of the fluid in the domain at any time. What enters the domain through one strait exits at the other. Appendix F.1.1 and F.1.2 display a copy of the FORTRAN routines which were modified to reproduce this type of boundary flow in the NEMO experiments. In reality we would expect an "adjustment time" to emerge if the inflow across one strait varies with time. Ocean dynamics will be responsible for carrying the "inflow signal" to the outflow strait. To capture this process the two straits basin experiment is modified as follows. Unsteady

(harmonic) transport is imposed at one strait (source) and the Flather open boundary condition (Flather, 1994) is imposed at the other strait (sink). Thus, at any instant the volume of the fluid in the domain is either increasing or decreasing, due to the finite time that information takes to travel from the inflow to the outflow strait. The Appendix F.2.1 and F.2.2 show a copy of the modified FORTRAN subroutines used in the third and fourth section, respectively.

The initial conditions for salinity, sea surface height, temperature and velocity are computed in *istate.F90*. We set salinity and temperature to 35.5 psu and 2^oC, respectively and they remain fixed throughout the model integration. The initial velocity field and the sea surface elevation are set to zero.

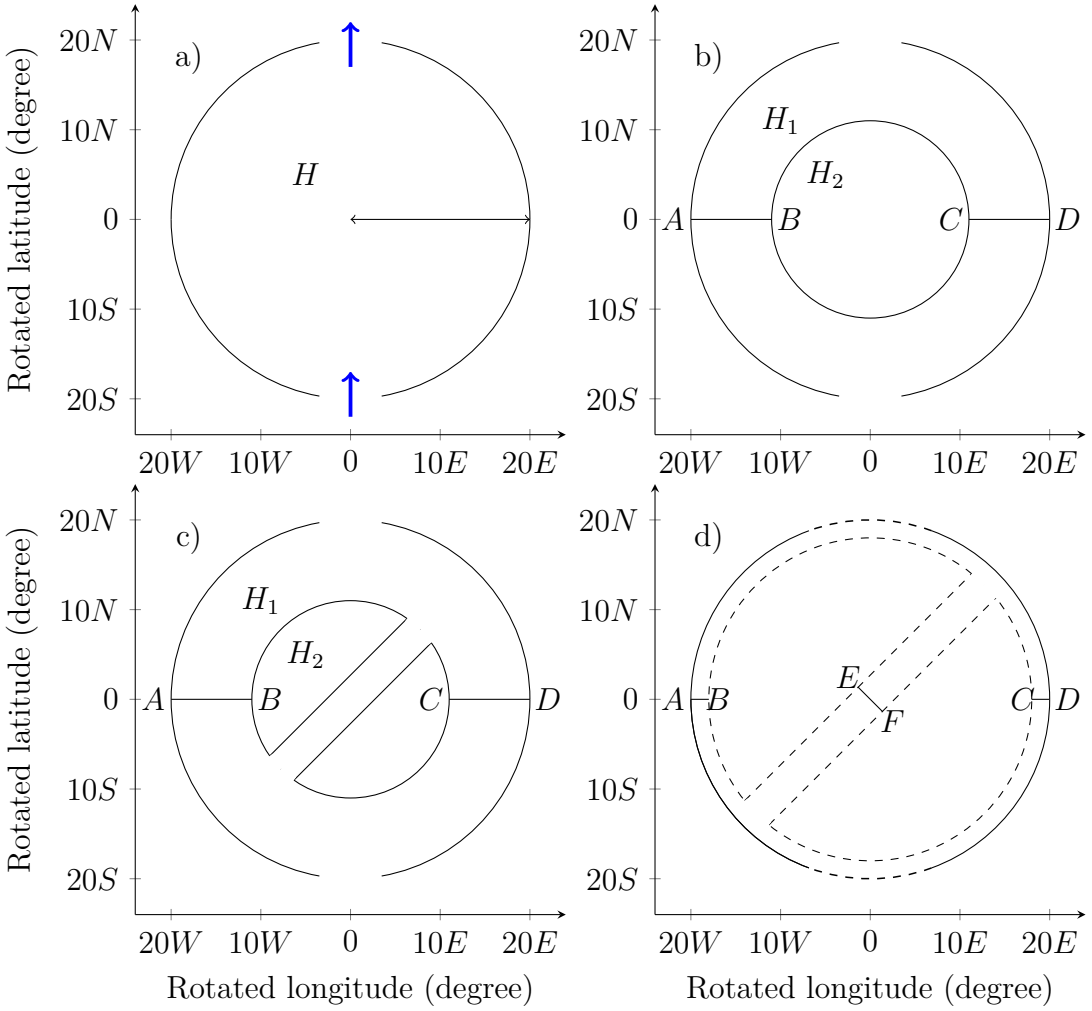

Figure 7.1: Schematic of; a) flat bottom basin; b) step-shelf basin; c) basin with step-shelf and ridge the top of which is level with the shelf; d) same as (c) except in a narrow step shelf.

7.3 SSH anomalies prescribed across both straits

This section calculates the SSH anomalies forced by a transport fluctuation across both straits in circular polar flat bottom basin with two straits (see Figure 7.1 (a)). A source–sink flow circulation is spun–up. Using the same ocean basin parameters as the flat bottom experiment in Chapter 4 (see Table 4.1), we observe that this type of flow reached the steady state in less than three years (see Figure 4.4). Once it reached this point, a transport fluctuation is prescribed in the inflow and the outflow of the form $a\sin(\omega t)$. Table 7.1 lists the amplitude, a, of the transport anomaly and the period $T = 2\pi\omega^{-1}$ used for the experiments.

The numerical experiments are listed in Table 7.1 and 7.2. Table 7.3 shows the planetary wave periods associated with the $1000m$ deep basin employed in experiments SSHA1 to SSHA5. These periods are calculated from the dispersion relation (3.25), and are used in SSHA1 to SSHA4. We observe from Table 7.3 that $T_{-2,1}$ and $T_{-3,1}$ are close in value which is sometimes referred to as "kissing" modes in wave dynamics (Allen, 1975). A consequence of this phenomenon is that the wave structure associated with $T_{-2,1}$ is also manifest in the experiment with a period anomaly of $T_{-3,1}$ (or vice-versa). One method to avoid this problem is to obtain the eigenfrequencies for a different depth where $T_{m,n}$ are more isolated. Experiments SSHA6 and SSHA7 display eigenfrequencies obtained by the dispersion relation (3.25) using a depth of $250m$. We note the eigenfrequencies associated with the modes $T_{-2,1}$ and $T_{-3,1}$ are now well separated (see Table 7.2).

Table 7.1: Summary of the boundary forced SSH anomaly numerical experiments in a flat bottom polar basin.

Numerical experiment	**Domain characteristics**	**Depth (m)**	**Transport anomaly period** (*days*)	**Transport anomaly magnitude** (a)	**Steady boundary transport**
SSHA1	Flat bottom 2 gaps	1000	$T_{-1,1}$ (101)	0.5 Sv	5 Sv
SSHA2	Flat bottom 2 gaps	1000	$T_{-1,2}$ (217)	0.5 Sv	5 Sv
SSHA3	Flat bottom 2 gaps	1000	$T_{-2,1}$ (74)	0.5 Sv	5 Sv
SSHA4	Flat bottom 2 gaps	1000	$T_{-3,1}$ (76)	0.5 Sv	5 Sv
SSHA5	Flat bottom 2 gaps	1000	30	0.5 Sv	5 Sv

Table 7.2: Summary of the boundary forced SSH anomaly numerical experiments in a flat bottom polar basin.

Numerical experiment	**Domain characteristics**	**Depth (m)**	**Transport anomaly period** (*days*)	**Transport anomaly magnitude** (*a*)	**Steady boundary transport**
SSHA6	Flat bottom 2 gaps	250	$T_{-2,1}$ (138)	0.5 Sv	5 Sv
SSHA7	Flat bottom 2 gaps	250	$T_{-3,1}$ (118)	0.5 Sv	5 Sv

Figures 7.2 and 7.3 show the instantaneous SSH anomalies field for numerical experiments SSHA1, 2, 4, 5, 6 and 7. The SSH anomaly is calculated by subtracting the steady-state boundary forced SSH field from the unsteady SSH field forced by the unsteady transport through one, or more, straits. The time at which the anomaly field is plotted is expressed as a fraction of T. The integral of the anomaly fields across the domain is zero in all plots of Figure 7.2 and 7.3 reflecting the fact that the imposed source and sink transport perturbations are exactly in phase. Thus, at any instant there is no change in the volume of the fluid inside the domain.

Table 7.3: Planetary wave period in days ($T_{m,n} = \pi\left(\Omega\sigma_{m,n}\right)^{-1}$) calculated from (3.25) using the ocean basin parameters of Table 4.1.

$m =$	-1	-2	-3	-4
$n = 1$	101	74	76	85
2	217	132	115	114
3	410	229	179	162
4	681	364	269	230
5	1,029	538	385	317

Figure 7.2 (a) shows a plot of the SSH anomaly field plotted at $t = 0.5T$ associated with the forcing period $T_{-1,1} = \pi\left(\Omega\sigma_{-1,1}\right)^{-1} = 101$ days. It takes the form of a two cell counter–rotating vortex field in the domain interior that propagates clockwise, the direction of planetary wave phase propagation (see Chapter 3). Figure 7.2 (b) shows the equivalent plot for the forcing period $T_{-1,2} = \pi\left(\Omega\sigma_{-1,2}\right)^{-1} = 217$ days. Recall that the index m and n denotes the azimuthal and meridional wave structure. In the domain interior there are four counter–rotating vortices associated with the $\sigma_{-1,2}$ mode. Figure 7.3 (a) shows the contour plot for a forcing period $T_{-3,1} = \pi\left(\Omega\sigma_{-3,1}\right)^{-1} = 76$ days. In the

interior we observe three pairs of waves propagating clockwise which agree with regard to the number of of waves in the radial direction. We do not show experiment SSHA3 because the anomaly field was the same as experiment SSHA4. This is probably caused by the"kissing wave phenomenon". Figure 7.3 (b) shows the anomaly field when the forcing period is 30 days (corresponding to experiment SSHA5). Propagating planetary waves are not possible for this (short) period and the SSH anomaly is an evanescent field decreasing in amplitude with increasing radial distance from the domain boundary.

Experiments SSHA6 and 7 are shown in Figure 7.3 (c) and (d), respectively. Figure 7.3 (c) shows a contour plot of the anomaly field with a forcing period $T_{-2,1} = \pi \left(\Omega\sigma_{-2,1}\right)^{-1} =$ 138 days that is characterised by a clockwise propagating two pairs of counter–rotating vortices. The number of waves agree with the period $T_{-2,1}$ displaying two pairs of planetary waves. Figure 7.3 (d) shows a contour plot of the anomaly field with a forcing period $T_{-3,1} = \pi \left(\Omega\sigma_{-3,1}\right)^{-1} = 118$ days. Again, we observe two pairs of waves travelling clockwise instead of three pair of waves as would be expected. In this shallow basin the anomaly structure forced by the $T_{-2,1}$ boundary anomaly is not properly "separated" from that forced by $T_{-3,1}$ boundary anomaly.

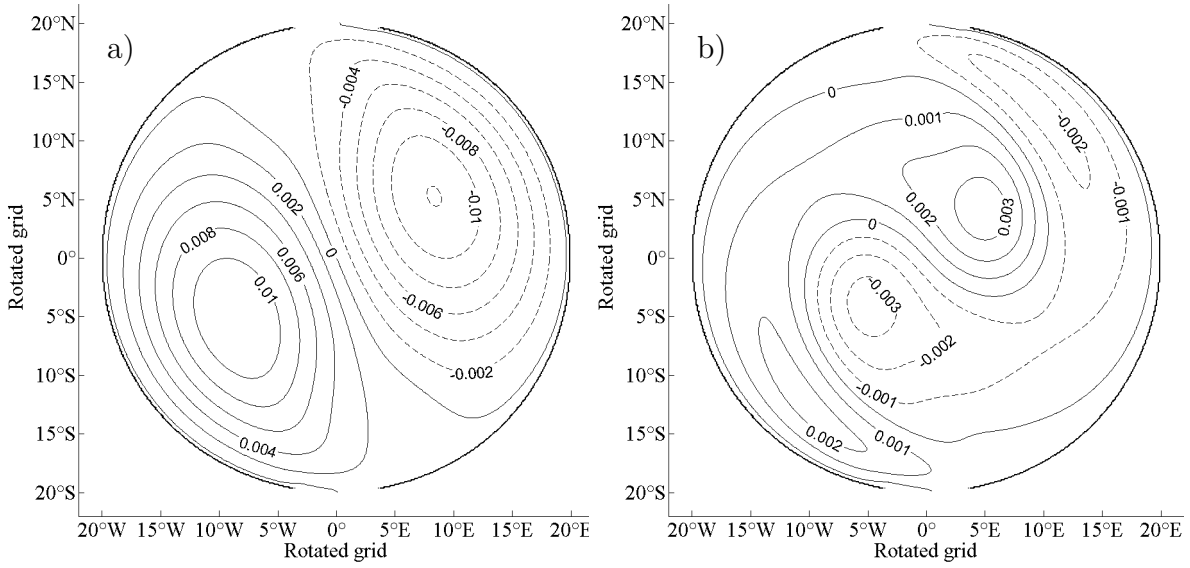

Figure 7.2: Plot of the SSH anomaly field associated with the source–sink planetary geostrophic flows with a periodic transport anomaly imposed at the inflow/outflow a) SSHA1; b) SSHA2. The continuous (dashed) contours denote positive (negative) sea surface elevation in metres.

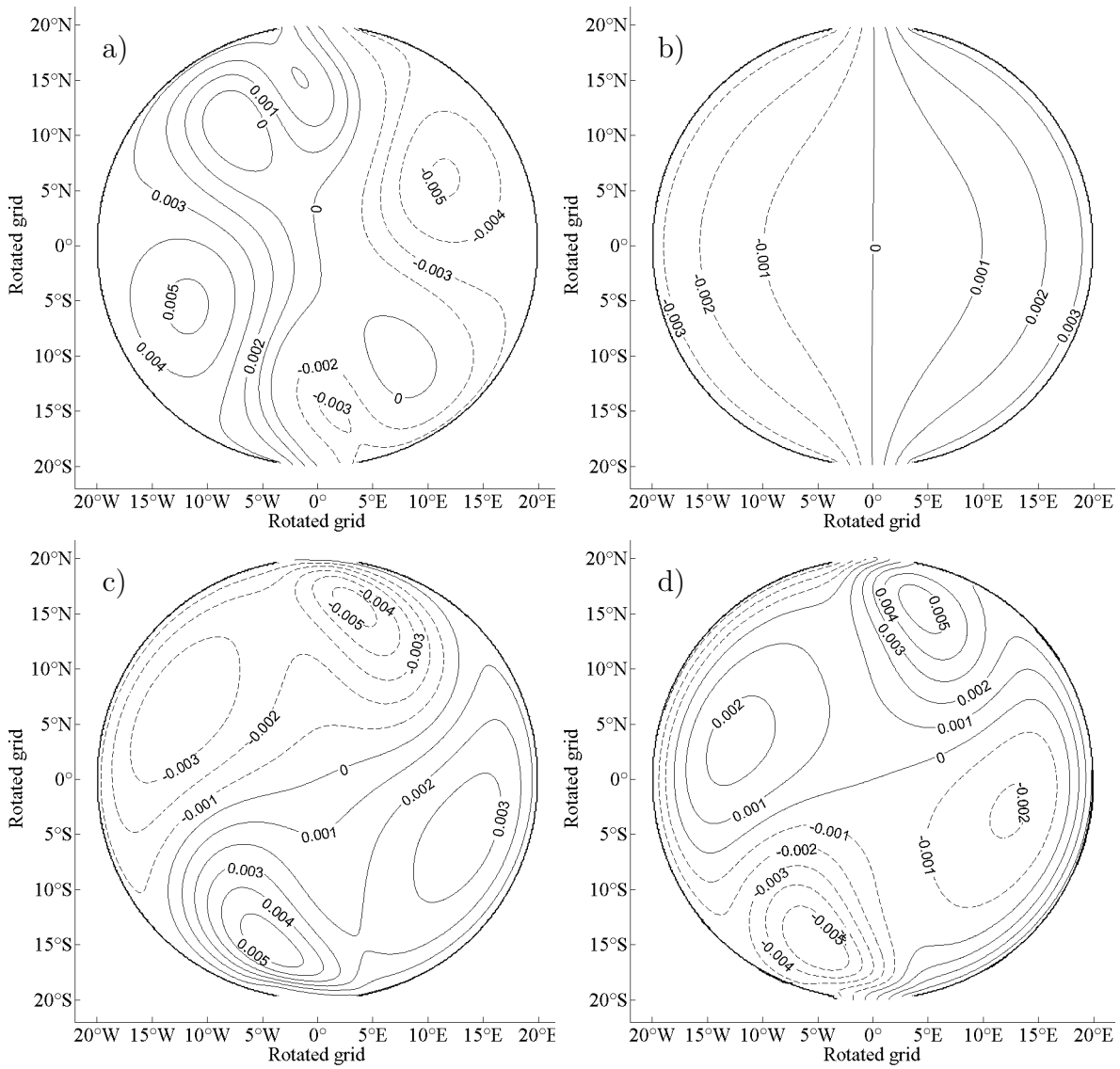

Figure 7.3: Plot of the SSH anomaly field associated with the source–sink planetary geostrophic flows with a periodic transport anomaly imposed at the inflow/outflow a) SSHA4; b) SSHA5; c) SSHA6; d) SSHA7. The continuous (dashed) contours denote positive (negative) sea surface elevation in metres.

7.4 Experiments with open boundary condition imposed at the outflow

In the previous section we studied the effect of a periodic variation in the inflow and the outflow. In reality, changes in the transport through the strait will result in wave propagation. At some point it will modify the transport in the other strait. Here, we investigate this adjustment process.

Numerical experiments SSHA8 to SSHA13 are summarised in Table 7.4 and 7.5 and they all share a common methodology for imposing the unsteady forcing at the inflow strait. As in the previous section the ocean basin parameters used to performed these experiments are listed in Table 4.1. At the outflow strait the Flather (1994) open boundary condition is imposed. Clearly, SSHA8 and 9 will be compared with SSHA1 and 5, respectively. The introduction of a ridge, the top of which is level with the step shelf, in SSHA 12 and 13 allows another potential pathway for the circulation flowing from source to sink. The anomaly period in SSHA10 to SSHA13 is chosen to be annual, which is of course one of the dominant (astronomical in origin) signals in the oceans, and more generally the climate system. We also note that there is no analytic dispersion relation available for barotropic vorticity waves in a polar basin with step-shelf and a ridge, which retains the variation of the Coriolis parameter with the co–latitude.

Table 7.4: Summary of the boundary forced SSH anomaly numerical experiments in a polar basin where an open boundary condition is also imposed.

Numerical experiment	**Domain characteristics**	**Boundary forcing**	**Transport anomaly period** (*days*)	**Transport anomaly magnitude**	**Steady boundary transport**
SSHA8	Flat bottom 2 gaps	Transport anomaly imposed at inflow and Flather boundary condition imposed at the outflow	$T_{-1,1}$ (101)	0.5 Sv	5 Sv
SSHA9	Flat bottom 2 gaps	Transport anomaly imposed at inflow and Flather boundary condition imposed at the outflow	30 days	0.5 Sv	5 Sv

Table 7.5: Summary of the boundary forced SSH anomaly numerical experiments in polar basins with varying idealised topographies.

Numerical experiment	**Domain characteristics**	**Boundary forcing**	**Transport anomaly period** (*days*)	**Transport anomaly magnitude**	**Steady boundary transport**
SSHA10	Wide step-shelf 2 gaps	Transport anomaly imposed at inflow and Flather boundary condition imposed at the outflow	365 days	0.5 Sv	5 Sv
SSHA11	Narrow step-shelf 2 gaps	Transport anomaly imposed at inflow and Flather boundary condition imposed at the outflow	365 days	0.5 Sv	5 Sv
SSHA12	Wide step-shelf Ridge 2 gaps	Transport anomaly imposed at inflow and Flather boundary condition imposed at the outflow	365 days	0.5 Sv	5 Sv
SSHA13	Narrow step-shelf Ridge 2 gaps	Transport anomaly imposed at inflow and Flather boundary condition imposed at the outflow	365 days	0.5 Sv	5 Sv

Figure 7.4 (a) shows a contour plot of the steady SSH and the depth-integrated transport vectors from the control simulation (i.e. without perturbation) of experiments SSHA8 and SSHA9 after 3 years of time integration. We observe that the steady–state obtained using the Flather open boundary condition on the outflow is qualitatively the same as the Figure 4.5 where the inflow and outflow were prescribed. This comparison inspires confidence that the open boundary condition is working sensibly.

Figure 7.4 (b) and (c) show the SSH anomaly field at $t = 0.25T$ and $t = 0.75T$, respectively for experiment SSHA8. The anomaly field behaviour is again characterised by a clockwise propagating forced planetary field taking the form of two counter-rotating gyres. However, during the first half of the forcing period there is a net increase in the volume of the fluid in the basin, reaching a maximum at $t = 0.25T$ (see Figure 7.4 (b)). During the second half of the forcing period the fluid volume decreases in the domain, reaching a minimum at $t = 0.75T$ (see Figure 7.4 (c)). When the forcing period is reduced to 30 days the SSH anomaly field takes the form of an evanescent structure with amplitude decaying with increasing distance from the domain boundary as shown in Figure 7.4 (d) for experiment SSHA9. This evanescent anomaly field also exhibits a "filling" and "emptying" behaviour reflecting the fact that there is a finite, non-zero, time for the imposed inflow anomaly transport to exit at the sink strait.

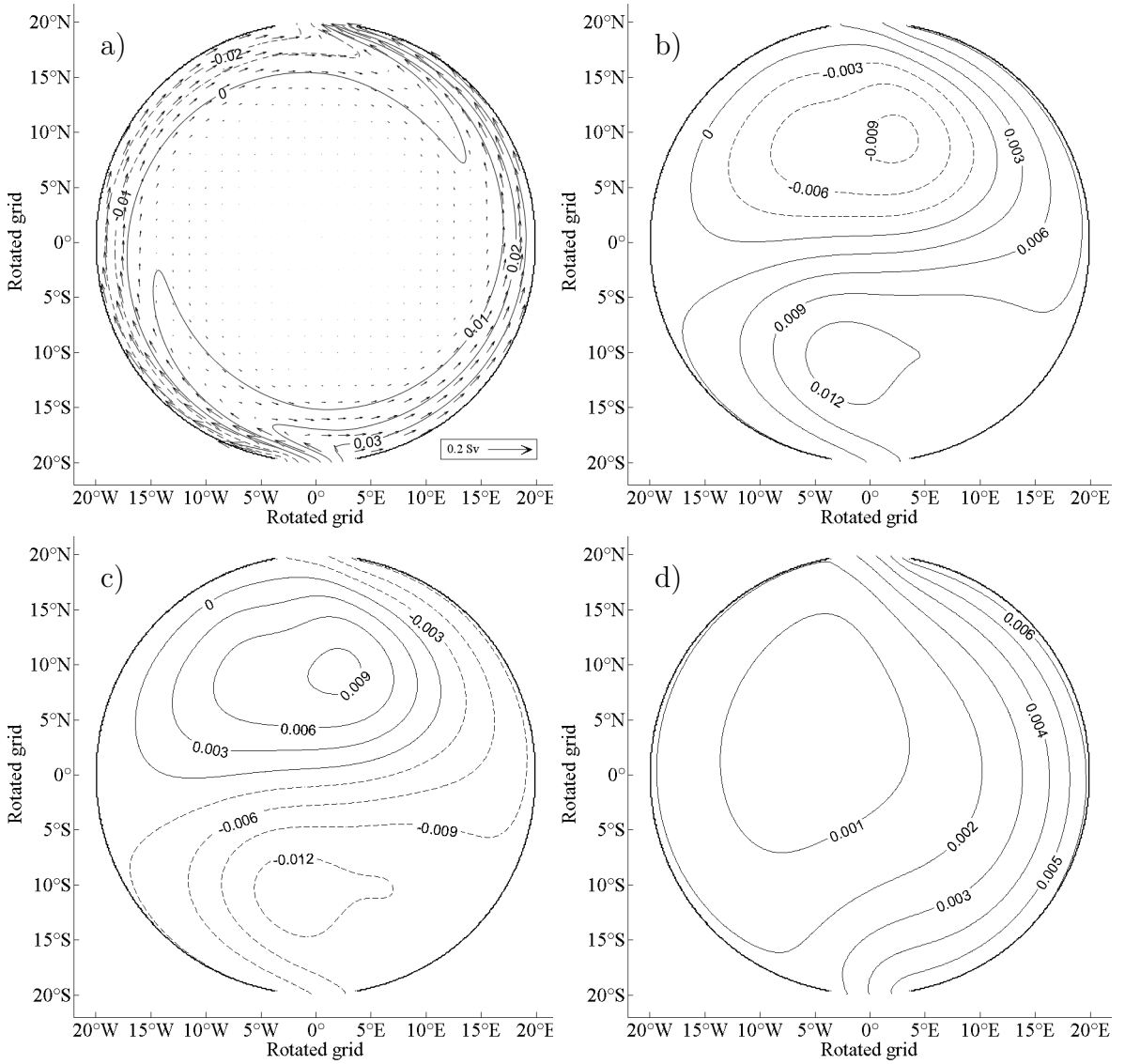

Figure 7.4: Source–sink flows with the Flather open boundary condition imposed at in the outflow; a) SSH field with depth–integrated transport vectors associated with the steady–state circulation; b) SSH anomaly field for SSHA8 at $t = 0.25T$; c) as (b) except $t = 0.75T$; d) SSH anomaly field for SSHA9 at $t = 0.5T$. Continuous (dashed) lines denote positive (negative) sea surface elevation in metres.

So far we have only considered sea surface anomalies in a flat bottom basin. Now, we introduce the effect of the bathymetry on the anomaly propagation. Firstly, we study the influence a basin with a step-shelf in experiments SSHA10 and SSHA11. Figure 7.5 (a) and (b) show contour plots of the sea surface anomaly field with depth-integrated transport vectors at $t = 0.25T$. These experiments assess the anomaly structure field on both a wide and narrow step-shelf. The width of the "wide shelf" exceeds the bottom friction boundary layer while the opposite is true for the narrow width shelf. For a basin with the geometric characteristics of Table 4.1 and a linear bottom friction of 5×10^{-4}

ms^{-1} the frictional boundary layer is $W \sim (\mu/(H_1 2\Omega))^{1/2} R \sin\theta$ where Ω and R are the velocity of rotation and the radius of the Earth. The frictional boundary layer on the polar plane is approximately 255 km.

Figure 7.5 (a) shows the circulation for a wide step-shelf with a width of 1000 km. It can be noted the major part of the anomaly flows forming a strong cyclonic current of 0.505 Sv (computed transport across the section $\overline{CD}$). The anticyclonic branch is nearly stagnant compared with the former one. The deep basin supports a weak rim anticlockwise circulation of 0.074 Sv. Figure 7.5 (b) displays the SSH anomaly and anomaly velocity field circulation in a narrow shelf with a width of 200 km. Here, we observe that the anomaly field on the shelf forms two boundary currents with similar intensity. The cyclonic and anticyclonic branch have a magnitude of 0.268 Sv and 0.185 Sv, respectively, at the cross section $\overline{CD}$ and $\overline{AB}$. The deep basin supports an anticlockwise circulation anomaly with a transport magnitude of 0.946 Sv. Interestingly, there is no planetary wave propagation in the deep basin, we only find "filling" and "emptying" modes (see Figure 7.5 (c)).

Figure 7.6 (a) shows contours of SSH anomaly and the vertical integral transport anomaly vectors for SSHA12. In this experiment the axis of the ridge is orientated at 45% to the diameter joining the mid–points of the two straits. The cyclonic shelf boundary current is the major signature of the anomaly leaving the anticyclonic and the transpolar current nearly stagnant. The calculation of the shelf transport across sections $\overline{AB}$ and $\overline{CD}$ reveals that the addition of the ridge reduces the magnitude of the anticyclonic and cyclonic boundary current to 0.032 Sv (0.074 Sv without ridge) and 0.362 Sv (0.505 Sv without ridge), respectively. This decrease in the boundary current transport feeds a transpolar current of 0.074 Sv (computed across the section $\overline{EF}$). The deep basin is almost stagnant with a transport of 0.058 Sv. Figure 7.6 (b) shows the equivalent solution for SSH13 where the step-shelf width is 200km. We can see the anomaly is partitioned almost equally into two branches on the shelf with transports of 0.299 Sv and 0.274 Sv for the anticyclonic and cyclonic branch, respectively. Once the western branch reaches the ridge, the majority of the anomaly crosses the ridge forming a transpolar anomaly current with a transport magnitude of 0.195 Sv (computed across the section $\overline{EF}$).

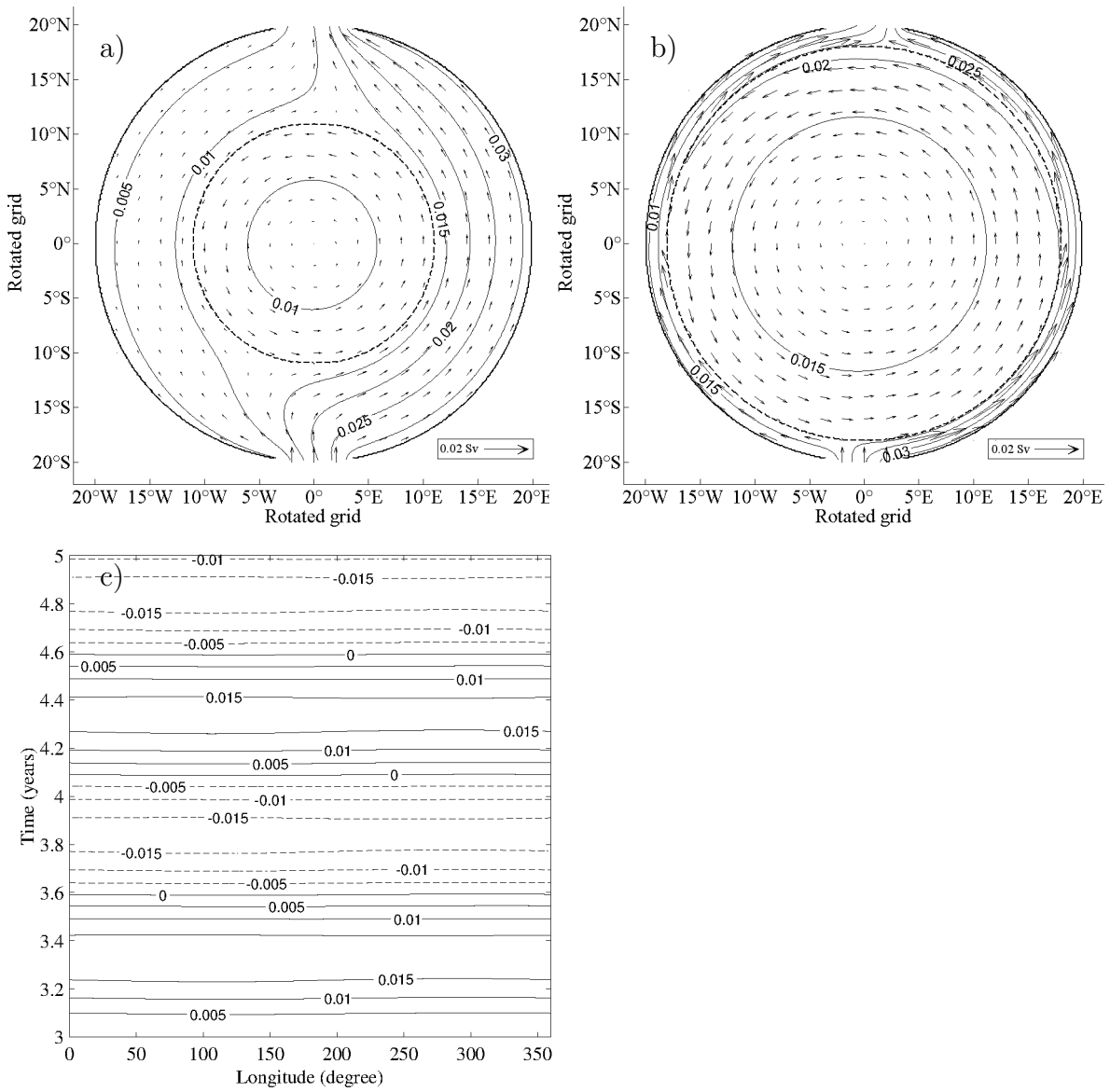

Figure 7.5: Plot of the SSH anomaly and anomaly depth-integrated transport field associated with the source–sink planetary geostrophic flows with a periodic transport anomaly imposed at the inflow; a) SSHA10 at $t = 0.25T$; b) SSHA11 at $t = 0.25T$; c) contours of SSH for SSHA11 in the longitude–time plane defined by $\theta = 10°$ (see blue line in Figure 4.4). Continuous lines denote positive sea surface elevation in metres. The shelf break is marked with a dashed line.

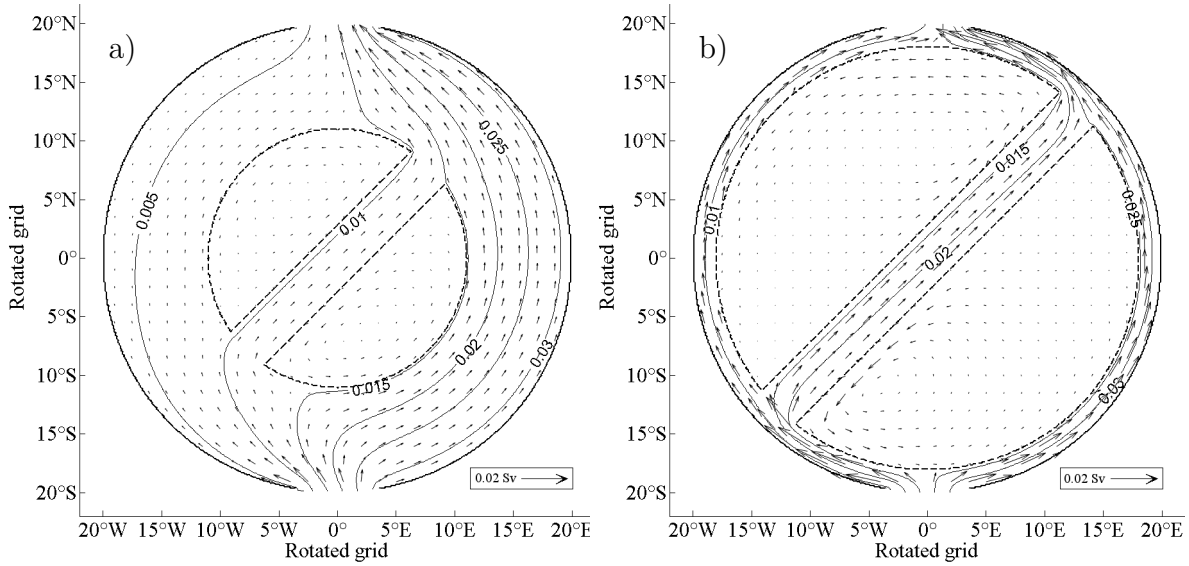

Figure 7.6: Plot of the SSH anomaly and anomaly depth-integrated transport field associated with the source–sink planetary geostrophic flows with a periodic transport anomaly imposed at the inflow; a) SSHA12 at $t = 0.25T$; b) SSHA13 at $t = 0.25T$. Continuous lines denote positive sea surface elevation in metres and the shelf edge is marked with dashed line.

7.5 SSH anomalies in a basin with three gaps

In this section, we introduce a basin with three gaps as a step towards a more realistic representation of the Arctic basin (see Figure 7.7 (a)). The Bering Strait exhibits a volume transport variability from seasonal to inter-annually which changes the magnitude of the inflow around 1 Sv. A perturbation of this magnitude would be expected to alter the inflow and outflow in the remaining straits. Here, we explore the anomaly propagation produced by a periodic perturbation prescribed in the Bering Strait.

The design of the next experiments is similar to the previous sections. There are, however, two differences; the bathymetry profiles and the boundary flows. Figure 7.7 shows the different bathymetries employed in this section. The flat bottom basin and the regular step-shelf were straight forward to implement in the model using the same routine *domzgr.F90* used in previous chapters. The irregular width–step shelf with/without ridge was implemented by an external file following the same procedure as Chapter 4.

At the boundary we imposed two inflows and two outflows with directions shown by the blue arrows in Figure 7.8 (a). The magnitude of the transports are listed in Table 7.6 (column two). The Flather boundary condition is applied in the Greenland–

Iceland–Norwian seas (GINs) and Davis Straits. At this point, reference should be made to the fact that the Flather boundary condition alters the transport across the open boundary as previously stated in section 7.2. Therefore, the final transport across Davis and GINs gap will differ from the initial once the steady–state is reached. Table 7.7 shows the final transports for the open boundaries for the four different basins. We note that the steady transport across the GINs and Davis straits varies with the shelf geometry.

Table 7.6: The transport boundary conditions initially imposed across the straits in the NEMO simulations.

Gap	**Intitial prescribed transport (Sv)**
Bering inflow	1
Davis outflow	−2.1
GINs inflow	6.5
GINs outflow	−5.4

Table 7.7: Final volume transport across boundaries at the steady–state.

	Boundary transport (Sv)			
Gap	**Flat bottom**	**Uniform width step-shelf**	**Irregular width step-shelf**	**Irregular width step-shelf with ridge**
Bering inflow	1	1	1	1
Davis outflow	−3.559	−3.691	−3.704	−2.943
GINs inflow	6.348	4.987	4.972	4.816
GINs outflow	−3.789	−2.296	−2.268	−2.873

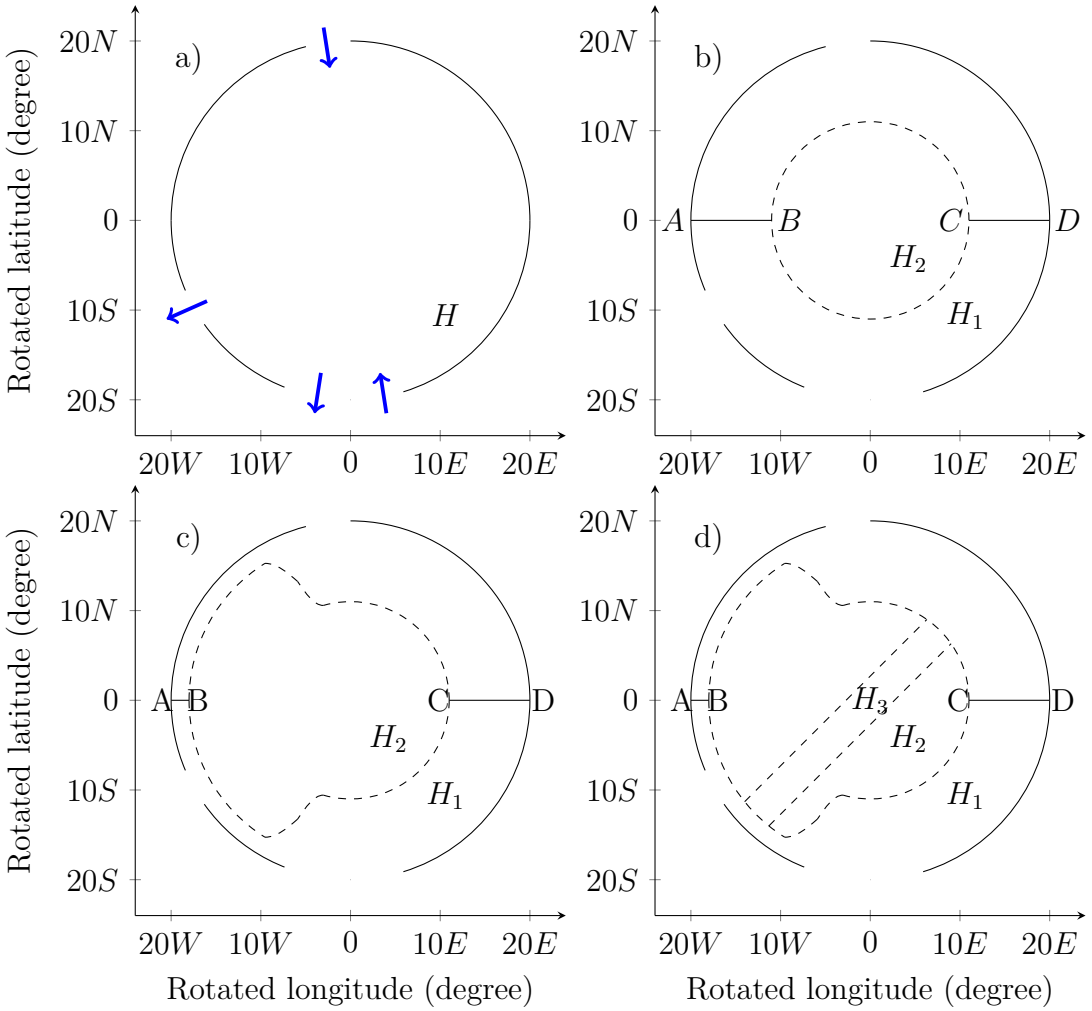

Figure 7.7: Schematic of a basin with three gaps. a) flat bottom. The transport through the straits is denoted with blue arrows; b) uniform width step-shelf; c) irregular width step-shelf; d) same as (c) with a rotated ridge 45^o respect from the gaps. The shelf edge is marked with dash line and the ridge is below the step-shelf. Sections $\overline{AB}$ and $\overline{CD}$ denote where the volume transport was computed.

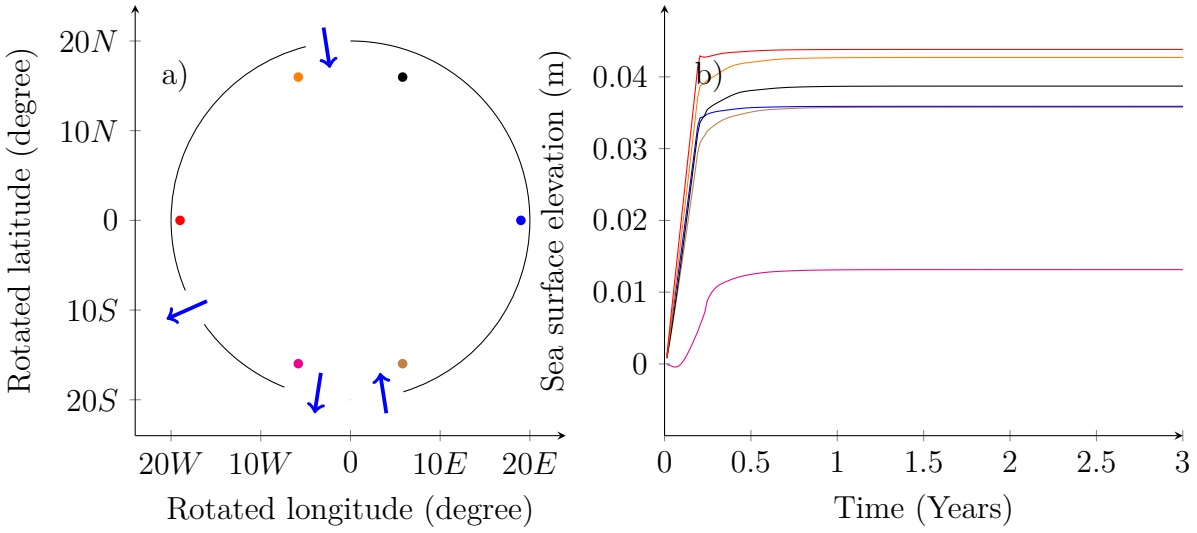

Figure 7.8: Three gap basin; a) schematic of the basin showing inflow/outflow across the straits and the locations of the time series plots in (b); b) Sea surface elevation time series. Each coloured curve in (b) corresponds to the time series at the location shown by the same coloured dot in (a).

These experiments follow the same method as the previous section, using the parameters of Table 4.1 and a linear bottom friction of $5 \times 10^{-4}\ ms^{-1}$. A circulation is forced from rest by the boundary source–sink flows. Figure 7.8 (b) shows different sea surface elevation points in the basin (see Figure 7.8 (a)). The flow reaches the steady–state in less than three years. In the steady–state the circulation is characterised by three main currents (see Figure 7.9 (a)) which were also observed in the equivalent analytical solution of Chapter 2 (see Figure 2.21 (a)). The GINs inflow bifurcates into three branches. The first branch re–circulates leaving the domain through the GINs strait and the second one flows to the Davis Strait merging with the Bering current before exiting the domain. The third branch flows towards the Bering Strait merging with the Bering inflow and flowing towards the Davis Strait forming a shelf boundary current. Next a transport anomaly is specified across the Bering Strait of form of $a \sin(\omega t)$ where a and ω are the amplitude and angular frequency of the anomaly. The amplitude and the period of the anomaly were set to 0.5 Sv and 1 year, respectively. We then examine the structure and propagation of the resulting anomaly field that is generated by the time varying Bering Strait transport.

Figure 7.9 (b) and (c) show the SSH anomaly field and depth-integrated transport vectors at $t = 0.25T$ and $t = 0.75T$, respectively for the flat bottom basin with three gaps. The anomaly field behaviour is characterised by a strong boundary current between the Bering and Davis Straits and a wider current connecting the Bering Strait with the GINs

strait. During the first half of the forcing period there is a net decrease of the volume of the fluid in the basin, reaching a minimum at $t = 0.25T$ (see Figure 7.9 (b)). During the second half of the forcing period the fluid volume increases in the domain, reaching a maximum at $t = 0.75T$ (see Figure 7.9 (c)). Notice these emptying and filling regimes correspond to reversals of the anomaly transport vectors.

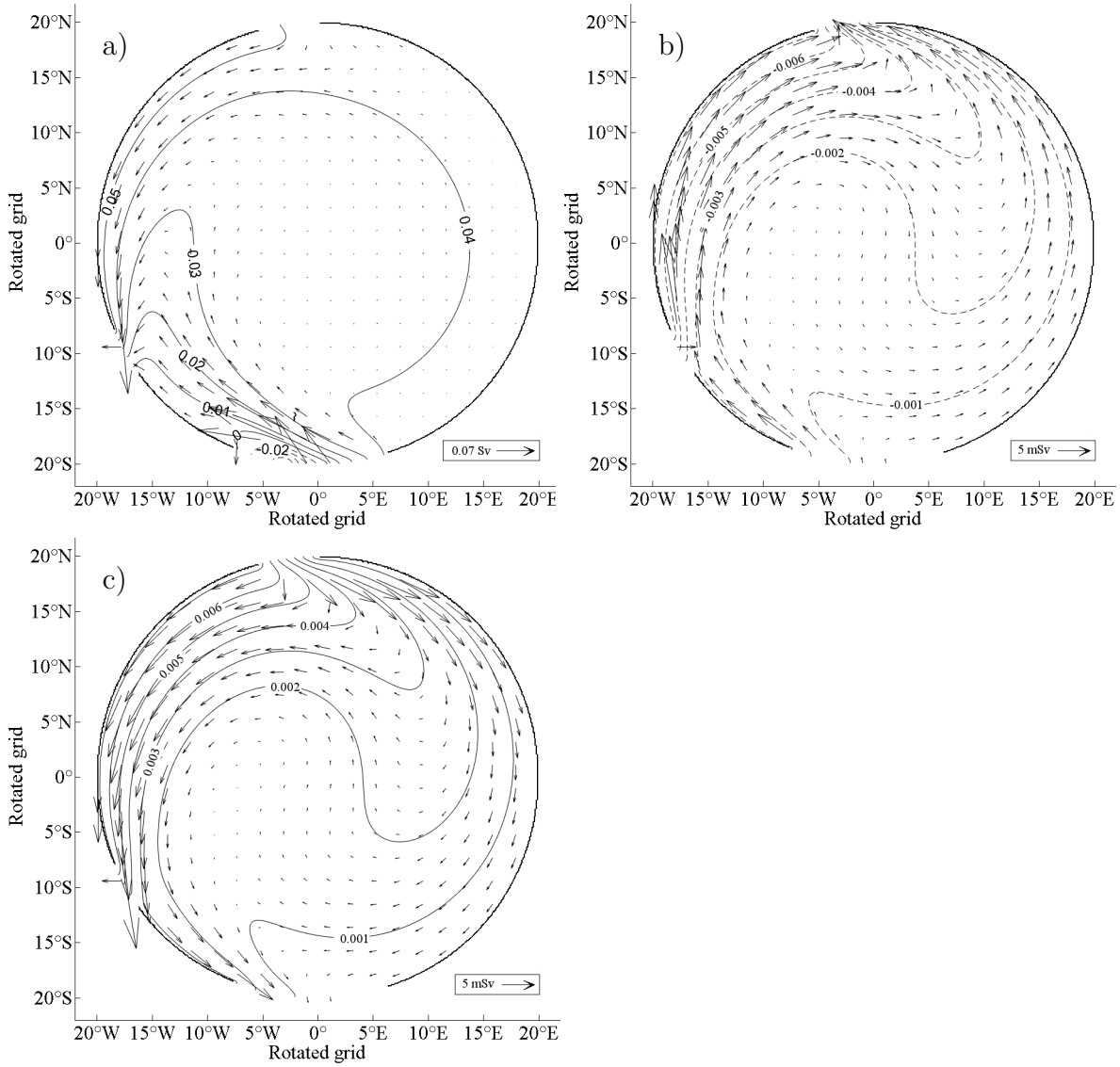

Figure 7.9: Source–sink flow in a flat bottom basin with three gaps; a) Contours of steady–state SSH and depth-integrated transport vectors; b) SSH anomaly field and anomaly depth-integrated transport vectors at time step $t = 0.25T$; c) same as (b) except at $t = 0.75T$.

The impact of a step-shelf on the anomaly field is considered in Figure 7.10 which shows the steady–state circulation (attained after 3 years of model integration) and the anomaly fields for the basins shown in Figure 7.7 (b) and (c), respectively. The SSH anomaly fields and the depth–integrated transport vectors corresponding to these basins,

at $t = 0.75T$, are shown in Figure 7.10 (c) and (d).

Figure 7.10 (a) shows a similar ocean circulation to that in Figure 4.13 (a) where we found a strong shelf circulation and an almost stagnant deep basin circulation. The GINs inflow is divided into three branches; the first branch forms a strong recirculation exiting through the same strait and the second flows towards the Davis Strait. The remaining flows cyclonically towards the Bering Strait with a magnitude of 0.284 Sv across the section $\overline{CD}$. The Bering inflow merges with the GINs current and flows cyclonically towards the Davis Strait with a magnitude of 1.212 Sv (computed transport across section $\overline{AB}$). The "missing" 0.06 Sv crosses the shelf forming a weak deep basin current. Figure 7.10 (b) shows the impact that an irregular width shelf has on the steady circulation. As above, there is strong recirculation in the GINs strait. In fact, the comparison between the uniform and irregular step-shelf reveals that the recirculation in the latter case is stronger (see Table 7.7). The remaining again flows towards the Bering and Davis Strait. The cyclonic GINs branch supports a volume transport of 0.594 Sv across section $\overline{CD}$. After merging the with Bering inflow, the cyclonic shelf current flows towards the Davis Strait with a magnitude of 0.927 Sv across the section $\overline{AB}$. Note there is a "missing" 0.7 Sv between Bering Strait and section $\overline{AB}$ which crosses the Canadian shelf forming two counter–rotating deep basin boundary currents. These are not visible in Figure 7.10 (b) because the volume transport vectors in the deep basin are much weaker than on the step-shelf.

The anomaly signal in the uniform step-shelf basin (see Figure 7.10 (c)) is stronger in the Bering–Davis branch where 73% (i.e 0.35 Sv across the section $\overline{AB}$) of the anomaly circulates. Also, we find a small anomaly signature on the eastern shelf containing only the 25% (i.e. 0.12 Sv across the section $\overline{CD}$) of the anomaly. The remaining 2% (i.e. 0.03 Sv) crosses the shelf break forming a cyclonic deep basin circulation (see Figure 7.9 (c)) although the computed transport of the deep basin circulation is 0.13 Sv. This inconsistency in the total flux is expected because the open boundaries do not change simultaneously revealing an "excess" of water volume in the basin.

Figure 7.10 (d) shows a basin with a non–uniform shelf width which more closely resembles the Arctic basin. This irregular shelf is characterised by a wide eastern (Siberian) shelf with a width around 900 km and narrow 100 km western shelf. Here, 58% of the anomaly (i.e. 0.27 Sv across the section $\overline{CD}$) propagates on the eastern shelf towards the GINs strait, whereas the anomaly transport on the western shelf decreases significantly to 28% (i.e. 0.14 Sv across $\overline{AB}$). The deep basin supports a cyclonic anomaly circulation

with a magnitude of 0.09 Sv.

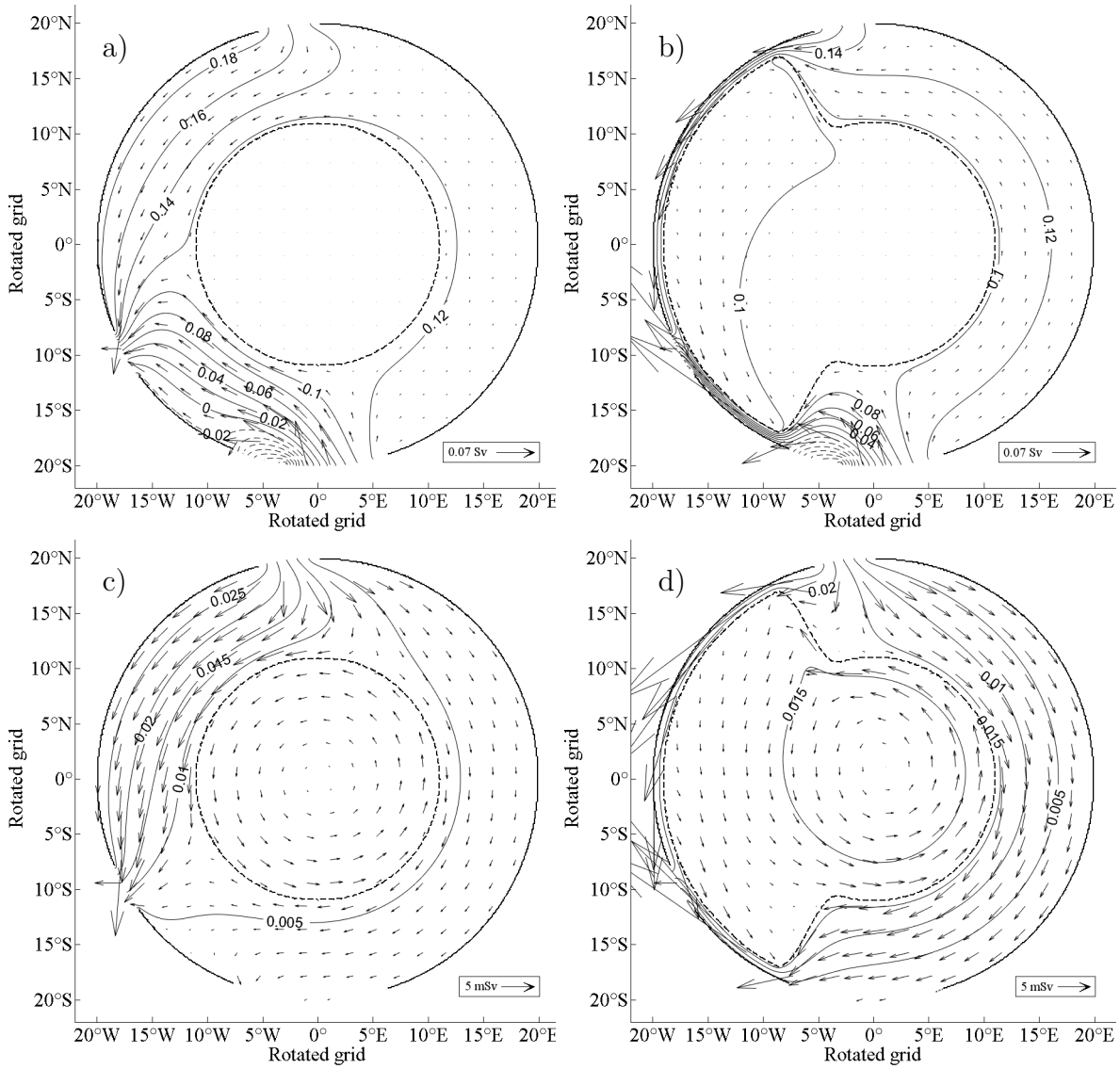

Figure 7.10: Source–sink flow in a basin with three gaps; a) Contours of steady–state SSH and depth-integrated transport vectors in a basin with a uniform width step-shelf; b) same as (a) except for an irregular width step-shelf; c) SSH anomaly field and anomaly depth-integrated transport vectors of (a) at time step at $t = 0.75T$; d) same as (c) but with (b).

The influence of a ridge on the irregular shelf solutions is shown in Figure 7.11. The steady state circulations shown in Figure 7.11 (a) is qualitatively the same as that in Figure 4.13 (b) as expected. The only difference between both simulations is the presence of the Flather boundary condition in the GINs and Davis straits. The structure of the anomaly on the shelf is similar to the previous case showing a strong anticyclonic boundary current (see Figure 7.11 (b)). The deep basin adjacent the "eastern wide shelf" supports a transport of 0.08 Sv whereas the deep basin adjacent to the "western narrow shelf" has

a transport of 0.18 Sv.

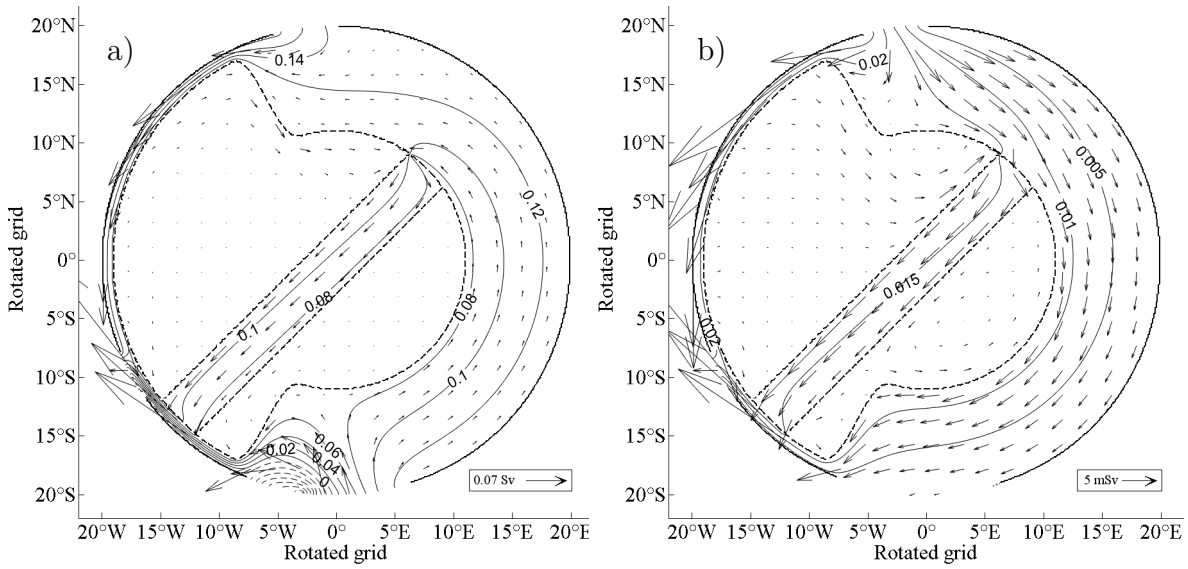

Figure 7.11: Source–sink flow on a irregular width step-shelf width three gaps and a ridge; a) Contours of steady–state SSH and depth-integrated transport vectors; b) SSH anomaly field and anomaly depth-integrated transport vectors at time step at $t = 0.75T$.

Finally we examine the anomaly boundary transport, in particular across the Davis and GINs strait where the Flather open boundary condition was imposed (see Figure 7.12). Note the anomalies are propagated in form of fast topographic waves. In particular, it takes around two days for the perturbation reach the straits. Therefore, we cannot observe the delay in the curves of Figure 7.12. Figure 7.12 (a) shows the anomaly transport time series calculated at the straits in a flat bottom basin. Note that a positive anomaly of the Bering inflow (i.e. the inflow increase) produces a positive anomaly in the outflow (i.e. the outflow increases) across the Davis strait and the GINs. Also, we observe that it generates a negative anomaly in the inflow across the GINs strait (i.e. the inflow decrease). This anomaly is almost uniformly distributed across both straits. In particular the Davis Strait receives the 58% and the GINs the 42%.

Figure 7.12 (b) displays the anomaly transport in a regular width step-shelf basin. We note that the Davis Strait accommodates the majority of the Bering Strait anomaly (81%), whereas the GINs strait only accommodates 19% of the Bering Strait anomaly transport. This result is consistent with Figure 7.10 (c) where the anomaly is constrained to the western shelf. In the non-uniform width shelf (Figure 7.12 (c)) the portions are similar. However, the anomaly propagation is different than the uniform step-shelf basin. The reason can be seen in Figure 7.10 (d) which reveals that majority of the anomaly

anticyclonically propagates towards the Davis Strait in form of boundary currents close to the edge in the “eastern wide shelf”.

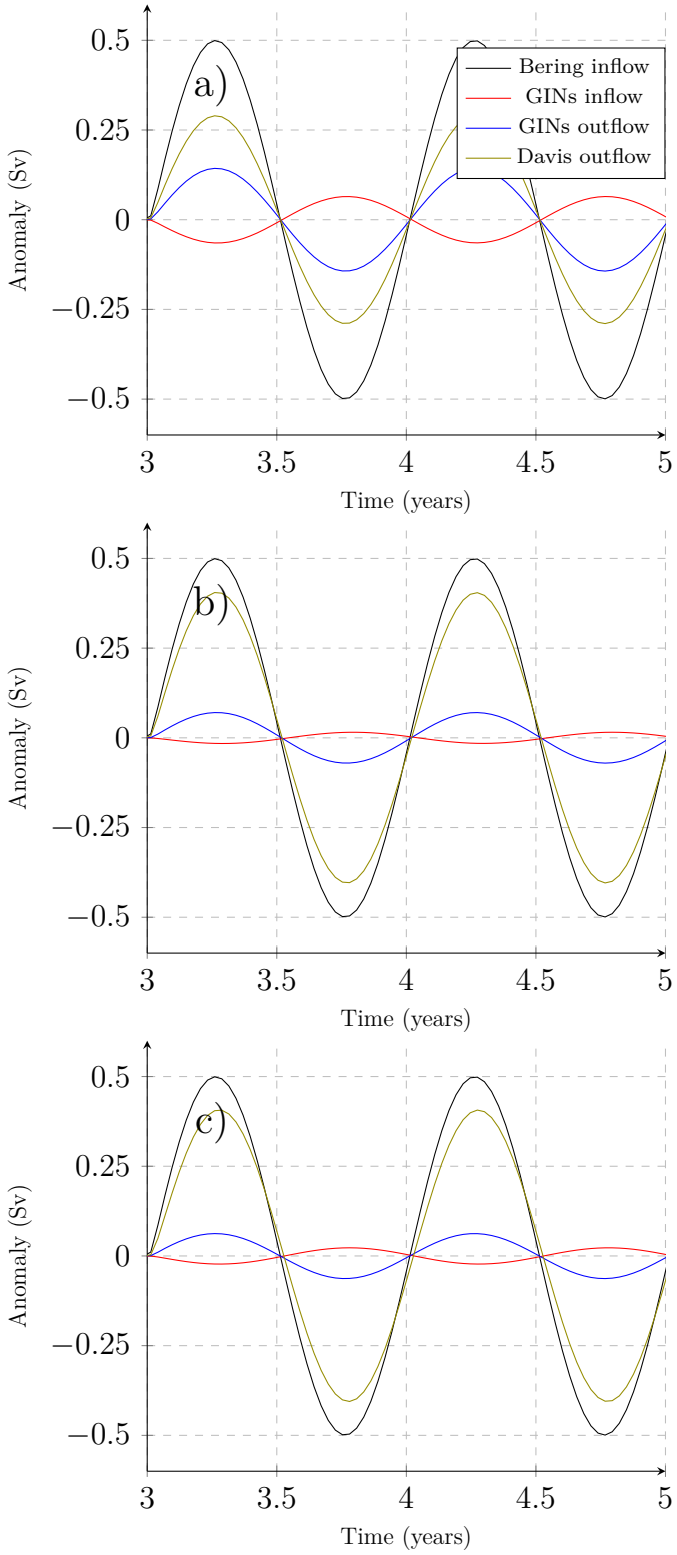

Figure 7.12: Time series of volume transport anomaly across the three straits; a) flat bottom basin; b) regular width step-shelf basin; c) irregular width step-shelf basin. Note that the transport across the GINs strait is partitioned into the inflow/outflow and the positive (negative) denotes an inflow (outflow) from the basin.

Table 7.8: The volume transport fluxes initially imposed across the straits in the NEMO simulations.

Gap	**Intial prescribed transport (Sv)**
Bering inflow	1.2
Davis outflow	−0.8
GINs inflow	3.6
GINs outflow	−4

7.6 Ramp–up of the inflow in a basin with three gaps

In collaboration with Agatha De Boer from Stockholm University, I have used the NEMO model to elucidate the physics controlling the relationships between the unsteady volume transport across the straits connecting the Arctic to its marginal seas. De Boer (private communication) investigated the capacity of straits of the Arctic Ocean to "compensate" themselves (i.e. the volume transport across the straits varies depending on the net inflow into the Arctic basin) after a change of the transport across one (or more) strait/s. De Boer (private communication), found a high correlation between the transient transport in the Bering Strait and that in the Fram Strait. Indeed, this correlation exceeds the correlation between the Bering and Davis Straits despite the fact that the Davis Strait is geographically closer to the Bering Strait. Here we study the possible physical mechanisms which might explain these observations. This research has been published (de Boer *et al.*, 2018).

We again consider a three gap circular polar basin. Figure 7.13 shows schematically the choice of continental shelf bathymetries used in the numerical studies reported in this section. Notice that the shelves in Figure 7.13 (c) and (d) contain a new feature not considered before. In both figures the shelf terminates in the neighbourhood of GINs strait to form a deep channel on the "western half" of the strait (i.e. a prototype Fram Strait). At the straits we prescribed volume transports as shown quantitatively in Table 7.8 and qualitatively in Figure 7.13 (a).

Table 7.9: Spun–up volume transports across the straits. Transports with negative (positive) sign denotes the flux in out (in) of the basin.

	Volume fluxes across the straits (Sv)			
Gap	**Uniform width step-shelf**	**Irregular width step-shelf**	**Uniform width step-shelf with channel**	**Irregular width step-shelf with channel**
Bering inflow	1.2	1.2	1.2	1.2
Davis outflow	−2.363	−2.177	−1.998	−0.892
GINs inflow	3.164	3.115	2.344	2.205
GINs outflow	−2.001	−2.138	−1.546	−2.513

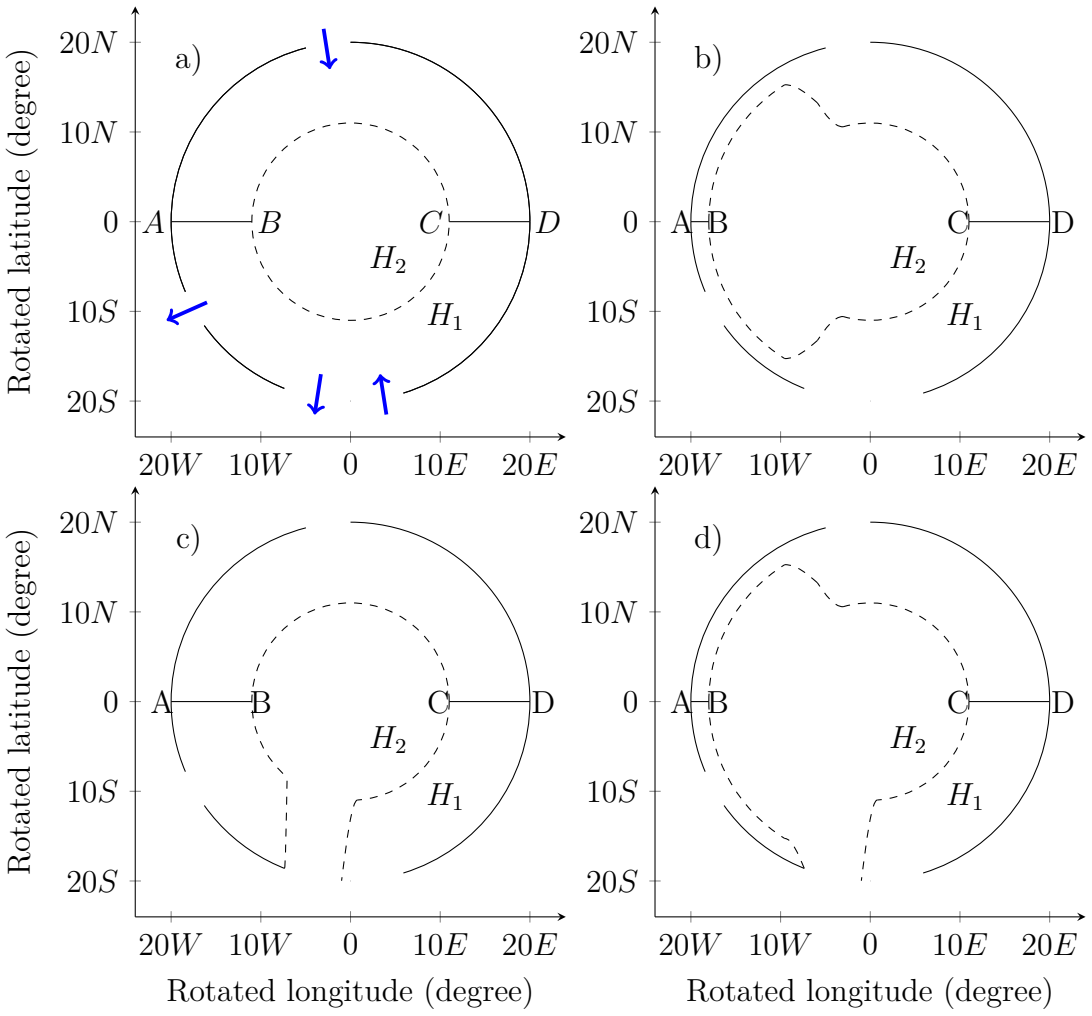

Figure 7.13: Schematic of a basin with three straits; a) uniform width step-shelf. b) irregular width step-shelf; c) same as (a) except there is a channel in the GINs outflow gap; d) same as (b) except there is a channel in the GINs outflow gap. The transport through the straits is denoted schematically with blue arrows and the shelf edge is marked with a dashed line. Sections $\overline{AB}$ and $\overline{CD}$ denote where the volume transport was computed.

The experimental methodology used to study the transient adjustment of the basin to an increase in the volume flux through one of the straits is as follows. We first spin–up the circulation to a steady state. During this spin–up phase the volume transport flux across the Bering Strait remains fixed and the Flather (1994) boundary condition is used to dynamically adjust the transports across the Davis and GINs straits. Table 7.8 shows the initial strait volume fluxes and Table 7.9 shows the final adjusted transports. Of course, the Bering Strait transport remains constant throughout the spin–up, by design.

The transient adjustment phase is forced by ramping–up the Bering Strait transport from 1.2 Sv to 2 Sv over a period of one year. We then address how this additional fluid entering the basin dynamically adjusts towards a new steady–state. In particular, how do the volume transports across the Davis and GINs straits adjust and what values do they attain in the new steady–state circulation? Does the Davis Strait, for example, increase its outflow to accommodate the increased volume transport across the Bering Strait?

Figure 7.14 shows the steady–state circulation in the four basins (see Figure 7.13) and the spun–up transport across the straits are given in Table 7.9. The circulation in Figures 7.14 (a) and (b) is qualitatively similar to that in Figures 7.10 (a) and (b), respectively. In fact, the computed transport across the sections $\overline{AB}$ and $\overline{CD}$ reveals that the direction of the transport is the same as in the previous section (see Table 7.10). The presence of a channel in the GINs strait constrains the shelf circulation to be in an anticlockwise direction (see Figure 7.14 (c)), whereas Figure 7.14 (a) reveals two shelf currents in opposite directions emanating from the Bering Strait inflow. The computed transport across sections $\overline{AB}$ and $\overline{CD}$ (see Table 7.10, third column) reveals that most inflowing transport from GINs strait circulates counter–clockwise on the shelf to merge with the Bering inflow. Subsequently, the merged shelf current flows towards the Davis Strait where the majority of it exits. A small portion continues on the shelf and exits through the GINs strait. The introduction of a narrow shelf on the western side of the basin modifies the circulation as shown in Figure 7.14 (d). Once more the presence of a channel produces an unidirectional cyclonic shelf circulation. The majority of the GINs inflow (1.91 Sv computed transport across the section $\overline{CD}$) reaches the Bering Strait and merges with the Bering inflow forming a current of approximately 3 Sv. However, at the narrowing of the width of the shelf the circulation converges to form a shelf–break current, decreasing the narrow shelf cyclonic current transport to 1.056 Sv (computed transport across the section $\overline{AB}$). The shelf break current also “feeds” the deep basin forming two counter–rotating boundary currents which exit through the GINs strait.

Next, the Bering inflow is ramped–up linearly to 2 Sv over one year. Following a transient adjustment phase the circulation reaches a new steady state. Figure 7.15 shows the contours of sea surface elevation with the depth–integrated transport vectors associated with the new steady–state. Figure 7.15 (a) shows the circulation for the uniform width step-shelf. The increase of Bering inflow increases the strength of the cyclonic shelf current in the Bering–Davis sector to 1.569 Sv (before the ramp–up it was 1.055 Sv) calculated at cross section $\overline{AB}$. The anticyclonic branch increases its magnitude slightly to 0.298 Sv (before the ramp–up it was 0.004 Sv) at cross section $\overline{CD}$. The non–uniform width step-shelf displays a similar response but the distribution of water volume is different (see Figure 7.15 (b)). The cyclonic branch becomes anticyclonic with a magnitude of 0.363 Sv (before the ramp–up it was 0.005 Sv) at cross section $\overline{CD}$, whereas the cyclonic branch only increases to 0.609 Sv (before the ramp–up it was 0.452 Sv) in cross section $\overline{AB}$. Figure 7.15 (c) displays similar change in the ramped–up circulation observed in Figure 7.15 (a), where the biggest impact is observed in the intensity of the Bering–Davis cyclonic branch. As before, the presence of a channel at the GINs strait forces a cyclonic shelf circulation. After increasing the Bering inflow the magnitude of the western cyclonic branch increases to 3.456 Sv (before the ramp–up it was 2.749 Sv) at cross section $\overline{AB}$. The eastern cyclonic branch decreases slightly to 2.007 Sv (before the ramp–up it was 2.029 Sv) at cross section $\overline{CD}$. The ramped–up circulation in a basin with an irregular width step-shelf in the presence of a channel is displayed in Figure 7.15 (d). The eastern cyclonic branch is reduced to 1.857 Sv (before the ramp–up it was 1.91 Sv) at cross section $\overline{CD}$ and the western cyclonic branch increases slightly to 1.329 Sv (before the ramp–up it was 1.056 Sv) at cross section $\overline{AB}$. The remaining fluid (i.e 0.5 Sv) crosses the shelf break increasing the strength of the deep basin current circulation.

To aid understanding of how the transports across the Davis and GINs straits respond to the ramp-up of the Bering Strait inflow we also calculate the "anomaly transports" across the former two straits. More precisely, at the Davis Strait, for example, the anomaly transport is calculated as

$$\frac{\delta T_D}{\delta T_B} \tag{7.1}$$

expressed as a percentage, where δT_D denotes $T_D^{FINAL} - T_D^{INITIAL}$ the difference between the outflow across the strait after and before the ramp-up and δT_B is the increase in Bering Strait transport (i.e. 0.8 Sv). An equivalent calculation is carried for the GINs strait inflow and outflow components (see Table 7.12).

First we consider the uniform width shelf response with no channel in the GINs strait. Approximately 82% of the additional Bering Strait inflow exits through the Davis Strait, as revealed in the change of transport across section $\overline{AB}$ from Table 7.10 to Table 7.11. Also, we observe the GINs strait inflow decreases and the outflow increases after the adjustment due to the strengthening of the anticyclonic current from the Bering Strait. For the irregular width shelf shown in Figure 7.15 (b), the partition of the transport across the Davis and GINs straits changes. Approximately 75% of the additional Bering Strait inflow exits directly through the Davis Strait via a shelf current. Therefore, there is an increase in the anomaly transport connecting the Bering and the GINs straits (i.e. an anticyclonic current over the "wide shelf") leading to an increase in the outflow through the GINs strait and a decrease of the inflow (see section $\overline{CD}$ in Table 7.10 and Table 7.11). In the case of a uniform step-shelf with a channel, Table 7.12 reveals that the majority of the additional of the Bering (76%) inflow leaves the domain throughout the Davis Strait via a cyclonic shelf current leading to a small decrease in the magnitude of the GINs strait inflow. Finally the presence of an irregular width shelf markedly alters the latter anomaly propagation. The Davis Strait only accommodates the 43% of the additional Bering inflow whereas the majority (50%) of the anomaly exits through the GINs outflow.

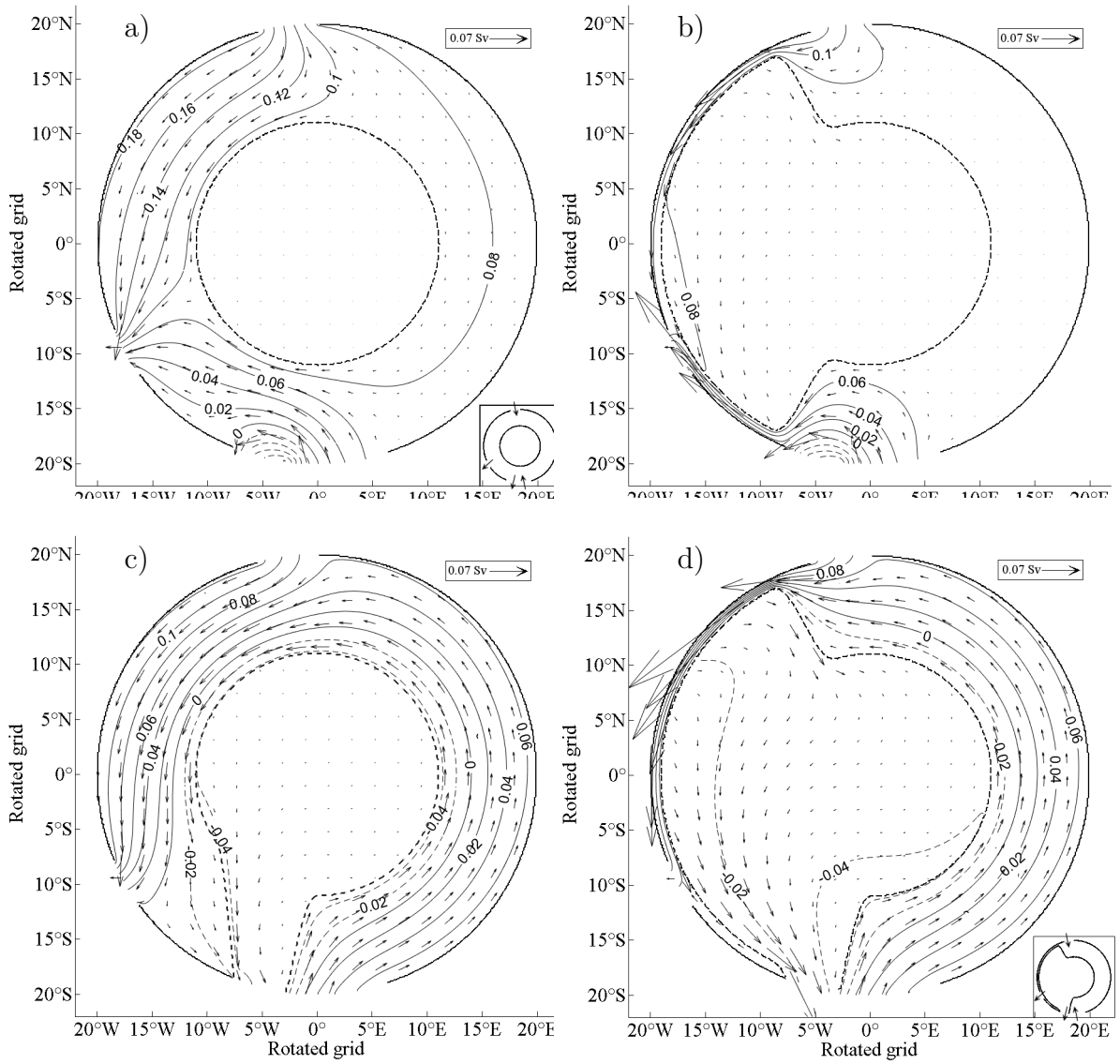

Figure 7.14: Plot of the SSH field and depth-integrated transport vectors in a basin with three gaps after ten years of integration; a) regular step-shelf; b) irregular step-shelf; c) same as (a) except with a channel in the GINs outflow gap. d) same as (b) except with a channel in the GINs outflow gap. The shelf edge is marked with a dashed line.

Table 7.10: Cross–section transport corresponding to Figure 7.14. The positive sign denotes the volume transport in the azimuthal direction.

Section	**Uniform width step-shelf**	**Irregular width step-shelf**	**Uniform width step-shelf with channel**	**Irregular width step-shelf with channel**
$\overline{AB}$	1.055	0.452	2.749	1.056
$\overline{CD}$	−0.004	0.005	2.029	1.91

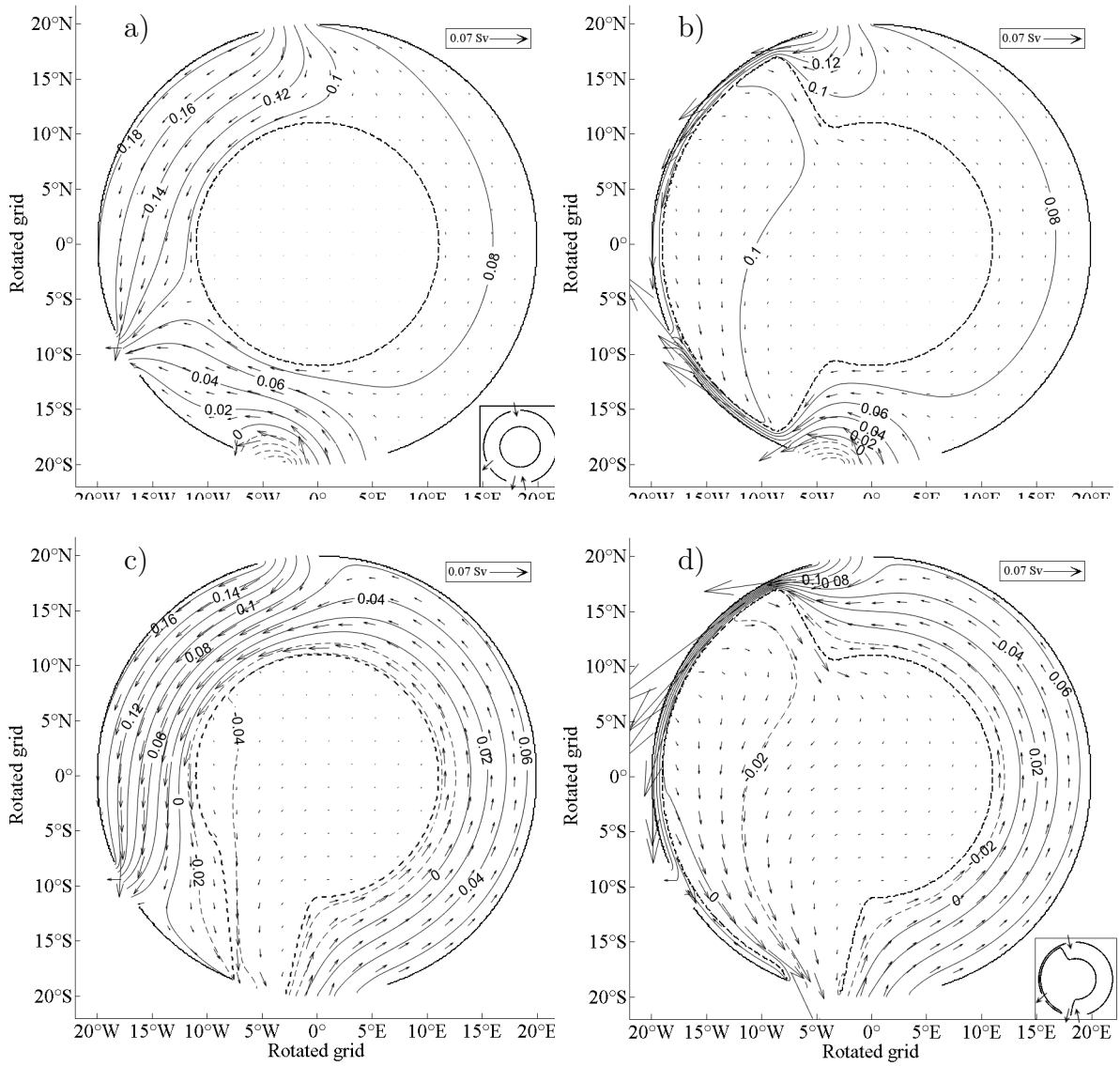

Figure 7.15: Plot of the SSH field and depth-integrated transport vectors in a basin with three gaps after fifteen years of integration a) regular step-shelf; b) irregular step-shelf; c) same as (a) except with a channel in the GINs outflow gap. d) same as (b) except with a channel in the GINs outflow gap. The shelf edge is marked with a dashed line.

Table 7.11: Cross–section transport corresponding to Figure 7.15.The positive sign denotes the volume transport in the azimuthal direction.

Section	Uniform width step-shelf	Irregular width step-shelf	Uniform width step-shelf with channel	Irregular width step-shelf with channel
$\overline{AB}$	1.569	0.609	3.456	1.329
$\overline{CD}$	−0.298	−0.363	2.007	1.857

Table 7.12: Anomaly transport across the straits expressed as a percentage.

Gap	Uniform width step-shelf	Irregular width step-shelf	Uniform width step-shelf with channel	Irregular width step-shelf with channel
Davis outflow	82	75	76	43
GINs inflow	−4	−7	−3	−7
GINs outflow	12	18	21	50

7.7 Conclusions

This chapter has studied the structure and propagation of sea surface elevation anomalies produced by a perturbation in the transport across one, or more, straits using the global ocean numerical model NEMO.

Firstly, we considered the boundary flux perturbation in a flat bottom polar basin with two diametrically opposed straits. As a first approach, we simultaneously prescribed perturbation transports across both straits. The period of the transport anomaly was set to be one of the periods of the unforced planetary waves whose dispersion relation is given in Chapter 3. The resulting SSH anomaly propagates as planetary waves with structure predicted by the dispersion relation for these waves in Chapter 3. If the period of the transport anomaly across the strait is set to a value of cut–off period of the gravest mode, no planetary waves are possible and the SSH anomaly takes form of an evanescent boundary trapped non propagating field.

Secondly, we studied anomalies produced by a perturbation of the inflow while the outflow was calculated by implementing the Flather (1994) open boundary condition. The treatment of the open boundaries generates an imbalance in the total volume of water inside the basin. The experiments performed in a flat bottom basin showed phases of "filling" and "emptying" in response to a net inflow, followed by outflow of water across the strait where the transport anomaly is prescribed. With the addition of a wide step-shelf most of the anomaly transport propagates as a boundary current on the "eastern" side of the shelf leaving the deep basin and the "western" side of the shelf almost stagnant. However, this asymmetrical distribution of the SSH anomaly is broken in the narrow shelf scenario where two almost identical boundary currents in the step-shelf are present. In addition, we also observe a cyclonic deep basin anomaly circulation. Interestingly the magnitude of the transport in the deep basin was twice that of the anomaly. This could related to the phase of volume transport across the straits. The addition of more complex

bathymetry features, such a ridge, reveals that the strongest changes to the circulation were seen in the narrow shelf where the increase of transport across the shelf formed western boundary currents in the deep basin.

Third, we studied a polar basin with three straits. The flat bottom basin scenario revealed that the anomaly transport was more intense on the western side of the basin. The addition of a regular width step-shelf constrains most the anomaly to the shelf connecting the Davis and the Bering Straits, representing 80% of the total anomaly. However, the introduction of an irregular width step-shelf changes this distribution showing that 65% is propagated across the "eastern" side shelf and only the 23% across the "western" side shelf. This difference is partly influenced by the formation of an anticyclonic shelf current from the Bering Strait in the irregular width step basin.

Also, we assessed the anomaly impact on the transport across the straits. In general, the Davis Strait was dynamically more responsive to a change in the inflow from the Bering Strait. However, this connection between the straits changes markedly in the case of the irregular width shelf showing an increase of 12% in the anomaly across the GINs strait.

Finally, in collaboration with De Boer from Stockholm University (personal communication), we attempt to find the underlying physics that explains the strait correlations observed in the Arctic basin. We studied the transient adjustment of a idealised Arctic basin and the change of the volume transport across the Davis and GINs straits after "ramping–up" the Bering inflow to $2Sv$. We observed that the geometry of the basin impacts on the anomaly propagation. In particular the addition of a narrow step-shelf and a channel representing the Canada shelf and the Fram depth, respectively, were revealed to be key in the formation of a deep boundary current which links the anomaly Bering inflow with the anomaly GINs outflow. The results from the collaborative project with De Boer have been published (de Boer *et al.*, 2018).

Chapter 8

Concluding remarks and future research

This thesis has investigated the underlying physics that controls the barotropic planetary geostrophic circulation in a circular polar basin which is viewed as a prototype Arctic Ocean basin. Although this study has only considered a barotropic circulation in an idealised circular polar basin, we were able to reproduce dynamics qualitatively similar to those achieved by more complex numerical Arctic Ocean studies. Among the different findings that have been discovered in this thesis we highlight the following:

8.1 β-sphere approximation

The β-sphere approximation proposed by Imawaki and Takano (1974) has been employed to develop analytical solutions for a steady, barotropic planetary flow driven by prescribed source/sinks on the boundary and wind stress in a polar basin. In addition, the same approximation was used to obtain the dispersion relation for planetary and inertia-gravity waves in polar basin. In comparison with other more accurate approximations such as the "polar β-plane" of LeBlond (1964), the β-sphere approximation fixes the co-latitude (i.e. θ_f) in the coefficients of the vorticity equation derived retaining full spherical geometry. The resulting constant coefficient partial differential equation can then be analysed using classical techniques in applied mathematics to derive, for example, the dispersion relation for azimuthally propagating planetary and inertial-gravity waves in a polar cap.

The accuracy of the planetary wave dispersion relation derived in Chapter 3 is assessed by comparing the eigenfrequencies with those obtained from the "polar β-plane" disper-

sion relation of LeBlond (1964). In general the lowest free modes are in good agreement between the two dispersion relations. In the numerical spin-up of the source-sink driven circulation studied in Chapter 4 the lowest mode planetary wave was observed to establish the steady-state solution. Subsequently, the accuracy of the approximate analytical solutions is assessed by comparing the error in the relative vorticity fields between the former and equivalent NEMO numerical solutions. Overall in the absence of wind stress, the β-sphere approximation successfully reproduces the steady source-sink circulation in a polar basin with relative vorticity errors below 20%. In the presence of wind stress, the selection of θ_f is a key parameter; there is a range of values for θ_f for which the analytical and numerical model solutions are in close agreement.

This study found two limitations associated with this approximation; θ_f and the basin depth. The first has been already mentioned above. The second was observed in Chapter 7 with the planetary wave propagation in the form of SSH anomalies. The dispersion relation derived in Chapter 3 was able to predict the planetary wave propagation for a deep basin (i.e. 1000 m depth). However, the eigenfrequencies associated with a shallow basin (i.e. 250 m depth) failed to accurately reproduce the planetary wave frequencies.

8.2 Topography

The impact of the continental shelf and a transpolar ridge on the polar circulation has been studied systematically in this dissertation. Overall the circulation in a step-shelf basin was characterised by two counter-rotating boundary currents. They were confined on the shelf for a uniform step shelf basin, although this constraint was broken if the shelf width was narrower than the frictional boundary layer allowing the flow to cross the shelf break. Integral constraints derived from the linearised momentum equation determine the permissible forms of the circulation that can exist in the deep basin.

The inclusion of a ridge, the top of which is at the same depth as the step-shelf, supports the formation of a transpolar current with western boundary currents on both sides of the ridge. Changing ridge orientation modifies the anticyclonic and cyclonic boundary current on the step-shelf, strengthening the anticyclonic branch in comparison with the cyclonic current.

A more realistic Arctic basin domain (i.e. a step-shelf basin with three gaps and a ridge) revealed a mainly cyclonic shelf circulation while the deep basin fluid is essentially at rest. The GINs inflow diverges forming three currents. The first recirculates exiting

throughout the same strait. The second flows towards the Davis Strait merging with the cyclonic boundary current before exiting. The third propagates cyclonically forming a boundary branch which converges with the Bering inflow flowing along the shelf towards the Davis Strait (qualitatively similar to results in Aksenov *et al.*, 2011). The presence of a narrow shelf on the "western side of the basin" alters the latter steady circulation. A weak anticyclonic deep boundary circulation is fed from the cyclonic boundary current on the narrow shelf. The nature of this deep current has been already discussed by Spall (2013) although he affirmed that this current was generated by buoyancy forces. In Chapter 7, it was again observed that the inclusion of a narrow shelf had a strong impact on the circulation. In particular, ramp-up experiments of the Bering inflow showed the formation of an anticyclonic branch from the Bering Strait propagating towards the GINs and Davis straits along the eastern shelf. This clockwise shelf branch has been observed in more realistic experiments by Aksenov *et al.* (2016) but they suggested that the wind stress was the main driving mechanism.

8.3 Wind stress

In comparison with the topography, the wind stress has not been investigated as extensively. Nevertheless, there are some results contained in Chapters 5 and 6 that are significant.

The analytic solutions showed that a wind stress curl with two opposite cells drives two and four ocean gyres in a flat bottom basin and step-shelf basin, respectively. The centre of these gyres is rotated clockwise due to the effect of the rotation of the Earth. This observation is really interesting because even though some studies (Yang, 2005; Zhang and Steele, 2007; Spall, 2013) employ the f-plane to study the Arctic circulation, these results suggest that the beta effect is important in a realistic representation of the wind-driven planetary geostrophic circulation. Further, numerical simulations examined the impact of a ridge in the step-shelf basin. As observed in Chapter 4, the addition of a transpolar ridge supports a transpolar current but in contrast with that chapter the ridge does not exhibit pronounced western boundary currents on both sides of the ridge.

More realistic experiments with the observed wind stress regimes of the Arctic basin revealed the importance of the wind stress in driving the surface circulation in the Arctic basin. In the presence of an anticyclonic wind stress regime, a well defined Beaufort Gyre is generated in the Canada basin (Proshutinsky *et al.*, 2011). The link between the

Bering and Davis Strait is weakened due to the formation of an intense transpolar current along the ridge as shown in Figure 6.12 (b). On the other hand, a cyclonic wind stress regime diminishes the size of the Beaufort Gyre by about 6cm in the SSH field. Also, the Bering inflow bifurcates into two currents; the first crosses the transpolar ridge and the second flows as an anticyclonic boundary current along the eastern or Euroasian shelf. These findings confirm the hypothesis of the dominant role of the wind stress in driving the surface circulation in the Arctic Ocean (Proshutinsky *et al.*, 2011; Davis *et al.*, 2014; Proshutinsky *et al.*, 2015).

8.4 Future research

Finally there are several important features of the Arctic Ocean have been neglected, notably. To a first approximation the Arctic Ocean can be viewed as a two–layer fluid; a surface cold freshwater layer and a deep warm salty layer. Therefore, the extension of the analytic model of Chapter 2 to a two layer model could give a further insight in the ocean dynamics in the Arctic basin. How much does the steady–state circulation differ from the barotropic model? In addition, this could be extended in order to include other important topographic features in a manner similar to that in Chapter 4. A study of this type will shed light on the "shielding" effect of stratification and the topographic steering effect (Hart, 1975; Yang *et al.*, 2016).

Another important aspect related to baroclinic ocean circulation models is wind stress driving. Chapter 5 and 6 studied a barotropic wind–driven circulation forced by a wind stress curl with two opposite signs. The addition in complexity of a two layer model could help to understand the impact of the wind stress regime on the deep circulation. Furthermore, using a numerical ocean model these solutions could be extended to consider different wind stress regimes, as in Chapter 6.

Chapter 7 investigated the SSH anomaly propagation (and associated anomaly currents) in a polar basin driven by unsteady volume fluxes through straits. These anomaly experiments elucidated the relationships between the SSH anomaly pattern (and its propagation) and the magnitude and period of the prescribed anomaly volume flux across one strait. It would be worthwhile to study whether the determination of the SSH anomalies in the Arctic basin (using altimeter data, for example) could be used in an "inverse method" to calculate the unsteady perturbation volume fluxes across the straits.

Finally, the presence of sea ice was briefly considered in this thesis. The numerical

studies with the NEMO coupled ice–ocean model demonstrated the importance of land–fast ice formation on the barotropic ocean circulation, especially in the presence of wind stress. Coupled ice–ocean studies of this type should be further studied with more complex bathymetries and a broader range of wind stress regimes.

Appendix A

A.1 Uniformly rotating sphere or "$f-$sphere" approximation in (2.3) with linear bottom friction.

Upon setting $\boldsymbol{\tau} = 0$ and taking the curl of (2.3).

$$-f_f u_\varphi - (f_f v \sin\theta)_\theta = \left(\mu \frac{u \sin\theta}{H}\right)_\theta - \left(\mu \frac{v}{H}\right)_\varphi \tag{A.1}$$

where f_f is the Coriolis parameter at a fixed colatitude. In terms of ψ, defined by (2.5), the vorticity equations takes the form

$$-\frac{f_f}{HR}\psi_{\varphi\theta} - \left(-\frac{f_f}{HR}\psi_\varphi\right)_\theta = \left(\mu \frac{\sin\theta}{H^2 R}\psi_\theta\right)_\theta - \left(\frac{-\mu}{H^2 R \sin\theta}\psi_\varphi\right)_\varphi \tag{A.2}$$

Expanding the partial derivatives we obtain

$$0 = \frac{\mu}{H^2 R}\left(\cos\theta\psi_\theta + \sin\theta\psi_{\theta\theta}\right) + \frac{\mu}{H^2 R \sin\theta}\psi_{\varphi\varphi} \tag{A.3}$$

We multiply equation (A.3) by $\mu^{-1} HR \sin\theta$ and rearrange:

$$\psi_{\varphi\varphi} + A\psi_{\theta\theta} + B\psi_\theta = 0, \tag{A.4}$$

The coefficients A and B in (A.4) are defined as

$$A \equiv \sin^2\theta, \qquad B \equiv \sin\theta\cos\theta. \tag{A.5}$$

Hereafter, we solve (A.5) as in section 2.1a.

A.2 MATLAB script for Source-sink driven solutions in presence of bottom friction

A.2.1 Flat bottom basin

```
clc
clear all
close all

%Ocean Basin Parameters

mu=1e-4;              %bottom friction coefficient
av=7.292115e-5;       %angular velocity of the earth
H=1000;               %depth
g=9.8;                %gravity
delta=10*pi/180;      %half of the gap aperture
R=6371e3;             %radius of the earth
phi1=pi;              %
thetab=20*pi/180;     %bondary colatitude in radians
thetaf=thetab/2;      %fix colatitude  in radians
PO=2.5e6;             %half of Transport across the boundary
N=150;                %summation terms of the FS in (2.13)

%Defining geographical grid in terms colatitude and longitude

lon=0:pi/1440:2*pi;           %longitude in radians
lat=0:pi/1440:thetab;         %colatitude in radians
[PH,TH,R3] = meshgrid(lon,pi/2-lat,R);
[X1,Y1,z] = sph2cart(PH,TH,R3);     %Conversion spherical to
                                    %cartessian coordiantes
L=length(lon);                %number of longitude points
M=length(lat);                %number of colatitude points

%Fourier series coefficients of the flow at the boundary
```

```
30
31 Aob=(PO/pi)*(phi1-pi);  %Ao at the boundary
32 for n=1:N;
33    Anb(n)=0;
34    Bnb(n)=2*PO/(pi*n^2*delta)*sin(n*delta)*(1-cos(n*phi1));
35 end
36
37 %Compute constant terms of vorticity equation (2.10)
38
39 B=cos(thetaf)*sin(thetaf);
40 A=sin(thetaf)^2;
41 C=(2*av*H*sin(thetaf)^2/mu);
42
43
44
45 %Compute lambda from (2.19)
46
47 for n=1:N
48  t(n)=n^2+i*n*C;
49  lambda1(n)=-B/(2*A)-(sqrt(B^2+4*A*t(n))/(2*A));
50  lambda2(n)=-B/(2*A)+(sqrt(B^2+4*A*t(n))/(2*A));
51 end
52
53 %Compute the ZN from (2.24)
54
55 for m=1:M
56    for n=1:N
57     ZN(m,n)=(Anb(n)+i*Bnb(n))*...
58                (exp(lambda1(n)*(lat(m)-thetab))...
59               -exp((lambda2(n)*(lat(m)))-(lambda1(n)*thetab)))...
60               /(1-exp((lambda2(n)-lambda1(n))*thetab));
61    end
62 end
```

```
63
64 %Retrive an and bn from ZN
65
66 An=real(ZN);    % Coeficient an is the real part of ZN
67 Bn=imag(ZN);    % Coeficcent bn is the imaginary part of ZN
68
69 %Fourier series expansion on the circular basin
70
71 Ao=0
72 for m=1:M
73  for k=1:L
74   term2=Ao;
75    for n=1:N
76     term2=term2+(An(m,n)*cos(n*lon(k))+Bn(m,n)*sin(n*lon(k)));
77    end
78   Fcb(m,k)=term2;
79  end
80 end
```

A.2.2 Step-shelf basin

```
clc
clear all
close all

%Ocean Basin Parameters

mu=1e-4;                %bottom friction coefficient
av=7.292115e-5;         %angular velocity of the earth
H2=1000;                %depth in basin
H1=250;                 %depth in shelf
s=H1/H2;                %depth ratio
g=9.8;                  %gravity
delta=10*pi/180;        %half of the gap aperture
R=6371e3;               %radius of the earth
phi1=pi;                %
thetab=20*pi/180;       %bondary colatitude in radians
thetaf=thetab/2;        %fix colatitude  in radians
thetas=11*pi/180;       %colatitude for the end of shelf
fs=2*av*cos(thetas);    %coriolis force in thetas
PO=2.5e6;               %half of Transport across the boundary
N=150;                  %summation terms of the FS in (2.31)

%Defining geographical grid in terms colatitude and longitude

lon=0:pi/1440:2*pi;             %longitude in radians
lat=0:pi/1440:thetab;           %colatitude in radians
[PH,TH,R3] = meshgrid(lon,pi/2-lat,R);
[X1,Y1,z] = sph2cart(PH,TH,R3);     %Conversion spherical to
                                    %cartessian coordiantes
L=length(lon);                  %number of longitude points
M=length(lat);                  %number of colatitude points

```

```
%Fourier series coefficients of the flow at the boundary

Aob=(PO/pi)*(phi1-pi);  %Ao at the boundary
for n=1:N;
 Anb(n)=0;
 Bnb(n)=2*PO/(pi*n^2*delta)*sin(n*delta)*(1-cos(n*phi1));
end









%Compute constant terms of vorticity equation (2.26)

B=cos(thetaf)*sin(thetaf);
A=sin(thetaf)^2;
C1=(2*av*H1*sin(thetaf)^2/mu);
C2=(2*av*H2*sin(thetaf)^2/mu);

%Compute lambda and omega from (2.19)

for n=1:N
 t(n)=n^2+i*n*C1;
 t1(n)=n^2+1i*n*C2;
 lambda1(n)=-B/(2*A)-(sqrt(B^2+4*A*t(n))/(2*A));
 lambda2(n)=-B/(2*A)+(sqrt(B^2+4*A*t(n))/(2*A));
 omega1(n)=-B/(2*A)+(sqrt(B^2+4*A*t1(n))/(2*A));
 omega2(n)=-B/(2*A)-(sqrt(B^2+4*A*t1(n))/(2*A));
end

%Compute arbitrary constants from (2.34)

```

```
for n=1:N
 AA(n)=(i*n*H1*fs/sin(thetas));
 CONS=[0  0  1  1;...
       exp(lambda1(n)*thetab) exp(lambda2(n)*thetab) 0 0 ;...
       exp(lambda1(n)*thetas) exp(lambda2(n)*thetas) -exp(omega1(
           n)*thetas) -exp(omega2(n)*thetas);...
       AA(n)*exp(lambda1(n)*thetas)+mu*lambda1(n)*exp(lambda1(n)*
           thetas) AA(n)*exp(lambda2(n)*thetas)+mu*lambda2(n)*exp(
           lambda2(n)*thetas) -(s*AA(n)*exp(omega1(n)*thetas)+s^2*
           mu*omega1(n)*exp(omega1(n)*thetas)) -(s*AA(n)*exp(
           omega2(n)*thetas)+s^2*mu*omega2(n)*exp(omega2(n)*thetas
           ))];

 VEC=[0;(Anb(n)+i*Bnb(n));0;0];
 a(:,n)=linsolve(CONS,VEC);

 fn(1,n)=a(1,n);
 gn(1,n)=a(2,n);
 Fn(1,n)=a(3,n);
 Gn(1,n)=a(4,n);

end









%Compute the ZN from (2.24)

for m=1:M
```

```
93  if (lat(m) < thetas);
94   for n=1:N
95    ZN(m,n)=Fn(n)*exp(omega1(n)*lat(m))+Gn(n)*exp(omega2(n)*lat(m
          ));
96   end
97  else
98   for n=1:N
99    ZN(m,n)=fn(n)*exp(lambda1(n)*lat(m))+gn(n)*exp(lambda2(n)*lat
          (m));
100  end
101 end
102 end
103
104 %Retrive an and bn from ZN
105
106 An=real(ZN);    % Coeficient an is the real part of ZN
107 Bn=imag(ZN);    % Coeficcent bn is the imaginary part of ZN
108
109 %Fourier series expansion on the circular basin
110
111 Ao=0
112 for m=1:M
113  for k=1:L
114   term=Ao
115    for n=1:N
116     term=term+(An(m,n)*cos(n*lon(k))+Bn(m,n)*sin(n*lon(k)));
117    end
118   Fcb(m,k)=term;
119  end
120 end
```

A.3 MATLAB script for Source-sink driven solutions in presence of lateral diffusion

A.3.1 Newton Method

```
function [ x, k, ex ] = newtondiffc( f, df, x0,n,P1,P2,P3,P4,P5,
    tol, nmax )
%
% NEWTON Newton's Method
%   Newton's method for finding successively better
   approximations to the
%   zeroes of a real-valued function.
%
% Input:
%   f - input funtion
%   df - derived input function
%   x0 - inicial aproximation
%   tol - tolerance
%   nmax - maximum number of iterations
%
% Output:
%   x - aproximation to root
%   ex - error estimate
%
% Author:       Modified version of Tashi Ravach
% Version:      1.0
% Date:     16/04/2007
%

f = inline(f,'x','n','P1','P2','P3','P4','P5');
df = inline(df,'x','n','P1','P2','P3','P4','P5');
x(1) = x0 - (f(x0,n,P1,P2,P3,P4,P5)/df(x0,n,P1,P2,P3,P4,P5));
ex(1) = abs(x(1)-x0);
k = 2;
```

```
28
29   while (ex(k-1) >= tol) && (k <= nmax)
30     x(k) = x(k-1) - (f(x(k-1),n,P1,P2,P3,P4,P5)/df(x(k-1),n,P1,P2,
           P3,P4,P5));
31     ex(k) = abs(x(k)-x(k-1));
32     k = k+1;
33   end
34 k=k-1;
35 end
```

A.3.2 Flat bottom basin

```
clc
clear all
close all

%Ocean Basin Parameters

A=10000;              % Eddy diffusivity
av=7.292115e-5;       %angular velocity of the earth
H=1000;               %depth
g=9.8;                %gravity
delta=10*pi/180;      %half of the gap aperture
R=6371e3;             %radius of the earth
phi1=pi;              %
thetab=20*pi/180;     %bondary colatitude in radians
thetaf=thetab/2;      %fix colatitude  in radians
PO=2.5e6;             %half of Transport across the boundary
N=150;                %summation terms of the FS in (2.13)

%Defining geographical grid in terms colatitude and longitude

lon=0:pi/1440:2*pi;           %longitude in radians
lat=0:pi/1440:thetab;         %colatitude in radians
[PH,TH,R3] = meshgrid(lon,pi/2-lat,R);
[X1,Y1,z] = sph2cart(PH,TH,R3);     %Conversion spherical to
%cartessian coordiantes
L=length(lon);                %number of longitude points
M=length(lat);                %number of colatitude points

%Fourier series coefficients of the flow at the boundary

Aob=(PO/pi)*(phi1-pi);  %Ao at the boundary
for n=1:N;
```

```
 Anb(n)=0;
 Bnb(n)=2*PO/(pi*n^2*delta)*sin(n*delta)*(1-cos(n*phi1));
end

%Compute constant terms of vorticity equation (2.43)

P1=cot(thetaf);
P2=(1+cos(thetaf)^2)/sin(thetaf)^4;
P3=2*cos(thetaf)/sin(thetaf)^3;
P4=1/sin(thetaf)^2;
P5=2*av*R^2/A;


%Compute the roots from (2.45)
au=zeros(N,5)
lambda=zeros(N,4)

for n=1:N;
 au(n,:)=[1 P1 -n^2*P4 n^2*P3 -n*(n*P2-i*P5)];
 S=roots(au(n,:));
 lambda(n,:)=S';
end

%Plot lambda to check the roots

figure (1)
plot(lambda(:,1),'.b','MarkerSize',18)
hold on
plot(lambda(:,2),'.r','MarkerSize',18)
plot(lambda(:,3),'.g','MarkerSize',18)
plot(lambda(:,4),'.k','MarkerSize',18)
set(gcf,'color','thetas');
set (gca,'FontName','Times','FontSize',18)
```

```
66 legend('\lambda_{1n}','\lambda_{2n}','\lambda_{3n}','\lambda_{4n}')
67
68 %Newton method
69
70 first=20;                    %first n value to use in the Newton method
71 nadj=first-0.1:-0.1:0.5;     %array of n values obtain lambda using the Newton method
72 N2=length(nadj);             %number of point in the array
73 lambdane=zeros(N2,4);        %nethetas lambda to compute
74 er1=zeros(N2,4);             %array for the error of the Newton mehod
75 lambdat=zeros(first-1,4);    %ultimate array thetasith the correct lambda values
76 lambda1=zeros(N,1);          %final lambda terms use in ()
77 lambda2=zeros(N,1);          %  ''    ''
78 lambda3=zeros(N,1);          %  ''    ''
79 lambda4=zeros(N,1);          %  ''    ''
80
81 %Compute first value of lambdae from lambda
82
83 for l=1:4
84  [x,knum,er]=newtonmethod('x^4+P1*x^3-n^2*P4*x^2+n^2*P3*x-n*(n*P2-1i*P5)',...
85  '4*x^3+3*P1*x^2-n^2*2*P4*x+n^2*P3',...
86  lambda(first,l),first-0.1,P1,P2,P3,P4,P5,0.5*10^-6, 100 );
87  lambdae(1,l)=x(1,knum);
88 end
89
90 %We use the previous root to get the next root
91
92 for n2=2:N2
```

```
93   for l=1:4
94     [x,knum,er]=newtonmethod('x^4+P1*x^3-n^2*P4*x^2+n^2*P3*x-n*(
         n*P2-1i*P5)',...
95     '4*x^3+3*P1*x^2-n^2*2*P4*x+n^2*P3',...
96     lambdae(n2-1,l),nadj(n2),P1,P2,P3,P4,P5, 0.5*10^-6, 100 );
97
98     lambdae(n2,l)=x(1,knum);
99     er1(n2,l)=er(knum);
100      if (rem(n2,10)==0)
101       lambdat(n2/10,nm)=lambdae(n2,l);  %choose only the integer
            terms of n
102      end
103   end
104 end
105
106 lambdat=flipud(lambdat);                %rearrange lambdat
107
108 % Merge and define particular lambda
109
110 for n=1:first-1
111   lambda1(n,1)=lambdat(n,1);
112   lambda2(n,1)=lambdat(n,2);
113   lambda3(n,1)=lambdat(n,3);
114   lambda4(n,1)=lambdat(n,4);
115 end
116
117 for n=first:N
118   lambda1(n,1)=lambda(n,1);
119   lambda2(n,1)=lambda(n,2);
120   lambda3(n,1)=lambda(n,3);
121   lambda4(n,1)=lambda(n,4);
122 end
123
```

```
124 %Compute the arbitrary contants from (2.46)
125
126 for n=1:N
127  CONS=[1 1 1 1;lambda1(n) lambda2(n) lambda3(n) lambda4(n);...
128  lambda1(n)*exp(lambda1(n)*thetab) lambda2(n)*exp(lambda2(n)*
         thetab)...
129  lambda3(n)*exp(lambda3(n)*thetab) lambda4(n)*exp(lambda4(n)*
         thetab);...
130  exp(lambda1(n)*thetab) exp(lambda2(n)*thetab) exp(lambda3(n)*
         thetab) exp(lambda4(n)*thetab) ];
131
132  VEC=[0;0;0;(Anb(n)+i*Bnb(n))];
133
134  a(:,n)=linsolve(CONS,VEC);
135
136  k1(1,n)=a(1,n);
137  k2(1,n)=a(2,n);
138  k3(1,n)=a(3,n);
139  k4(1,n)=a(4,n);
140 end
141
142 %Compute the ZN from (2.44)
143
144 for m=1:M;
145   for n=1:N;
146    ZN(m,n)=k1(n)*exp(lambda1(n)*lat(m))+...
147    k2(n)*exp(lambda2(n)*lat(m))+...
148    k3(n)*exp(lambda3(n)*lat(m))+...
149    k4(n)*exp(lambda4(n)*lat(m));
150   end
151 end
152
153 %Retrive an and bn from ZN
```

```
154
155 An=real(ZN);    % Coeficient an is the real part of ZN
156 Bn=imag(ZN);    % Coeficcent bn is the imaginary part of ZN
157
158 %Fourier series expansion on the circular basin
159
160 Ao=0
161 for m=1:M
162  for k=1:L
163   term=Ao;
164    for n=1:N;
165     term=term+(An(m,n)*cos(n*lon(k))+Bn(m,n)*sin(n*lon(k)));
166    end
167   Fcb(m,k)=term;
168  end
169 end
```

A.3.3 Step shelf basin

```
clc
clear all
close all

%Ocean Basin Parameters

A=10000;                %Eddy diffusivity
av=7.292115e-5;         %angular velocity of the earth
H2=1000;                %depth in basin
H1=250;                 %depth in shelf
s=H1/H2;                %depth ratio
g=9.8;                  %gravity
delta=10*pi/180;        %half of the gap aperture
R=6371e3;               %radius of the earth
phi1=pi;                %
thetab=20*pi/180;       %bondary colatitude in radians
thetaf=thetab/2;        %fix colatitude  in radians
thetas=11*pi/180;       %colatitude for the end of shelf
fs=2*av*cos(thetas);    %coriolis force in thetas
PO=2.5e6;               %half of Transport across the boundary
N=150;                  %summation terms of the FS in (2.13)

%Defining geographical grid in terms colatitude and longitude

lon=0:pi/1440:2*pi;             %longitude in radians
lat=0:pi/1440:thetab;           %colatitude in radians
[PH,TH,R3] = meshgrid(lon,pi/2-lat,R);
[X1,Y1,z] = sph2cart(PH,TH,R3);     %Conversion spherical to
%cartessian coordiantes
L=length(lon);                  %number of longitude points
M=length(lat);                  %number of colatitude points

```

```
%Fourier series coefficients of the flow at the boundary

Aob=(PO/pi)*(phi1-pi);  %Ao at the boundary
 for n=1:N;
 Anb(n)=0;
 Bnb(n)=2*PO/(pi*n^2*delta)*sin(n*delta)*(1-cos(n*phi1));
end

%Compute constant terms of vorticity equation (2.43)

P1=cot(thetaf);
P2=(1+cos(thetaf)^2)/sin(thetaf)^4;
P3=2*cos(thetaf)/sin(thetaf)^3;
P4=1/sin(thetaf)^2;
P5=2*av*R^2/A;


%Compute the roots from (2.45)
au=zeros(N,5);
lambda=zeros(N,4);

for n=1:N;
 au(n,:)=[1  P1  -n^2*P4  n^2*P3  -n*(n*P2-i*P5)];
 lambda(n,:)=roots(au(n,:));
end

%Plot lambda to check the roots

figure (1)
plot(lambda(:,1),'.b','MarkerSize',18)
hold on
plot(lambda(:,2),'.r','MarkerSize',18)
plot(lambda(:,3),'.g','MarkerSize',18)
```

```
66 plot(lambda(:,4),'.k','MarkerSize',18)
67 set (gca,'FontName','Times','FontSize',18)
68 legend('\lambda_{1n}','\lambda_{2n}','\lambda_{3n}','\lambda_{4n
       }')
69
70 %Newton method
71
72 first=20;                    %first n value to use in the Newton
       method
73 nadj=first-0.1:-0.1:0.5;     %array of n values obtain lambda
       using the Newton method
74 N2=length(nadj);             %number of point in the array
75 lambdane=zeros(N2,4);        %nethetas lambda to compute
76 er1=zeros(N2,4);             %array for the error of the Newton
       mehod
77 lambdat=zeros(first-1,4);    %ultimate array thetasith the correct
        lambda values
78 lambda1=zeros(N,1);          %final lambda terms use in ()
79 lambda2=zeros(N,1);          %  ''     ''
80 lambda3=zeros(N,1);          %  ''     ''
81 lambda4=zeros(N,1);          %  ''     ''
82
83 %Compute first value of lambdae from lambda
84
85 for l=1:4
86  [x,knum,er]=newtondiffc('x^4+P1*x^3-n^2*P4*x^2+n^2*P3*x-n*(n*
       P2-1i*P5)',...
87  '4*x^3+3*P1*x^2-n^2*2*P4*x+n^2*P3',...
88  lambda(first,l),first-0.1,P1,P2,P3,P4,P5,0.5*10^-6, 100 );
89  lambdae(1,l)=x(1,knum;
90 end
91
92 %We use the previous root to get the next root
```

```
93
94  for n2=2:N2
95   for l=1:4
96    [x,knum,er] =newtondiffc('x^4+P1*x^3-n^2*P4*x^2+n^2*P3*x-n*(n*
          P2-1i*P5)',...
97    '4*x^3+3*P1*x^2-n^2*2*P4*x+n^2*P3',...
98    lambdae(n2-1,l),nadj(n2),P1,P2,P3,P4,P5, 0.5*10^-6, 100 );
99
100   lambdae(n2,l)=x(1,knum);
101   er1(n2,l)=er(knum);
102    if(rem(n2,10)==0)
103     lambdat(n2/10,l)=lambdae(n2,l);  %choose only the integer
            terms of n
104    end
105  end
106 end
107
108 lambdat=flipud(lambdat);              %rearrange lambdat
109
110 %Merge and define particular lambda
111
112 for n=1:first-1
113  lambda1(n,1)=lambdat(n,1);
114  lambda2(n,1)=lambdat(n,2);
115  lambda3(n,1)=lambdat(n,3);
116  lambda4(n,1)=lambdat(n,4);
117 end
118
119 for n=first:N
120  lambda1(n,1)=lambda(n,1);
121  lambda2(n,1)=lambda(n,2);
122  lambda3(n,1)=lambda(n,3);
123  lambda4(n,1)=lambda(n,4);
```

```
124 end
125
126 %Compute the arbitrary contants from  boundary and matching
      conditions (2.11), (2.40), (2.41) and (2.56)
127
128 gamma=A*sin(thetas)/(fs*R^2);
129 B=A*(1+cos(thetas)^2)/(sin(thetas)^3*R^2*fs);
130 C=A/(sin(thetas)^2*R^2*av);
131 D=A/(fs*R^2*sin(thetas));
132
133
134
135
136 for n=1:N
137  CONS=[1 1 1 1 0 0 0 0;...
138  lambda1(n) lambda2(n)...
139  lambda3(n) lambda4(n) 0 0 0 0;...
140  0 0 0 0 exp(lambda1(n)*thetab)...
141  exp(lambda2(n)*thetab) exp(lambda3(n)*thetab) ...
142  exp(lambda4(n)*thetab);...
143  0 0 0 0 lambda1(n)*exp(lambda1(n)*thetab)...
144  lambda2(n)*exp(lambda2(n)*thetab) ...
145  lambda3(n)*exp(lambda3(n)*thetab) ...
146  lambda4(n)*exp(lambda4(n)*thetab);...
147  -lambda1(n)*exp(lambda1(n)*thetas) ...
148  -lambda2(n)*exp(lambda2(n)*thetas) ...
149  -lambda3(n)*exp(lambda3(n)*thetas) ...
150  -lambda4(n)*exp(lambda4(n)*thetas) ...
151  lambda1(n)*exp(lambda1(n)*thetas) ...
152  lambda2(n)*exp(lambda2(n)*thetas) ...
153  lambda3(n)*exp(lambda3(n)*thetas) ...
154  lambda4(n)*exp(lambda4(n)*thetas);...
155  -exp(lambda1(n)*thetas) -exp(lambda2(n)*thetas) ...
```

```
-exp(lambda3(n)*thetas) -exp(lambda4(n)*thetas) ...
exp(lambda1(n)*thetas) exp(lambda2(n)*thetas) ...
exp(lambda3(n)*thetas) exp(lambda4(n)*thetas);...
-s*exp(lambda1(n)*thetas)*(gamma*lambda1(n)^3-i*n) ...
-s*exp(lambda2(n)*thetas)*(gamma*lambda2(n)^3-i*n) ...
-s*exp(lambda3(n)*thetas)*(gamma*lambda3(n)^3-i*n) ...
-s*exp(lambda4(n)*thetas)*(gamma*lambda4(n)^3-i*n) ...
exp(lambda1(n)*thetas)*(gamma*lambda1(n)^3-1i*n) ...
exp(lambda2(n)*thetas)*(gamma*lambda2(n)^3-i*n) ...
exp(lambda3(n)*thetas)*(gamma*lambda3(n)^3-i*n) ...
exp(lambda4(n)*thetas)*(gamma*lambda4(n)^3-i*n);...
-(lambda1(n)-i*C*n*lambda1(n)+i*n*B+lambda1(n)^2*i*n*D)*s*exp(
    lambda1(n)*thetas) ...
-(lambda2(n)-i*C*n*lambda2(n)+i*n*B+lambda2(n)^2*i*n*D)*s*exp(
    lambda2(n)*thetas) ...
-(lambda3(n)-i*C*n*lambda3(n)+i*n*B+lambda3(n)^2*i*n*D)*s*exp(
    lambda3(n)*thetas) ...
-(lambda4(n)-i*C*n*lambda4(n)+i*n*B+lambda4(n)^2*i*n*D)*s*exp(
    lambda4(n)*thetas) ...
(lambda1(n)-i*C*n*lambda1(n)+i*n*B+lambda1(n)^2*i*n*D)*exp(
    lambda1(n)*thetas) ...
(lambda2(n)-i*C*n*lambda2(n)+i*n*B+lambda2(n)^2*i*n*D)*exp(
    lambda2(n)*thetas) ...
(lambda3(n)-i*C*n*lambda3(n)+i*n*B+lambda3(n)^2*i*n*D)*exp(
    lambda3(n)*thetas) ...
(lambda4(n)-i*C*n*lambda4(n)+i*n*B+lambda4(n)^2*i*n*D)*exp(
    lambda4(n)*thetas)];

VEC=[0;0;(Anb(n)+i*Bnb(n));0;0;0;0;0];

a(:,n)=linsolve(CONS,VEC);

K1(1,n)=a(1,n);
```

```
181   K2(1,n)=a(2,n);
182   K3(1,n)=a(3,n);
183   K4(1,n)=a(4,n);
184   k1(1,n)=a(5,n);
185   k2(1,n)=a(6,n);
186   k3(1,n)=a(7,n);
187   k4(1,n)=a(8,n);
188
189 end
190
191 %Compute the ZN from (2.55)
192
193 for m=1:M
194   for n=1:N
195     if (lat(m) < thetas);
196       ZN(m,n)=K1(n)*exp(lambda1(n)*lat(m))+...
197       K2(n)*exp(lambda2(n)*lat(m))+...
198       K3(n)*exp(lambda3(n)*lat(m))+...
199       K4(n)*exp(lambda4(n)*lat(m));
200     else
201      ZN(m,n)=k1(n)*exp(lambda1(n)*lat(m))+...
202      k2(n)*exp(lambda2(n)*lat(m))+...
203      k3(n)*exp(lambda3(n)*lat(m))+...
204      k4(n)*exp(lambda4(n)*lat(m));
205   end
206 end
207
208 %Retrive an and bn from ZN
209
210 An=real(ZN);    % Coeficient an is the real part of ZN
211 Bn=imag(ZN);    % Coeficcent bn is the imaginary part of ZN
212
213 %Fourier series expansion on the circular basin
```

```
214
215 Ao=0
216 for m=1:M
217  for k=1:L
218   term=Ao;
219    for n=1:N;
220     term=term+(An(m,n)*cos(n*lon(k))+Bn(m,n)*sin(n*lon(k)));
221    end
222   Fcb(m,k)=term;
223  end
224 end
```

A.4 Three gaps domain

```
clc
clear all
close all

%Ocean Basin Parameters

N=150;                  %summation terms of the FS in (2.13)
GI=4.5e6;               %GIN inflow
BE=1.e6;                %Bering inflow
DV=2.1e6;               %Davies outflow
GO=5.4e6;               %GIN outflow
GI2=2.e6;               %GIN inflow
phi1=18*pi/180;
phi2=180*pi/180;
phi3=195*pi/180;
phi4=293*pi/180;
phi5=305*pi/180;
phi6=338*pi/180;
phi7=352*pi/180;

A0=1/(2*pi)*((-1/2)*GI*phi1 ...
    +BE*(-1/2)*(phi2+phi3) ...
    -DV*(1/2)*(-phi4-phi5) ...
    -GO*(1/2)*(-phi6-phi7) ...
    +GI2*(1/2)*(-phi7-2*pi))

for n=1:N;
 AN(n)=1/(pi)*(GI*(cos(n*phi1)-1.)/(phi1*n^2) ...
         +BE*(-cos(n*phi3)+cos(n*phi2))/(n^2*(phi2-phi3)) ...
         -DV*(cos(n*phi4)-1.*cos(n*phi5))/((phi4-phi5)*n^2) ...
         -GO*(cos(n*phi6)-1.*cos(n*phi7))/((phi6-phi7)*n^2) ...
         +GI2*(cos(n*phi7)-1.*cos(2.*n*pi))/((phi7-2.*pi)*n^2));
```

```
33
34  BN(n)=1/(pi)*(-GI*(-sin(n*phi1))/(phi1*n^2)...
35          -BE*(sin(n*phi3)-sin(n*phi2))/(n^2*(phi2-1.*phi3))...
36          -DV*(sin(n*phi4)-1.*sin(n*phi5))/((phi4-1.*phi5)*n^2)...
37          +GO*(sin(n*phi7)-1.*sin(n*phi6))/((phi6-1.*phi7)*n^2)...
38          +GI2*sin(n*phi7)/((phi7-2.*pi)*n^2));
39  end
```

Appendix B

B.1 Uniformly rotating sphere or "$f-$sphere" approximation in (3.1).

This approximation is exactly the same as section 3.1 until (3.8) where the f does not vary with the latitude. Then, we expand the partial derivative and we obtain,

$$-\frac{i\omega R^2}{H}F+\frac{ig}{D\sin\theta}\left[m\left(fF'-\frac{m\omega}{\sin\theta}F\right)+\sin\theta\left(wF''-\frac{mf}{\sin\theta}F'\right.\right. \tag{B.1}$$
$$\left.\left.+\frac{2\Omega\cos^2\theta m}{\sin^2\theta}\right)+\left(\omega F'-\frac{mf}{\sin\theta}F\right)\cos\theta\right] = 0,$$

If we multiply (B.1) by $D\left(ig\omega\right)^{-1}$

$$-\frac{R^2D}{gH}F+\frac{1}{\omega\sin\theta}\left[m\left(fF'-\frac{m\omega}{\sin\theta}F\right)+\sin\theta\left(wF''-\frac{mf}{\sin\theta}F'\right.\right. \tag{B.2}$$
$$\left.\left.+\frac{2\Omega\cos^2\theta m}{\sin^2\theta}\right)+\left(\omega F'-\frac{mf}{\sin\theta}F\right)\cos\theta\right] = 0,$$

Removing the brackets, (B.2) can be simplified in

$$F''+\frac{\cos\theta}{\sin\theta}F'-\frac{R^2D}{gH}F-\frac{m^2}{\sin^2\theta}F=0, \tag{B.3}$$

Defining the dimensionless wave frequency, $\sigma=\omega/2\Omega$

$$F''+\frac{\cos\theta}{\sin\theta}F'-\frac{R^2 4\Omega^2\left(\cos^2\theta-\sigma^2\right)}{gH}F-\frac{m^2}{\sin^2\theta}F = 0,$$

Finally, we obtain the wave amplitude equation for freely-propagating waves in polar cap:

$$F''+\cot\theta F'-\left\{\frac{m^2}{\sin^2\theta}+\left(\frac{R}{r_e}\right)^2\left(\cos^2\theta-\sigma^2\right)\right\}F=0, \tag{B.4a}$$

where

$$r_e^2=\frac{gH}{4\Omega^2}. \tag{B.4b}$$

We note that r_e is the external Rossby radius of deformation. Subsequently, we can solve (B.4a) as in section 3.1.

B.2 MATLAB script for Planetary waves

```
clc
close all
clear all

%Ocean Basin Parameters

R=6.371e6;                          %radius of the earth
H=5753;                             %depth
g=9.81;                             %gravity
av=7.2921159e-5;                    %angular velocity of the earth
Rb=1.424598908465116e+06;           %radius of the basin
thetab=asin(Rb/R);                  %bondary colatitude in radians
thetaf=thetab*2/4;                  %fixed colatitude  in radians
N=5;                                %wave number
m=-1:-1:-8;                         %mode number

%Defining geographical grid in terms colatitude and longitude

lon=0:pi/1800:2*pi;                     %longitude in radians
lat=0:pi/1800:thetab;                   %colatitude in radians
[PH,TH,R3] = meshgrid(lon,pi/2-lat,R);
[X1,Y1,z] = sph2cart(PH,TH,R3);         %Conversion spherical to
%cartessian coordiantes
Lo=length(lon);                         %number of longitude points
La=length(lat);                         %number of colatitude points


%Compute constants and solving (3.25)

re=sqrt(g*H)/(2*av);
term3=(R/re)^2*cos(thetaf)^2+sec(thetaf)^2+1/4*cot(thetaf)^2;

```

```
for n=1:N
 for nm=1:8
  term1(n)=(n*pi/thetab)^2;
  term2(nm)=m(nm)^2/sin(thetaf)^2;
  term4(n,nm)=(term1(n)+term2(nm)+term3)/abs(m(nm));
  sigma(n,nm)=1/term4(n,nm);
 end
end


%Compute constants and solving (3.23)

A=2*tan(thetaf)+cot(thetaf);

%Newton method

for n=1:N
 for nm=1:length(m);
  [x,knum,er] = newtonpl('-abs(m)*cot(thetab)*tan(thetab*sqrt(
      abs(m)/x-m^2/sin(thetaf)^2-term3))/x+(1/2)*A*tan(thetab*
      sqrt(abs(m)/x-m^2/sin(thetaf)^2-term3))-sqrt(abs(m)/x-m^2/
      sin(thetaf)^2-term3)'...
  ,'abs(m)*cot(thetab)*tan(thetab*sqrt(abs(m)/x-m^2/sin(thetaf)
      ^2-term3))/x^2+(1/2)*abs(m)^2*cot(thetab)*thetab*(1+tan(
      thetab*sqrt(abs(m)/x-m^2/sin(thetaf)^2-term3))^2)/(x^3*sqrt
      (abs(m)/x-m^2/sin(thetaf)^2-term3))-(1/4)*A*thetab*abs(m)
      *(1+tan(thetab*sqrt(abs(m)/x-m^2/sin(thetaf)^2-term3))^2)/(
      sqrt(abs(m)/x-m^2/sin(thetaf)^2-term3)*x^2)+(1/2)*abs(m)/(
      sqrt(abs(m)/x-m^2/sin(thetaf)^2-term3)*x^2)'...
  ,sigma(n,nm),m(nm),A,term3,thetab,thetaf, 0.5*10^-7, 100 );
  sigmar(n,nm)=x(knum);
  er1(n,nm)=er(knum);
 end
```

```
end

%compute sea surface elevation

n=2;                %select wave number
for nm=1            %select mode number
 for k=1:La
  kappa(nm)=sqrt(abs(m(nm))/sigmar(n,nm)-((m(nm))/sin(thetaf))
      ^2-term3);
  F(k)=exp(-A*lat(k)/2)*sin(kappa(nm)*lat(k)) ;
 end
end

for k=1:La
 for l=1:Lo
  eta(k,l)=F(k)*cos(abs(m(nm))*lon(l));
 end
end

%%%%%%%%%%%%%%%%%%%%%%%%%%%%%%%%%%%%%%%%%%%%
%%%% LeBlond (1968) Frequency %%%%
%%%%%%%%%%%%%%%%%%%%%%%%%%%%%%%%%%%%%%%%%%%%

Beta=besselzero(1,1,1);
M=4*av^2*R^2/(g*H);
LBvalue=20;                 %

for nm=1:8
 beta=besselzero(nm,5,1);
  for n=1:5
   LB(n,nm)=abs(m(nm))/(M+LBvalue*beta(n)^2);
  end
end
```

```
89
90 %compute period (days) for LeBlond (1968) and eigenfrequencies
       (3.23)
91
92 persigr=round(pi*86400./(av*sigmar));
93 perLB=round(pi*86400./(av*LB));
94
95 %compute relative error between LeBlond (1968) and
       eigenfrequencies (3.23)
96
97 for n=1:N
98  for nm=1:8
99   rr(n,nm)=abs(sigmar(n,nm)-LB(n,nm))/sigmar(n,nm)*100
100  end
101 end
```

B.3 Newton method for planetary waves

```
function [ x, k, ex ] = newtonpl( f, df, x0,n,A,term3,thetab,
    thetaf, tol, nmax )
%
% NEWTON Newton's Method
%   Newton's method for finding successively better
    approximations to the
%   zeroes of a real-valued function.
%
% Input:
%   f - input funtion
%   df - derived input function
%   x0 - inicial aproximation
%   tol - tolerance
%   nmax - maximum number of iterations
%
% Output:
%   x - aproximation to root
%   ex - error estimate
%
% Example:
%       [ x, ex ] = newton( 'exp(x)+x', 'exp(x)+1', 0,
    0.5*10^-5, 10 )
%
% Author:       Based on script from Tashi Ravach
% Version:      1.0
% Date:     16/04/2007
%

f = inline(f,'x','m','A','term3','thetab','thetaf');
df = inline(df,'x','m','A','term3','thetab','thetaf');
x(1) = x0 - (f(x0,n,A,term3,thetab,thetaf)/df(x0,n,A,term3,
    thetab,thetaf));
```

```
29 ex(1) = abs(x(1)-x0);
30 k = 2;
31
32 while (ex(k-1) >= tol) && (k <= nmax)
33  x(k) = x(k-1) - (f(x(k-1),n,A,term3,thetab,thetaf)/df(x(k-1),n,
       A,term3,thetab,thetaf));
34  ex(k) = abs(x(k)-x(k-1));
35  k = k+1;
36
37 end
38 k=k-1;
39 end
```

B.4 MATLAB script for Gravity waves

```
clc
close all
clear all

%Ocean Basin Parameters

R=6.371e6;                          %radius of the earth
H=5753;                             %depth
g=9.81;                             %gravity
av=7.2921159e-5;                    %angular velocity of the earth
Rb=1.424598908465116e+06;           %radius of the basin
thetab=asin(Rb/R);                  %bondary colatitude in radians
thetaf=thetab*2/4;                  %fixed colatitude  in radians
m=[-4 -3 -2 -1 1 2 3 4];            %mode number

%Defining geographical grid in terms colatitude and longitude

lon=0:pi/1800:2*pi;                     %longitude in radians
lat=0:pi/1800:thetab;                   %colatitude in radians
[PH,TH,R3] = meshgrid(lon,pi/2-lat,R);
[X1,Y1,z] = sph2cart(PH,TH,R3);         %Conversion spherical to
                                        %cartessian coordiantes
Lo=length(lon);                         %number of longitude points
La=length(lat);                         %number of colatitude points


k=1.05;
x=1;

for s=1:5001
 sigma(x)=k;
 x=x+1;
```

```
33   k=k+0.01;
34  end
35
36
37
38  M=length(m);
39  S=length(sigma);
40
41  %find the approximate roots computing (3.30) and (3.34)
42
43  for nm=1:M
44   for s=1:S
45    re=sqrt(g*H)/(2*av);
46    P(s)=2*sin(thetaf)*cos(thetaf)/(cos(thetaf)^2-sigma(s)^2)+cot(
          thetaf);
47    Q(nm,s)=(R/re)^2*(sigma(s)^2-cos(thetaf)^2)-(m(nm)/sin(thetaf)
          )^2  ...
48                -(m(nm)/sigma(s))*(cos(thetaf)^2+sigma(s)^2)/(cos(
                     thetaf)^2-sigma(s)^2);
49
50    if (-1/4*P(s)^2+Q(nm,s))>=0
51     kk(nm,s)=1;
52     mu(nm,s)=sqrt(-1/4*P(s)^2+Q(nm,s));
53     G(nm,s)=tan(mu(nm,s)*thetab)*(P(s)/2+m(nm)/sigma(s)*cot(
            thetab))-mu(nm,s);
54    else
55     kk(nm,s)=0;
56     mu(nm,s)=sqrt(1/4*P(s)^2-Q(nm,s));
57     G(nm,s)=tanh(mu(nm,s)*thetab)*(P(s)/2+m(nm)/sigma(s)*cot(
            thetab))-mu(nm,s);
58    end
59   end
60  end
```

```
61
62 %use bisection method to refine the roots
63
64 % 1) find max and min to use bisection method
65
66 x=1;
67
68 for s=2:S
69  for nm=1:M
70   if G(nm,s-1)<0 && G(nm,s)>=0
71    Gpeakmax(nm,x)=G(nm,s);
72    sigmamax(nm,x)=sigma(s);
73    Gpeakmin(nm,x)=G(nm,s-1);
74    sigmamin(nm,x)=sigma(s-1);
75    x=x+1;
76   end
77  end
78 end
79
80
81 % 2) get a new sigma value
82
83 X=x-1;
84
85 for s=1:X
86  for nm=1:M
87   x(nm,s)=(sigmamin(nm,s)+sigmamax(nm,s))/2 ;
88   P1(nm,s)=2*sin(thetaf)*cos(thetaf)/(cos(thetaf)^2-x(nm,s)^2)+
       cot(thetaf);
89   Q1(nm,s)=(R/re)^2*(x(nm,s)^2-cos(thetaf)^2)-(m(nm)/sin(thetaf)
       )^2 ...
90              -(m(nm)/x(nm,s))*(cos(thetaf)^2+x(nm,s)^2)/(cos(
                  thetaf)^2-x(nm,s)^2);
```

```
91
92    if (-1/4*P1(nm,s)^2+Q1(nm,s))>=0
93     mu1(nm,s)=sqrt(-1/4*P1(nm,s)^2+Q1(nm,s));
94     mid(nm,s)=tan(mu1(nm,s)*thetab)*(P1(nm,s)/2+m(nm)/x(nm,s)*cot
           (thetab))-mu1(nm,s);
95    else
96     mu1(nm,s)=sqrt(1/4*P1(nm,s)^2-Q1(nm,s));
97     mid(nm,s)=tanh(mu1(nm,s)*thetab)*(P1(nm,s)/2+m(nm)/x(nm,s)*
           cot(thetab))-mu1(nm,s);
98    end
99   end
100 end
101
102 % 3) reapeat same operation until the root is smaller than
      0.0001
103
104 for s=1:X
105  for nm=1:M
106   while abs(mid(nm,s))>1.e-4
107    if mid(nm,s)<0
108     sigmamin(nm,s)=x(nm,s);
109    else
110     sigmamax(nm,s)=x(nm,s);
111    end
112
113    x(nm,s)=(sigmamin(nm,s)+sigmamax(nm,s))/2 ;
114
115    P2(nm,s)=2*sin(thetaf)*cos(thetaf)/(cos(thetaf)^2-x(nm,s)^2)+
           cot(thetaf);
116    Q2(nm,s)=(R/re)^2*(x(nm,s)^2-cos(thetaf)^2)-(m(nm)/sin(thetaf
           ))^2 ...
117                -(m(nm)/x(nm,s))*(cos(thetaf)^2+x(nm,s)^2)/(cos(
                     thetaf)^2-x(nm,s)^2);
```

```
118
119     if (-1/4*P2(nm,s)^2+Q2(nm,s))>=0
120      mu2(nm,s)=sqrt(-1/4*P2(nm,s)^2+Q2(nm,s));
121      mid(nm,s)=tan(mu2(nm,s)*thetab)*(P2(nm,s)/2+m(nm)/x(nm,s)*
             cot(thetab))-mu2(nm,s);
122     else
123      mu2(nm,s)=sqrt(1/4*P2(nm,s)^2-Q2(nm,s));
124      mid(nm,s)=tanh(mu2(nm,s)*thetab)*(P2(nm,s)/2+m(nm)/x(nm,s)*
             cot(thetab))-mu2(nm,s);
125     end
126    end
127   end
128 end
129
130 %transpose matrix for output
131
132 sigmab=sigmamin';
133
134 %Select only the first 5 roots
135
136 [H1,S1,K1]=find(sigmab);          %removing zeros
137
138 H2=length(H1);
139 s1=1;
140 h1=1;
141
142 for z2=1:H2
143   if S1(z2)==s1
144     sigmagr(h1,s1)=K1(z2)
145     h1=h1+1;
146   end
147   if h1==6
148     s1=s1+1;
```

```
149     h1=1;
150   end
151 end
152
153 csvwrite('gravitten.csv',sigmagr,0,0)
154
155
156 %compute sea surface elevation associated to the
      eigenfrequencies
157
158 %transpose matrix to get eta
159
160 sigmagr=sigmagr';
161 s1=1
162
163 for k=1:La
164   for nm=4          %select mode number
165     for s=2         %select wave number
166       P3(nm,s)=2*sin(thetaf)*cos(thetaf)/(cos(thetaf)^2-sigmagr(nm,
            s)^2)+cot(thetaf);
167       Q3(nm,s)=(R/re)^2*(sigmagr(nm,s)^2-cos(thetaf)^2)-(m(nm)/sin(
            thetaf))^2 ...
168                 -(m(nm)/sigmagr(nm,s))*(cos(thetaf)^2+ sigmagr(nm,s)
                      ^2)/(cos(thetaf)^2-sigmagr(nm,s)^2);
169
170       if (-1/4*P3(nm,s)^2+Q3(nm,s))>=0
171         mu3(nm,s)=sqrt(-1/4*P3(nm,s)^2+Q3(nm,s));
172         F(k)=exp(-P3(nm,s)*lat(k)/2)*sin(mu3(nm,s)*lat(k)) ;
173       else
174         mu3(nm,s)=sqrt(1/4*P3(nm,s)^2-Q3(nm,s));
175         F(k)=exp(-P3(nm,s)*lat(k)/2)*sinh(mu3(nm,s)*lat(k)) ;
176       end
177     end
```

```
178   end
179 end
180
181 %compute eta
182
183 for k=1:La
184   for l=1:Lo
185     eta(k,l)=F(k)*cos(m(nm)*lon(l));
186   end
187 end
```

Appendix C

C.1 domzgr.F90

```
 ! inserted between 381 - 427 lines
! of the original domzgr.F90
INTEGER  ::   ji, jj, jl                  ! dummy loop indices
INTEGER  ::   jk,zk,zzj                   ! EGPA
INTEGER  ::   inum                        ! temporary logical unit
INTEGER  ::   ierror                      ! error flag
INTEGER  ::   ii_bump, ij_bump, ih        ! bump center position
INTEGER  ::   ii0, ii1, ij0, ij1, ik      ! local indices
REAL(wp) ::   r_bump , h_bump , h_oce     ! bump characteristics
REAL(wp) ::   zi, zj, zh, zhmin           ! local scalars
REAL(wp) ::   rn_rc_depth
INTEGER  :: ridgori,i45  ! ridge level
INTEGER  :: ridgelabel  ! ridge level
REAL(wp) :: ridgedepth  ! ridge depth
REAL(wp) :: ridge_w,res ! ridge width and resolution
REAL(wp) :: rn_rcbasin  ! radius of the basin
REAL(wp) :: rn_deep_b   ! radius of the deep basin
INTEGER , ALLOCATABLE, DIMENSION(:,:) :: idta  ! depth level
REAL(wp), ALLOCATABLE, DIMENSION(:,:) :: zdta  ! depth meter
REAL(wp), ALLOCATABLE, DIMENSION(:,:) :: rn_disfc
!
IF( nn_timing == 1 )  CALL timing_start('zgr_bat')
!
```

```
IF(lwp) WRITE(numout,*)
IF(lwp) WRITE(numout,*) 'zgr_bat: defines level and meter bathy'
IF(lwp) WRITE(numout,*)
!
IF( ntopo /= 1 ) THEN
!
ALLOCATE( idta(jpidta,jpjdta), STAT=ierror )
IF( ierror > 0 )   CALL ctl_stop( 'STOP', &
    &'zgr_bat: unable to allocate idta array' )
ALLOCATE( zdta(jpidta,jpjdta), STAT=ierror )
IF( ierror > 0 )   CALL ctl_stop( 'STOP', &
    &'zgr_bat: unable to allocate zdta array' )
!EGPA add extra mesgrid
ALLOCATE( rn_disfc(jpidta,jpjdta), STAT=ierror )
IF( ierror > 0 )   CALL ctl_stop( 'STOP', &
    &'zgr_bat: unable to allocate rn_disfc array' )
        !
IF( ntopo == 0 ) THEN                          ! flat basin
 IF(lwp) WRITE(numout,*)
 IF(lwp) WRITE(numout,*) 'bathymetry field: flat basin'
 IF( rn_bathy > 0.01 ) THEN
  IF(lwp) WRITE(numout,*) 'Depth = rn_bathy read in namelist'
   zdta(:,:) = rn_bathy
    IF( ln_sco ) THEN
     idta(:,:) = jpkm1
    ELSE
     idta(:,:) = jpkm1
     DO jk = 1, jpkm1
      WHERE( gdept_1d(jk) < zdta(:,:) .AND. &
          & zdta(:,:) <= gdept_1d(jk+1) )   idta(:,:) = jk
     END DO
    ENDIF
   ELSE
```

```
    IF(lwp) WRITE(numout,*) 'Depth = depthw(jpkm1)'
     idta(:,:) = jpkm1
     zdta(:,:) = gdepw_1d(jpk)
     h_oce     = gdepw_1d(jpk)
    ENDIF
ELSEIF( ntopo==2 .OR. ntopo==3)THEN   !Flat bottom or Step-shelf
 rn_rcbasin = 20.0_wp
 h_oce=gdepw_1d(jpk)
 rn_deep_b=11.0_wp

 IF( rn_bathy > 0.01 ) THEN
  zdta(:,:) = rn_bathy
  IF( ln_sco ) THEN
   idta(:,:) = jpkm1
  ELSE
   idta(:,:) = jpkm1
   DO jk = 1,jpkm1
    WHERE( gdept_1d(jk) < zdta(:,:) .AND. zdta(:,:) &
     & <=gdept_1d(jk+1) )idta(:,:) = jk
   END DO
  ENDIF
 ELSE
  idta(:,:) = 0
  zdta(:,:) = 0._wp
  DO jj = 1, jpjdta
   DO ji = 1, jpidta
    zi = FLOAT( ji - (jpidta+1)/2 )*ppe1_deg*rad
    zj = FLOAT( jj - (jpjdta+1)/2 )*ppe2_deg*rad
    rn_disfc(ji,jj)=ACOS(COS(zj)*COS(zi))*1/rad

    IF( rn_disfc(ji,jj) < rn_rcbasin )THEN
     idta(ji,jj) = jpkm1
     zdta(ji,jj) = h_oce
```

```
 IF( ntopo == 3)THEN
  IF(rn_disfc(ji,jj) >= rn_deep_b) THEN
   zdta(ji,jj) = gdepw_1d(3)
   idta(ji,jj) = 2
  ENDIF
 ENDIF
ENDIF

IF(jj>=21 .AND. jj<=25)THEN
     IF(ji >=186  .AND. ji <= 256)THEN
      IF( rn_disfc(ji,jj) < rn_rcbasin .AND. &
        & rn_disfc(ji,jj) > (rn_rcbasin-0.1))THEN
       IF(ji/=221)THEN
        zdta(ji,jj-1) = gdepw_1d(3)
        idta(ji,jj-1) = 2
       ENDIF
      ENDIF
     ENDIF
    ENDIF

    IF(jj>=418 .AND. jj<=421)THEN
     IF( ji >=186  .AND. ji <= 256 )THEN
      IF( rn_disfc(ji,jj) < rn_rcbasin )THEN
       zdta(ji,jj+1) = gdepw_1d(3)
       idta(ji,jj+1) = 2
      ENDIF
     ENDIF
    ENDIF

    IF(ntopo==3 )THEN
     IF(jj>=21 .AND. jj<=25)THEN
  IF(ji >=186  .AND. ji <= 256)THEN
```

```
        IF( rn_disfc(ji,jj) < rn_rcbasin .AND. &
          & rn_disfc(ji,jj) > (rn_rcbasin-0.1))THEN
    IF(ji/=221)THEN
     zdta(ji,jj-1) = gdepw_1d(3)
         idta(ji,jj-1) = 2
        ENDIF
   ENDIF
  ENDIF
 ENDIF

    IF(jj>=418 .AND. jj<=421)THEN
  IF( ji >=186  .AND. ji <= 256 )THEN
   IF( rn_disfc(ji,jj) < rn_rcbasin )THEN
    zdta(ji,jj+1) = gdepw_1d(3)
    idta(ji,jj+1) = 2
   ENDIF
  ENDIF
 ENDIF

   ELSE
 IF(jj>=21 .AND. jj<=25)THEN
  IF(ji >=186  .AND. ji <= 256)THEN
   IF( rn_disfc(ji,jj) < rn_rcbasin .AND. &
    & rn_disfc(ji,jj) > (rn_rcbasin-0.1) )THEN
    IF(ji/=221)THEN
     idta(ji,jj-1) = jpkm1
              zdta(ji,jj-1) = h_oce
    ENDIF
      ENDIF
     ENDIF
    ENDIF

    IF(jj>=418 .AND. jj<=421)THEN
```

```
          IF( ji >=186  .AND. ji <= 256 )THEN
           IF( rn_disfc(ji,jj) < rn_rcbasin )THEN
                idta(ji,jj+1) = jpkm1
                zdta(ji,jj+1) = h_oce
           ENDIF
          ENDIF
     ENDIF

    ENDIF

        IF( jj == 21 .AND. ji == 221 )THEN
         idta(ji,jj) = jpkm1
         zdta(ji,jj) = h_oce
        ENDIF

        IF( jj == 20 .OR. jj == 422 )THEN
         idta(ji,jj) = 0
         zdta(ji,jj) = 0._wp
        ENDIF

        IF( ji == 21 .OR. ji == 421 )THEN
         idta(ji,jj) = 0
         zdta(ji,jj) = 0._wp
        ENDIF

   END DO
  END DO
 ENDIF


ELSEIF( ntopo==4 )THEN  !Step--shelf with ridge
 rn_rcbasin = 20.0_wp
 h_oce    = gdepw_1d(jpk)
```

```
rn_deep_b=11_wp
ridge_w=4
res=10

IF( rn_bathy > 0.01 ) THEN
 zdta(:,:) = rn_bathy
 IF( ln_sco ) THEN
  idta(:,:) = jpkm1
 ELSE
  idta(:,:) = jpkm1
  DO jk = 1, jpkm1
   WHERE( gdept_1d(jk) < zdta(:,:) .AND. &
    & zdta(:,:) <=gdept_1d(jk+1) )idta(:,:) = jk
  END DO
 ENDIF
ELSE
 idta(:,:) = 0
 zdta(:,:) = 1._wp
 ridgeori = 45
 ridgedepth=gdepw_1d(3)
 ridgelabel=2
 i45=int(ridge_w*res/(2*SIN(45*rad)))
 DO jj = 1, jpjdta
  DO ji = 1, jpidta

   zi = FLOAT( ji - (jpidta+1)/2 )*ppe1_deg
   zj = FLOAT( jj - (jpjdta+1)/2 )*ppe2_deg
   rn_disfc(ji,jj)=ACOS(COS(zj*rad)*COS(zi*rad))*1/rad

   IF( rn_disfc(ji,jj) < rn_rcbasin)THEN
    IF(zdta(ji,jj) /= ridgedepth) THEN
     zdta(ji,jj) = gdepw_1d(jpk)
         idta(ji,jj) = jpkm1
```

```
     IF(rn_disfc(ji,jj) > rn_deep_b) THEN
      zdta(ji,jj) = gdepw_1d(3)
      idta(ji,jj) = 2
     ENDIF
    ENDIF
   ELSE
    idta(ji,jj) = 0
    zdta(ji,jj) = 0
   ENDIF

   IF( rn_disfc(ji,jj) < 23 )THEN
    IF( ridgeori == 0 )THEN
     IF( zdta(ji,jj) == gdepw_1d(jpk) )THEN
      IF ( zi >=-2  .AND. zi <= 2 )THEN
       zdta(ji,jj) = ridgedepth
       idta(ji,jj) = ridgelabel
      ENDIF
     ENDIF
    ELSEIF( ridgeori == 45 )THEN
     IF( int(zj*10) == int(zi*10) )THEN
      DO zk=-i45,i45
       zzj=jj+zk
       IF( zdta(ji,zzj) /= gdepw_1d(3) .AND. &
        &   zdta(zzj,jj)/= 0 )THEN
        zdta(ji,zzj) = ridgedepth
        idta(ji,zzj) = ridgelabel
       ENDIF
      END DO
     ENDIF
    ENDIF
   ENDIF
  END DO
END DO
```

```
DO jj = 1, jpjdta
 DO ji = 1, jpidta

  IF( rn_disfc(ji,jj) < rn_rcbasin)THEN
   IF(rn_disfc(ji,jj) > rn_deep_b) THEN
    zdta(ji,jj) = gdepw_1d(3)
    idta(ji,jj) = 2
   ENDIF
  ENDIF
 END DO
END DO

DO jj = 1, jpjdta
 DO ji = 1, jpidta

  IF(jj>=21 .AND. jj<=25)THEN
   IF(ji >=186  .AND. ji <= 256)THEN
    IF( rn_disfc(ji,jj) < rn_rcbasin .AND. &
      & rn_disfc(ji,jj) > (rn_rcbasin-0.1) )THEN
     IF(ji/=221)THEN
      zdta(ji,jj-1) = gdepw_1d(3)
      idta(ji,jj-1) = 2
     ENDIF
    ENDIF
   ENDIF
  ENDIF

  IF( jj == 21 .AND. ji == 221 )THEN
   zdta(ji,jj) = gdepw_1d(3)
   idta(ji,jj) = 2
  ENDIF
```

```
    IF(jj==20 .OR. jj==422)THEN
     idta(ji,jj) = 0
     zdta(ji,jj) = 0
    ENDIF

    IF(ji==21  .OR. ji== 421)THEN
     idta(ji,jj) = 0
     zdta(ji,jj) = 0
    ENDIF
   END DO
  END DO

  DO jj = 1, jpjdta
   DO ji = 1, jpidta

    IF(jj>=418 .AND. jj<=421)THEN
     IF( ji >=186  .AND. ji <= 256 )THEN
      IF( rn_disfc(ji,jj) < rn_rcbasin )THEN
       IF(ji/=221)THEN
        zdta(ji,jj+1) = gdepw_1d(3)
        idta(ji,jj+1) = 2
       ENDIF
      ENDIF
     ENDIF
    ENDIF
   END DO
  END DO
 ENDIF
!EGPA
ELSE ! bump centered in the basin
 IF(lwp) WRITE(numout,*)
...
```

C.2 bdydyn.F90

```
 ! inserted at 105 line of the original bdydyn.F90
!EGPA
 dis_bound(:,:)=ACOS(COS(glamt(:,:)*rad)* &
        &        COS(gphit(:,:)*rad))*tmask(:,:,1)
  DO jk = 1 , jpkm1
   DO ij = 1, jpj
    DO ii = 1, jpi

     IF(dis\_bound(ii,ij) > 20*rad )THEN
      IF(gphit(ii,ij) < 0)THEN
       va(ii,ij,jk) =0
       IF(glamu(ii,ij)<2)THEN
        ua(ii,ij,jk) = 0
            ELSEIF(glamu(ii,ij)>2)THEN
        ua(ii-1,ij,jk) = 0
       ENDIF
      ELSE
            va(ii,ij-1,jk) = 0
            IF(glamu(ii,ij)<2)THEN
             ua(ii,ij,jk) = 0
            ELSEIF(glamu(ii,ij)>2)THEN
        ua(ii-1,ij,jk) = 0
       ENDIF
      ENDIF
     ENDIF

    IF(glamt(ii,ij)==0)THEN
     IF(gphit(ii,ij) == -20)THEN
     va(ii,ij,jk) =0
     ua(ii,ij,jk) =0
    ELSEIF(gphit(ii,ij) == 20)THEN
     va(ii,ij-1,jk) = 0
```

```
     ua(ii,ij,jk) = 0
    ENDIF
   ENDIF


  END DO
 END DO
END DO
!EGPA
to line 130
! "Before" velocities (required for Orlanski condition):

IF ( ll_orlanski ) THEN
 DO jk = 1 , jpkm1
  ub(:,:,jk) = (ub(:,:,jk) - ub_b(:,:)) * umask(:,:,jk)
  vb(:,:,jk) = (vb(:,:,jk) - vb_b(:,:)) * vmask(:,:,jk)
 END DO
END IF
...
```

C.3 bdydyn2d.F90

```
 ! inserted between 180 - 217 lines
! of the original bdydyn2d.F90
igrd = 2      ! Flather bc on u-velocity;
bdy_acc_u=0
DO jb = 1, idx%nblenrim(igrd)
 ii   = idx%nbi(jb,igrd)
 ij   = idx%nbj(jb,igrd)
 zforc = dta%u2d(jb)
  IF(kt<=5000)THEN !10000
   pua2d(ii,ij) = zforc * REAL(kt)/5000
  ELSE
```

```
   pua2d(ii,ij) = zforc
  ENDIF
END DO
!
igrd = 3       ! Flather bc on v-velocity
bdy_acc_v=0
DO jb = 1, idx%nblenrim(igrd)
 ii   = idx%nbi(jb,igrd)
 ij   = idx%nbj(jb,igrd)

 zforc = dta%v2d(jb)
 IF(kt<=5000)THEN
  pva2d(ii,ij) = zforc * REAL(kt)/5000
 ELSE
  pva2d(ii,ij) = zforc
 ENDIF
END DO
!to line 278
CALL lbc_bdy_lnk( pua2d,'U', -1., ib_bdy ) ! Boundary points
CALL lbc_bdy_lnk( pva2d,'V', -1., ib_bdy ) ! should be updated
...
```

C.4 Three gaps: non–uniform step shelf basin

```
       program openb
!CALCULATE OPEN BOUNARY CONDITIONS
!DECLARATION OF VARIABLES

use netcdf

INTEGER ::       jpk1,ji,jj
INTEGER,PARAMETER    ::     C=441,jpk=9
DOUBLE PRECISION,DIMENSION(C,C) ::  depth, rn_disfc
```

```
DOUBLE PRECISION,DIMENSION(C,C) ::  rn_deep_b_ts
DOUBLE PRECISION,DIMENSION(C,C) ::  tmask,zdta, idta
DOUBLE PRECISION,DIMENSION(C,C) ::  glamt,gphit
INTEGER :: ridgelabel,i45,zzj,zk,res
DOUBLE PRECISION    ::    rn_depth, ridgedepth, ridgeori
DOUBLE PRECISION    ::    rn_deep_b2,rn_deep_b
DOUBLE PRECISION    ::    depthw,i_gp,o_gp
DOUBLE PRECISION    ::    pi,zj,zi,rad
DOUBLE PRECISION    ::    k1,k2

CHARACTER(LEN=20),PARAMETER :: FILE_NAME="bathy_meter.nc"
CHARACTER(LEN=20),PARAMETER :: FILE_NAME2="bathy_level.nc"
CHARACTER(LEN=20),PARAMETER :: FILE_NAMEIN="mesh_mask.nc"

integer , parameter :: NDIMS=2

integer  :: varid1,varid2,varid17,varid18
integer  :: dimidnbit(NDIMS),ncid
integer  :: vaphit
integer  :: valamt
integer  :: vabat
integer  :: valev
integer  :: xt_dimid,yt_dimid


pi = 3.141592653589793
rad = pi/180   !conversion from degre into radian

call check( nf90_open(FILE_NAMEIN, NF90_NOWRITE, ncid) )
call check( nf90_inq_varid(ncid, "glamt", varid1) )
call check( nf90_inq_varid(ncid, "gphit", varid2) )
call check( nf90_inq_varid(ncid, "tmaskutil", varid17) )
call check( nf90_inq_varid(ncid, "gdepw_1d", varid18) )
```

```
call check( nf90_get_var(ncid, varid1, glamt) )
call check( nf90_get_var(ncid, varid2, gphit) )
call check( nf90_get_var(ncid, varid17, tmask) )
call check( nf90_get_var(ncid, varid18, gdepw_1d) )



call check( nf90_close(ncid) )

!!!!!!!!!!!!!!!!!!!!!!!!!!!!!!!!!!!!!!!!!!!!!!!!!!!
!!Define Bathymetry to locate open boundaries!!
!!!!!!!!!!!!!!!!!!!!!!!!!!!!!!!!!!!!!!!!!!!!!!!!!!!

rn_rcbasin = 20.0
rn_deep_b=11.0
rn_deep_b2=19.0
ridge_w=4
res=10
jpkm1=jpk-1
idta(:,:) = 0
zdta(:,:) = 1
ridgeori = 45
ridgedepth=gdepw_1d(4)
ridgelabel=3

i45=int(ridge_w*res/(2*SIN(45*rad)))
 DO jj = 1, C                                    !zdta :
  DO ji = 1, C
   zi = FLOAT( ji - (C+1)/2 )*0.1
   zj = FLOAT( jj - (C+1)/2 )*0.1
   rn_disfc(ji,jj)=ACOS(COS(zj*rad)*COS(zi*rad))*1/rad

   IF( rn_disfc(ji,jj) < rn_rcbasin)THEN
    IF(zdta(ji,jj) /=  ridgedepth) THEN
```

```
    zdta(ji,jj) = gdepw_1d(jpk)
    idta(ji,jj) = jpkm1
   ENDIF
  ELSE
   idta(ji,jj) = 0
   zdta(ji,jj) = 0
  ENDIF

  IF(jj>=21 .AND. jj<=36)THEN
   IF(ji >=146  .AND. ji <= 283)THEN
    IF( rn_disfc(ji,jj) < rn_rcbasin .AND. &
     &  rn_disfc(ji,jj)> (rn_rcbasin-0.1) )THEN
     IF(ji/=221)THEN
      zdta(ji,jj-1) = gdepw_1d(3)
      idta(ji,jj-1) = 2
     ENDIF
    ENDIF
   ENDIF
  ENDIF

  IF(jj>=104 .AND. jj<=141)THEN
   IF(ji>=37 .AND. ji<=58)THEN
    IF( rn_disfc(ji,jj) < rn_rcbasin .AND. &
     &  rn_disfc(ji,jj) > (rn_rcbasin-0.1) )THEN
     zdta(ji-1,jj) = gdepw_1d(3)
     idta(ji-1,jj) = 2
    ENDIF
   ENDIF
  ENDIF

 IF( rn_disfc(ji,jj) < 22.7 )THEN
  IF( ridgeori == 45 )THEN
   IF( int(zj*10) == int(zi*10) )THEN
```

```
     DO zk=-i45,i45
      zzj=jj+zk
      IF( zdta(ji,zzj) /= gdepw_1d(3) .AND. &
       &  zdta(zzj,jj) /= 0 )THEN
       zdta(ji,zzj) = ridgedepth
       idta(ji,zzj) = ridgelabel
      ENDIF
     END DO
    ENDIF

   ENDIF
  ENDIF
 END DO
END DO

DO jj = 1, C
 DO ji = 1, C

  IF( rn_disfc(ji,jj) < rn_rcbasin)THEN
   IF (glamt(ji,jj) >= -9 .AND. glamt(ji,jj) <= -3)THEN
   rn_deep_b_ts(ji,jj)=15-4*SIN(pi/2 *ABS(glamt(ji,jj))/3)
    IF(rn_disfc(ji,jj) > rn_deep_b_ts(ji,jj)) THEN
     IF(gphit(ji,jj) > 0)THEN
      zdta(ji,jj) = gdepw_1d(3)
          idta(ji,jj) = 2
     ELSE
      zdta(ji,jj) = gdepw_1d(3)
          idta(ji,jj) = 2
     ENDIF
   ENDIF

   ELSEIF(glamt(ji,jj) > -3)THEN
    IF(gphit(ji,jj) > 0)THEN
```

```
     IF(rn_disfc(ji,jj) > rn_deep_b) THEN
      zdta(ji,jj) = gdepw_1d(3)
      idta(ji,jj) = 2
     ENDIF
    ELSE
     IF(rn_disfc(ji,jj) > rn_deep_b) THEN
      zdta(ji,jj) = gdepw_1d(3)
          idta(ji,jj) = 2
     ENDIF
    ENDIF

   ELSEIF (glamt(ji,jj) < -9)THEN
    IF(gphit(ji,jj) > 0)THEN
     IF(rn_disfc(ji,jj) > rn_deep_b2) THEN
      zdta(ji,jj) = gdepw_1d(3)
      idta(ji,jj) = 2
     ENDIF
    ELSE
     IF(rn_disfc(ji,jj) > rn_deep_b2) THEN
      zdta(ji,jj) = gdepw_1d(3)
      idta(ji,jj) = 2
     ENDIF
    ENDIF
   ENDIF
  ENDIF

  IF( jj == 21 .AND. ji == 221 )THEN
   zdta(ji,jj) = gdepw_1d(3) !gdepw_1d(3)
   idta(ji,jj) = 2
  ENDIF
 END DO
END DO
```

```
DO jj = 1, C
 DO ji = 1, C

  IF(jj>=414 .AND. jj<=421)THEN
   IF( ji >=169  .AND. ji <= 221 )THEN
    IF( rn_disfc(ji,jj) < rn_rcbasin )THEN
     zdta(ji,jj+1) = gdepw_1d(3)
         idta(ji,jj+1) = 2
    ENDIF
   ENDIF
  ENDIF

  IF(jj==20 .OR. jj==422)THEN
   idta(ji,jj) = 0
   zdta(ji,jj) = 0
  ENDIF

  IF( ji ==21  .OR. ji == 421)THEN
   idta(ji,jj) = 0
   zdta(ji,jj) = 0
  ENDIF

  IF( ji ==105  .AND. jj == 56)THEN
   idta(ji,jj) = 0
   zdta(ji,jj) = 0
  ENDIF

  IF( ji ==104 .AND. jj == 57)THEN
   idta(ji,jj) = 0
   zdta(ji,jj) = 0
  ENDIF

  IF( ji ==331 .AND. jj == 221)THEN
```

```
   idta(ji,jj) = 2
   zdta(ji,jj) = gdepw_1d(3)
  ENDIF

  IF( ji ==221 .AND. jj == 331)THEN
   idta(ji,jj) = 2
   zdta(ji,jj) = gdepw_1d(3)
  ENDIF

  IF( ji ==221 .AND. jj == 111)THEN
   idta(ji,jj) = 2
   zdta(ji,jj) = gdepw_1d(3)
  ENDIF

  IF( ji ==31 .AND. jj == 221)THEN
   idta(ji,jj) = 2
   zdta(ji,jj) = gdepw_1d(3)
  ENDIF
 END DO
END DO

DO jj = 1, C
 DO ji = 1, C

  zdta(ji,jj) = zdta(ji,jj)*tmask(ji,jj)
  idta(ji,jj) = idta(ji,jj)*tmask(ji,jj)
 END DO
END DO

!!!!!!!!!!!!!!!!!!!!!!!!!!!!!!!!!!!!
!!!!!!!!NetCDF file creation!!!!!!!!
!!!!!!!!!!!!!!!!!!!!!!!!!!!!!!!!!!!!
```

```
! This is the name of the data file we will create
call check( nf90_create(FILE_NAME, NF90_CLOBBER,ncid) )
call check( nf90_def_dim(ncid, "x", C, xt_dimid) )
call check( nf90_def_dim(ncid, "y", C, yt_dimid) )

! The dimids array is used to
! pass the IDs of the dimensions of
! the variables. Note that in fortran
! arrays are stored in column-major format.
dimidnbit =  (/ xt_dimid, yt_dimid /)

! Define the variable.
! The type of the variable in this case is
! NF90_INT (4-byte integer).

call check(nf90_def_var(ncid,"nav_lon", &
       &    NF90_DOUBLE,dimidnbit,valamt))
call check(nf90_def_var(ncid,"nav_lat", &
       &    NF90_DOUBLE,dimidnbit,vaphit))
call check(nf90_def_var(ncid,"bathymetry", &
       &    NF90_DOUBLE,dimidnbit,vabat))


! End define mode. This tells netCDF
! we are done defining metadata.
call check( nf90_enddef(ncid) )

! Write the pretend data to the file.
! Although netCDF supports
! reading and writing subsets of data,
! in this case we write all the
```

```
! data in one operation.

call check(nf90_put_var(ncid,valamt,glamt(1:C,1:C)))
call check(nf90_put_var(ncid,vaphit,gphit(1:C,1:C)))
call check(nf90_put_var(ncid,vabat,zdta(1:C,1:C)))

! Close the file. This frees up any internal netCDF resources
! associated with the file, and flushes any buffers.
call check( nf90_close(ncid) )

call check( nf90_create(FILE_NAME2, NF90_CLOBBER,ncid) )
call check( nf90_def_dim(ncid, "x", C, xt_dimid) )
call check( nf90_def_dim(ncid, "y", C, yt_dimid) )

! The dimids array is used to
! pass the IDs of the dimensions of
! the variables. Note that in fortran
! arrays are stored in column-major format.
dimidnbit =  (/ xt_dimid, yt_dimid /)

! Define the variable.
! The type of the variable in this case is
! NF90_INT (4-byte integer).

call check(nf90_def_var(ncid,"nav_lon", &
           &   NF90_DOUBLE,dimidnbit,valamt))
call check(nf90_def_var(ncid,"nav_lat", &
           &   NF90_DOUBLE,dimidnbit,vaphit))
call check(nf90_def_var(ncid,"bathymetry", &
           &   NF90_DOUBLE,dimidnbit,vabat))
call check(nf90_def_var(ncid,"Bathy_level", &
       &   NF90_INt,dimidnbit,valev))
```

```
! End define mode. This tells netCDF
! we are done defining metadata.
call check( nf90_enddef(ncid) )

! Write the pretend data to the file.
! Although netCDF supports
! reading and writing subsets of data,
! in this case we write all the
! data in one operation.

call check(nf90_put_var(ncid,valamt,glamt(1:C,1:C)))
call check(nf90_put_var(ncid,vaphit,gphit(1:C,1:C)))
call check(nf90_put_var(ncid,valev,idta(1:C,1:C)))


! Close the file. This frees up any internal netCDF resources
! associated with the file, and flushes any buffers.
call check( nf90_close(ncid) )

STOP
contains
subroutine check(status)
integer, intent ( in) :: status
if(status /= nf90_noerr) then
print *, trim(nf90_strerror(status))
stop "Stopped"
end if
end subroutine check
END
```

C.5 limthd_2.F90

```
 ! inserted between 155 - 181 lines
! of the original limthd_2.F90
#if defined key_thermo  !new key to remove thermodynamics
DO jj = 1, jpj
 DO ji = 1, jpi
  ! snow is transformed into ice if
  ! the original ice cover disappears.
  zindg = tms(ji,jj) *  MAX( rzero , &
      &   SIGN( rone , -hicif(ji,jj) ) )
  hicif(ji,jj)  = hicif(ji,jj) + zindg *  &
      &   rhosn * hsnif(ji,jj) / rau0
  hsnif(ji,jj)  = ( rone - zindg ) * hsnif(ji,jj) + &
      &  zindg * hicif(ji,jj) * ( rau0 - rhoic ) / rhosn
  dmgwi(ji,jj)  = zindg * (1.0 - frld(ji,jj)) * &
      &  rhoic * hicif(ji,jj)   ! snow/ice mass

  ! the lead fraction, frld, must be little
  ! than or equal to amax (ice ridging).

  zthsnice = hsnif(ji,jj) + hicif(ji,jj)
  zindb = tms(ji,jj) * ( 1.0 - MAX( rzero , &
      &    SIGN( rone , - zthsnice ) ) )
  za = zindb * MIN( rone, ( 1.0 - frld(ji,jj) ) * uscomi )
  hsnif (ji,jj) = hsnif(ji,jj)  * za
  hicif (ji,jj) = hicif(ji,jj)  * za
  qstoif(ji,jj) = qstoif(ji,jj) * za
  frld  (ji,jj) = 1.0 - zindb *  &
      & ( 1.0 - frld(ji,jj) ) / MAX( za, epsi20 )

  ! the in situ ice thickness,
  ! hicif, must be equal to or greater than hiclim.
  zh=    MAX( rone , zindb * &
      &  hiclim  / MAX( hicif(ji,jj), epsi20 ) )
```

```
  hsnif (ji,jj) = hsnif(ji,jj)  * zh
  hicif (ji,jj) = hicif(ji,jj)  * zh
  qstoif(ji,jj) = qstoif(ji,jj) * zh
  frld  (ji,jj) = ( frld(ji,jj) + ( zh - 1.0 ) ) / zh
 END DO
END DO
#endif       !finish first key
...
```

```
 ! inserted key between 190 - 418
! and between 425 - 426
! of the original limthd_2.F90
#if defined key_thermo

!-------------------------------!
!   Thermodynamics of sea ice   !
!-------------------------------!

!..
!..

#endif   ! finish second key

! Recover frld values between 0 and 1
! in the Southern Hemisphere (tricky trick)
! Update daily thermodynamic ice production.
!-------------------------------------------------------
DO jj = 1, jpj
 DO ji = 1, jpi
  frld  (ji,jj) = MIN( frld(ji,jj), ABS( frld(ji,jj) - 2.0 ) )
  fr_i  (ji,jj) = 1.0 - frld(ji,jj)
#if key_thermo
  hicifp(ji,jj) = hicif(ji,jj) * fr_i(ji,jj) - hicifp(ji,jj)
#else
```

```
  hicifp(ji,jj) = 0.
#endif
 END DO
END DO
!to line 437
! Outputs
!-----------------------------------------------------
....
```

C.6 bdyice_lim.F90

```
 ! inserted between 120 - 130 lines
! of the original bdyice_lim.F90
      !
#if defined key_lim2

DO jb = 1, idx%nblenrim(jgrd)
 ji    = idx%nbi(jb,jgrd)
 jj    = idx%nbj(jb,jgrd)
 zwgt  = idx%nbw(jb,jgrd)
 zwgt1 = 1.e0 - idx%nbw(jb,jgrd)
!EGPA

 IF (gphit(ji,jj) > 0) THEN
  frld (ji,jj) = frld (ji,jj) * tmask(ji,jj,1) ! Leads fraction
  hicif(ji,jj) = hicif(ji,jj) * tmask(ji,jj,1) ! Ice depth
  hsnif(ji,jj) = hsnif(ji,jj) * tmask(ji,jj,1) ! Snow depth
 ELSE
  frld (ji,jj) = ( frld (ji,jj) * zwgt1 + &
         &         0 * zwgt ) * tmask(ji,jj,1)
  hicif(ji,jj) = ( hicif(ji,jj) * zwgt1 + &
         &         0.5 * zwgt ) * tmask(ji,jj,1)
  hsnif(ji,jj) = 0 * tmask(ji,jj,1) ! Snow depth
```

```
 !
 ENDIF
END DO
!EGPA
CALL lbc_bdy_lnk( frld,  'T', 1., ib_bdy ) ! lateral boundary
...
```

Appendix D

D.1 MATLAB script for Source-sink driven solutions

D.1.1 Flat bottom basin

```
clc
clear all
close all

%Ocean Basin Parameters

mu=1e-4;              %bottom friction coefficient
av=7.292115e-5;       %angular velocity of the earth
H=1000;               %depth
g=9.8;                %gravity
tau=0.1;              %wind stress magnitude
delta=10*pi/180;      %half of the gap aperture
deltaw=10*pi/180;     %half of the wind transition zone
R=6371e3;             %radius of the earth
phi1=pi;              %
phi1w=2*pi/4;         %
phi2w=6*pi/4;         %
rho=1025;
thetab=20*pi/180;     %bondary colatitude in radians
thetaf=thetab/1;      %fix colatitude  in radians
thetas=2*pi/9;  %Angle that controls the meridional structure of
```

```
    the curl
WO=tau/(R*rho);    %Wind stress Curl/density
PO=delta*R^2*WO*(sin(pi*thetab/thetas))/(2*av);  %Inflow/outflow
N=100;                %summation terms of the FS in (2.13)


%Defining geographical grid in terms colatitude and longitude

lon=0:pi/1880:2*pi;              %longitude in radians
lat=0:pi/1880:thetab;            %colatitude in radians
[PH,TH,R3] = meshgrid(lon,pi/2-lat,R);
[X1,Y1,z] = sph2cart(PH,TH,R3); %Conversion spherical to
                                 %cartessian coordiantes
L=length(lon);                   %number of longitude points
M=length(lat);                   %number of colatitude points

%Fourier series coefficients of the flow at the boundary

Aob=(PO/pi)*(phi1-pi);  %Ao at the boundary
for n=1:N;
 Anb(n)=0;
 Bnb(n)=2*PO/(pi*n^2*delta)*sin(n*delta)*(cos(n*phi1)-1);
end

%Fourier series coefficients of the wind curl

Aow=(WO/pi)*(phi2w-phi1w-pi);  %Ao at the boundary
for n=1:N;
 Anw(n)=2*WO/(pi*n^2*delta)*sin(n*deltaw)*(sin(n*phi2w)-sin(n*
     phi1w));
 Bnw(n)=2*WO/(pi*n^2*delta)*sin(n*deltaw)*(cos(n*phi1w)-cos(n*
     phi2w));
end
```

```
52
53 %Compute constant terms of vorticity equation (5.7)
54
55 B=cos(thetaf)*sin(thetaf);
56 A=sin(thetaf)^2;
57 C=(2*av*H*sin(thetaf)^2/mu);
58
59 %Compute lambda from (5.24)
60
61 for n=1:N
62  t(n)=n^2+i*n*C;
63  lambda1(n)=-B/(2*A)+(sqrt(B^2+4*A*t(n))/(2*A));
64  lambda2(n)=-B/(2*A)-(sqrt(B^2+4*A*t(n))/(2*A));
65 end
66
67 %Compute constant of particular integral
68
69 Q=H*R^2/mu;
70 rps=pi/thetas;
71
72 for n=1:N;
73  alpha1(n)=-(Anw(n)+i*Bnw(n))*Q*rps*B/((B^2*rps^2+(rps^2*A+t(n))
       ^2)*2);
74  beta1(n)=-(Anw(n)+i*Bnw(n))*Q*(rps^2*A+t(n))/((B^2*rps^2+(rps
       ^2*A+t(n))^2)*2);
75  alpha2(n)=(Anw(n)+i*Bnw(n))*Q*(2+rps)*B/((B^2*(2+rps)^2+((2+rps
       )^2*A+t(n))^2)*4);
76  beta2(n)=(Anw(n)+i*Bnw(n))*Q*((2+rps)^2*A+t(n))/((B^2*(2+rps)
       ^2+((2+rps)^2*A+t(n))^2)*4);
77  alpha3(n)=-(Anw(n)+i*Bnw(n))*Q*(2-rps)*B/((B^2*(2-rps)^2+((2-
       rps)^2*A+t(n))^2)*4);
78  beta3(n)=-(Anw(n)+i*Bnw(n))*Q*((2-rps)^2*A+t(n))/((B^2*(2-rps)
       ^2+((2-rps)^2*A+t(n))^2)*4);
```

```
79 end
80
81 %Compute the constants from matching conditions (5.36)
82
83 for n=1:N;
84  E12b(n)=alpha1(n)*cos(rps*thetab)+beta1(n)*sin(rps*thetab);
85  E34b(n)=alpha2(n)*cos((2+rps)*thetab)+beta2(n)*sin((2+rps)*
        thetab);
86  E56b(n)=alpha3(n)*cos((2-rps)*thetab)+beta3(n)*sin((2-rps)*
        thetab);
87
88  CONS=[1  1;exp(lambda1(n)*thetab) exp(lambda2(n)*thetab)];
89  VEC=[-(alpha1(n)+alpha2(n)+alpha3(n));(Anb(n)+i*Bnb(n))-(E12b(n
        )+E34b(n)+E56b(n))];
90
91  a(:,n)=linsolve(CONS,VEC);
92
93  Rn(1,n)=a(1,n);
94  Sn(1,n)=a(2,n);
95 end
96
97 %Compute the ZN from (5.31)
98
99 for m=1:M
100  for n=1:N
101   ZN(m,n)=Rn(1,n)*exp(lambda1(n)*lat(m))...
102    +Sn(1,n)*exp(lambda2(n)*lat(m))...
103    +alpha1(n)*cos(rps*lat(m))...
104    +beta1(n)*sin(rps*lat(m))...
105    +alpha2(n)*cos((2+rps)*lat(m))...
106    +beta2(n)*sin((2+rps)*lat(m))...
107    +alpha3(n)*cos((2-rps)*lat(m))...
108    +beta3(n)*sin((2-rps)*lat(m));
```

```
 end
end

%Retrive an and bn from ZN

An=real(ZN);    % Coeficient an is the real part of ZN
Bn=imag(ZN);    % Coeficcent bn is the imaginary part of ZN

%Fourier series expansion on the circular basin

Ao=0;
for m=1:M
 for k=1:L
 term2=Ao;
  for n=1:N
   term2=term2+(An(m,n)*cos(n*lon(k))+Bn(m,n)*sin(n*lon(k)));
  end
  Fcb(m,k)=term2;
 end
end
```

D.1.2 Step-shelf basin

```
clc
clear all
close all

%Ocean Basin Parameters

mu=1e-4;              %bottom friction coefficient
av=7.292115e-5;       %angular velocity of the earth
H1=500;               %depth of the step shelf
H2=1000;              %depth of the deep basin
```

```
s=H1/H2;              %depth ratio
g=9.8;                %gravity
tau=0.1;              %wind stress magnitude
rho=1025;             %water density
delta=10*pi/180;      %half of the gap aperture
deltaw=10*pi/180;     %half of the wind transition zone
R=6371e3;             %radius of the earth
phi1=pi;              %
phi1w=pi/2;           %
phi2w=3*pi/2;         %
thetab=20*pi/180;     %boundary colatitude in radians
thetaf=thetab/2;      %fix colatitude  in radians
thetash=10*pi/180;    %colatitude at the shef edge
thetas=40*pi/180;     %Angle that controls
%the meridional structure of the curl
WO=tau/(R*rho);       %Wind stress Curl/density
PO=delta*R^2*WO*(sin(pi*thetab/thetas))/(2*av);
N=150;                %summation terms of the FS in (2.13)


%Defining geographical grid in terms colatitude and longitude

lon=0:pi/1800:2*pi;           %longitude in radians
lat=0:pi/1800:thetab;         %colatitude in radians
[PH,TH,R3] = meshgrid(lon,pi/2-lat,R);
[X1,Y1,z] = sph2cart(PH,TH,R3);    %Conversion spherical to
%cartessian coordiantes
L=length(lon);                %number of longitude points
M=length(lat);                %number of colatitude points

%Fourier series coefficients of the flow at the boundary

Aob=(PO/pi)*(phi1-pi);  %Ao at the boundary
```

```
for n=1:N
 Anb(n)=0;
 Bnb(n)=2*PO/(pi*n^2*delta)*sin(n*delta)*(cos(n*phi1)-1);
end

%Fourier series coefficients of the wind curl

Aow=(WO/pi)*(phi2w-phi1w-pi);  %Ao at the boundary
for n=1:N
 Anw(n)=2*WO/(pi*n^2*deltaw)*sin(n*deltaw)*...
   (sin(n*phi2w)-sin(n*phi1w));
 Bnw(n)=2*WO/(pi*n^2*deltaw)*sin(n*deltaw)*...
   (cos(n*phi1w)-cos(n*phi2w));
end

%Compute constant terms of vorticity equation (5.7)

B=cos(thetaf)*sin(thetaf);
A=sin(thetaf)^2;
C1=(2*av*H1*sin(thetaf)^2/mu);
C2=(2*av*H2*sin(thetaf)^2/mu);

%Compute lambda and omega from (2.19)

for n=1:N
 t(n)=n^2+i*n*C1;
 t1(n)=n^2+1i*n*C2;
 lambda1(n)=-B/(2*A)+(sqrt(B^2+4*A*t(n))/(2*A));
 lambda2(n)=-B/(2*A)-(sqrt(B^2+4*A*t(n))/(2*A));
 omega1(n)=-B/(2*A)+(sqrt(B^2+4*A*t1(n))/(2*A));
 omega2(n)=-B/(2*A)-(sqrt(B^2+4*A*t1(n))/(2*A));
end

```

```
77 %Compute constants of particular integral on the step shelf
78
79 Qs=H1*R^2/mu;
80 rps=pi/thetas;
81
82 for n=1:N;
83  alpha1s(n)=-(Anw(n)+i*Bnw(n))*Qs*rps*B/...
84    ((B^2*rps^2+(rps^2*A+t(n))^2)*2);
85  beta1s(n)=-(Anw(n)+i*Bnw(n))*Qs*(rps^2*A+t(n))/...
86    ((B^2*rps^2+(rps^2*A+t(n))^2)*2);
87  alpha2s(n)=(Anw(n)+i*Bnw(n))*Qs*(2+rps)*B/...
88    ((B^2*(2+rps)^2+((2+rps)^2*A+t(n))^2)*4);
89  beta2s(n)=(Anw(n)+i*Bnw(n))*Qs*((2+rps)^2*A+t(n))/...
90    ((B^2*(2+rps)^2+((2+rps)^2*A+t(n))^2)*4);
91  alpha3s(n)=-(Anw(n)+i*Bnw(n))*Qs*(2-rps)*B/...
92    ((B^2*(2-rps)^2+((2-rps)^2*A+t(n))^2)*4);
93  beta3s(n)=-(Anw(n)+i*Bnw(n))*Qs*((2-rps)^2*A+t(n))/...
94    ((B^2*(2-rps)^2+((2-rps)^2*A+t(n))^2)*4);
95 end
96
97 %Compute constants of particular integral in the deep basin
98
99 Qb=H2*R^2/mu;
100
101 for n=1:N;
102  alpha1b(n)=-(Anw(n)+i*Bnw(n))*Qb*rps*B/...
103    ((B^2*rps^2+(rps^2*A+t1(n))^2)*2);
104  beta1b(n)=-(Anw(n)+i*Bnw(n))*Qb*(rps^2*A+t1(n))/...
105    ((B^2*rps^2+(rps^2*A+t1(n))^2)*2);
106  alpha2b(n)=(Anw(n)+i*Bnw(n))*Qb*(2+rps)*B/...
107    ((B^2*(2+rps)^2+((2+rps)^2*A+t1(n))^2)*4);
108  beta2b(n)=(Anw(n)+i*Bnw(n))*Qb*((2+rps)^2*A+t1(n))/...
109    ((B^2*(2+rps)^2+((2+rps)^2*A+t1(n))^2)*4);
```

```
110  alpha3b(n)=-(Anw(n)+i*Bnw(n))*Qb*(2-rps)*B/...
111    ((B^2*(2-rps)^2+((2-rps)^2*A+t1(n))^2)*4);
112  beta3b(n)=-(Anw(n)+i*Bnw(n))*Qb*((2-rps)^2*A+t1(n))/...
113    ((B^2*(2-rps)^2+((2-rps)^2*A+t1(n))^2)*4);
114 end
115
116 %Compute the constants from matching conditions (5.53)
117
118 for n=1:N;
119
120 %Particular integral for matching conditions (5.54b)
121
122  E12b(n)=alpha1s(n)*cos(rps*thetab)...
123   +beta1s(n)*sin(rps*thetab);
124  E34b(n)=alpha2s(n)*cos((2+rps)*thetab)...
125   +beta2s(n)*sin((2+rps)*thetab);
126  E56b(n)=alpha3s(n)*cos((2-rps)*thetab)...
127   +beta3s(n)*sin((2-rps)*thetab);
128
129 %Particular integral for  matching conditions (5.54c and d)
130
131  E12sb(n)=alpha1b(n)*cos(rps*thetash)...
132   +beta1b(n)*sin(rps*thetash);
133  E34sb(n)=alpha2b(n)*cos((2+rps)*thetash)...
134   +beta2b(n)*sin((2+rps)*thetash);
135  E56sb(n)=alpha3b(n)*cos((2-rps)*thetash)...
136   +beta3b(n)*sin((2-rps)*thetash);
137  E12ss(n)=alpha1s(n)*cos(rps*thetash)...
138   +beta1s(n)*sin(rps*thetash);
139  E34ss(n)=alpha2s(n)*cos((2+rps)*thetash)...
140   +beta2s(n)*sin((2+rps)*thetash);
141  E56ss(n)=alpha3s(n)*cos((2-rps)*thetash)...
142   +beta3s(n)*sin((2-rps)*thetash);
```

```
143
144 %Shelf edge first derivative on theta (5.54d)
145
146  E12sbd(n)=-rps*alpha1b(n)*sin(rps*thetash)...
147   +rps*beta1b(n)*cos(rps*thetash);
148  E34sbd(n)=-(2+rps)*alpha2b(n)*sin((2+rps)*thetash)...
149   +(2+rps)*beta2b(n)*cos((2+rps)*thetash);
150  E56sbd(n)=-(2-rps)*alpha3b(n)*sin((2-rps)*thetash)...
151   +(2-rps)*beta3b(n)*cos((2-rps)*thetash);
152
153  E12ssd(n)=-rps*alpha1s(n)*sin(rps*thetash)...
154   +rps*beta1s(n)*cos(rps*thetash);
155  E34ssd(n)=-(2+rps)*alpha2s(n)*sin((2+rps)*thetash)...
156   +(2+rps)*beta2s(n)*cos((2+rps)*thetash);
157  E56ssd(n)=-(2-rps)*alpha3s(n)*sin((2-rps)*thetash)...
158   +(2-rps)*beta3s(n)*cos((2-rps)*thetash);
159
160 end
161
162 %Constants for the matching conditions (5.54d)
163
164 Sw=sin((1-pi/thetas)*thetash)/(1-pi/thetas)- ...
165     sin((1+pi/thetas)*thetash)/(1+pi/thetas);
166 S1=H1*2*av*cos(thetash)/sin(thetash);
167 S2=H1*R^2*Sw/(2*sin(thetash));
168
169 for n=1:N;
170  CONS=[1  1  0  0;...
171    0  0  exp(lambda1(n)*thetab)  exp(lambda2(n)*thetab);...
172    exp(omega1(n)*thetash)  exp(omega2(n)*thetash)  ...
173    -exp(lambda1(n)*thetash)  -exp(lambda2(n)*thetash);...
174    (S1*i*s*n+mu*s^2*omega1(n))*exp(omega1(n)*thetash)  ...
175    (S1*i*s*n+mu*s^2*omega2(n))*exp(omega2(n)*thetash)  ...
```

```
176     -(S1*i*n+mu*lambda1(n))*exp(lambda1(n)*thetash)  ...
177     -(S1*i*n+mu*lambda2(n))*exp(lambda2(n)*thetash)];
178   VEC=[-(alpha1b(n)+alpha2b(n)+alpha3b(n));...
179     (Anb(n)+i*Bnb(n))-(E12b(n)+E34b(n)+E56b(n));...
180     E12ss(n)+E34ss(n)+E56ss(n) -...
181     (E12sb(n)+E34sb(n)+E56sb(n));...
182     S1*i*n*(E12ss(n)+E34ss(n)+E56ss(n))+...
183     mu*(E12ssd(n)+E34ssd(n)+E56ssd(n)) -...
184     S1*i*n*s*(E12sb(n)+E34sb(n)+E56sb(n)) -...
185     mu*s^2*(E12sbd(n)+E34sbd(n)+E56sbd(n)) -...
186     S2*(Anw(n)+i*Bnw(n))*(1-s)];
187
188   a(:,n)=linsolve(CONS,VEC);
189
190   fn(1,n)=a(1,n);
191   gn(1,n)=a(2,n);
192   Fn(1,n)=a(3,n);
193   Gn(1,n)=a(4,n);
194 end
195
196 %Compute the ZN from (5.31)
197
198 for m=1:M
199   for n=1:N
200
201   if (lat(m) < thetash);
202     ZN(m,n)=fn(1,n)*exp(omega1(n)*lat(m))...
203             +gn(1,n)*exp(omega2(n)*lat(m))...
204                     +alpha1b(n)*cos(rps*lat(m))...
205                     +beta1b(n)*sin(rps*lat(m))...
206                     +alpha2b(n)*cos((2+rps)*lat(m))...
207                     +beta2b(n)*sin((2+rps)*lat(m))...
208                     +alpha3b(n)*cos((2-rps)*lat(m))...
```

```
209                     +beta3b(n)*sin((2-rps)*lat(m));
210   else
211    ZN(m,n)=Fn(1,n)*exp(lambda1(n)*lat(m))...
212                     +Gn(1,n)*exp(lambda2(n)*lat(m))...
213                     +alpha1s(n)*cos(rps*lat(m))...
214                     +beta1s(n)*sin(rps*lat(m))...
215                     +alpha2s(n)*cos((2+rps)*lat(m))...
216                     +beta2s(n)*sin((2+rps)*lat(m))...
217                     +alpha3s(n)*cos((2-rps)*lat(m))...
218                     +beta3s(n)*sin((2-rps)*lat(m));
219    end
220  end
221 end
222
223 %Retrive an and bn from ZN
224
225 An=real(ZN);    % Coeficient an is the real part of ZN
226 Bn=imag(ZN);    % Coeficcent bn is the imaginary part of ZN
227
228 %Fourier series expansion on the circular basin
229
230 Ao=0
231 for m=1:M
232  for k=1:L
233  term2=Ao;
234    for n=1:N
235      term2=term2+(An(m,n)*cos(n*lon(k))+Bn(m,n)*sin(n*lon(k)));
236    end
237    Fcb(m,k)=term2;
238  end
239 end
```

Appendix E

E.1 bdydyn.F90

```
 !inserted at 105 line of the original bdydyn.F90
!EGPA
dis_bound(:,:)=ACOS(COS(glamt(:,:)*rad)* &
         &        COS(gphit(:,:)*rad))*tmask(:,:,1)
DO jk = 1 , jpkm1
 DO ij = 1, jpj
  DO ii = 1, jpi

   IF(dis\_bound(ii,ij) > 20*rad )THEN
    IF(gphit(ii,ij) > 0)THEN
          va(ii,ij-1,jk) = 0
          IF(glamu(ii,ij)<2)THEN
           ua(ii,ij,jk) = 0
          ELSEIF(glamu(ii,ij)>2)THEN
           ua(ii-1,ij,jk) = 0
          ENDIF
    ENDIF
   ENDIF

   IF(glamt(ii,ij)==0)THEN
    IF(gphit(ii,ij) == 20)THEN
          va(ii,ij-1,jk) = 0
          ua(ii,ij,jk) = 0
```

```
    ENDIF
   ENDIF
  END DO
 END DO
END DO
!EGPA
to line 130
! "Before" velocities (required for Orlanski condition):

IF ( ll_orlanski ) THEN
 DO jk = 1 , jpkm1
  ub(:,:,jk) = (ub(:,:,jk) - ub_b(:,:)) * umask(:,:,jk)
  vb(:,:,jk) = (vb(:,:,jk) - vb_b(:,:)) * vmask(:,:,jk)
 END DO
END IF
...
```

E.2 bdydyn2d.F90

```
 ! inserted between 180 - 217 lines
! of the original bdydyn2d.F90
igrd = 2      ! Flather bc on u-velocity;
bdy_acc_u=0
DO jb = 1, idx%nblenrim(igrd)
 ii   = idx%nbi(jb,igrd)
 ij   = idx%nbj(jb,igrd)
 flagu => idx%flagu(jb,igrd)
 iim1 = ii + MAX( 0, INT( flagu ) ) ! T pts i-indice
 iip1 = ii - MIN( 0, INT( flagu ) ) ! T pts i-indice
 zcorr = - flagu * SQRT( grav * phvr(ii, ij) ) * &
     &   ( pssh(ii, ijm1) - spgu(ii,ijp1) )
 ! jchanut tschanges: Set zflag to 0 below
 ! to revert to std Flather scheme
```

```
 ! Use characteristics method instead
 zforc = dta%u2d(jb)
 zflag = ABS(flagu)

 IF(kt<=5000)THEN
  IF(gphit(ii,ij) < 0 .AND. glamt(ii,ij)< -2.8)THEN
   delta_i= zforc* REAL(kt)/5000  * &
     &      (1._wp - z1_2*zflag) + z1_2 * zflag * pua2d(iim1,ij)
   pua2d(ii,ij)= delta_i+ (1._wp - z1_2*zflag) &
     &           * zcorr * umask(ii,ij,1)
  ELSE
   pua2d(ii,ij) = zforc * REAL(kt)/5000
  ENDIF
 ELSE
  IF(gphit(ii,ij)<0)THEN
   delta_i= zforc  * (1._wp - z1_2*zflag) + z1_2 &
        &   * zflag *pua2d(iim1,ij)
   pua2d(ii,ij)= delta_i + (1._wp - z1_2*zflag) &
        &         * zcorr * umask(ii,ij,1)
  ELSE
   pua2d(ii,ij) = zforc
  ENDIF
 ENDIF
END DO
!
igrd = 3       ! Flather bc on v-velocity
bdy_acc_v=0
DO jb = 1, idx%nblenrim(igrd)
 ii   = idx%nbi(jb,igrd)
 ij   = idx%nbj(jb,igrd)
 flagv => idx%flagv(jb,igrd)
 ijm1 = ij + MAX( 0, INT( flagv ) ) ! T pts j-indice
 ijp1 = ij - MIN( 0, INT( flagv ) ) ! T pts j-indice
```

```
 zcorr = - flagv * SQRT( grav * phvr(ii, ij) )&
  &       * ( pssh(ii, ijm1) - spgu(ii,ijp1) )
 ! jchanut tschanges: Set zflag to 0 below
 ! to revert to std Flather scheme
 ! Use characteristics method instead
 !EGPA
 zforc = dta%v2d(jb)
 zflag = ABS(flagv)

 IF(kt<=5000)THEN
  IF(gphit(ii,ij) < 0 .AND. glamt(ii,ij)< -2.8)THEN
   delta_i= zforc* REAL(kt)/5000  * (1._wp - &
    &        z1_2*zflag) + z1_2 * zflag * pva2d(ii,ijm1)
   pva2d(ii,ij)= delta_i+ (1._wp - z1_2*zflag) &
    &        * zcorr * vmask(ii,ij,1)
  ELSE
   pva2d(ii,ij) = zforc * REAL(kt)/5000
  ENDIF
 ELSE
  IF(gphit(ii,ij)<0)THEN
   delta_i= zforc  * (1._wp - z1_2*zflag) + &
     &      z1_2 * zflag *pva2d(ii,ijm1)
   pva2d(ii,ij)= delta_i + (1._wp - z1_2*zflag) &
     & * zcorr * vmask(ii,ij,1)
  ELSE
   pva2d(ii,ij) = zforc
  ENDIF
END DO
!to line 278
CALL lbc_bdy_lnk( pua2d,'U', -1., ib_bdy ) ! Boundary points
CALL lbc_bdy_lnk( pva2d,'V', -1., ib_bdy ) ! should be updated
...
```

E.3 sbcbulk_core.F90

```
 ! inserted at line 310 of sbcblk_core.F90
!EGPA
zqlw(:,:) = 0._wp
!EGPA
! ------------------------------- !
!     II    Turbulent FLUXES      !
! ------------------------------- !
...
```

```
 ! inserted at 570 line of sbcblk_core.F90
!EGPA
z_qlw(ji,jj,jl) = 0._wp
z_dqlw(ji,jj,jl) = 0._wp
!EGPA
!to line 593
! ----------------------------!
!     II    Turbulent FLUXES  !
! ----------------------------!
```

Appendix F

F.1 SSH anomalies prescribed across both straits

F.1.1 bdydyn.F90

```
! inserted at 105 line of the original bdydyn.F90
dis_bound(:,:)=ACOS(COS(glamt(:,:)*rad)* &
       &        COS(gphit(:,:)*rad))*tmask(:,:,1)
 DO jk = 1 , jpkm1
  DO ij = 1, jpj
   DO ii = 1, jpi

    IF(dis\_bound(ii,ij) > 20*rad )THEN
     IF(gphit(ii,ij) < 0)THEN
      va(ii,ij,jk) =0
      IF(glamu(ii,ij)<2)THEN
       ua(ii,ij,jk) = 0
          ELSEIF(glamu(ii,ij)>2)THEN
       ua(ii-1,ij,jk) = 0
      ENDIF
     ELSE
          va(ii,ij-1,jk) = 0
          IF(glamu(ii,ij)<2)THEN
           ua(ii,ij,jk) = 0
          ELSEIF(glamu(ii,ij)>2)THEN
       ua(ii-1,ij,jk) = 0
```

```
       ENDIF
      ENDIF
     ENDIF

    IF(glamt(ii,ij)==0)THEN
     IF(gphit(ii,ij) == -20)THEN
     va(ii,ij,jk) =0
     ua(ii,ij,jk) =0
    ELSEIF(gphit(ii,ij) == 20)THEN
     va(ii,ij-1,jk) = 0
     ua(ii,ij,jk) = 0
    ENDIF
   ENDIF

  END DO
 END DO
END DO
!EGPA
!to line 130
! "Before" velocities (required for Orlanski condition):

IF ( ll_orlanski ) THEN
 DO jk = 1 , jpkm1
  ub(:,:,jk) = (ub(:,:,jk) - ub_b(:,:)) * umask(:,:,jk)
  vb(:,:,jk) = (vb(:,:,jk) - vb_b(:,:)) * vmask(:,:,jk)
 END DO
END IF
...
```

F.1.2 bdydyn2d.F90

```
 ! inserted at in between 180 - 217
! of the original bdydyn2d.F90
```

```
igrd = 2       ! Flather bc on u-velocity;
bdy_acc_u=0
DO jb = 1, idx%nblenrim(igrd)
 ii   = idx%nbi(jb,igrd)
 ij   = idx%nbj(jb,igrd)
 zforc = dta%u2d(jb)

  IF(kt<=5000)THEN
   pua2d(ii,ij) = zforc * REAL(kt)/5000
  ELSE
   pua2d(ii,ij) = zforc
  ENDIF
END DO
!
igrd = 3       ! Flather bc on v-velocity
bdy_acc_v=0
DO jb = 1, idx%nblenrim(igrd)
 ii   = idx%nbi(jb,igrd)
 ij   = idx%nbj(jb,igrd)
 zforc = dta%v2d(jb)

 IF(kt<=5000)THEN
  pva2d(ii,ij) = zforc * REAL(kt)/5000
 ELSE
  pva2d(ii,ij) = zforc
 ENDIF
END DO
!to line 278
CALL lbc_bdy_lnk( pua2d,'U', -1., ib_bdy ) ! Boundary points
CALL lbc_bdy_lnk( pva2d,'V', -1., ib_bdy ) ! should be updated
...
```

F.2 Experiments with open boundary condition imposed at the outflow

F.2.1 bdydyn.F90

```
 ! inserted at 105 line of the original bdydyn.F90
!EGPA
dis_bound(:,:)=ACOS(COS(glamt(:,:)*rad)* &
        &       COS(gphit(:,:)*rad))*tmask(:,:,1)
DO jk = 1 , jpkm1
 DO ij = 1, jpj
  DO ii = 1, jpi

   IF(dis\_bound(ii,ij) > 20*rad )THEN
    IF(gphit(ii,ij) < 0)THEN
     va(ii,ij,jk) =0
         IF(glamu(ii,ij)<2)THEN
      ua(ii,ij,jk) = 0
         ELSEIF(glamu(ii,ij)>2)THEN
          ua(ii-1,ij,jk) = 0
         ENDIF
    ENDIF
   ENDIF

   IF(glamt(ii,ij)==0)THEN
    IF(gphit(ii,ij) == -20)THEN
     va(ii,ij,jk) =0
         ua(ii,ij,jk) =0
        ENDIF
   ENDIF

  END DO
 END DO
END DO
```

```
!EGPA
to line 130
! "Before" velocities (required for Orlanski condition):

IF ( ll_orlanski ) THEN
 DO jk = 1 , jpkm1
  ub(:,:,jk) = (ub(:,:,jk) - ub_b(:,:)) * umask(:,:,jk)
  vb(:,:,jk) = (vb(:,:,jk) - vb_b(:,:)) * vmask(:,:,jk)
 END DO
END IF
...
```

F.2.2 bdydyn2d.F90

```
 !inserted between 180 - 217 lines
! of the original bdydyn2d.F90
!
igrd = 2       ! Flather bc on u-velocity;
!              ! remember that flagu=-1 if
!              ! normal velocity direction is outward
!              ! I think we should rather use after ssh ?
bdy_acc_u=0
DO jb = 1, idx%nblenrim(igrd)
 ii   = idx%nbi(jb,igrd)
 ij   = idx%nbj(jb,igrd)
 flagu => idx%flagu(jb,igrd)
 iim1 = ii + MAX( 0, INT( flagu ) )
 iip1 = ii - MIN( 0, INT( flagu ) )
 zcorr = - flagu * SQRT( grav * phur(ii, ij) ) &
    &     * ( pssh(iim1, ij) - spgu(iip1,ij) )
 ! jchanut tschanges: Set zflag to 0 below
 ! to revert to Flather scheme
 ! Use characteristics method instead
```

```
 zflag = ABS(flagu)
 zforc = dta%u2d(jb)
 ep=zforc/10

 IF(kt<=5000)THEN
  IF(gphit(ii,ij)>0 )THEN
   delta_i= zforc* REAL(kt)/5000  * (1._wp - &
       &    z1_2*zflag) + z1_2 * zflag *pua2d(ii,ijm1)
   pua2d(ii,ij)= delta_i + (1._wp - z1_2*zflag)  &
       &    * zcorr * umask(ii,ij,1)
  ELSE
   pua2d(ii,ij) = zforc * REAL(kt)/5000
  ENDIF
 ELSEIF(kt>78840)THEN
  IF(gphit(ii,ij) > 0)THEN
   delta_i= zforc  * (1._wp - z1_2*zflag) + &
     &      z1_2 * zflag *pua2d(ii,ijm1)
   pua2d(ii,ij)= delta_i + (1._wp - z1_2*zflag) &
     &      * zcorr * umask(ii,ij,1)
  ELSE
   pua2d(ii,ij) = zforc + &
     &  ep * SIN(2*rpi*(78840-REAL(kt))/26280 )
  ENDIF
 ELSE
  IF(gphit(ii,ij)>0 )THEN
   pua2d(ii,ij)= delta_i + (1._wp - z1_2*zflag) &
     &  * zcorr * umask(ii,ij,1)
  ELSE
   pua2d(ii,ij) = zforc
  ENDIF
 ENDIF
END DO
!
```

```
igrd = 3       ! Flather bc on v-velocity
!              ! remember that flagv=-1 if
               ! normal velocity direction is outward
bdy_acc_v=0
DO jb = 1, idx%nblenrim(igrd)
 ii   = idx%nbi(jb,igrd)
 ij   = idx%nbj(jb,igrd)
 flagv => idx%flagv(jb,igrd)
 ijm1 = ij + MAX( 0, INT( flagv ) )
 ijp1 = ij - MIN( 0, INT( flagv ) )
 zcorr = - flagv * SQRT( grav * phvr(ii, ij) ) &
    &     * ( pssh(ii, ijm1) - spgu(ii,ijp1) )
 ! jchanut tschanges: Set zflag to 0
 ! below to revert to std Flather scheme
 ! Use characteristics method instead
 zforc =  dta%v2d(jb)
 ep=zforc/10
 zflag = ABS(flagv)

 IF(kt<=5000)THEN
  IF(gphit(ii,ij)>0 )THEN
   delta_i= zforc* REAL(kt)/5000  * (1._wp - &
        &     z1_2*zflag) + z1_2 * zflag * pva2d(ii,ijm1)
   pva2d(ii,ij)= delta_i + (1._wp - z1_2*zflag) &
        &     * zcorr * vmask(ii,ij,1)
  ELSE
   pva2d(ii,ij) = zforc * REAL(kt)/5000
  ENDIF
 ELSEIF(kt>78840)THEN
  IF(gphit(ii,ij)>0)THEN
   pva2d(ii,ij) =  delta_i + (1._wp - &
        &     z1_2*zflag) * zcorr * vmask(ii,ij,1)
  ELSE
```

```
   pva2d(ii,ij) = zforc + &
        &     ep * SIN(2*rpi*(78840-REAL(kt))/26280)
  ENDIF
 ELSE
  IF(gphit(ii,ij)>0 ) THEN
   pva2d(ii,ij)= delta_i + (1._wp - z1_2*zflag) &
        &        * zcorr * vmask(ii,ij,1)
  ELSE
   pva2d(ii,ij) = zforc
  ENDIF
 ENDIF
END DO
CALL lbc_bdy_lnk( pua2d, 'U', -1., ib_bdy ) ! Boundary points
CALL lbc_bdy_lnk( pva2d, 'V', -1., ib_bdy ) ! should be updated
...
```

References

Aagaard, K. and E. C. Carmack (1989). "The role of sea ice and other fresh water in the Arctic circulation". In: *Journal of Geophysical Research: Oceans* 94 (C10), pp. 14485–14498. ISSN: 2156-2202. DOI: 10.1029/JC094iC10p14485.

Abramowitz, M. and I. A. Stegun, eds. (1965). *Handbook of Mathematical Functions*. New edition edition. New York: Dover Publications Inc. 1046 pp. ISBN: 978-0-486-61272-0.

Aksenov, Y., S. Bacon, A. C. Coward, and A. J. G. Nurser (2010). "The North Atlantic inflow to the Arctic Ocean: High-resolution model study". In: *Journal of Marine Systems* 79.1, pp. 1–22. ISSN: 0924-7963. DOI: 10.1016/j.jmarsys.2009.05.003.

Aksenov, Y., V. V. Ivanov, A. J. G. Nurser, S. Bacon, I. V. Polyakov, A. C. Coward, A. C. NaveiraGarabato, and A. BeszczynskaMoeller (2011). "The Arctic Circumpolar Boundary Current". In: *Journal of Geophysical Research: Oceans* 116 (C9). ISSN: 2156-2202. DOI: 10.1029/2010JC006637.

Aksenov, Y. *et al.* (2016). "Arctic pathways of Pacific Water: Arctic Ocean model intercomparison experiments". In: *Journal of Geophysical Research: Oceans* 121.1, pp. 27–59. ISSN: 21699275. DOI: 10.1002/2015JC011299.

Allen, J. S. (1975). "Coastal Trapped Waves in a Stratified Ocean". In: *Journal of Physical Oceanography* 5.2, pp. 300–325. ISSN: 0022-3670. DOI: 10.1175/1520-0485(1975)005<0300:CTWIAS>2.0.CO;2.

Ambaum, M. H. P., B. J. Hoskins, and D. B. Stephenson (2001). "Arctic Oscillation or North Atlantic Oscillation?" In: *Journal of Climate* 14.16, pp. 3495–3507. ISSN: 0894-8755. DOI: 10.1175/1520-0442(2001)014<3495:AOONAO>2.0.CO;2.

Armitage, T. W. K., S. Bacon, A. L. Ridout, S. F. Thomas, Y. Aksenov, and D. J. Wingham (2016). "Arctic sea surface height variability and change from satellite radar altimetry and GRACE, 2003-2014". In: *Journal of Geophysical Research: Oceans* 121, pp. 4303–4322. ISSN: 21699275. DOI: 10.1002/2015JC011579.

Arrigo, K. R. and G. L. van Dijken (2015). "Continued increases in Arctic Ocean primary production". In: *Progress in Oceanography*. Synthesis of Arctic Research (SOAR) 136, pp. 60–70. ISSN: 0079-6611. DOI: 10.1016/j.pocean.2015.05.002.

Beszczynska-Möller, A., E. Fahrbach, U. Schauer, and E. Hansen (2012). "Variability in Atlantic water temperature and transport at the entrance to the Arctic Ocean, 19972010". In: *ICES Journal of Marine Science* 69.5, pp. 852–863. ISSN: 1054-3139. DOI: 10.1093/icesjms/fss056.

Björk, G., M. Jakobsson, K. Assmann, L. G. Andersson, J. Nilsson, C. Stranne, and L. Mayer (2018). "Bathymetry and oceanic flow structure at two deep passages crossing the Lomonosov Ridge". In: *Ocean Science; Katlenburg-Lindau* 14.1, pp. 1–13. DOI: 10.5194/os-14-1-2018.

Bridger, A. F. C. and D. E. Stevens (1980). "Long Atmospheric Waves and the Polar-Plane Approximation to the Earths Spherical Geometry". In: *Journal of the Atmospheric Sciences* 37.3, pp. 534–544. ISSN: 0022-4928. DOI: 10.1175/1520-0469(1980)037<0534:LAWATP>2.0.CO;2.

Comiso, J. C. (2011). "Large Decadal Decline of the Arctic Multiyear Ice Cover". In: *Journal of Climate* 25.4, pp. 1176–1193. ISSN: 0894-8755. DOI: 10.1175/JCLI-D-11-00113.1.

Cushman-Roisin, B. and J.-M. Beckers (2011). *Introduction to Geophysical Fluid Dynamics*. 2nd. Vol. 101. Academic Press. 875 pp.

Danielson, S. L., T. J. Weingartner, K. S. Hedstrom, K. Aagaard, R. Woodgate, E. Curchitser, and P. J. Stabeno (2014). "Coupled wind-forced controls of the BeringChukchi shelf circulation and the Bering Strait throughflow: Ekman transport, continental shelf waves, and variations of the PacificArctic sea surface height gradient". In: *Progress in Oceanography* 125, pp. 40–61. ISSN: 0079-6611. DOI: 10.1016/j.pocean.2014.04.006.

Davis, P. E. D., C. Lique, and H. L. Johnson (2014). "On the Link between Arctic Sea Ice Decline and the Freshwater Content of the Beaufort Gyre: Insights from a Simple Process Model". In: *Journal of Climate* 27.21, pp. 8170–8184. ISSN: 0894-8755. DOI: 10.1175/JCLI-D-14-00090.1.

de Boer, A. M., E. Gavilan PascualAhuir, D. P. Stevens, L. Chafik, D. K. Hutchinson, Q. Zhang, L. C. Sime, and A. J. Willmott (2018). "Interconnectivity between volume transports through Arctic straits". In: *Journal of Geophysical Research: Oceans* 123 (ja). ISSN: 2169-9291. DOI: 10.1029/2018JC014320.

Delworth, T. L., F. Zeng, L. Zhang, R. Zhang, G. A. Vecchi, and X. Yang (2017). "The Central Role of Ocean Dynamics in Connecting the North Atlantic Oscillation to the Extratropical Component of the Atlantic Multidecadal Oscillation". In: *Journal of Climate* 30.10, pp. 3789–3805. ISSN: 0894-8755. DOI: 10.1175/JCLI-D-16-0358.1.

Deser, C. (2000). "On the teleconnectivity of the Arctic Oscillation". In: *Geophysical Research Letters* 27.6, pp. 779–782. ISSN: 1944-8007. DOI: 10.1029/1999GL010945.

Dickson, R. R., T. J. Osborn, J. W. Hurrell, J. Meincke, J. Blindheim, B. Adlandsvik, T. Vinje, G. Alekseev, and W. Maslowski (2000). "The Arctic Ocean Response to the North Atlantic Oscillation". In: *Journal of Climate* 13.15, pp. 2671–2696. ISSN: 0894-8755. DOI: 10.1175/1520-0442(2000)013<2671:TAORTT>2.0.CO;2.

Dukhovskoy, D., M. Johnson, and A. Proshutinsky (2006). "Arctic decadal variability from an idealized atmosphere-ice-ocean model: 2. Simulation of decadal oscillations". In: *Journal of Geophysical Research: Oceans* 111 (C6). ISSN: 2156-2202. DOI: 10.1029/2004JC002820.

Flather, R. A. (1994). "A Storm Surge Prediction Model for the Northern Bay of Bengal with Application to the Cyclone Disaster in April 1991". In: *Journal of Physical Oceanography* 24.1, pp. 172–190. ISSN: 0022-3670. DOI: 10.1175/1520-0485(1994)024<0172:ASSPMF>2.0.CO;2.

Gerdes, R. and C. Küberle (1999). "Numerical simulation of salinity anomaly propagation in the Nordic seas and the Arctic Ocean". In: *Polar Research* 18.2, pp. 159–166. ISSN: null. DOI: 10.3402/polar.v18i2.6569.

Gill, A. E. (1982). *Atmosphere-Ocean Dynamics - 1st Edition*. 1st. Academic Press. 682 pp.

Gordienko, P. (1958). "Arctic ice drift". In: *Proc. of the Arctic Sea Ice Conference*. Arctic Sea Ice Conference. Easton, US: National Academy of Sciences-National Research Council, pp. 210–220.

Gray, L., D. Burgess, L. Copland, M. N. Demuth, T. Dunse, K. Langley, and T. V. Schuler (2015). "CryoSat-2 delivers monthly and inter-annual surface elevation change for Arctic ice caps". In: *The Cryosphere* 9.5, pp. 1895–1913. ISSN: 1994-0424. DOI: 10.5194/tc-9-1895-2015.

Gray, N. and L. Morland (1994). "A two-dimensional model for the dynamics of sea ice". In: *Phil. Trans. R. Soc. Lond. A* 347.1682, pp. 219–290. ISSN: 0962-8428, 2054-0299. DOI: 10.1098/rsta.1994.0045.

Harlander, U. (2005). "A high-latitude quasi-geostrophic delta plane model derived from spherical geometry". In: *Tellus A* 57.1, pp. 43–54. ISSN: 0280-6495, 1600-0870. DOI: 10.1111/j.1600-0870.2005.00083.x.

Hart, J. E. (1975). "The Flow of a Two-Layer Fluid over Topography in a Polar Ocean". In: *Journal of Physical Oceanography* 5.4, pp. 615–624. ISSN: 0022-3670. DOI: 10.1175/1520-0485(1975)005<0615:TFOATL>2.0.CO;2.

Haurwitz, B. (1975). "Long circumpolar atmospheric waves". In: *Archiv für Meteorologie, Geophysik und Bioklimatologie, Serie A* 24.1, pp. 1–18. ISSN: 0066-6416, 1436-5065. DOI: 10.1007/BF02247554.

IHO (2002). *Limits of Oceans and Seas, rep S-23*. Draft 4th Edition, 2002. International Hydrographic Organization.

Imawaki, S. and K. Takano (1974). "Planetary flow in a circular basin". In: *Deep Sea Research and Oceanographic Abstracts* 21.1, 69–IN3. ISSN: 0011-7471. DOI: 10.1016/0011-7471(74)90020-5.

Itkin, P., M. Karcher, and R. Gerdes (2014). "Is weaker Arctic sea ice changing the Atlantic water circulation?" In: *Journal of Geophysical Research: Oceans* 119.9, pp. 5992–6009. ISSN: 2169-9291. DOI: 10.1002/2013JC009633.

Jakobsson, M. (2002). "Hypsometry and volume of the Arctic Ocean and its constituent seas". In: *Geochemistry, Geophysics, Geosystems* 3.5, pp. 1–18. ISSN: 1525-2027. DOI: 10.1029/2001GC000302.

Jakobsson, M. *et al.* (2012). "The International Bathymetric Chart of the Arctic Ocean (IBCAO) Version 3.0". In: *Geophysical Research Letters* 39.12, p. L12609. ISSN: 1944-8007. DOI: 10.1029/2012GL052219.

Jiang, L. and R. W. Garwood (1998). "Effects of topographic steering and ambient stratification on overflows on continental slopes: A model study". In: *Journal of Geophysical Research: Oceans* 103 (C3), pp. 5459–5476. ISSN: 2156-2202. DOI: 10.1029/97JC03201.

Jin, M., C. Deal, S. H. Lee, S. Elliott, E. Hunke, M. Maltrud, and N. Jeffery (2012). "Investigation of Arctic sea ice and ocean primary production for the period 19922007 using a 3-D global iceocean ecosystem model". In: *Deep Sea Research Part II: Topical Studies in Oceanography*. Biogeochemical studies from the Chinese National Arctic Research Expeditions (CHINAREs) 8184, pp. 28–35. ISSN: 0967-0645. DOI: 10.1016/j.dsr2.2011.06.003.

Karcher, M., F. Kauker, R. Gerdes, E. Hunke, and J. Zhang (2007). "On the dynamics of Atlantic Water circulation in the Arctic Ocean". In: *Journal of Geophysical Research: Oceans* 112 (C4), C04S02. ISSN: 2156-2202. DOI: 10.1029/2006JC003630.

Kim, H.-M., P. J. Webster, and J. A. Curry (2012). "Seasonal prediction skill of ECMWF System 4 and NCEP CFSv2 retrospective forecast for the Northern Hemisphere Winter". In: *Climate Dynamics* 39.12, pp. 2957–2973. ISSN: 0930-7575, 1432-0894. DOI: 10.1007/s00382-012-1364-6.

Kitauchi, H. and M. Ikeda (2009). "An analytic solution of steady Stokes flow on a rotating polar cap". In: *Fluid Dynamics Research* 41.4, p. 045505. ISSN: 1873-7005. DOI: 10.1088/0169-5983/41/4/045505.

Kjeldsen, K. K. *et al.* (2015). "Spatial and temporal distribution of mass loss from the Greenland Ice Sheet since AD 1900". In: *Nature* 528.7582, pp. 396–400. ISSN: 1476-4687. DOI: 10.1038/nature16183.

Koldunov, N. V. *et al.* (2014). "Multimodel simulations of Arctic Ocean sea surface height variability in the period 19702009". In: *Journal of Geophysical Research: Oceans* 119.12, pp. 8936–8954. ISSN: 2169-9291. DOI: 10.1002/2014JC010170.

LeBlond, P. H. (1964). "Planetary waves in a symmetrical polar basin". In: *Tellus* 16.4, pp. 503–512. ISSN: 2153-3490. DOI: 10.1111/j.2153-3490.1964.tb00185.x.

Longuet-Higgins, M. S. (1968). "The Eigenfunctions of Laplace's Tidal Equations over a Sphere". In: *Philosophical Transactions of the Royal Society of London A: Mathematical, Physical and Engineering Sciences* 262.1132, pp. 511–607. ISSN: 1364-503X, 1471-2962. DOI: 10.1098/rsta.1968.0003.

Luneva, M. V., A. J. Willmott, and M. A. M. Maqueda (2012). "Geostrophic Adjustment Problems in a Polar Basin". In: *Atmosphere-Ocean* 50.2, pp. 134–155. ISSN: 0705-5900. DOI: 10.1080/07055900.2012.659719.

Madec, G. (2008). "NEMO ocean engine". In: *Note du Pole de modelisation de lInstitut Pierre-Simon Laplace (IPSL)* 27. ISSN: 1288-1619.

Manucharyan, G. E. and M. A. Spall (2016). "Wind-driven freshwater buildup and release in the Beaufort Gyre constrained by mesoscale eddies". In: *Geophysical Research Letters* 43.1, 2015GL065957. ISSN: 1944-8007. DOI: 10.1002/2015GL065957.

Maqueda, M. A. M. and A. J. Willmott (2000). "A Two-Dimensional Time-Dependent Model of a Wind-Driven Coastal Polynya: Application to the St. Lawrence Island Polynya". In: *Journal of Physical Oceanography* 30.6, pp. 1281–1304. ISSN: 0022-3670. DOI: 10.1175/1520-0485(2000)030<1281:ATDTDM>2.0.CO;2.

Martin, T., M. Steele, and J. Zhang (2014). "Seasonality and long-term trend of Arctic Ocean surface stress in a model". In: *Journal of Geophysical Research: Oceans* 119.3, pp. 1723–1738. ISSN: 2169-9291. DOI: 10.1002/2013JC009425.

Meier, W. N. *et al.* (2014). "Arctic sea ice in transformation: A review of recent observed changes and impacts on biology and human activity". In: *Reviews of Geophysics* 52.3, 2013RG000431. ISSN: 1944-9208. DOI: 10.1002/2013RG000431.

Morland, L. and R. Staroszczyk (1998). "A material coordinate treatment of the seaice dynamics equations". In: *Proceedings of the Royal Society of London A: Mathematical, Physical and Engineering Sciences* 454.1979, pp. 2819–2857. ISSN: 1364-5021, 1471-2946. DOI: 10.1098/rspa.1998.0283.

Nansen, F. (1902). *The norwegian north polar expedition 1893-1896: scientific results*. Vol. 3. Christiania J. Bybwad.

Newton, B., L. B. Tremblay, M. A. Cane, and P. Schlosser (2006). "A simple model of the Arctic Ocean response to annular atmospheric modes". In: *Journal of Geophysical Research: Oceans* 111 (C9), p. C09019. ISSN: 2156-2202. DOI: 10.1029/2004JC002622.

Paldor, N. (2015). *Shallow Water Waves on the Rotating Earth*. SpringerBriefs in Earth System Sciences. Springer International Publishing.

Paldor, N., Y. De-Leon, and O. Shamir (2013). "Planetary (Rossby) waves and inertiagravity (Poincaré) waves in a barotropic ocean over a sphere". In: *Journal of Fluid Mechanics* 726, pp. 123–136. ISSN: 0022-1120, 1469-7645. DOI: 10.1017/jfm.2013.219.

Pickard, G. L. and W. J. Emery (2002). *Descriptive Physical Oceanography: An Introduction*. 5th. Butterworth-Heinemann. 320 pp.

Pnyushkov, A. V., I. V. Polyakov, V. V. Ivanov, Y. Aksenov, A. C. Coward, M. Janout, and B. Rabe (2015). "Structure and variability of the boundary current in the Eurasian Basin of the Arctic Ocean". In: *Deep Sea Research Part I: Oceanographic Research Papers* 101, pp. 80–97. ISSN: 0967-0637. DOI: 10.1016/j.dsr.2015.03.001.

Pnyushkov, A. V., I. V. Polyakov, V. V. Ivanov, and T. Kikuchi (2013). "Structure of the Fram Strait branch of the boundary current in the Eurasian Basin of the Arctic Ocean". In: *Polar Science* 7.2, pp. 53–71. ISSN: 1873-9652. DOI: 10.1016/j.polar.2013.02.001.

Polyakov, I. V. *et al.* (2010). "Arctic Ocean Warming Contributes to Reduced Polar Ice Cap". In: *Journal of Physical Oceanography* 40.12, pp. 2743–2756. ISSN: 0022-3670. DOI: 10.1175/2010JPO4339.1.

Pond, S. and G. L. Pickard (1983). *Introductory Dynamical Oceanography*. 2nd. Elsevier. 349 pp.

Prange, M. and R. Gerdes (2006). "The role of surface freshwater flux boundary conditions in Arctic Ocean modelling". In: *Ocean Modelling* 13.1, pp. 25–43. ISSN: 1463-5003. DOI: 10.1016/j.ocemod.2005.09.003.

Proshutinsky, A., R. H. Bourke, and F. A. McLaughlin (2002). "The role of the Beaufort Gyre in Arctic climate variability: Seasonal to decadal climate scales". In: *Geophysical Research Letters* 29.23, p. 2100. ISSN: 1944-8007. DOI: 10.1029/2002GL015847.

Proshutinsky, A., D. Dukhovskoy, M.-L. Timmermans, R. Krishfield, and J. L. Bamber (2015). "Arctic circulation regimes". In: *Phil. Trans. R. Soc. A* 373.2052, p. 20140160. ISSN: 1364-503X, 1471-2962. DOI: 10.1098/rsta.2014.0160.

Proshutinsky, A. and M. Johnson (1997). "Two circulation regimes of the wind-driven Arctic Ocean". In: *Journal of Geophysical Research: Oceans* 102 (C6), pp. 12493–12514. ISSN: 2156-2202. DOI: 10.1029/97JC00738.

Proshutinsky, A. *et al.* (2011). "Recent Advances in Arctic Ocean Studies Employing Models from the Arctic Ocean Model Intercomparison Project". In: *Oceanography* 24.3, pp. 102–113. ISSN: 10428275. DOI: 10.5670/oceanog.2011.61.

Rabe, B., M. Karcher, F. Kauker, U. Schauer, J. M. Toole, R. A. Krishfield, S. Pisarev, T. Kikuchi, and J. Su (2014). "Arctic Ocean basin liquid freshwater storage trend 19922012". In: *Geophysical Research Letters* 41.3, pp. 961–968. ISSN: 1944-8007. DOI: 10.1002/2013GL058121.

Rahmstorf, S., J. E. Box, G. Feulner, M. E. Mann, A. Robinson, S. Rutherford, and E. J. Schaffernicht (2015). "Exceptional twentieth-century slowdown in Atlantic Ocean overturning circulation". In: *Nature Climate Change* 5.5, pp. 475–480. ISSN: 1758-6798. DOI: 10.1038/nclimate2554.

Rigor, I. G., J. M. Wallace, and R. L. Colony (2002). "Response of Sea Ice to the Arctic Oscillation". In: *Journal of Climate* 15.18, pp. 2648–2663. ISSN: 0894-8755. DOI: 10.1175/1520-0442(2002)015<2648:ROSITT>2.0.CO;2.

Rudels, B. (2015). "Arctic Ocean circulation, processes and water masses: A description of observations and ideas with focus on the period prior to the International Polar Year 20072009". In: *Progress in Oceanography*. Oceanography of the Arctic and North Atlantic Basins 132, pp. 22–67. ISSN: 0079-6611. DOI: 10.1016/j.pocean.2013.11.006.

Sakai, S. and S. Imawaki (1981a). "Fourier Filtering in a Barotropic Polar Ocean Model". In: 19, pp. 118–125.

— (1981b). "Notes on linear and nonlinear barotropic flows in a polar circular basin". In: *Journal of the Oceanographical Society of Japan* 37.5, pp. 287–293. ISSN: 1573-868X. DOI: 10.1007/BF02070583.

Schulkes, R. M. S. M., L. W. Morland, and R. Staroszczyk (1998). "A finite-element treatment of sea ice dynamics for different ice rheologies". In: *International Journal for Numerical and Analytical Methods in Geomechanics* 22.3, pp. 153–174. ISSN: 1096-9853. DOI: 10.1002/(SICI)1096-9853(199803)22:3<153::AID-NAG912>3.0.CO;2-E.

Semenov, V. A. and M. Latif (2012). "The early twentieth century warming and winter Arctic sea ice". In: *The Cryosphere* 6.6, pp. 1231–1237. ISSN: 1994-0424. DOI: 10.5194/tc-6-1231-2012.

Spall, M. A. (2013). "On the Circulation of Atlantic Water in the Arctic Ocean". In: *Journal of Physical Oceanography* 43.11, pp. 2352–2371. ISSN: 0022-3670. DOI: 10.1175/JPO-D-13-079.1.

Steele, M., J. Morison, W. Ermold, I. Rigor, M. Ortmeyer, and K. Shimada (2004). "Circulation of summer Pacific halocline water in the Arctic Ocean". In: *Journal of Geophysical Research: Oceans* 109 (C2). ISSN: 2156-2202. DOI: 10.1029/2003JC002009.

Stephenson, D. B., V. Pavan, and R. Bojariu (1999). "Is the North Atlantic Oscillation a random walk?" In: *International Journal of Climatology* 20.1, pp. 1–18. ISSN: 1097-0088. DOI: 10.1002/(SICI)1097-0088(200001)20:1<1::AID-JOC456>3.0.CO;2-P.

Stroeve, J. C., M. C. Serreze, M. M. Holland, J. E. Kay, J. Malanik, and A. P. Barrett (2012). "The Arctics rapidly shrinking sea ice cover: a research synthesis". In: *Climatic Change* 110.3, pp. 1005–1027. ISSN: 0165-0009, 1573-1480. DOI: 10.1007/s10584-011-0101-1.

Sugimura, P. J. (2008). "Arctic Ocean circulation in an idealized numerical model". Thesis. Massachusetts Institute of Technology.

Taniguchi, Y. and M. Yamada (2012). "A Note on the Transition of the Polar Cap Flow to the Westward Flow on a Rotating Sphere". In: *Theoretical and Applied Mechanics Japan* 60, pp. 29–42. DOI: 10.11345/nctam.60.29.

Thompson, D. W. J. and J. M. Wallace (1998). "The Arctic oscillation signature in the wintertime geopotential height and temperature fields". In: *Geophysical Research Letters* 25.9, pp. 1297–1300. ISSN: 1944-8007. DOI: 10.1029/98GL00950.

Tomczak, M. and J. S. Godfrey (2002). *Regional oceanography: An introduction*. 2nd. Vol. 15. Pergamon.

Tsubouchi, T. *et al.* (2012). "The Arctic Ocean in summer: A quasi-synoptic inverse estimate of boundary fluxes and water mass transformation". In: *Journal of Geophysical Research: Oceans* 117 (C1), p. C01024. ISSN: 2156-2202. DOI: 10.1029/2011JC007174.

Uotila, P. *et al.* (2006). "An energy-diagnostics intercomparison of coupled ice-ocean Arctic models". In: *Ocean Modelling* 11.1, pp. 1–27. ISSN: 1463-5003. DOI: 10.1016/j.ocemod.2004.11.003.

Vandenberghe, J., H. Renssen, D. M. Roche, H. Goosse, A. A. Velichko, A. Gorbunov, and G. Levavasseur (2012). "Eurasian permafrost instability constrained by reduced sea-ice cover". In: *Quaternary Science Reviews* 34, pp. 16–23. ISSN: 0277-3791. DOI: 10.1016/j.quascirev.2011.12.001.

Wallcraft, A. J., A. B. Kara, and H. E. Hurlburt (2005). "Convergence of Laplacian diffusion versus resolution of an ocean model". In: *Geophysical Research Letters* 32.7, p. L07604. ISSN: 1944-8007. DOI: 10.1029/2005GL022514.

Walsh, J. E., F. Fetterer, J. S. Stewart, and W. L. Chapman (2017). "A database for depicting Arctic sea ice variations back to 1850". In: *Geographical Review* 107.1, pp. 89–107. ISSN: 1931-0846. DOI: 10.1111/j.1931-0846.2016.12195.x.

Wang, M. and J. E. Overland (2009). "A sea ice free summer Arctic within 30 years?" In: *Geophysical Research Letters* 36.7, p. L07502. ISSN: 1944-8007. DOI: 10.1029/2009GL037820.

Wanner, H., S. Brönnimann, C. Casty, D. Gyalistras, J. Luterbacher, C. Schmutz, D. B. Stephenson, and E. Xoplaki (2001). "North Atlantic Oscillation Concepts And Studies". In: *Surveys in Geophysics* 22.4, pp. 321–381. ISSN: 0169-3298, 1573-0956. DOI: 10.1023/A:1014217317898.

Willmott, A. J. and E. Gavilan Pascual-Ahuir (2017). "Planetary and Gravity Waves in a Polar Basin". In: *Journal of Physical Oceanography* 47.6, pp. 1433–1440. ISSN: 0022-3670. DOI: 10.1175/JPO-D-16-0253.1.

Willmott, A. J. and M. V. Luneva (2015). "Steady, barotropic wind and boundary-driven circulation on a polar plane". In: *Geophysical & Astrophysical Fluid Dynamics* 109.3, pp. 216–233. ISSN: 0309-1929. DOI: 10.1080/03091929.2015.1050589.

Wingham, D. J. *et al.* (2006). "CryoSat: A mission to determine the fluctuations in Earths land and marine ice fields". In: *Advances in Space Research*. Natural Hazards and

Oceanographic Processes from Satellite Data 37.4, pp. 841–871. ISSN: 0273-1177. DOI: 10.1016/j.asr.2005.07.027.

Yang, J. (2005). "The Arctic and Subarctic Ocean Flux of Potential Vorticity and the Arctic Ocean Circulation*". In: *Journal of Physical Oceanography* 35.12, pp. 2387–2407. ISSN: 0022-3670. DOI: 10.1175/JPO2819.1.

Yang, J., A. Proshutinsky, and X. Lin (2016). "Dynamics of an idealized Beaufort Gyre: 1. The effect of a small beta and lack of western boundaries". In: *Journal of Geophysical Research: Oceans* 121.2, pp. 1249–1261. ISSN: 2169-9291. DOI: 10.1002/2015JC011296.

Zhang, J. and M. Steele (2007). "Effect of vertical mixing on the Atlantic Water layer circulation in the Arctic Ocean". In: *Journal of Geophysical Research: Oceans* 112 (C4). ISSN: 2156-2202. DOI: 10.1029/2006JC003732.

Zhang, X., M. Ikeda, and J. E. Walsh (2003). "Arctic Sea Ice and Freshwater Changes Driven by the Atmospheric Leading Mode in a Coupled Sea IceOcean Model". In: *Journal of Climate* 16.13, pp. 2159–2177. ISSN: 0894-8755. DOI: 10.1175/2758.1.

Zhong, W. and J. Zhao (2014). "Deepening of the Atlantic Water Core in the Canada Basin in 200311". In: *Journal of Physical Oceanography* 44.9, pp. 2353–2369. ISSN: 0022-3670. DOI: 10.1175/JPO-D-13-084.1.